

# Monitoring of Protein and pH Levels in Human Biofluids using FD-SOI Silicon Nanowire Arrays

Présentée le 22 septembre 2023

Faculté des sciences et techniques de l'ingénieur  
Laboratoire des dispositifs nanoélectroniques  
Programme doctoral en microsystemes et microélectronique

pour l'obtention du grade de Docteur ès Sciences

par

**Luca CAPUA**

Acceptée sur proposition du jury

Prof. L. G. Villanueva Torrijo, président du jury  
Prof. M. A. Ionescu, Dr D. Locca, directeurs de thèse  
Prof. A. van den Berg, rapporteur  
Prof. A. Hierlemann, rapporteur  
Prof. C. Enz, rapporteur

*“Time’s arrow neither stands still nor reverses. It merely marches forward.”*

from BoJack Horseman



*“La freccia del Tempo non rimane ferma, né torna indietro. Si muove semplicemente avanti.”*

da BoJack Horseman



# Acknowledgements

The reality of my Ph.D. journey proved to be vastly different from my initial expectations. Yet, I am grateful for the remarkable individuals who were part of this experience, and I extend my heartfelt appreciation to many of them.

First and foremost, I would like to express my gratitude to my advisor, Professor Adrian Ionescu. He allowed me to undertake this journey, and to be part of a challenging project that spanned different topics and areas of expertise, helping me expand my knowledge and foster my ability to be independent. I am also thankful to my co-advisor, Dr. Didier Locca, for providing valuable insights about the medical world and engaging in interesting discussions about the cross-disciplinary need of engineering and medicine. Moreover, I want to extend my appreciation to the jury president of my oral exam, Prof. Guillermo Villanueva, and the esteemed jury members: Prof. Christian Enz, Prof. Andreas Hierlemann, and Prof. Albert van den Berg. Especially, I want to thank Prof. van den Berg for the numerous informal discussions we had during his time at Nanolab.

This journey would not have been the same without my colleagues in Nanolab, both former and current ones. I decided to join Nanolab following Nicoló's suggestions, even though he never admitted it, and probably never will. Therefore, I am grateful to him for giving me the opportunity to meet so many wonderful people over the last 5 years. Thanks to Emanuele for his kindness, his contagious energy, and warm welcome at Nanolab. Matteo, thank you for our numerous discussions and the way you shared your perspective of the world with me. Among the former Nanolab members, my sincere gratitude goes also to the people from the other end of the corridor for their help at the beginning of my Ph.D.: Francesco, Maneesha, Junrui, and Fatemeh. I want to extend my heartfelt thanks to the recent generation of Nanolabers. Michele, Victoria, and Justyna: even with your Ph.D. already in hand, you effortlessly became part of the group, spreading kindness and creating a fun and enjoyable atmosphere. Cyrille, Zahra, Vanessa, Ehsan, and Eloi (Nanolab?) the youngest Ph.D. generation, thank you for bringing fresh energy to the lab and for not running away after witnessing my struggles during the last months of my Ph.D. I wish each of you success in your PhD journeys. I want to express my gratitude to Ali Gilani and Hung-Wei for always being ready to help anyone in the lab, wearing smiles on your faces, and trying to lift everyone's spirits. A big thank you goes out to Lotte for her contagious happiness, positive mood, and exceptional ability in organizing

## Acknowledgements

---

group events. I am especially thankful to you, Lotte, for saving my life during our Consortium Meeting in Enschede. A big thank you must go to Teddy, the best office mate I could have hoped for. You have been an example of resilience, a great colleague, and a wonderful friend. I need to express my sincere gratitude to three people in particular, without whom I could not have finished my Ph.D. Fabio, thank you for the time you dedicated to helping me, for the scientific support, and your patience. You have a bright future ahead. Yann, this work would not have been possible without your invaluable assistance. You helped me and shared with me not only the research topic but also the struggle. You always kept helping me and for this reason, I extend my most sincere thanks to you. Ali Saeidi, you have been a constant source of encouragement, even when I doubted my results. You generously shared your knowledge, and you never hesitated to offer your precious time to help. Thank you. Other than a professional relationship I have shared a deep friendship with three people in particular. I spent months writing the thesis with Sadegh, and I am sincerely sure that only thanks to his presence I could achieve this final result. He has been the perfect buddy for this journey, surpassing cultural barriers and differences, every day listening to my discussions about social justice. Felix, he not only taught me how to kite, but also how to enjoy more life. I have some of the best memories of the last five years with you. Thank you for the wonderful times we've had together. Finally, I want to express my gratitude to Carlotta. We spent almost the entire Ph.D. journey together, and you welcomed me into the lab like no one else. Your friendship has meant a lot to me. Thanks to all the other people I met in the last five years with whom I developed sincere friendships, in particular, Jacopo, Chiara, Mariazel, and Helen. I want to thank the Nanotech community: Massimo and Alessandro, it's always a pleasure to see your redheads and to exchange words with you. Thank you to the people with whom I shared a house here in Lausanne: Matteo, Andrea, and Gabriele. It has been an immense pleasure to share this part of my life with you. Thanks to all the other members of the Nanotech 13 community in Lausanne: Valentina, Iuts, and Fedele.

From the past, through the present, and to the future, two people have never failed to make me feel their friendship, even when hundreds of kilometers were separating us. An immense gratitude goes to Simone and Federico, two precious friends I could not do without.

I could spend hours thinking about how to thank my dad, my mum, and my brother, but one thing immediately comes to mind for which I am grateful: thank you for teaching me the value of humbleness and respecting others. Thank you for showing me your support in your unique ways. And thank you, Mum and Dad, for the hard work you put in to allow me to undertake my journey. Lastly, I want to thank the person who has been closest to me in the last five years, someone who was able to calm me down, cheer me up, and help me think calmly about what was best at each moment. Most importantly, she made me smile because she is 'uno spasso'. Francesca, thank you for being with me from the start to the end of this journey.

To all of you mentioned above, and to everyone else who played a part in my journey, I am deeply grateful for your contributions and support throughout my Ph.D. Thank you all.

*Lausanne, 22 September 2023*









# Abstract

Medical research and technological advancements are heading towards tailored healthcare approaches that prioritize individual needs, allowing for more accurate diagnoses, more effective treatments, and better patient outcomes overall. One such approach is the use of digital twins, which involves creating a unique computational and technological representation of an individual's medical copy based on data collected from multiple edge AI technologies. Digital twins can help develop new treatments and medications, optimize drug dosages, and predict side effects before they occur. Furthermore, they can identify potential risk factors and detect early symptoms before they become severe, aiding in disease prevention. Moving towards preventive and personalized healthcare requires real-time monitoring of key biomarkers directly on-body. However, there is still a need for robust and low-power wearable sensors that can continuously monitor multiple biomarkers in human biofluids. These sensors would have the potential to serve two primary purposes: firstly, early detection of change in concentration of biomarkers, enabling doctors to make faster treatment decisions. Secondly, the large amount of data collected from different patients in hospitals can be used to develop personalized healthcare solutions that improve patient outcomes. FET-based biosensors have emerged as promising candidates for the next generation of low-power and label-free biosensors due to their ease of miniaturization, low-power consumption, and the possibility of integration into CMOS technology. This project aims to lay the groundwork for the creation of robust and low-power multimodal biomarker ISFET-type wearable sensors that can quasi-continuously monitor multiple biomarkers in human interstitial fluid. In this work, fully-depleted silicon nanowire array Field-Effect Transistors (SiNWs FET) on SOI technology have been proposed as biosensors to detect biomarkers in human biofluids, such as interstitial fluid. Two different platforms have been fabricated, one entirely at the Centre of MicroNanotechnology (CMi) of EPFL, and one at CEA-LETI in Grenoble. The fabricated SiNW FETs have demonstrated excellent performance in terms of electrical characterization, with an OFF to ON ratio larger than 6 orders of magnitude and a subthreshold swing of 80 mV/decade, two key requirements to obtain an efficient biosensor. A dependable method of surface functionalization for detecting C-Reactive Protein (CRP) has been developed. This method employs antibody fragments on high- $\kappa$  oxides, and it has been extensively validated using various characterization techniques such as Surface Plasmon Resonance (SPR), X-Ray spectroscopy (XPS), and Quartz Crystal Microbalance with Dissipation Monitoring (QCM-D). Efficient and reliable monitoring of C-Reactive Protein in dual-gate configuration and preliminary results in constant current mode have been demonstrated. Moreover, we have proven a reliable and reproducible detection

of pH levels both in buffer and human ISF-like solutions. The intrinsic double gate structure of the system has been exploited to obtain signal amplification (from Nernstian sensitivity of 59 mV/pH up to 3 V/pH), and a constant current configuration has been introduced to obtain a system with voltage output and the possibility to have fine-tuning of the output dose response through the selection of the system operating point. The results obtained in this thesis move toward real-life applications of wearable sensing, thus considering stability, reliability, and miniaturization. The proposed biosensors offer a promising solution for the detection of biomarkers in human biofluids, enabling real-time health evolution monitoring, and preventive and personalized care.

**Keywords:** Biosensors, Biomarkers, Field-Effect Transistor (FET), Silicon Nanowires, Fully-Depleted FET, Silicon-on-Insulator, ISFET, MOSFET, label-free sensor, pH sensor, low-power, high- $\kappa$  dielectric, affinity-based biosensors, signal amplification, wearable sensors, Digital Twin, Edge-AI sensors, C-Reactive Protein, protein sensing, interstitial fluid (ISF), low-invasive sensors.

# Sommario

La ricerca medica e i progressi tecnologici si stanno dirigendo verso approcci sanitari personalizzati che danno priorità alle esigenze individuali, consentendo diagnosi più accurate, trattamenti più efficaci e risultati complessivamente migliori per i pazienti. Uno di questi approcci è l'uso dei Gemelli Digitali, che prevede la creazione di una rappresentazione computazionale e tecnologica unica della copia medica di un individuo, basata sui dati raccolti da più tecnologie di endpoint di Intelligenza Artificiale (Edge-AI) all'avanguardia. I gemelli digitali possono aiutare a sviluppare nuovi trattamenti e farmaci, ottimizzare i dosaggi e prevedere gli effetti collaterali prima che si verifichino. Inoltre, possono identificare potenziali fattori di rischio e rilevare i primi sintomi prima che diventino gravi, favorendo la prevenzione delle malattie. L'evoluzione verso una salute preventiva e personalizzata richiede il monitoraggio in tempo reale dei biomarcatori chiave direttamente sul corpo. Tuttavia, c'è ancora bisogno di sensori indossabili robusti e a basso consumo energetico, in grado di monitorare continuamente più biomarcatori nei biofluidi umani. Questi sensori potrebbero servire a due scopi principali: in primo luogo, il rilevamento precoce dei cambiamenti nella concentrazione dei biomarcatori, consentendo ai medici di prendere decisioni terapeutiche più rapide. In secondo luogo, la grande quantità di dati raccolti da diversi pazienti negli ospedali può essere utilizzata per sviluppare soluzioni sanitarie personalizzate che migliorino i risultati dei pazienti. I biosensori basati su transistori a effetto di campo (FET) sono emersi come candidati promettenti per la prossima generazione di biosensori a basso consumo e 'label-free', grazie alla loro facilità di miniaturizzazione, al basso consumo energetico e alla possibilità di integrazione nella tecnologia CMOS. Questo progetto mira a gettare le basi per la creazione di sensori indossabili di tipo ISFET (Transistori a effetto di campo sensibili a ioni) per biomarcatori multimodali, robusti e a basso consumo, in grado di monitorare in modo quasi continuo più biomarcatori nel liquido interstiziale umano. In questo lavoro, i transistor a effetto di campo ad array di nanofili di silicio (SiNWs FET) 'Fully Depleted' su tecnologia SOI (silicio su isolante) sono stati proposti come biosensori per rilevare i biomarcatori nei biofluidi umani, come il liquido interstiziale. Sono state fabbricate due diverse piattaforme, una interamente presso il Centro di MicroNanotecnologie (CMi) dell'EPFL e una presso il CEA-LETI di Grenoble. I FET SiNW fabbricati hanno dimostrato prestazioni eccellenti in termini di caratterizzazione elettrica, con un rapporto OFF/ON superiore a 6 ordini di grandezza e una 'subthreshold slope' di 80 mV/decade, due requisiti fondamentali per ottenere un biosensore efficiente. È

stato sviluppato un metodo affidabile di funzionalizzazione della superficie per rilevare la Proteina C-Reattiva (PCR). Questo metodo impiega frammenti di anticorpi su ossidi ad alta costante dielettrica (high- $\kappa$ ) ed è stato ampiamente convalidato utilizzando varie tecniche di caratterizzazione, come la risonanza plasmonica di superficie (SPR), la spettroscopia a raggi X (XPS) e la microbilancia a cristallo di quarzo con monitoraggio della dissipazione (QCM-D). È stato dimostrato un monitoraggio efficiente e affidabile della proteina C-reattiva in configurazione dual-gate e risultati preliminari in modalità di corrente costante. Inoltre, abbiamo dimostrato un rilevamento affidabile e riproducibile dei livelli di pH sia in soluzione buffer che in soluzione che rispecchia il liquido interstiziale della pelle umana. La struttura intrinseca a doppio gate del sistema è stata sfruttata per ottenere l'amplificazione del segnale (da una sensibilità nernstiana di 59 mV/pH fino a 3 V/pH), ed è stata introdotta una configurazione a corrente di drain costante per ottenere un sistema con un'uscita in tensione e la possibilità di avere una regolazione fine della risposta alla dose in uscita attraverso la selezione del punto di bias del sistema. I risultati ottenuti in questa tesi si orientano verso applicazioni reali di rilevamento indossabile, tenendo conto di stabilità, affidabilità e miniaturizzazione. I biosensori proposti offrono una soluzione promettente per la rilevazione di biomarcatori nei biofluidi umani, consentendo il monitoraggio in tempo reale dell'evoluzione della salute, la prevenzione e la cura personalizzata.

**Parole chiave:** Biosensori, Biomarcatori, Transistore a effetto di campo (FET), Nanofili di silicio, FET a svuotamento completo, silicio su isolante (SOI), ISFET, MOSFET, sensori label-free, sensore di pH, sensori a basso consumo, dielettrici ad alta costante dielettrica, biosensori basati su affinità, amplificazione di segnali, sensori indossabili, Gemelli Digitali, sensori Edge-AI, Proteina C-Reattiva, sensori di proteine, liquido interstiziale (ISF), sensori a bassa invasività.

# Contents

<b>Acknowledgements</b>	<b>iii</b>
<b>Abstract</b>	<b>vi</b>
<b>Sommario</b>	<b>ix</b>
<b>Contents</b>	<b>x</b>
<b>List of Figures</b>	<b>xiv</b>
<b>List of Tables</b>	<b>xix</b>
<b>Acronyms and abbreviations</b>	<b>xxiii</b>
<b>List of symbols</b>	<b>xxvii</b>
<b>List of elements and materials</b>	<b>xxx</b>
<b>Thesis Outline</b>	<b>1</b>
<b>1 Introduction</b>	<b>5</b>
1.1 Biomarkers monitoring for Digital Twins applications . . . . .	5
1.2 Interstitial Fluid as a biological fluid of interest . . . . .	7
1.3 Biomarkers sensing with FET technology . . . . .	18
1.3.1 The Field Effect Transistor . . . . .	18
1.3.2 The Ion-Sensitive Field-Effect-Transistor . . . . .	26
1.3.3 FET-based biosensors: limitations . . . . .	31
1.4 SiNWs as biosensors: state-of-the-art . . . . .	33
1.5 Summary . . . . .	35
<b>2 Silicon nanowires technology</b>	<b>37</b>
2.1 Introduction . . . . .	37
2.2 CEA-LETI silicon nanowire arrays . . . . .	38
2.2.1 Chip description and fabrication process flow . . . . .	38
2.2.2 DC Electrical characterization . . . . .	40
2.3 Fabrication and characterization of in-house SiNWs biosensors . . . . .	43

2.3.1	TCAD simulations for source and drain regions implantation . . . . .	43
2.3.2	Cleanroom process flow for SiNWs-FET fabrication . . . . .	47
2.3.3	Ohmic contacts on thin silicon and doping level test . . . . .	54
2.3.4	Critical steps in the fabrication process flow . . . . .	56
2.3.5	Electrical characterization of the fabricated SiNWs . . . . .	58
2.3.6	On-chip Ag/AgCl quasi reference electrode . . . . .	60
2.4	Summary . . . . .	61
<b>3</b>	<b>Surface functionalization and methods</b>	<b>65</b>
3.1	Surface functionalization study . . . . .	65
3.1.1	Materials . . . . .	65
3.1.2	Employed functionalization for antibody fragments immobilization on high- $\kappa$ oxide surfaces . . . . .	66
3.1.3	Surface Plasmon Resonance (SPR) . . . . .	67
3.1.4	X-Ray Spectroscopy (XPS) . . . . .	70
3.1.5	Quartz Crystal Microbalance (QCM) . . . . .	74
3.2	Measurement setup . . . . .	78
3.2.1	Low-volume microfluidic . . . . .	78
3.2.2	Printed-Circuit-Board . . . . .	81
3.3	Electrical characterization methods . . . . .	81
3.3.1	Reference-compensated response . . . . .	82
3.3.2	Front-Gate operation . . . . .	83
3.3.3	Double-gate operation . . . . .	84
3.3.4	Constant Drain current operation . . . . .	87
3.4	Summary . . . . .	95
<b>4</b>	<b>pH sensing</b>	<b>97</b>
4.1	pH monitoring . . . . .	97
4.1.1	pH monitoring in buffer . . . . .	98
4.1.2	pH monitoring in ISF-like solutions . . . . .	100
4.1.3	In-house pH sensing . . . . .	108
4.2	Integration and Compatibility Demonstration of the pH Sensor with On-Chip Read-Out through an Intermediary Board . . . . .	113
4.3	Summary . . . . .	117
<b>5</b>	<b>C-Reactive Protein sensing</b>	<b>119</b>
5.1	C-Reactive Protein sensing . . . . .	119
5.1.1	Front-Gate operation . . . . .	120
5.1.2	Back-gate configuration . . . . .	121
5.1.3	Constant drain current operation . . . . .	125
5.2	Summary . . . . .	129

## CONTENTS

---

<b>6 Conclusions and future perspective</b>	<b>131</b>
6.1 Main achievements . . . . .	131
6.2 Future Perspective . . . . .	133
6.3 Concluding remarks . . . . .	135
<b>A Runcard of SiNWs fabrication</b>	<b>137</b>
<b>B TEM lamella preparation</b>	<b>141</b>
<b>C Script for source and drain implantation TCAD simulation</b>	<b>143</b>
<b>D Read-out circuit and sensor demonstrator: setup</b>	<b>145</b>
<b>Bibliography</b>	<b>147</b>
<b>Publications</b>	<b>175</b>
<b>Curriculum Vitae</b>	<b>177</b>





# List of Figures

1.1	Biosensor schematic. . . . .	7
1.2	Skin anatomy. . . . .	7
1.3	Dwelled or external sensors on microneedles array. . . . .	10
1.4	Tehrani et al. Microneedle-based sensor in ISF. . . . .	10
1.5	Microneedle-based sensors in ISF. . . . .	11
1.6	Schematic of the final integrated sensor, with passive microfluidic, and microneedles ISF extractor. . . . .	12
1.7	Microneedle-based sensors in ISF. . . . .	15
1.8	Rabbani et al. CRP biosensor. . . . .	16
1.9	Microneedle-based sensors in ISF. . . . .	17
1.10	Tu et al. CRP biosensor in sweat. . . . .	18
1.11	MOS structure. . . . .	19
1.12	MOSFET transfer characteristic. . . . .	20
1.13	Equivalent capacitor networks for bulk and FD-SOI MOS. . . . .	23
1.14	Oxide-electrolyte interface models. . . . .	26
1.15	Schematic comparison between MOSFET and ISFET. . . . .	28
1.16	Site-binding model for charging mechanism of an oxide-electrolyte interface. . . . .	29
1.17	Debye screening in affinity-based detection mechanism. . . . .	32
2.1	CEA-LETI chip: picture and layout. . . . .	38
2.2	CEA-LETI SiNWs process flow. . . . .	39
2.3	AFM and SEM images of the CEA-LETI SiNW array. . . . .	40
2.4	Transfer and output characteristics of a CEA-LETI SiNW array. . . . .	41
2.5	SiNW array subthreshold slope and transconductance efficiency. . . . .	42
2.6	Back-gate transfer characteristics. . . . .	43
2.7	Stopping layer thickness TCAD simulation results. . . . .	44
2.8	Source and drain simulated phosphorous concentration profiles at different implantation energy values. . . . .	45
2.9	Source and drain simulated active dopants concentration at different implantation energy values. . . . .	45
2.10	Source and drain simulated phosphorous concentration at different implantation dose values. . . . .	46

2.11 Source and drain simulated active dopants concentration at different implanta- tion dose values. . . . .	47
2.12 Fabrication step: top Si layer thinning. . . . .	48
2.13 Fabrication step: electron beam markers creation. . . . .	48
2.14 Fabrication step: source and drain regions implantation. . . . .	49
2.15 Fabrication step: silicon nanowires creation by electron beam lithography. . . . .	49
2.16 Fabrication step: metallic stopping layers deposition for the next Ion Beam Etching step. . . . .	50
2.17 Fabrication step: gate and field oxide deposition. . . . .	50
2.18 Fabrication step: source and drain region opening by ion beam etching. . . . .	51
2.19 Fabrication step: metallic lines deposition. . . . .	51
2.20 Fabrication step: passivation layer deposition. . . . .	52
2.21 Fabrication step: opening-up of the passivation layer to reach SiNWs surface. . . . .	52
2.22 Fabricated SiNWs chip. . . . .	53
2.23 TEM, STEM, and EDS characterization of the in-house fabricated SiNWs. . . . .	54
2.24 On-chip test structures to measure source and drain doping level. . . . .	55
2.25 Linear I-V curves between two contacts placed at an increasing distance on a doped Si line. . . . .	56
2.26 Optical microscope pictures highlighting the lateral over-etching. . . . .	57
2.27 Flowing current between two random contacts on the chip. . . . .	57
2.28 Transfer and output characteristics of the in-house fabricated SiNW array. . . . .	58
2.29 Subthreshold swing and transconductance efficiency of the in-house fabricated SiNW array. . . . .	59
2.30 Back-gate transfer characteristic and threshold voltage shift of the in-house fabricated SiNW array. . . . .	59
2.31 Quasi reference electrode stability study in ISF-like solutions. . . . .	61
3.1 High- $\kappa$ oxide surface functionalization process. . . . .	67
3.2 Surface Plasmon resonance study in buffer solutions. . . . .	69
3.3 Surface Plasmon resonance Fab study in ISF solutions. . . . .	70
3.4 X-ray spectroscopy carbon peak modulation after each functionalization step. . . . .	71
3.5 X-ray spectroscopy nitrogen peak modulation after each functionalization step. . . . .	73
3.6 QCM frequency shift upon anti-CRP immobilization. . . . .	76
3.7 QCM frequency shift upon BSA injections. . . . .	77
3.8 QCM frequency shift upon CRP injections. . . . .	78
3.9 Soft lithography process for PDMS microfluidic stamps fabrication. . . . .	79
3.10 Influence of PDMS transferring on the chip on the transistor performance. . . . .	80
3.11 PDMS microfluidics on the two different chips. . . . .	81
3.12 Printed circuit boards used to facilitate the SiNWs chips measurement. . . . .	82
3.13 Reference-compensated schematic representation. . . . .	83
3.14 Front-gate and back-gate operation schematics. . . . .	84
3.15 Silicon on Insulator Fully-Depleted Transistor with dual gate structure. . . . .	85

## LIST OF FIGURES

---

3.16	Constant drain current operation schematic. . . . .	87
3.17	Obtained results in constant current operation and weak inversion regime. . .	89
3.18	Obtained results in constant current operation and moderate inversion regime (1). 90	
3.19	Obtained results in constant current operation and moderate inversion regime (2). 90	
3.20	Obtained results in constant current operation and moderate inversion regime (3). 91	
3.21	Obtained results in constant current operation and strong inversion regime (1). 92	
3.22	Obtained results in constant current operation and strong inversion regime (2). 93	
3.23	Obtained results in constant current operation and strong inversion regime with the proposed model fit. . . . .	94
3.24	Constant-current method sensitivity in different working regimes. . . . .	95
4.1	pH sensing in buffer and in top-gate configuration with the first batch of CEA- LETI chips. . . . .	99
4.2	pH sensing in buffer and in back-gate configuration with the first batch of CEA- LETI chips. . . . .	99
4.3	Real-time pH sensing in buffer and in top-gate configuration with the first batch of CEA-LETI chips. . . . .	100
4.4	Transmission electron microscopy cross-section of the SiNW arrays. . . . .	101
4.5	pH sensing in buffer solutions and in top-gate configuration with the second batch of CEA-LETI chips. . . . .	102
4.6	pH sensing in ISF-like solutions and in top-gate configuration with the second batch of CEA-LETI chips. . . . .	103
4.7	Comparison between pH response in buffer and ISF-like solutions. . . . .	104
4.8	Real-time pH sensing in ISF-like solution in top-gate configuration with the second batch of CEA-LETI chips. . . . .	104
4.9	pH calibration curve in ISF-like solution and in top-gate configuration and model prediction of the pH values of unknown samples. . . . .	105
4.10	Real-time pH sensing in ISF-like solution in constant drain current configuration with the second batch of CEA-LETI chips. . . . .	106
4.11	pH calibration curve in ISF-like solution and in constant drain current configu- ration with the second batch of CEA-LETI chips. . . . .	107
4.12	SEM and optical images of one of the SiNW arrays fabricated at CMi. . . . .	108
4.13	Repeated measurement at different pH in top-gate configuration with an in- house fabricated SiNW array chip. . . . .	109
4.14	pH sensing in buffer and in top-gate configuration with the in-house fabricated chips. . . . .	110
4.15	Repeated measurement at different pH in back-gate configuration with an in- house fabricated SiNW array chip. . . . .	111
4.16	pH sensing in buffer and in back-gate configuration with the in-house fabricated chips. . . . .	112
4.17	Schematic representing the interface system between pH and lactate sensors with the on-chip read-out. . . . .	113

4.18 pH measurements conducted using the on-chip readout system developed by imec. . . . .	115
4.19 Simultaneous pH and lactate sensing. . . . .	116
5.1 CRP monitoring in 0.01xPBS in top-gate configuration with the second batch of CEA-LETI chips. . . . .	121
5.2 Comparison between sensor's response to CRP in top-gate configuration in 0.01x and 0.1xPBS. . . . .	122
5.3 CRP detection in back-gate configuration in 0.1xPBS: drift, hysteresis study, and response to blank injections for CEA-LETI chips. . . . .	123
5.4 CRP detection in back-gate configuration in 0.1xPBS: dose-response at different back-gate voltages. . . . .	124
5.5 CRP detection in back-gate configuration in 0.1xPBS: current sensitivity for different back-gate voltage values. . . . .	125
5.6 CRP detection in constant drain current configuration in 0.1xPBS. . . . .	126
5.7 CRP Voltage sensitivity in constant current configuration in 0.1xPBS . . . . .	127
B.1 TEM Lamella preparation. . . . .	141
B.2 TEM diffraction patterns. . . . .	142
D.1 Biosensor and chip-readout system. . . . .	145

# List of Tables

1.1	Comparison between plasma and ISF composition. . . . .	8
1.2	Different oxides pH sensitivity. . . . .	31
1.3	SiNW FET as biosensors, previous works. . . . .	34
2.1	ISF-like solution composition. . . . .	60
2.2	SiNW platforms performance comparison. . . . .	62
3.1	Description of the two channels for the SPR experiment, conducted in buffer solutions. . . . .	68
3.2	Description of the two channels for the SPR experiment, conducted in ISF-like solutions. . . . .	68
3.3	Different electrical methods employed for pH and CRP sensing. . . . .	87
4.1	Comparison of pH readings in ISF-like solution by the SiNWs in top-gate configuration and a commercial pH meter. . . . .	105
4.2	Comparison of pH readings in ISF-like solution by the SiNWs in constant drain current configuration and a commercial pH meter. . . . .	107
5.1	CRP electrical detection methods performance comparison. . . . .	129



# Acronyms

<b>1D</b>	One Dimensional
<b>2D</b>	Two Dimensional
<b>3D</b>	Three Dimensional
<b>4PL</b>	4-Parameter Logistic
<b>AC</b>	Alternating current
<b>AFM</b>	Atomic Force Microscopy
<b>AI</b>	Artificial Intelligence
<b>ALD</b>	Atomic Layer Deposition
<b>ASIC</b>	Application-Specific Integrated Circuit
<b>BHF</b>	Buffered hydrofluoric acid
<b>CE</b>	Counter Electrode in a electrochemical cell
<b>CEA-LETI</b>	Grenoble Research Institute for Electronics and Information Technologies
<b>CI<sub>ME</sub></b>	Interdisciplinary Centre for Electron Microscopy
<b>CMi</b>	Center of MicroNanoTechnology
<b>CMOS</b>	Complementary Metal-Oxide-Semiconductor
<b>CRP</b>	C-Reactive Protein
<b>cTnI</b>	Cardiac Troponin I
<b>CVD</b>	Chemical Vapor Deposition
<b>DC</b>	Direct Current
<b>DUT</b>	Device Under Test
<b>e-beam</b>	Electron Beam
<b>e.g.</b>	Exempli Gratia
<b>EDS</b>	Energy-Dispersive X-ray Spectroscopy
<b>EGFET</b>	Extendend Gate Field-Effect Transistor
<b>ELISA</b>	Enzyme-Linked Immunosorbent Assay
<b>EOT</b>	Equivalent Oxide Thickness
<b>EPFL</b>	École Polytechnique Fédérale de Lausanne



<b>F(ab)<sub>2</sub></b>	Two Fragment Antigen-Binding regions of an antibody
<b>Fab</b>	Fragment Antigen-Binding region of an antibody
<b>FD-SOI</b>	Fully Depleted Silicon On Insulator
<b>FET</b>	Field-Effect Transistor
<b>FIB</b>	Focused Ion Beam
<b>FinFET</b>	Fin Field-Effect Transistor
<b>HDL</b>	High-Density Lipoprotein
<b>IC</b>	Integrated Circuit
<b>ISF</b>	Interstitial Fluid
<b>ISFET</b>	Ion-sensitive Field-Effect Transistor
<b>LDL</b>	Low-Density Lipoprotein
<b>LUT</b>	Liquid Under Test
<b>MOSFET</b>	Metal-Oxide-Semiconductor Field-Effect Transistor
<b>MUX</b>	Multiplexer
<b>NW</b>	Nanowire
<b>PCB</b>	Printed Circuit Board
<b>PVD</b>	Physical Vapor Deposition
<b>QCM</b>	Quartz-Crystal Microbalance
<b>QCM-D</b>	Quartz-Crystal Microbalance with Dissipation mechanism
<b>RCA</b>	Radio Corporation of America (cleaning)
<b>RE</b>	Reference Electrode in a electrochemical cell
<b>SaO<sub>2</sub></b>	Oxygen Saturation of arterial blood
<b>SEM</b>	Scanning Electron Microscopy
<b>SiNW</b>	Silicon Nanowire
<b>SMB</b>	SubMiniature version B (cables)
<b>SMU</b>	Source Monitor Unit
<b>SOI</b>	Silicon On Insulator
<b>SP</b>	Surface Plasmon
<b>SPR</b>	Surface Plasmon Resonance
<b>STEM</b>	Scanning Transmission Electron Microscopy
<b>TCAD</b>	Technology Computer-Aided Design

## Acronyms

---

<b>TEM</b>	Transmission Electron Microscopy
<b>UHV</b>	Ultra-High Vacuum
<b>UV</b>	Ultra-Violet
<b>WE</b>	Working Electrode in a electrochemical cell
<b>XPS</b>	X-Ray Spectroscopy



# List of symbols

Symbol	Unit	Description
$A$	$m^2$	Surface area
$C_{Box}$	F	Bottom oxide capacitance in a MOS
$C_D$	F	Depletion capacitance in a MOS
$C_{Liq}$	F	Liquid under test capacitance
$C_{Si}$	F	Bulk silicon capacitance in a MOS
$C_{Tox}$	F	Top oxide capacitance in a MOS
$C_{diff}$	F	Diffusion capacitance
$C_{ox}$	F	Oxide capacitance in a MOS
$C_{ss}$	F	Capacitance related to the interface trapped charge in a MOS
$E_{ref}$	V	Constant reference electrode potential
$G$	Pa	Quartz shear modulus
$I$	A	Current
$I_s$	M	Ionic strength
$I_{BG}$	A	Current flowing in the back-gate terminal in a MOSFET
$I_{DS}$	A	Current flowing between source and drain terminals in a MOSFET
$I_D$	A	Current flowing in the drain terminal in a MOSFET
$I_G$	A	Current flowing in the gate terminal in a MOSFE.
$I_S$	A	Current flowing in the source terminal in a MOSFET
$K_D$	M	Dissociation constant
$L$	m	Transistor's channel length
$N_s$	-	Amphoteric charged group density
$N_A$	$m^{-3}$	Acceptor-type dopant concentration
$N_D$	$m^{-3}$	Donor-type dopant concentration
$Q_D$	C	Depletion charge in a MOS
$Q_{ox}$	C	Oxide charge in a MOS
$Q_{ss}$	C	Interface trapped charge in a MOS
$R_{sheet}$	$\Omega/\text{square}$	Sheet resistance
$SS$	mV/decade	Subthreshold swing
$S_I$	-	Relative current sensitivity

Symbol	Unit	Description
$T$	K	Temperature
$V$	V	Voltage
$V_{BGS}$	V	Voltage drop between back-gate and source terminal
$V_{BG}$	V	Voltage drop between back-gate terminal and ground
$V_{DS}$	V	Voltage drop between drain and source terminals
$V_D$	V	Voltage drop between drain terminal and ground
$V_{GB}$	V	Voltage drop between gate and bulk terminals
$V_{GS}$	V	Voltage drop between gate and source terminal
$V_{GS}$	V	Voltage drop between gate terminal and ground
$V_{REF}$	V	Voltage drop between reference electrode in a ISFET and ground
$V_S$	V	Voltage drop between source terminal and ground
$V_{th}$	V	Threshold voltage
$W$	m	Transistor's channel width
$X^{sol}$	V	Surface dipole potential
[B]	-	Amount of amphoteric charged group on the oxide surface
$\Phi_F$	eV	Difference between Fermi level and intrinsic Fermi level in bulk semiconductor
$\Phi_{MS}$	eV	Metal-Semiconductor work-function difference
$\Phi_S$	eV	Semiconductor work-function
$\Psi_0$	V	Electrostatic potential at the proximity of the oxide surface
$\Psi_{liquid}$	V	Bulk liquid potential
$\Psi_{ox}$	V	Gate oxide potential in a MOS
$\Psi_{surface}$	V	Electrostatic charged surface potential
$\Psi_s$	V	Silicon surface potential in a MOS
$\Psi_{target}$	V	Electrostatic potential created by a charged target analyte
$\beta$	mV/pH	pH top-gate sensitivity
$\beta_s$	-	Oxide buffer capacity
$\epsilon_0$	F·m <sup>-1</sup>	Vacuum permittivity = 8.85418782 × 10 <sup>-12</sup> F·m <sup>-1</sup>
$\epsilon_{high-\kappa}$	-	Material permittivity of an high- $\kappa$ material
$\epsilon_{material}$	-	Material permittivity
$\lambda$	V <sup>-1</sup>	Channel-length modulation
$\lambda_D$	m	Debye length
$\mu_n$	cm <sup>2</sup> /(V·s)	Electrons mobility
$\mu_p$	cm <sup>2</sup> /(V·s)	Holes mobility
$\rho$	kg·m <sup>-3</sup>	Material density
$\rho_{Si}$	$\Omega \cdot m$	Silicon resistivity
$a_{H_b^+}$	-	Bulk hydrogen ions activity
$a_{H_s^+}$	-	Surface hydrogen ions activity

## List of symbols

---

<b>Symbol</b>	<b>Unit</b>	<b>Description</b>
$f$	Hz	Frequency.
$f_0$	Hz	Resonance frequency
$g_m$	S	Transconductance
$k_B$	$\text{eV}\cdot\text{K}^{-1}$	Boltzmann constant = $8.6173436\times 10^{-5} \text{ eV}\cdot\text{K}^{-1}$
$m$	kg	Mass
$n_i$	$\text{m}^{-3}$	Carriers intrinsic concentration
$pH_B$	-	Bulk pH
$pH_s$	-	Surface pH
$q$	C	Elementary charge = $1.60206\times 10^{-19} \text{ C}$
$t_{high-\kappa}$	m	Dielectric constant of a High- $\kappa$ material
$t_{ox}$	m	Gate oxide thickness
$x_D$	m	Depletion region extension in MOS
RPM	-	Rotation per minute
sccm	-	standard cubic centimeter per minute



## List of elements and materials

<b>Ag</b>	Silver
<b>Al<sub>2</sub>O<sub>3</sub></b>	Aluminium oxide
<b>Au</b>	Gold
<b>AZ 1512 HS</b>	Positive Thin Resists for Wet Etching
<b>AZECI 3007</b>	High Resolution resist for dry etching
<b>BSA</b>	Bovine serum albumin
<b>C</b>	Carbon
<b>C<sub>4</sub>F<sub>8</sub></b>	Octafluorocyclobutane
<b>Ca<sup>2+</sup></b>	Calcium cation
<b>Cl</b>	Chlorine
<b>Cl<sup>-</sup></b>	Chlorine anion
<b>CO<sub>2</sub></b>	Carbon dioxide
<b>CSAR62</b>	High-contrast positive-tone e-beam resists
<b>DSG</b>	Di(N-succinimidyl) glutarate
<b>EDC</b>	1-ethyl-3-(3-dimethylaminopropyl) carbodiimide hydrochloride
<b>H<sub>2</sub>O</b>	Hydrogen dioxide, water
<b>H<sub>2</sub>O<sub>2</sub></b>	Hydrogen peroxide
<b>H<sub>3</sub>PO<sub>4</sub></b>	Phosphoric acid
<b>HCl</b>	Hydrochloric acid
<b>HEPES</b>	4-(2-hydroxyethyl)-1-piperazineethanesulfonic acid
<b>HF</b>	Hydrofluoric acid
<b>HfO<sub>2</sub></b>	Hafnium oxide
<b>HMDS</b>	Bis(trimethylsilyl)amine
<b>HSQ</b>	Hydrogen silsesquioxane, negative-tone e-beam resist
<b>IPA</b>	Isopropyl alcohol
<b>ITO</b>	Indium tin oxide



<b>K<sup>+</sup></b>	Potassium cation
<b>LOR</b>	Resist for bi-layer lift-off processing
<b>MES</b>	2-(N-morpholino)ethanesulfonic acid
<b>Mg<sup>2+</sup></b>	Magnesium cation
<b>MiBK</b>	Methyl isobutyl ketone
<b>MMA</b>	Methyl methacrylate
<b>MUA</b>	11-Mercaptoundecanoic acid
<b>N</b>	Nitrogen
<b>Na<sup>+</sup></b>	Sodium cation
<b>NH<sub>2</sub></b>	Amino radical
<b>NH<sub>3</sub><sup>+</sup></b>	Ammonium ion
<b>NH<sub>4</sub>OH</b>	Ammonium peroxide
<b>NHS</b>	N-hydroxysuccinimide
<b>Ni</b>	Nichel
<b>nLOF</b>	Thermally stable negative resist
<b>O</b>	Oxygen
<b>O<sub>2</sub></b>	Oxygen molecule
<b>PBS</b>	Phosphate-buffered saline
<b>PDMS</b>	Polydimethylsiloxane
<b>PMMA</b>	Poly(methyl methacrylate)
<b>Pt</b>	Platinum
<b>Si</b>	Silicon
<b>Si<sub>3</sub>N<sub>4</sub></b>	Silicon nitride
<b>SiO<sub>2</sub></b>	Silicon oxide
<b>Ta<sub>2</sub>O<sub>5</sub></b>	Tantalum pentoxide
<b>TEOS</b>	Tetraethyl Orthosilicate
<b>Ti</b>	Titanium
<b>TiO<sub>2</sub></b>	Titanium dioxide
<b>TnO<sub>2</sub></b>	Tin dioxide
<b>ZnO</b>	Zinc oxide
<b>ZrO<sub>2</sub></b>	Zirconium dioxide

# Thesis Outline

This thesis takes a holistic approach, where each subsequent chapter builds upon the notions introduced in the previous ones to provide a comprehensive and interconnected analysis of the topic. To ensure that each chapter is readable and comprehensible on its own, a brief introduction is provided at the beginning of each. These introductions summarize the key notions and concepts introduced in the preceding ones, providing readers with the necessary context to understand the current chapter's analysis. Overall, this approach allows readers to engage with the manuscript on both a chapter-by-chapter basis and as a cohesive whole.

## Thesis Objective

This thesis work proposes a Fully Depleted Silicon Nanowire Field-Effect Transistor as the ideal candidate for the transducer component of biosensor systems designed for wearable and low-power solutions. The entire project was conducted within the Digipredict European project, which aimed to develop *Edge AI-deployed Digital Twins for predicting disease progression and needs for early intervention in infectious and cardiovascular diseases beyond COVID-19* [1]. Wearable biosensors play a crucial role in real-time biomarker detection, serving as Edge-AI IoT nodes that collect physiological data to create a personalized health copy or Digital Twin. This data can be exploited for diagnosis and disease prediction, making biosensors a central element of personalized healthcare. The targeted human bio-fluid for this biosensor system is the interstitial fluid since it allows the usage of biomedical systems employing low-invasive technology. This fluid can be collected by piercing the skin to a depth of only a few hundred micrometers, painlessly and with minimal discomfort, just below the first epidermal layer. To meet the project goals, the biosensor system must be compatible with the electronic read-out system and the microneedle collection platform that has been designed and developed by consortium partners. This compatibility ensures that the biosensor system can be integrated seamlessly into the overall project framework and that it can provide reliable and accurate data for disease prediction and diagnosis.

## Chapter 1: Introduction and State of the Art

In this introductory chapter, the framework of the thesis is presented, along with the main objective of the work, the scientific research context, and the current needs in personalized

healthcare. In addition, the chapter introduces the concept of biosensors and their role in creating a Healthcare Digital Twin. The selection of dermal interstitial fluid as the fluid of interest for detecting selected biomarkers is explained, with a discussion of the most recent works on the composition of this fluid and the cutting-edge technologies for its collection. Furthermore, the necessary fundamentals of the Ion-Sensitive Field-Effect transistor are introduced to understand the choice of using this device as the transducer component of the biosensors. Finally, the chapter reports on the choice of using high- $\kappa$  oxides as the sensing layer and Fully-Depleted Silicon Nanowire FET as the base of the biosensor system. These choices are presented with a discussion of the advantages of this approach and its potential for advancing the field of biosensing.

### **Chapter 2: Silicon Nanowires technology**

In this chapter, the technology at the base of the biosensor transducer is reported. Two similar platforms, respectively designed and fabricated at CEA-LETI and at EPFL are presented. For the first platform, the main steps of the fabrication process flow are reported, followed by its DC electrical characterization. For the chips designed and fabricated in-house at EPFL, a more detailed description is reported: the performed simulation to select the best process parameter is described, together with the detailed fabrication process flow. The main critical steps in the fabrication process flow are presented before the DC electrical performance of the obtained devices.

### **Chapter 3: Surface functionalization and methods**

In this chapter, a fundamental part of the project is discussed: the functionalization protocol used to immobilize specific probes to capture protein analytes in complex biofluids is described in detail. The characterization techniques used to confirm the correct covalent immobilization of the chosen antibodies are also reported to confirm the good quality of the functionalization layer, and the importance of each component to ensure stability, low drift, and high specificity of the sensor.

After the first part, the chapters introduce three different electrical methods exploited to measure and detect analytes concentrations, namely front-gate operation, back-gate operation, and constant drain current operation. We explain in detail the latter, being a novel method exploited to enhance the sensor's sensitivity and stability.

### **Chapter 4: pH sensing**

This chapter presents the results of pH detection in both ISF-like solution and buffer. Building upon the devices introduced in Chapter 2 and the electrical detection methods discussed in Chapter 3, it serves as a natural continuation of the previous chapters. The results are organized based on the platform used and the characterization technique employed. Initially,

## List of elements and materials

---

pH monitoring in buffer is examined, followed by the successful monitoring of pH in ISF-like solutions using two distinct techniques: top-gate detection and constant drain current method.

### **Chapter 5: CRP sensing**

In this chapter, we present the results of C-Reactive Protein (CRP) detection in buffer. We utilized the functionalization method discussed in Chapter 3 to immobilize antibody fragments on high- $\kappa$  oxides of SiNWs structures. The detection experiments were conducted in two different configurations. First, we performed CRP detection in a top-gate configuration using 100 times diluted buffer. Subsequently, we explored the bottom-gate configuration, which allowed for successful CRP detection in 10 times diluted buffers with thanks to the internal signal amplification. Additionally, we conducted preliminary experiments using a constant drain current method, which demonstrated enhanced sensitivity and response to protein concentrations.

### **Chapter 6: Conclusions and future perspective**

This conclusive chapter highlights the obtained advancements and contributions of this work in the field of low-power biosensors for real-time monitoring of biomarkers in human interstitial fluid. Future perspectives and further studies are proposed to enhance the obtained results in this work and exploit them for an integrated wearable solution.



# 1 Introduction

*This chapter provides an overview of the concept of Digital Twin, which forms the basis for the development of a miniaturized and low-power biosensor for protein and pH monitoring in human biofluids. Section 1.1 introduces the concept of Digital Twins and its relevance to the biosensor design. In Section 1.2, the biofluid of interest, Interstitial Fluid (ISF), is described in terms of its composition, clinical extraction methods, and the current State of the Art for extraction and simultaneous analysis. The integrated system concept, which includes sensors, microfluidic components, and microneedle extractors, is presented in this chapter as well. In Sections 1.3.1 and 1.3.2, fundamental theoretical concepts related to the Metal-Oxide-Semiconductor Field-Effect Transistor (MOSFET) and the Ion Sensitive FET (ISFET) technologies are discussed, along with the reasons for choosing high- $\kappa$  dielectric and Fully-Depleted Silicon On Insulator (FD-SOI) technologies for the biosensor transducer. Furthermore, this chapter provides an overview of the current State of the Art in biosensing based on FET, particularly focusing on FD-SOI silicon nanowires FET as biosensors. This chapter serves as a comprehensive introduction to the concepts and technologies that form the foundation of the biosensor design and fabrication discussed in subsequent chapters.*

## 1.1 Biomarkers monitoring for Digital Twins applications

In recent years, we have witnessed the critical significance of medical research and advancements in healthcare systems. The COVID-19 pandemic has further emphasized the need for tailored healthcare approaches, as it has become increasingly clear that patients respond differently to the virus and its treatments. Researchers and healthcare professionals have worked tirelessly to understand the virus' impact on different patient populations and to develop tailored treatment plans based on individual needs [2, 3, 4, 5, 6]. Patient-centered analysis of the disease's pathologies has been shown to be essential in effectively treating SARS-CoV-2. Rather than relying on general curing philosophies, a tailored approach to the patient's unique symptoms and circumstances has been found to be more effective.

By leveraging cutting-edge technologies and developing more precise diagnostic tools, health-

care providers can better understand patients' unique needs and deliver targeted treatments that improve outcomes. It is essential to recognize that personalized healthcare is not just important during pandemics; it is a vital aspect of promoting overall health and well-being. As we continue to navigate the challenges posed by COVID-19, we must also focus on building a healthcare system that prioritizes personalized care for all patients. The concept of Digital Twins aligns perfectly with the idea of personalized healthcare. It entails creating a unique computational and technological representation of an individual, including their disease dysfunctions. This representation is based on data collected from multiple Edge AI technologies such as organs on chip (OoC) and real-time biosensor readings. The implementation of Digital Twins could provide faster and more accurate diagnoses while also predicting disease trajectories. The possibilities offered by Digital Twins in healthcare are immense: this technology can aid in the development of new treatments and medications, optimize drug dosages, and predict side effects before they occur. Additionally, it can help prevent diseases by identifying potential risk factors and detecting early symptoms before they become severe.

This work finds its natural development in such a framework: the main goal of this project is to lay the groundwork for the creation of robust and low-power multimodal biomarker ISFET-type wearable sensors that can quasi-continuously monitor multiple biomarkers in human interstitial fluid (ISF). By collecting data on highly diluted biomarkers, such as specific proteins, these *biosensors* will serve two main purposes. Firstly, early changes in biomarkers concentrations can be detected, enabling doctors to make faster treatment decisions. Secondly, the large amount of data collected from different patients in hospitals can be used to train machine learning models, ultimately leading to personalized healthcare solutions.

In the scientific literature, there are various definitions of what a *biosensor* is. Here we report an adapted definition from [7]:

*A biosensor is a self-contained device that is capable of providing real-time analytical information about a test sample, by exploiting a recognition system based on biochemical or biological mechanisms.*

Figure 1.1 provides a simplified schematic of a biosensor system. The biological recognition system is the first to respond to the sensed event. In our specific case, antibodies immobilized on the transducer's surface recognize the specific antigen, capturing it close to the sensing surface. The recognized event creates a perturbation in the working mechanism of the transducer, resulting in a readable signal that can later be analyzed and related to a specific quantity of the captured antigen.

Our work specifically employs devices from the Field-Effect Transistor (FET) family as transducers. We will introduce the most important notions on the physics behind the devices for the understanding of this work in Section 1.3.1, and their use as liquid-gated devices in 1.3.2.

This work is part of a larger project that aims to integrate the fabricated sensors with compatible silicon microneedles, enabling the extraction of human interstitial fluid for quasi-

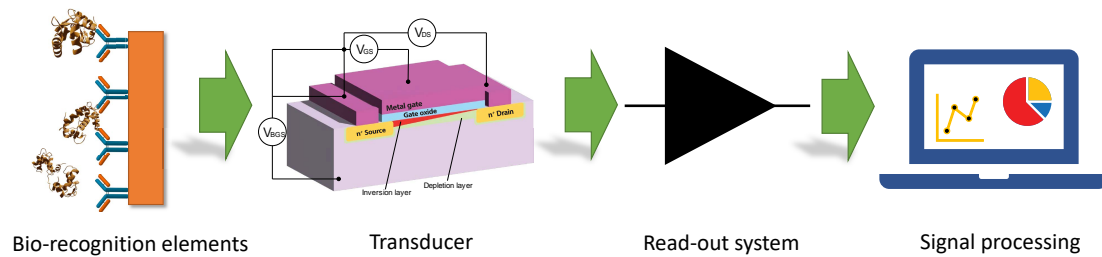


**Figure 1.1:** Biosensor schematic.

continuous on-body biomarker monitoring. This study specifically focuses on the design, fabrication, and characterization of the sensors, and does not include a report on the integration process.

## 1.2 Interstitial Fluid as a biological fluid of interest

Interstitial fluid (ISF) serves as the cellular environment [8], and represents between 15 to 25% of the total body weight [9]. It fills the space between cells and is responsible for delivering them essential nutrients and removing metabolic waste [10]. Moreover, it constitutes 75% of the extracellular fluid, it does not clot [11], and can be a source for continuous real-time biomarkers monitoring. Previous works have demonstrated that ISF is very similar to plasma in terms of protein composition, but it could show a different quantity, not strictly correlated to the one in plasma or blood [12, 13].

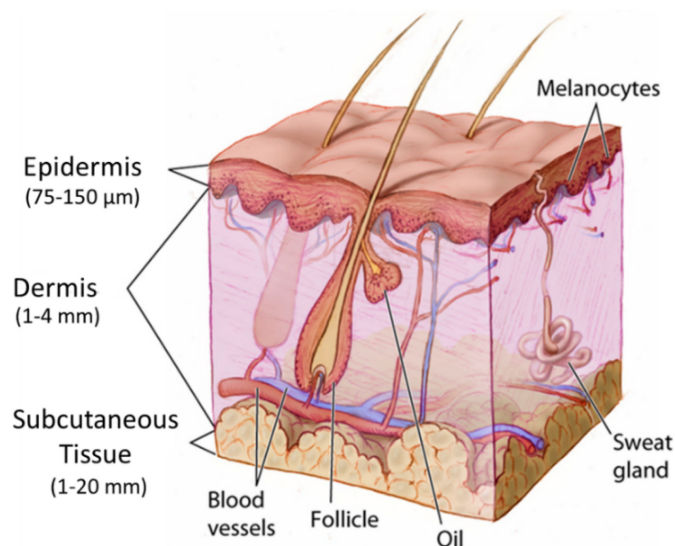


**Figure 1.2:** Skin anatomy, adapted from [14].

Of the whole volume of ISF, dermal ISF represents 30-40% of the total amount [9]. Dermal ISF is found in the extracellular space in the *dermis*, a skin layer of an average thickness between



1 mm and 4 mm, that lays under the first layer of the skin, called *epidermis*, which has an average thickness between 75  $\mu\text{m}$  and 150  $\mu\text{m}$  (Figure 1.2). Dermal ISF represents an attractive alternative to blood or plasma for human biomarker detection since micro-sized needles can be used to collect ISF by penetrating the skin only a few hundred microns, enabling a low-invasive and pain-free method of biomarker detection [15]. In addition, this on-skin setup can be carried by patients, eliminating the need for cumbersome equipment.

Even if further research is required to fully characterize the proteomic profile of ISF, previous studies have shown that only a small fraction (less than 2%) of biomarkers present in the blood is not found also in ISF [12, 16, 17, 18], and that only 5% of the proteins are unique in ISF [19]. Future studies have to focus their attention on the correlation between the concentration of biomarkers in blood and in ISF. A general snapshot of interesting biomarkers concentration in ISF compared to human plasma or whole blood is reported in Table 1.1.

	<b>Plasma/Blood</b>	<b>Interstitial fluid</b>
Total protein [8]	73.7 g/L	20.6 g/L
Albumin [8]	0.676 mM	0.188 mM
Glucose [20]	5-25 mM	5-25 mM
Cholesterol (HDL) [21]	1-2.5	0.3-0.8 mM
Cholesterol (LDL) [21]	1.5-4 mM	0.3-0.9 mM
Cortisol [22]	82 - 550 nM	30-50 nM
Lactate [23]	1-13 mM	1-13 mM
Lipids [24, 25]	9.2 $\mu\text{M}$	1.5 $\mu\text{M}$
Ca <sup>2+</sup> [8]	1.257 mM	1.189 mM
Mg <sup>2+</sup> [8]	0.532 mM	0.506 mM
Na <sup>+</sup> [8, 24]	138.8 mM	135-150 mM
K <sup>+</sup> [8, 24]	4.28 mM	3.2-4.9 mM
Cl <sup>-</sup> [24]	90-120 mM	99-117 mM
CO <sub>2</sub> [8]	29.7 mM	23.9 mM
Phosphate [8]	1.177 mM	0.61 mM

**Table 1.1:** Comparison between plasma and ISF composition.

To the best of our knowledge, the only commercialized wearable devices that can perform markers monitoring at a molecular level in ISF are the ones involving electrochemical continuous glucose monitoring (CGM) [24, 26]. The best examples are the devices from Dexcom, Freestyle Libre from Abbot, and Minimed<sup>TM</sup> from Medtronic. These devices are described as minimally invasive since the sensing element is inserted a couple of millimeters underneath the skin.

As of today, improved solutions for ISF extraction are still needed, due to a still difficult extraction of valuable ISF. In fact, there are only 120  $\mu\text{L}$  of available ISF for one  $\text{cm}^2$  of skin, and the maximum collection volume results in around 10  $\mu\text{L}$  [19]. To collect larger volumes, previous works have suggested the application of external pressure. The main problem

resulting from pressure-driven extraction methods is known as *filtration*: water and smaller molecules respond to the applied pressure quicker than larger ones, creating unreal analytes concentrations that could lead to false sensing outputs [27, 28]. Nowadays, different available extraction methods are available and used in the medical world, the main ones are listed below.

- Capillary wicking: it involves inserting a wicking material into the dermal space, to absorb ISF for analysis. The material could be pre-saturated of unwanted analytes, to collect only the necessary ones. The major drawbacks are the slow collection rate and its invasiveness.
- Suction blisters: it provides high extraction rates (up to 5  $\mu\text{L}$  per minute) thanks to a suction mechanism that creates blisters on the skin surface. The main drawback is the falsification of large analytes concentrations compared to the serum levels, due to the filtration effect.
- Microdialysis and ultrafiltration: either whole ISF or only analytes are collected through a semipermeable membrane inserted into the dermis. The collection method in this case could be by a fluid flowing in the membrane (microdialysis) or by applying pressure (ultrafiltration). It provides a long-term collection method, but it is very invasive and due to the nature of the membrane it has a physical cutoff for larger analytes, with a five to ten times diluted ISF.
- Reverse iontophoresis (electroosmosis): by applying an electrical voltage across the skin an electroosmotic flow of analytes is created through the epidermis. This method results in highly-diluted ISF samples (up to 1000-fold dilution).
- Needle-based extraction: a small needle is inserted in the dermis, and ISF is collected by applying pressure around it. This method could guarantee constant extraction rates of 2.6-5.3 nL per minute per needle [19].

Promising and innovative solutions are offered by devices exploiting microneedles structures, that penetrate the skin for only a few hundred micrometers ( $<700 \mu\text{m}$ ). These structures offer two types of sensing: in-vivo dwelling sensors if the sensing structures are placed onto the microneedles, or ex-vivo if the hollow microneedles are used to collect ISF and direct it on the external part of the skin, where the sensors are then placed (Figure 1.3).

Tehrani et al. offer a great example of a microneedles-based sensor in ISF in their work [15]: continuous, simultaneous, and real-time prolonged monitoring of analytes such as glucose and lactate are performed in a label-free manner, during normal daily activities of the tested volunteers. Figure 1.4 shows the great integration level of the system, from the sensors and the PMMA-microneedle array to the wireless communication electronics placed directly on the skin of the patient. This technology employs an in-vivo setup since the sensing layers are deposited directly on the microneedles, thus no ISF extraction is needed. This example

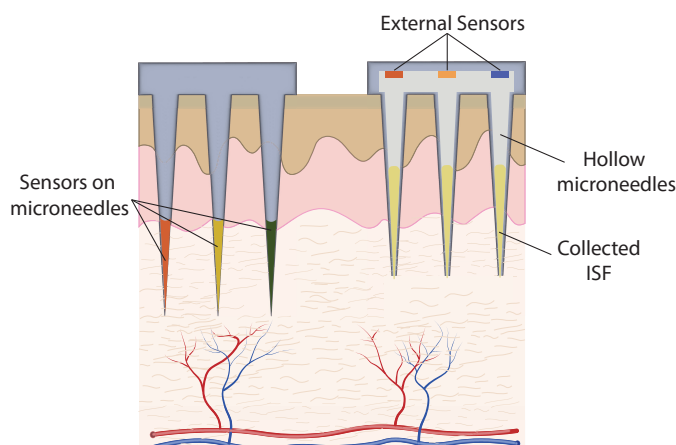


**Figure 1.3:** Dwelled or external sensors on microneedles array. Adapted from [19].

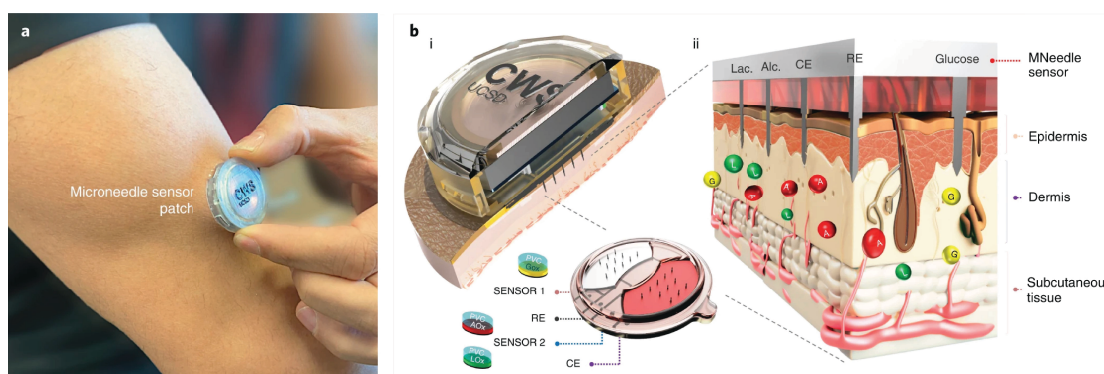
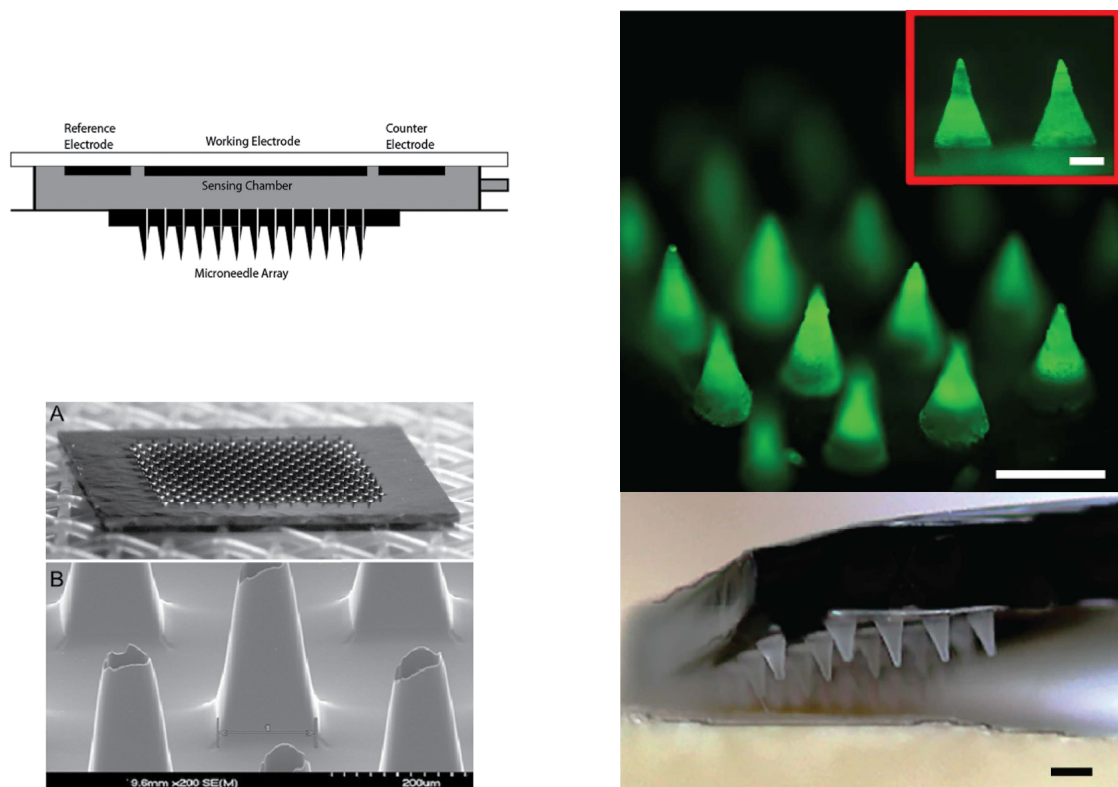


**Figure 1.4:** Tehrani et al. Microneedle-based sensor in ISF [15].

shows a great level of integration, and optimal results for the tracking of important markers such as glucose or lactate, revealing an important correlation between the values in blood and ISF. Due to the choice of exploiting an intra-dermal sensor placement, this solution is not yet compatible with protein sensing, which requires more complex functionalization protocols and can not ensure the safety of the patient. An interesting clinical study has been carried out by Ming et al. [23]: they exploit a similar technology to Tehrani et al., but they focus their attention on the detection of lactate levels in dermal ISF. With their study, they demonstrate a good correlation between lactate levels in ISF and the ones in venous blood.

The study from Jina et al. [29] is another example of continuous ambulatory monitoring in ISF, and it employs microneedles for CGM. This type of sensor differs from the one of Tehrani et al. because the sensing elements and the transducer structures are not placed on the surface of the microneedles, thus dwelling in the dermis, but they are placed externally in a sensing chamber filled with buffer solution. The sensing is based on amperometric detection employing glucose oxidase cross-linked with bovine serum albumin.

An example of ex-vivo protein measurement in ISF is offered by the work of Wang et al. Their



(a) Jina et al. Microneedle-based sensor in ISF for CGM [29].

(b) Wang et al. Microneedle-based sensor in ISF [30].

**Figure 1.5**

work exploits a cheap and disposable polystyrene microneedles patch, functionalized with specific antibodies for high-sensitivity protein detection. The sensing mechanism is based on an optical immunoassay that requires secondary antibodies with a fluorescent tag. The need to perform an ELISA-based assay imposes the necessity to peel off the patch and proceed with an ex-vivo quantification of the captured analyte. This method imposes straightforward limitations: this system is optimal for low Limit of Detection and high-accuracy sensing but does not integrate with continuous monitoring of the analyte of interest. Moreover, the placement of the sensing layer onto the microneedles could lead to capturing probes desorption from the surface, and degradation in the dermal tissue, as reported by the same authors. Similar ex-vivo detection is reported by Zheng et al. [31], where they exploit fluorescence detection of glucose, adenosine triphosphate, L-tyrosinamide, and thrombin with the aid of fluorescently tagged aptamers.

Venugopal et al. [22] report a sampled measurement of cortisol in ISF, by combining a collection of ISF in the stratum corneum and Electrochemical Impedance Spectroscopy detection. The collection of ISF happens every 6 hours, and the cortisol detection is performed on an external platform. Their extraction is based on micropores created by a low-energy infrared laser-focused on a black dye material on the skin, guaranteeing a painless extraction. Also

in this case the main limitation to continuous biomarkers monitoring lies in the ex-vivo measurements since the electronic components are not integrated into the patch.

Dervisevic et al. [32] proposed a potentiometric sensor able to monitor pH values in ISF with a sensitivity of 62.9 mV/pH and in a range between 4.0 and 8.6. These results encourage our work, also because it highlights the importance of monitoring pH levels in ISF, but they are limited by only sensing pH levels, and not other biomarkers. The system is based on invasive dwelling sensors, that are not compatible with affinity-based biosensors based on specific antibody probes.

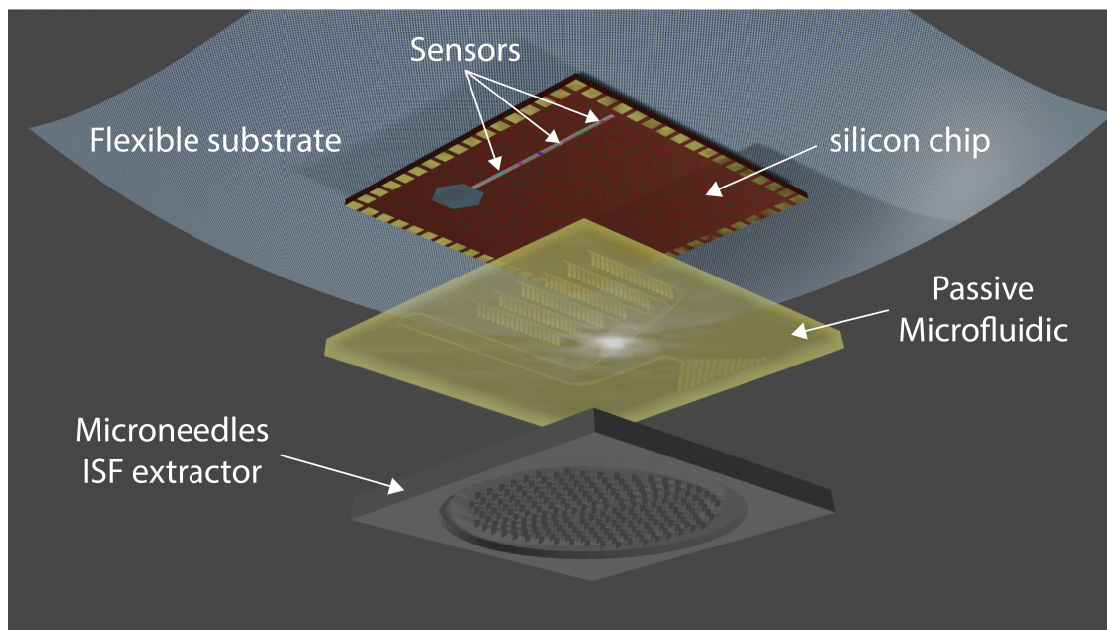


**Figure 1.6:** Schematic of the final integrated sensor, with passive microfluidic, and microneedles ISF extractor. In this work, we lay the groundwork for the design and fabrication of the sensing component of the system. The microfluidic and microneedles fabrication and integration are the core of collaborative efforts involving other partners within the European Consortium.

In this study, we propose a cutting-edge sensor technology that can be seamlessly integrated into a wearable patch, as depicted in Figure 1.6. This figure illustrates a conceptual representation of the final product, which includes a sensor based on CMOS-compatible technology, a passive microfluidic system that guides the collected interstitial fluid (ISF) to the surface of the sensor, and a microneedle extractor for dermal ISF collection. While the main focus of this thesis is the development of the sensor technology, the design and creation of the microfluidic system and the microneedle extractor are collaborative efforts involving other partners within the European Consortium.

**pH and C-Reactive Protein as biomarker of interest**

The pH value of a solution reflects its acidity or alkalinity, with a neutral solution having a pH of 7, acidic solutions having a pH below 7, and alkaline solutions having a pH above 7. In humans, the normal pH value is slightly alkaline, with an average of 7.40 [33]. Acidemia or alkalemia are indicators of body dysfunction and health status. For example, metabolic acidosis is associated with increased mortality in critically ill patients, and a pH correction of  $\geq 1.16\%$  within the first 24 hours had the best predictive ability for survival in ICU hospitalized patients with acidemia of presumed metabolic origin [34]. The rate of change in pH may be a better predictor of ICU mortality than other metabolic indices. Similarly, other studies have shown that both base excess and arterial lactate samples upon admission have good prognostic abilities [35].

The pH of the interstitial fluid is around 7.4, while the intracellular fluid pH is within 7.2-7.6 [36]. Both blood and interstitial fluid pH are regulated by bicarbonate-carbonate and phosphoric acid-mediated pH-buffering systems [36, 37, 38]. The protein-mediated pH-buffering system is a notable difference between blood and interstitial fluid pH-buffering mechanisms, with blood containing potent pH-buffering proteins like hemoglobin, while they are absent in the interstitial fluid. This means that even under metabolic disorder conditions except for severe cases, the arterial blood pH remains constant within the normal range (7.35-7.45), while the interstitial fluid pH easily drops below the normal level due to much lower pH-buffer capacitances than that in blood [39, 40, 41]. The intracellular pH-buffering system and proton-transporting system from the intracellular space to the extracellular space are two significant systems that prevent the interstitial fluid pH from dropping. The dysfunction of these transporters leads to abnormal intracellular fluid pH of cells, leading to the development of metabolic diseases.

Patients with type 2 diabetes mellitus and mitochondrial dysfunction produce high levels of protons, which reduce the pH of the interstitial fluid, leading to insulin resistance via a reduction in insulin-binding affinity to its receptor. Therefore, the lowering of interstitial fluid pH should be considered as one of the therapeutic targets for the amelioration of insulin resistance and the onset of metabolic dysfunction [36, 41]. In summary, pH changes play a critical predictive role in the development of metabolic diseases and their complications, with a lowering of interstitial fluid pH leading to insulin resistance and metabolic dysfunction. It is believed that a local change in interstitial tissue (ISF) pH could be an early warning sign for shock onset. Therefore, continuous pH monitoring in ISF could be critical to detect circulatory shock earlier and to reduce mortality in ICU. Moreover, the possibility to multiplex pH monitoring with other inflammatory markers, such as C-Reactive protein (CRP), may offer greater insights into the pathological trajectory of patients and provide better therapeutic strategies.

C-Reactive Protein (CRP) is an exceptional biomarker protein that provides valuable information for both early detection and diagnosis of diseases. This pentameric acute-phase protein

is composed of five subunits of 23 kDa and is primarily expressed by liver cells (hepatocytes) in response to inflammation or tissue injury [42, 43]. CRP plays a crucial role in the human body's immune response, and its values in blood or serum have been correlated with several clinical complications. The diagnostic applications of CRP measurement span various fields, including immunology [44], oncology [45], cardiology [46, 47], nephrology [48], diabetology [49, 50], and other chronic conditions.

Moreover, recent research works have highlighted the potential of CRP as a source of information for predicting mortality in severe cases of SARS-CoV-2 infection. Hospitalized patients who died had significantly higher median CRP levels than those who survived, while survivors had lower peak CRP levels and earlier declines [51, 52]. This finding highlights the crucial role of CRP in assessing a patient's condition during COVID-19 infection [53].

Multiple studies have demonstrated the predictive importance of CRP baseline blood levels. CRP is a strong predictor of various cardiovascular events, such as incident myocardial infarction, stroke, peripheral arterial disease, and sudden cardiac death. Additionally, it is a useful predictor of recurrent ischemia. Based on CRP levels of <1, 1 to 3, and >3 mg/L, individuals can be categorized into low-, moderate-, and high-risk groups for future cardiovascular events [46]. In fact, elevated CRP levels can be a predictor of future heart problems and inflammation leading to atherosclerotic vascular disease, up to 5-20 years before the actual event occurs [47]. Notably, CRP provides independent prognostic information on risk at all levels of severity of the metabolic syndrome [54].

CRP levels are stable over long periods of time, are not affected by food intake, and demonstrate almost no circadian variation, thus changes in blood or serum concentration are strictly correlated to health issues. The baseline level of CRP in blood is approximately 0.8  $\mu\text{g}/\text{mL}$  (6.66 nM), with values of 0.3, 0.6, 1.5, 3.5, and 6.6 mg/L being reported as the 10<sup>th</sup>, 25<sup>th</sup>, 50<sup>th</sup>, 75<sup>th</sup>, and 90<sup>th</sup> percentile cut-offs [55]. CRP concentration can increase by up to 10,000-fold in the presence of an acute infection, being values between 0.1  $\mu\text{g}/\text{mL}$  and 100  $\mu\text{g}/\text{mL}$  of physiological relevance. To detect CRP over a wide dynamic concentration range (from pM to  $\mu\text{M}$ ), it is necessary to develop new biosensing platforms and analytical techniques. However, conventional bioanalytical techniques such as laser nephelometry, fluorescence, and chemiluminescence measurements are expensive and require sample pretreatment and trained personnel. A label-free CRP immunosensor, which could be low-cost, fast, and portable, is a promising alternative to current clinical tests. Several label-free biosensing platforms, including electrochemical sensors, capacitors, transistors, and surface plasmon resonance, have been developed. Nevertheless, most of these methods can only detect CRP within a narrow concentration range and involve multi-step, demanding processes to immobilize bioreceptors. Developing a continuous, label-free CRP biosensor that can detect CRP over a wide range of concentrations without the need for sample pre-treatment and labeling steps could revolutionize the diagnosis of acute and chronic conditions. This would lead to faster and more accurate diagnoses, better treatment outcomes, and ultimately saving lives.

Numerous electrochemical biosensors have been suggested as viable options for rapid and affordable CRP detection platforms. Unlike optical measurements, these sensors enable the use of minimal sample volumes, label-free techniques, and quicker detection processes. FET-based devices, widely utilized for biosensing, have also been extensively explored for their efficacy in CRP detection. The following references highlight some notable works related to CRP sensing using FET-based devices.

In their study, Kim et al. introduced a chip-based point-of-care sensor designed to detect CRP in serum [56]. The sensor's fundamental technology relied on a nanogap-embedded FET, as illustrated in Figure 1.7a, with silicon-binding proteins utilized for specific antigen detection. The incorporation of the nanogap enabled the sensor to achieve an impressive limit of detection at 0.1 ng/mL, covering a detected concentration range from 0.1 ng/mL to 0.1  $\mu\text{g/mL}$ .

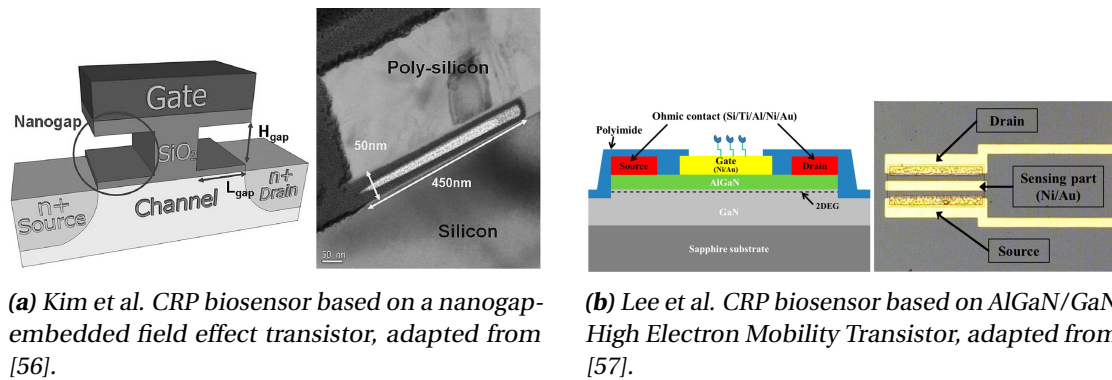


**Figure 1.7**

Lee et al. exploited an AlGaN/GaN high electron mobility transistor (HEMT) combined with a null-balancing circuit to detect CRP in a detection range between 10 ng/mL and 1  $\mu\text{g/mL}$  [57]. To enable CRP detection, the Ni/Au gate of the system was functionalized with CRP antibodies, enhancing its specificity towards the target analyte (Figure 1.7b). Thanks to the two-dimensional electron gas at the very interface with the oxide, HEMTs offer improved sensitivity, higher speed, and lower noise.

The use of one-dimensional structures as efficient transducers for protein sensing has been demonstrated in numerous studies. Rabbani et al. conducted a noteworthy study where they employed a carbon nanotube Field Effect Transistor (CNT-FET) as an immunosensor to detect CRP [58]. In their setup (Figure 1.8), a CNT was deposited onto a Si/SiO<sub>2</sub> surface, forming a conductive channel between the source and drain contacts to create the FET structure. The device exhibited a remarkable response within a concentration range of 10 ng/mL to 1000  $\mu\text{g/mL}$ , with an impressive response time of only 3 minutes.

The proposed sensor showcased reliable electrochemical detection of C-Reactive protein, effectively capitalizing on the CNT-FET's large surface-to-volume ratio. Moreover, the approach offers scalability and affordability, making it a promising solution for practical and



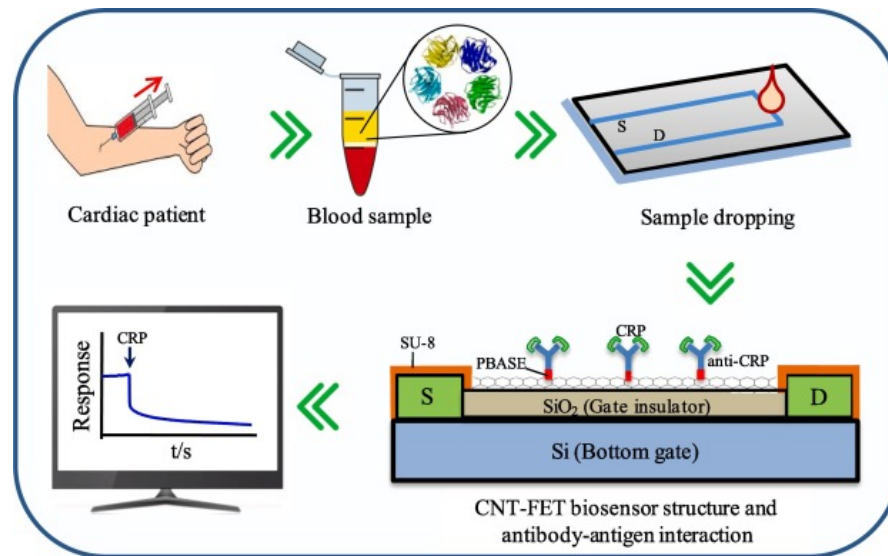


**Figure 1.8:** Rabbani et al. CRP biosensor based on carbon nanotube FET, adapted from [58].

cost-effective biosensing applications.

Lee et al. [59] presented a pioneering example of a CRP biosensor utilizing silicon nanowire arrays fabricated through a top-down approach (Figure 1.9a). Their innovative work demonstrated a multiplexed biosensor capable of detecting multiple proteins simultaneously. By employing sol-gel materials encapsulating protein-specific antibodies, they achieved CRP detection within the range of 0.12 ng/mL to 10 ng/mL, alongside pH sensing.

The integration of silicon nanowires (SiNWs) with the sol-gel antibodies facilitated high-sensitivity and label-free immunoassays, requiring only a small amount of serum and yielding results in just a few minutes. This novel approach opens doors to efficient and rapid detection of CRP and other proteins, showcasing the potential of silicon nanowire-based biosensors in advancing diagnostic capabilities.

Chu et al. [60] have presented a remarkable fully integrated system designed for CRP sensing. This cutting-edge system utilizes aptamer-immobilized AlGaIn/GaN high-electron-mobility transistors (HEMTs) as the core sensing technology, achieving an astonishing limit of detection (LoD) as low as 1 fM. To facilitate an automated experimental process, the researchers incorporated an integrated microfluidic chip, as depicted in Figure 1.9b. This microfluidic chip consisted of two polydimethylsiloxane (PDMS) layers: a liquid channel layer and a pneumatic layer, in addition to a printed circuit board and an AlGaIn/GaN HEMT-based FET sensor. The compact design of this integrated system enables wide-range concentration detection of CRP, encompassing the entire range for the three categories of CRP concentrations typically used as cardiovascular disease markers. Moreover, the system's unprecedented ultra-low detection limit (1 fM) demonstrates its exceptional sensitivity. Considering these advancements, the developed system holds immense potential for evaluating the risks of cardiovascular diseases

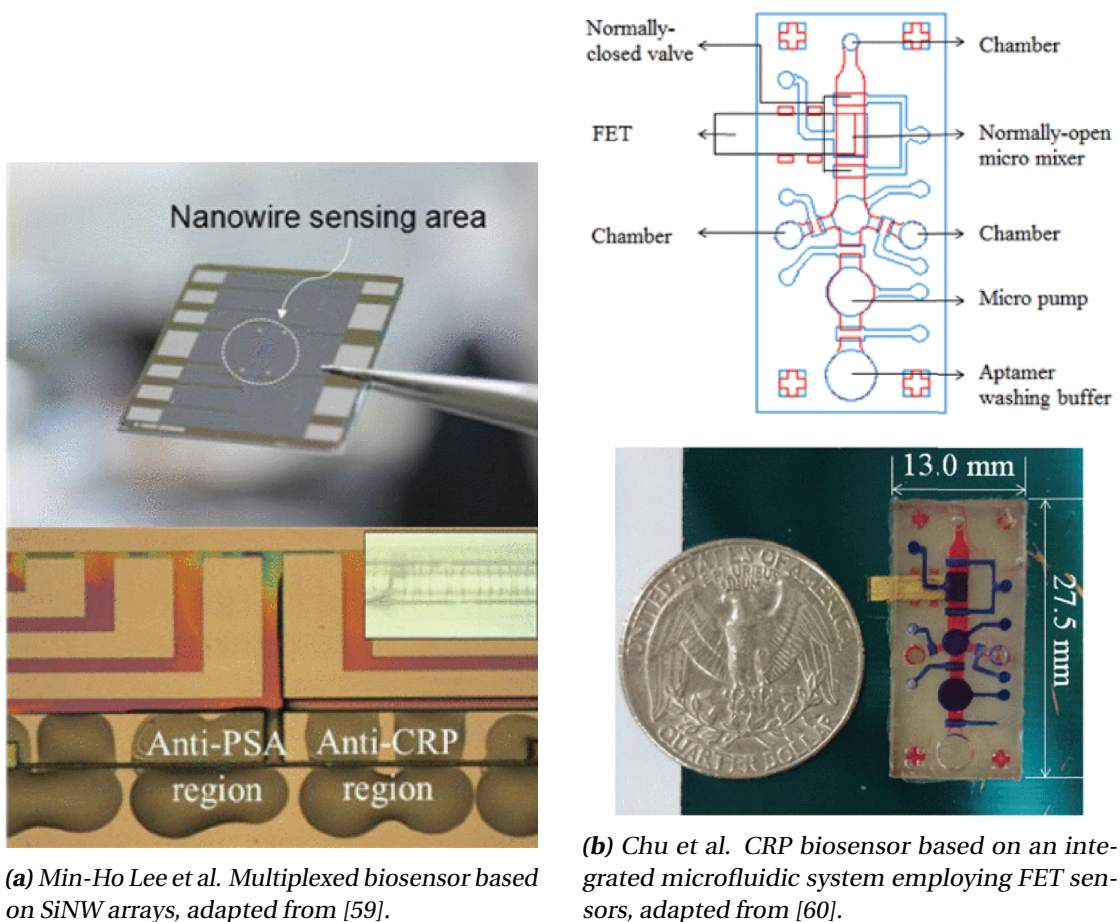


**Figure 1.9**

at the point of care in the future. The successful integration of aptamer-based sensing and microfluidics brings forth a promising avenue for highly sensitive and automated CRP detection, thereby enhancing early disease diagnosis and management.

Tu et al. [61] have presented one of the latest advancements in CRP sensing, showcasing a wearable and wireless patch designed for real-time electrochemical detection of the inflammatory biomarker C-reactive protein (CRP) in sweat. This cutting-edge system makes use of innovative technologies, including iontophoretic sweat extraction, microfluidic channels for sweat sampling, and reagent routing and replacement. The core of the sensor array consists of anti-CRP antibodies-conjugated gold nanoparticles graphene-based sensors for accurate CRP quantification. The sensor patch, based on a polyimide substrate and a flexible printed circuit board, is depicted in Figure 1.10. It ensures wireless communication to seamlessly transmit the collected data. The sensor array is comprised of several components, such as an electrodeposited AuNP-decorated Laser Engraved Graphene (LEG) working electrode immobilized with anti-CRP capture antibodies (cAbs), an Ag/AgCl reference electrode, a LEG counter electrode for sweat CRP capturing and electrochemical analysis, a LEG-based impedi-

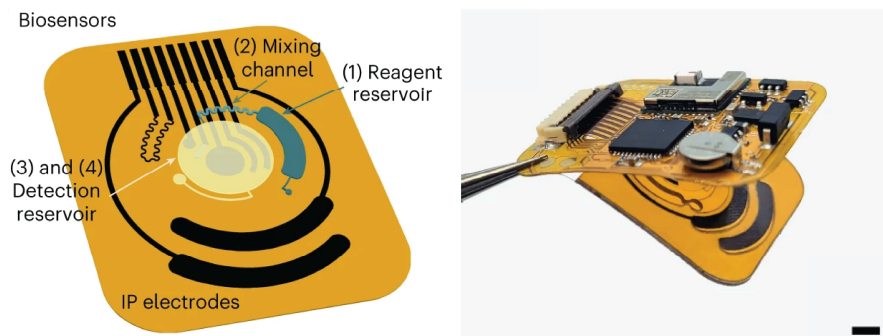


**Figure 1.10:** Tu et al. wireless CRP biosensor in sweat, adapted from [61].

metric ionic strength sensor, a LEG-polyaniline-based potentiometric sweat pH sensor, and a strain-insensitive resistive graphene temperature sensor. This wearable sensor is equipped to perform autonomous sweat extraction, collection, biomarker analysis, and wireless data transmission, all while individuals engage in their daily activities, even during sedentary periods. Remarkably, the sensor exhibits an ultralow limit of detection, boasting an impressive sensitivity of 8 pM. With its real-time monitoring capability and high sensitivity, this wireless patch represents a significant advancement in non-invasive CRP detection, paving the way for potential applications in personalized health monitoring and disease management.

### 1.3 Biomarkers sensing with FET technology

#### 1.3.1 The Field Effect Transistor

The primary objective of this project is to create a biosensor that can be integrated into a wearable system, making it compact and energy-efficient. FET-based sensors are an ideal choice for this task, as they meet the necessary requirements. In addition, using the same technology for sensing and other electronic components (such as read-out circuits and communication) can result in unparalleled miniaturization and reliability. By leveraging this approach, we aim to develop a biosensor that can be seamlessly integrated into wearable devices, facilitating the monitoring of a range of biological parameters in real-time.

The Field-Effect transistor (FET) is an electronic device in which the current flowing in a semiconductor channel between two terminals (Source and Drain) is controlled by the electric field created by applying an electric voltage on a third terminal (Gate). Of the various types of FETs, the Metal Oxide Semiconductor FET (MOSFET) is the most widely used in the world of information technology. MOSFETs are based on a fundamental structure called a MOS capacitor, which consists of a bulk silicon (with low p or n doping), an oxide layer (originally silicon dioxide), and a metal layer (or highly doped polysilicon) on top, as illustrated in Figure 1.11.

The great breakthrough that allowed the fabrication of the first MOSFET was achieved by Atalla

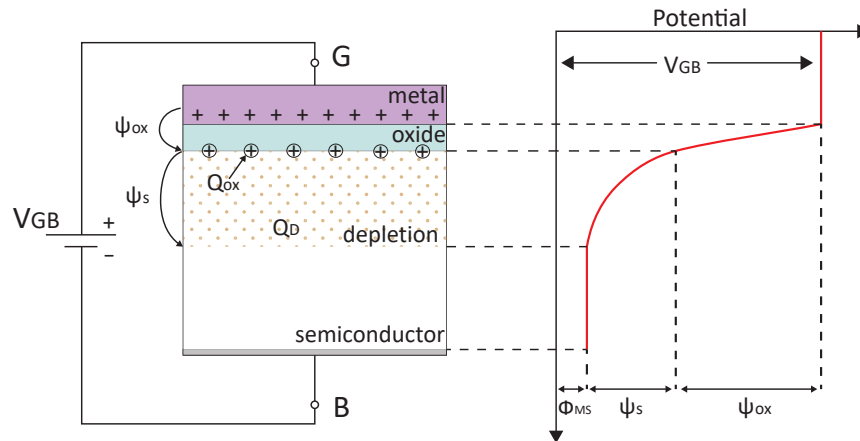


**Figure 1.11:** MOS structure, adapted from Figure 4.8 of [62].

in 1959 [63], by being able to neutralize the silicon surface states by growing thin silicon oxide on the silicon surface. Atalla, worked at the Bell Laboratories, following the first advancements in the FET technology pursued by Bardeen, Brattain, and Shockley in the second half of the 40s and in the 50s. In 1960 Mohamed Atalla and Dawon Kahng announced their MOSFET [64], starting a new era in information technology.

A MOS capacitor is an electronic device where the total charge at the interface between the oxide and the silicon can be regulated by an external voltage applied between the p-doped bulk silicon and the top metal ( $V_{GB}$ ). Depending on the magnitude and polarity of  $V_{GB}$ , the MOS capacitor can operate in three distinct regions: accumulation, depletion, or inversion. While a detailed description of the working principle of a MOS capacitor is beyond the scope of this work, interested readers can find comprehensive explanations in [62] and [65].

The modern MOSFET is typically a four-terminal device consisting of the gate, source, drain, and body terminal (often referred to as bulk). However, in many applications, the body and source terminals are short-circuited, resulting in a three-terminal device. In digital applications, the MOSFET functions as a switch, with the enhancement mode MOSFET being a "usually OFF" transistor. When no gate voltage is applied, no current flows between the source and drain. However, when the gate voltage surpasses a certain threshold voltage ( $V_{th}$ ), the device switches to the ON mode and conducts current, thanks to the formation of a charge inversion layer at the oxide-semiconductor interface. It is worth noting that even for gate voltages lower than the threshold voltage, the device conducts a small amount of current that exponentially increases with the voltage itself. This operating region is known as the subthreshold regime (or *weak inversion*) and is of significant interest in sensing applications. While this simplified description does not cover all aspects of the MOSFET, it serves as an essential foundation for understanding the device's characteristics and behavior.

In the following description, we always consider the bulk terminal as grounded, and the source terminal connected to the bulk, thus the drain to source current can be written as  $I_{DS} = I_D$ ,

and the gate to source voltage can be written as  $V_{GS} = V_G$ . The relationship between the current flowing between the drain and source, and the gate voltage  $V_G$  is usually denominated transfer characteristic. To include a large range of currents, the transfer characteristic could be represented in a semi-logarithmic plot [62], as in Figure 1.12.

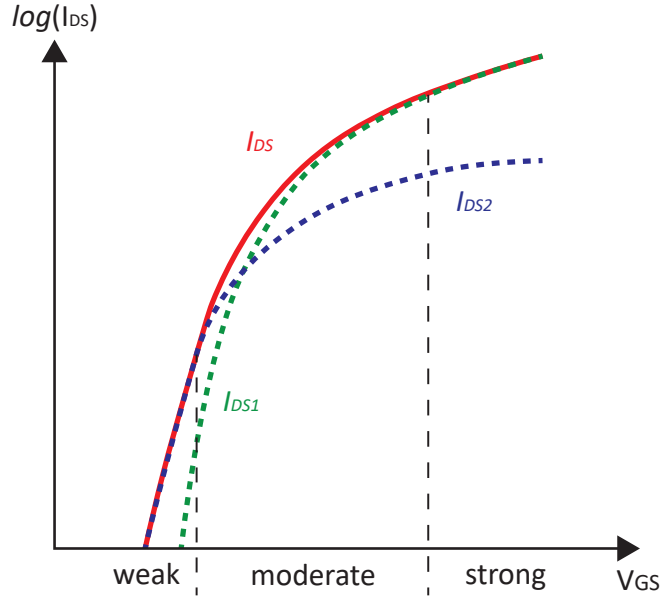


**Figure 1.12:** MOSFET transfer characteristic, adapted from Figure 4.8 of [62].

This current could be described by a complete all-region model, as the one proposed in Section 4.3 of [62]. What is important for this thesis is that the conduction mechanism in the MOSFET is composed of two types of currents: a minority carriers diffusion component ( $I_{DS1}$  in Figure 1.12) and a drift component ( $I_{DS2}$  in Figure 1.12). The diffusion component ( $I_{DS1}$ ) is dominating the conduction when the applied gate voltage does not allow the complete formation of an inversion channel in the undoped silicon (*weak inversion*), while the drift component dominates the conduction when the applied gate voltage is high enough to create an inversion channel close to the oxide interface (*strong inversion*). A third working region in which both current components play an important role in the conduction is usually denominated *moderate inversion*.

As aforementioned, the inversion layer is completely formed when the applied gate voltage is larger than the threshold voltage. The threshold voltage of a MOSFET (in an extremely simplified description) can be defined as the voltage at which the surface potential  $\Psi_s$  is equal to  $2\Phi_F$ , where  $\Phi_F$  is the difference between the Fermi level of the doped silicon and the intrinsic Fermi level (in the case of an n-MOSFET):

$$\Phi_F = \frac{kT}{q} \ln \frac{N_A}{n_i} \quad (1.1)$$

where  $N_A$  is the bulk silicon doping, and  $n_i$  the intrinsic carrier concentration of silicon.

The threshold voltage can be expressed by the equation:

$$V_{th} = \frac{\Phi_M - \Phi_{Si}}{q} - \frac{Q_{ox} + Q_D - Q_{ss}}{C_{ox}} + 2\phi_F \quad (1.2)$$

where  $\Phi_M$  and  $\Phi_{Si}$  are respectively the gate metal and the silicon work function,  $Q_{ox}$  is the charge in the gate oxide,  $Q_D$  is the depletion charge in the silicon layer, and  $Q_{ss}$  is the charge trapped at the interface,  $q$  is the elementary charge and  $C_{ox}$  is the oxide capacitance.

Other than the threshold voltage, two important parameters for biosensing applications based on Field-Effect Transistors are the subthreshold swing (SS) and the drain current ON/OFF ratio. The subthreshold swing indicates the inverse of the slope of the linear part of the transfer characteristic while plotted in a semi-logarithmic fashion, thus representing the steepness of the exponential growth of the drain current in the weak inversion region. The subthreshold swing in a bulk MOSFET can be expressed by equation 1.3:

$$SS = \left( \frac{\delta \log_{10}(I_D)}{\delta V_{GS}} \Big|_{V_{GS} < V_{th}} \right)^{-1} = \frac{kT}{q} \ln(10) \left( 1 + \frac{C_D + C_{ss}}{C_{ox}} \right) \quad (1.3)$$

where,  $C_D$  is the depletion capacitance,  $C_{ss}$  is the capacitance associated with the trapped charges in the oxide, and  $C_{ox}$  is the oxide capacitance. The value of the swing is usually reported in the amount of millivolt needed to grant one order of magnitude change in the drain current. As mentioned before, in weak inversion the main current contribution has a diffusion origin, thus the physical limitation of the subthreshold swing in MOSFET technology is related to the thermionic injections of carriers and it is equivalent to 59.5 mV/decade. This parameter is fundamental in biosensing applications since the current sensitivity of the system is inversely proportional to the subthreshold swing. The second fundamental parameter is the  $I_{ON}/I_{OFF}$  ratio, being the ratio between the current value while the transistor is on, and the value when no gate voltage is applied. This parameter is strictly correlated to the concentration sensing range of the biosensor [66].

### High- $\kappa$ dielectrics and fully-depleted technology

As discussed above, the minimum physical value of the subthreshold swing at room temperature is 59.5 mV/decade. This value is obtained when the oxide capacitance  $C_{ox}$  is infinite, or when the depletion capacitance  $C_D$  and the capacitance related to trapped charge  $C_{ss}$  are both zero. However, achieving an infinite oxide capacitance is not feasible, and to increase the

capacitance value, the SiO<sub>2</sub> gate oxide layer has been thinned down over the years. Scaling down the oxide thickness, however, reached a natural limit when gate leakage became unsustainable, preventing the proper functioning of transistors [67]. To continue scaling down technology nodes, high- $\kappa$  dielectrics like hafnium oxide (HfO<sub>2</sub>) were introduced [68], leading to the sub-1 nm Equivalent Oxide Thickness (EOT) era. Since high- $\kappa$  dielectrics have a higher dielectric constant, achieving the same oxide capacitance value requires a thicker layer of HfO<sub>2</sub> compared to SiO<sub>2</sub>. To facilitate comparison between high- $\kappa$  dielectrics, the concept of equivalent oxide thickness was introduced. EOT is a parameter that indicates the thickness of the silicon oxide film required to match the electrical performance of a high- $\kappa$  material in use and can be calculated using Equation 1.4:

$$EOT = t_{high-\kappa} \frac{\epsilon_{SiO_2}}{\epsilon_{high-\kappa}} \quad (1.4)$$

where  $t_{high-\kappa}$  is the thickness of the high- $\kappa$  oxide,  $\epsilon_{SiO_2}$  is the dielectric constant of silicon dioxide, and  $\epsilon_{high-\kappa}$  the dielectric constant of the high- $\kappa$  oxide. High- $\kappa$  oxides are not only advantageous for MOSFETs' electrical performance, but they are also crucial to achieving ion sensitivity close to the Nernstian limit, as already demonstrated in literature [69]. While optimizing the oxide capacitance value could help achieve ideal subthreshold swing values, the optimization of the depletion and the oxide traps capacitances should be addressed as well. The minimization of the capacitance linked to the trapped charges in the oxide can be achieved by optimal fabrication strategies.

In a MOS capacitor, the depletion capacitance is equivalent to the variation of charges in the depletion region given by the variation of the gate voltage ( $C_D = \delta Q_D / \delta V_G$ ), being the depletion charge equivalent to  $Q_D = -qN_A x_D$ , where  $N_A$  is the substrate doping, and  $x_D$  is the extension of the depletion region. Equation 1.5, describes how the depletion region thickness varies with the surface potential  $\Psi_s$ :

$$x_d = \sqrt{\frac{2\epsilon_{Si}\Psi_s}{qN_A}} \quad (1.5)$$

being  $\epsilon_{Si}$  the dielectric constant of silicon. The maximum extension of the depletion region is achieved when the strong inversion conditions are set, thus when the surface potential is  $\Psi_s = 2\Phi_F$ .

The depletion capacitance  $C_D$  has been reduced through the introduction of *Fully Depleted* (FD) technology. The FD technology utilizes a thin, low-doped Si layer that is sandwiched between two oxide layers: the top-gate oxide and the bottom oxide (also known as the box-

oxide or back-gate oxide). This configuration can be achieved, for instance, by exploiting a Silicon-on-Insulator (SOI) substrate. In the case of SOI substrates, with a silicon layer thickness  $t_{Si} < x_{Dmax}$ , the depletion charge can not vary with the variation of the gate voltage, thus  $C_D = \delta Q_D / \delta V_G = 0$  [70]. This condition is called full depletion and enables the achievement of ideal values of subthreshold slopes. It is imperative to specify that this explanation is not completely accurate because it does not take into account the capacitive coupling between the front and back interfaces. A complete analysis is offered in [71]. In Figure 1.13 we compare the equivalent capacitor networks for the bulk MOSFET and the fully depleted SOI case.

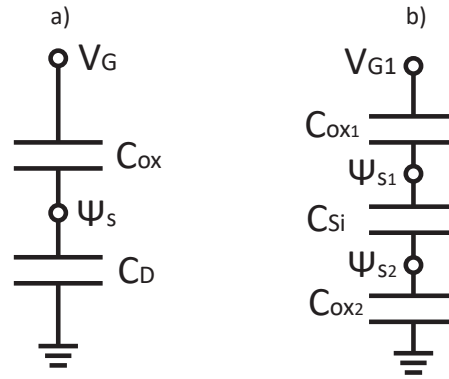


**Figure 1.13:** Equivalent capacitor networks for a) bulk and b) FD-SOI MOS. Adapted from [71].

Equation 1.6 provides the complete expression for subthreshold swing in FD-SOI devices:

$$SS_{FD,SOI} = \frac{\delta V_{G1}}{\delta \log(ID)} = \frac{kT}{q} \ln(10) \left[ \left( 1 + \frac{C_{ss,1}}{C_{ox,1}} + \frac{C_{Si}}{C_{ox,1}} \right) - \frac{\frac{C_{Si}}{C_{ox,2}} \frac{C_{Si}}{C_{ox,1}}}{1 + \frac{C_{ss,2}}{C_{ox,2}} + \frac{C_{Si}}{C_{ox,2}}} \right] \quad (1.6)$$

In this equation,  $C_{ss,1}$  and  $C_{ss,2}$  are the top and bottom interface trap capacitances, while  $C_{ox,1}$  and  $C_{ox,2}$  are the front and bottom gate oxide capacitances, respectively.  $C_{Si}$ , which is the silicon film capacitance, is calculated as  $\epsilon_{Si} / t_{Si}$ . The multiplying factor in the square brackets of Equation 1.6 is almost equal to 1 for FD-SOI structures. In this work, we obtain a calculated multiplying factor of 1.0588 and a subthreshold slope of 63 mV/decade for our devices when the contributions of the trapped charges in the oxide layers are not considered, and considering the following used parameters:

- $t_{Si} = 27$  nm, and  $\epsilon_{Si} = 11.7$ .
- $t_{ox,1} = 7$  nm, and  $\epsilon_{ox,1} = \epsilon_{HfO_2} = 16$ .
- $t_{ox,2} = 20$  nm, and  $\epsilon_{ox,2} = \epsilon_{SiO_2} = 3.9$ .

More details on this will be provided in Section 2.3.



In this work, we will exploit two different SiNW array platforms, but both of them are characterized by a thin silicon layer ( $t_{Si} < 30$  nm), and thin SiO<sub>2</sub> box thickness ( $t_{SiO_2, box}$  is 120 nm and 20 nm in the two cases). They can be described as Ultra-thin Double-Gate SOI Transistors and accurate modeling of the threshold voltage and the subthreshold current is offered in [72].

In the case of fully depleted structures (such as the ones exploited in this work), the depletion charge is constant, as previously stated, and it is expressed by Equation 1.7:

$$Q_{D,FD-SOI} = qN_A t_{Si} \quad (1.7)$$

These double-gate SOI transistors face the effect of *volume inversion* [73]: when the silicon thickness is lower than the sum of the extension of the depletion regions created at the two interfaces the entire silicon layer is depleted and the two depletion region interacts, thus the inversion layer is not created only at the top and bottom interfaces, but throughout the entire silicon volume. This effect differentiates the behavior of this family of devices with respect to bulk MOSFETs, bringing higher carriers' concentration and mobility, an increase in drain current and transconductance, and lower frequency noise [73, 74].

The threshold voltage could be modified as in Equation 1.8:

$$V_{th,FD-SOI} = \frac{\Phi_M - \Phi_{Si}}{q} + \psi_S^* - \frac{Q_{D,FD-SOI}}{C_{ox}} \sqrt{1 + \frac{\delta}{\zeta}} \quad (1.8)$$

where the depletion charge is divided by two because equally shared by the two gates, and the two parameters:

$$\zeta = \frac{q}{kT} \frac{Q_{D,FD-SOI}}{8C_{Si}} \quad (1.9)$$

and

$$\delta = \frac{C_{ox}}{4C_{Si}} \quad (1.10)$$

create a correction factor under the square root that ranges between 1 and  $\sqrt{2}$ . Moreover,

the surface potential at the threshold  $\psi_S^*$  in a thin SOI structure can be modified as in the equation below:

$$\psi_S^* = 2\phi_F + \frac{kT}{q} \ln \left( \delta \frac{1}{1 - e^{-\alpha}} \right) \quad (1.11)$$

For sensing applications, the most interesting working region for the transistor is the weak inversion, since the highest current sensitivity is obtained at lower voltages. In their work [72], Francis et al. also propose an analytical equation for the drain current in subthreshold regime for an FDSOI n-MOSFET (Equation 1.12):

$$I_D = \frac{W}{L} \mu_n^4 C_{Si} \left( \frac{kT}{q} \right)^2 \left[ 1 - e^{(-q/kT)(Q_D/8C_{Si})} \right] \cdot \left[ 1 - e^{(-qV_{DS}/kT)} \right] \cdot e^{(q/kT)(V_G - V_{FB} - [(Q_D/2)C_{ox}] - 2\phi_F)} \quad (1.12)$$

where  $\mu_n$  is the electron mobility,  $V_{DS}$  and  $V_G$  are the drain to source voltage and the gate voltage, respectively. As expected we have an exponential behavior of the subthreshold current, the main factor that allows to achieve higher current sensitivity. Moreover, Equation 1.12 agrees with the assumptions previously discussed: the subthreshold slope of this kind of device reaches the ideal value of 59.5 mV/decade for MOS transistors, according to Equation 1.6.

In this work, the best-case achieved subthreshold swing is 80 mV/decade. We could impute the difference from the ideal value to the presence of traps at the two Si-oxide interfaces, an effect described by Equation 1.13:

$$SS_{real} = SS_{ideal} \left( 1 + \frac{C_{ss}}{C_{ox}} \right) \quad (1.13)$$

In this work, and in general, for sensing applications based on FET, the theoretical definition of the threshold will not be used to calculate the voltage sensitivity, but we will exploit the concept of threshold voltage arbitrarily defined at a constant drain current  $I_{th}$ .

### 1.3.2 The Ion-Sensitive Field-Effect-Transistor

#### Fundamentals of solid-liquid interface: oxide materials

Before digging into the theory of the Ion-Sensitive FET (ISFET), it is worth introducing some concepts about the charge distribution in oxide-electrolyte interface systems. When an oxide (or another material) is immersed in an ionic liquid, an electrical potential is generated in the proximity of the interface. In fact, an oxide surface usually shows a negative surface charge that attracts counter ions from the electrolyte, to assure the electrical neutrality of the system. The modeling of the charge distribution in the electrolyte has evolved over time.

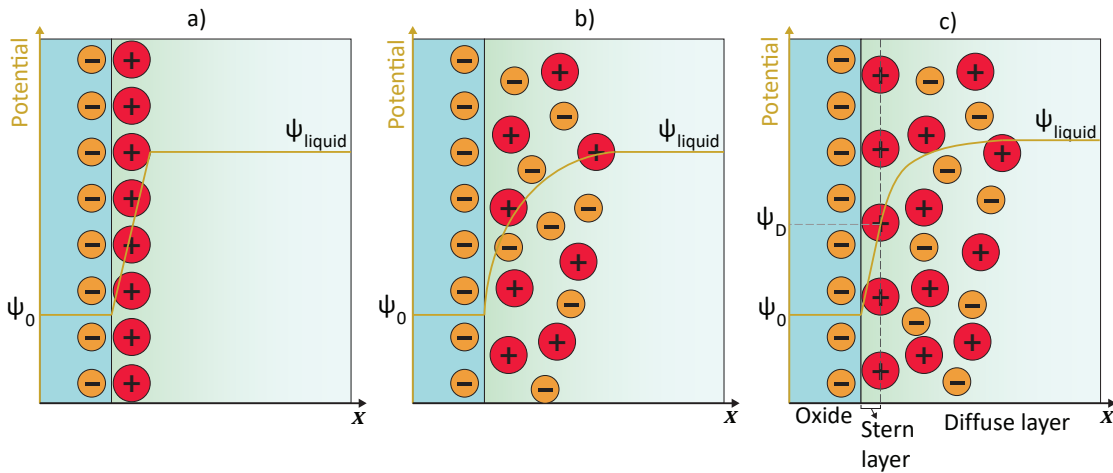


**Figure 1.14:** Oxide-electrolyte interface models.

The first to propose a model for this charge distribution was Hermann von Helmholtz in 1853 [75]. In the first model, the negative surface charge is compensated by a compact layer of counter ions in a very thin region in proximity to the interface. This results in a parallel plate capacitor behavior with a linear potential drop, as depicted in Figure 1.14a.

Figure 1.14b shows the Gouy-Chapman model, which takes its name from the two scientists that independently proposed it [76, 77]. They introduced the idea of a diffuse double layer that has an excess charge that is equal and opposite to the one of the oxide surface, to guarantee the system neutrality. The distribution of the ions creates an exponential decrease in the surface potential along the electrolyte solution. Overall, this model overestimates the expected capacitance compared to experimental results.

In 1924, Otto Stern proposed a model taking into consideration the ionic radius of the charges in the electrolyte by combining the two previous models [78]. As shown in Figure 1.14c, the distribution of the ions can be divided into two regions: a first compact layer (inner Stern layer) is formed by counterions in direct proximity to the solid-electrolyte interface thanks to electrostatic Coulomb attraction. This compact layer is followed by a diffuse layer, in which the ions are not fixed, but tend to diffuse. The potential distribution in the electrolyte is split across two capacitors: across the Stern layer ( $C_S$ ) the potential has a linear drop, that becomes

exponential across the diffuse layer ( $C_{diff}$ ). The overall capacitance can be modeled as two capacitors in series (Double Layer Capacitance,  $C_{DL}$ ), thus leading to Equation 1.14:

$$C_{DL} = \frac{C_{diff}C_{DL}}{C_{diff} + C_{DL}} \quad (1.14)$$

Newer and more precise model systems have been proposed, the Stern model remains acceptable in first approximation, and it will be the reference one in this work.

### Fundamentals of the ISFET

In 1970, Piet Bergveld suggested for the first time that the MOSFET, which physics has already been discussed in the previous Section 1.3.1, could also be utilized for ion sensing, leading to the creation of a new technology, named Ion-Sensitive Field Effect Transistor (ISFET). After its debut in a short communication in 1970 [79], the author proposed a detailed description of the device in a full paper in 1972 [80]. Over the past 50 years, numerous research studies have been conducted on the ISFET technology, leading to the proposal of various related devices such as CHEMFET [81], PRESSFET [82], Bio-FET [83, 84], and more.

An ISFET can be described as a MOSFET where an electrolyte replaces the metal gate, and the threshold voltage can be modulated by chemical phenomena at the interface between the gate oxide and the electrolyte itself. The gate voltage is usually applied through a reference electrode immersed in the electrolyte, also called *Liquid Under Test* (LUT). Two schematic representations of a bulk MOSFET and an ISFET are shown in 1.15 to highlight the differences between them. It is important to note that ISFETs were not originally designed to replace conventional pH glass electrodes. Instead, they were developed to provide alternative options for scenarios where glass electrodes were not suitable, such as when measuring small volumes or requiring a fast response time. However, despite their potential practical applications, ISFETs have often been compared to pH glass electrodes, which has shifted the focus of discussions in research [85].

The equation describing the threshold voltage of an ISFET should be slightly modified compared to Equation 1.2 because the role of the metal gate is played by a *liquid gate*. Hence, the threshold voltage of the ISFET can be represented as in Equation 1.15:

$$V_t = E_{ref} - \Psi_0 + \chi^{sol} - \frac{\phi_{Si}}{q} - \frac{Q_{ox} - Q_{ss} + Q_B}{C_{ox}} + 2\phi_f \quad (1.15)$$

Compared to the equation of the MOSFET threshold voltage, we have two additional contribu-

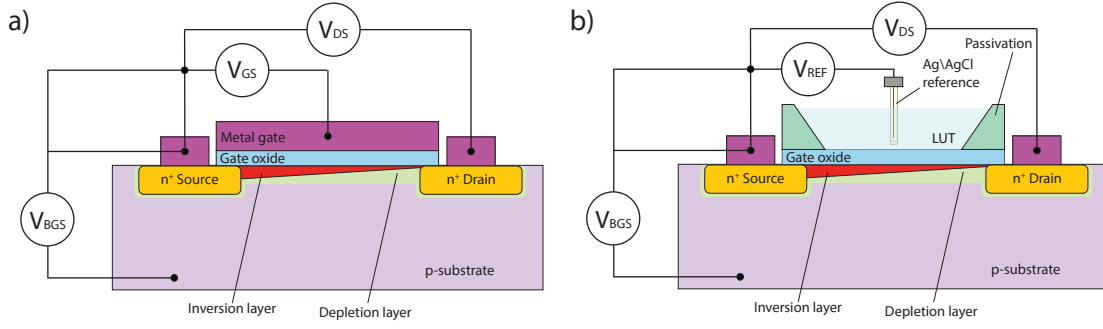


**Figure 1.15:** Schematic comparison between MOSFET and ISFET. a) Bulk Si-MOSFET cross-section, b) ISFET cross-section. The metallic gate of the MOSFET is replaced with a liquid gate, and the gate voltage is applied through a reference electrode immersed in the same liquid under test.

tions:  $E_{ref}$  is the constant potential of the reference electrode, while  $\Psi_0 + \chi^{sol}$  is the interface potential at the electrolyte/oxide surface. In particular,  $\Psi_0$  is the chemical potential (that depends on the chemical reaction, or species concentration), and  $\chi^{sol}$  is the surface dipole potential of the solvent, and it is considered constant.

The key role in the equation for biosensing applications is played by  $\Psi_0$ , which will change as a function of the analyte concentration in the solution, depending on the application. Any chemical activity on the oxide surface could modify the value of  $\Psi_0$ , thus creating a threshold voltage shift ( $\Delta V_{th}$ ). In our work, we introduce the theoretical explanations for ISFET behavior considering the case of pH detection. This explanation can be extended to different ions and analytes detection.

If we take into consideration Equation 1.16 describing the ISFET drain current in the unsaturated region [86, 87], we notice that changes in drain current due to pH variations could derive only by a shift in the surface potential  $\Psi_0$ :

$$I_D = \mu_n C_{ox} \frac{W}{L} \left\{ \left[ V_{GS} - \left( E_{ref} - \Psi_0 + \chi^{sol} - \frac{\Phi_{Si}}{q} - \frac{Q_{ox} - Q_{ss} + Q_D}{C_{ox}} + 2\phi_f \right) \right] V_{DS} - \frac{1}{2} V_{DS}^2 \right\} \quad (1.16)$$

To link a shift of the surface potential ( $\Delta\Psi_0$ ) with a shift in pH ( $\Delta pH$ ) we need to introduce the site-binding model proposed in 1974 by Yates et al. [88] and later adapted to the case of ISFETs [89, 90].

The site-binding model describes the charging mechanism of an oxide-electrolyte interface. The hydroxyl groups of the oxide surface are amphoteric: they can be neutral (A-OH), protonated and thus positively charged (A-OH<sub>2</sub><sup>+</sup>), or deprotonated and thus negatively charged (A-O<sup>-</sup>). In the presence of an ionic liquid, we can define the following surface reactions [87]:

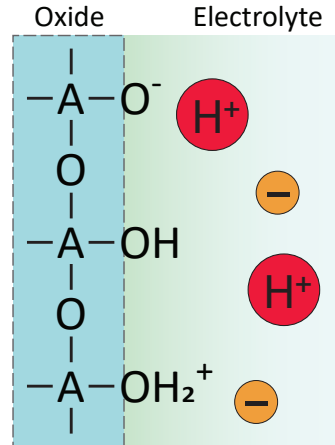
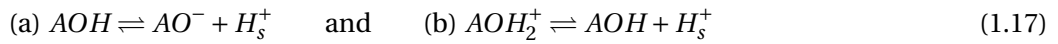


**Figure 1.16:** Amphoteric sites on the oxide surface. Site-binding model for charging mechanism of an oxide-electrolyte interface.



where  $H_s^+$  are the hydrogen ions located directly near the oxide surface. Thanks to the surface reactions described in Equation 1.17, a surface charge ( $-q[B]$ ) is built up, thus developing an electrostatic potential  $\Psi_0$  at the proximity of the oxide surface. This potential creates the difference between the surface proton chemical activity [ $a_{H_s^+}$ ] and the bulk proton chemical activity [ $a_{H_B^+}$ ], related by the Boltzmann distribution equation [90, 91]:

$$a_{H_s^+} = a_{H_B^+} \cdot \exp\left(\frac{-q\Psi_0}{kT}\right) \quad (1.18)$$

that can be rewritten in terms of pH values as:

$$\text{pH}_s = \text{pH}_B + \frac{q\Psi_0}{2.3kT} \quad (1.19)$$

where  $\text{pH}_s$  and  $\text{pH}_B$  indicate the surface and bulk pH values, respectively.

The pH sensitivity arises from the ability of the oxide to keep [ $H_s^+$ ] constant, upon variations of [ $H_B^+$ ]. This property is described by the so-called *intrinsic buffer capacity*  $\beta_s$ , and it corresponds to the variation of the number of charged groups [B] (equal to the number of deprotonated hydroxyl groups minus the protonated ones) divided by the variation of  $\text{pH}_s$ . A complete

expression of the buffer capacity is given in Equation 1.20:

$$\beta_s = \frac{\delta[B]}{\delta pH_s} = N_s \frac{K_b a_{H_s^+}^2 + 4K_a K_b a_{H_s^+} + K_a K_b^2}{\left(K_a K_b + K_b a_{H_s^+} + a_{H_s^+}^2\right)^2} 2.3 a_{H_s^+} \quad (1.20)$$

where  $N_s$  is the density of available amphoteric sites,  $K_a$  and  $K_b$  are the dissociation constants related to the reactions in Equation 1.17. These three parameters are characteristic of the oxide nature, thus different oxides have different buffering abilities and will generate different pH sensitivity. Equation 1.20 holds true for all oxides whose charge generation mechanism can be explained by the association and dissociation of the amphoteric groups.

The buffering activity of the oxide creates a surface charge density ( $\sigma_0$ ) that has to be balanced by an equal but opposite charge in the electrolyte solution side of the double layer ( $\sigma_{DL}$ ). The ability of the electrolyte solution to balance the two charges is related to the double-layer capacitance.

The final value of the potential shift  $\Delta\Psi_0$  is related to the shift in the pH value of the bulk solution by Equation 1.21:

$$\Delta\Psi_0 = -2.3\alpha \frac{kT}{q} \Delta pH_B \quad (1.21)$$

where  $\alpha$  is expressed by:

$$\alpha = \left(1 + \frac{2.3kTC_{DL}}{q^2\beta_s}\right)^{-1} \quad (1.22)$$

$\alpha$  is a dimensionless parameter that varies between 0 and 1 depending on the buffering ability of the oxide, and the double-layer capacitance value.

### High- $\kappa$ dielectrics for sensing

As previously discussed in section 1.3.1, the use of high- $\kappa$  dielectric in computing technology was introduced to respond to the need of scaling down the transistor dimensions. It has already been reported that a strong correlation between the high dielectric constant of an oxide and its buffer capacity exists [92]. Other than the dielectric constant, also the ionicity of

Oxide	$\epsilon_r$ or $\kappa$	Sensitivity (mV/pH)
SiO <sub>2</sub>	3.9	10-45 [69, 85, 87, 95, 96, 97, 98, 99, 100]
Si <sub>3</sub> N <sub>4</sub>	7	45-56 [97, 101]
Al <sub>2</sub> O <sub>3</sub>	9	50-57.8 [89, 97, 102, 103, 104]
SnO <sub>2</sub>	9.86	52.8-58 [69, 105]
Ta <sub>2</sub> O <sub>5</sub>	22	56-59 [69, 99, 106, 107]
ZrO <sub>2</sub>	25	50-55.5 [69, 99, 100, 108]
HfO <sub>2</sub>	25	54-59 [69, 100, 108, 109]

**Table 1.2:** Different oxides pH sensitivity.

the oxide (the number of oxygen atoms around a central atom) plays a fundamental role in the maximum sensitivity guaranteed by a certain oxide.

SiO<sub>2</sub> has shown from the very first works that could not achieve pH Nernstian sensitivity [87], and also that tends to absorb other ions in the electrolyte, thus creating instability and drift [93].

Table 1.2 summarizes some of the sensitivities offered by various oxides in ISFET systems present in the literature. Among the high- $\kappa$  oxides, Ta<sub>2</sub>O<sub>5</sub> and HfO<sub>2</sub> offer the highest sensitivity. Since its extended application in computing technology, the high pH sensitivity and temporal stability [94], in this work, we chose to use high-quality hafnium oxide deposited by Atomic Layer Deposition (ALD) as a sensing layer.

### 1.3.3 FET-based biosensors: limitations

Due to their miniaturization, low-power, and integrability properties, a vast number of previous studies have exploited Field-Effect Transistors (FETs) as biosensors. However, this section aims to highlight the existing limitations of this technology and how this work intends to address them.

The primary limitation of FET-based biosensors is the Debye screening of charges in ionic liquids. As previously discussed, when a charged surface is submerged in an electrolyte solution, a Double Layer of charges forms on the surface, leading to an exponential potential drop in the solution. If a charged analyte needs to be detected using an affinity-based mechanism on a biosensor (e.g., an antibody-antigen mechanism), the Coulomb potential created by the charge is also exponentially screened by the solution, as illustrated in Figure 1.17a, over a distance known as the Debye length. This length can be expressed as in Equation 1.23:

$$\lambda_D = \sqrt{\frac{\epsilon_0 \epsilon_r kT}{q^2 I_s}} \quad (1.23)$$



where  $\epsilon_0$  and  $\epsilon_r$  are respectively the vacuum and media permittivity,  $k$  is the Boltzmann constant,  $T$  is the temperature,  $q$  is the elementary charge, and  $I$  the ionic strength of the liquid. The higher the ionic strength, thus the concentration of ions, the shorter the Debye length and the stronger the charge screening. This limitation is the main factor that makes researchers study FET-based biosensors in diluted samples, to increase the Debye length.

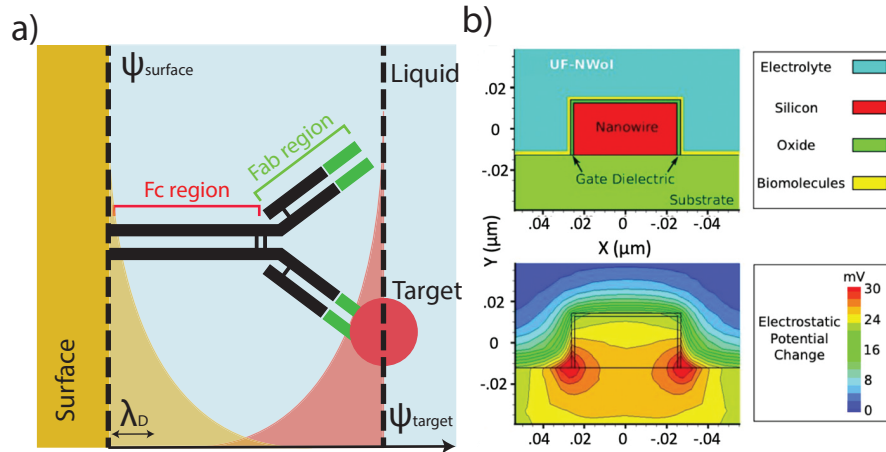


**Figure 1.17:** a) Schematic representation of the Debye screening in affinity-based detection mechanism. The electrostatic potential created by the charged analyte exponentially decreases depending on the ionic strength of the solution. If the probe-analyte capturing site is too far from the surface, the charge can not affect the conduction properties of the surface. Adapted from [110]. b) Concave corners reduce the screening effect in nanowires FET structures. Adapted from [111].

This work proposes two solutions to overcome the charge screening: 1) the exploitation of not suspended planar SiNWs, and 2) the immobilization of fragments antigen-binding region (Fab) antibody on the sensing surface, rather than full antibodies, to use the affinity-based protein recognition mechanism.

The first solution has proved to enhance sensitivities when dealing with label-free FET-based biosensors, thanks to the very large surface-to-volume ratio, and also thanks to the Debye volume limitation guaranteed by concave surfaces, as simulated by Shoorideh et al. [111], and shown in Figure 1.17b. The Debye volume can be defined as the volume that surrounds a defined surface within one Debye length distance: in the case of concave surfaces (such as the lower corners in non-suspended NWs structures) this volume is reduced compared to convex ones, thus increasing the surface-to-volume ratio and limiting the possibility of double layer creation.

The second method exploited in this work to overcome the Debye screening is the use of antibody fragments: a full antibody can have a length between 10 and 15 nm, thus exceeding the Debye length by a factor of 20 in standard human biofluids. By removing the non-antigen-specific part of the antibody, known as the fragment crystallizable region (Fc region), it is possible to obtain either a couple of Fab regions (known as  $F(ab)_2$  region) or a single one.

This study exploits anti-CRP Fab, to shorten the distance between the binding site and the oxide-sensitive surface of the system.

The choice of using SiNWs on SOI for biosensing applications is strongly supported also by previous works. These devices have proven to be optimal candidates for the detection of different biomarkers, from pH and ions [112, 113, 114, 115], DNA [116], proteins [117, 118, 119], cortisol [120], vascular endothelial growth factor molecules [121], cancer risk biomarkers [122], and many others.

#### 1.4 SiNWs as biosensors: state-of-the-art

Silicon Nanowire Field-Effect Transistors (SiNWs FETs) have been widely adopted in our system for several compelling reasons, already mentioned in the previous sections. Their unique characteristics, such as an increased surface-to-volume ratio, lead to enhanced sensing capabilities, making them highly suitable for detecting a wide range of biomolecules and analytes. The nanoscale dimensions of SiNWs enable the detection of even minute concentrations of target molecules, amplifying their sensitivity and reliability as biosensors.

Moreover, previous research and pioneering works have consistently demonstrated the remarkable potential of SiNWs as sensors. These studies have showcased the exceptional sensitivity, selectivity, and label-free nature of SiNWs FETs, making them an attractive choice for biosensing applications.

To present a comprehensive overview of the state-of-the-art in SiNWs FET-based biosensors, we have compiled Table 1.3 summarizing the main works in the field. This table showcases the key features, performance metrics, and applications of these influential studies, highlighting the significant advancements and breakthroughs that have further reinforced the use of SiNWs FETs in biosensing applications. Additionally, it is worth noting that while the focus of Table 1.3 is on SiNWs FET-based biosensors, there has been an increasing body of work exploring double-gate FET structures (DG-FETs) for enhancing sensitivity in biosensing applications [123, 124, 125, 126, 127, 128, 129]. While not listed in the table, these studies have provided a solid basis for harnessing the advantages of dual-gate structures to further improve sensor performance. DG-FETs offer the potential for fine-tuning and optimizing sensor characteristics, such as threshold voltage and transconductance, leading to enhanced sensitivity and selectivity in detecting target molecules. As research in this area continues to evolve, the combination of SiNWs and DG-FET architectures holds the promise of opening new avenues in biosensing technology, pushing the boundaries of sensitivity and paving the way for innovative and highly efficient biosensor platforms.

By leveraging the vast potential of Ultra-Thin SOI SiNWs FETs and building upon the achievements of these landmark works, our system endeavors to push the boundaries of biosensing technology, offering a powerful tool for rapid and precise detection of pH and C-Reactive Protein.

Ref.	Technology*	Analyte	Fluid	LoD	Gate oxide	Sensitivity
[117]	TD, SG	cTnI	0.1xPBS	0.092 ng/mL	Native SiO <sub>2</sub>	6.5%/dec <sup>†</sup>
[130]	BU, SG	Fl-ATPases	Tris-buffer	single protein	Native SiO <sub>2</sub>	1nA/molecule <sup>†</sup>
[121]	TD, SG	VEGF	PBS	1 fM ( $\approx$ 21 fg/mL)	Native SiO <sub>2</sub>	0.1 $\mu$ S/fM <sup>†</sup>
[131]	TD, SG	CRP and cTnI	PBS	1 pg/mL	SiO <sub>2</sub>	35mV/dec <sup>†</sup>
[118]	TD, SG	cTnT	Human Serum	30 fg/mL	SiO <sub>2</sub>	2.5%/dec <sup>†</sup>
[116]	TD, SG	DNA	0.01 $\times$ SSC	10 fM ( $\approx$ 6.5 fg/mL)	Native SiO <sub>2</sub>	4%/dec <sup>†</sup>
[132]	BU, SG	Cancer biomarkers	Undiluted Serum	0.9 pg/mL	Native SiO <sub>2</sub>	-50nS/dec <sup>†</sup>
[133]	TD, SG	cTnI, cTnT	PBS	50 fg/mL	Native SiO <sub>2</sub>	-50 mV/dec <sup>†</sup>
[120]	TD, SG	Cortisol	Human Saliva	0.05 ng/mL	SiO <sub>2</sub>	-100mV/dec <sup>†</sup>
[115]	TD, DG	pH	Buffer	NA	Al <sub>2</sub> O <sub>3</sub>	96mV/pH
[134]	TD, SG	pH	Buffer	NA	Native SiO <sub>2</sub>	100 nS/pH
[134]	TD, SG	streptavidin	Buffer	10 pM ( $\approx$ 0.6 ng/mL)	Native SiO <sub>2</sub>	7.5 nS/nM <sup>†</sup>
[135]	TD, DG	pH	Buffer	NA	SiO <sub>2</sub>	984.1 mV/pH
This Work	TD, DG	pH, CRP	ISF-like, 0.1xPBS	0.16 $\mu$ g/mL <sup>**</sup>	HfO <sub>2</sub>	3V/pH, 60%/dec

**Table 1.3:** SiNW FET as biosensors, previous works. \* TD = Top-Down, BU = Bottom-Up, SG = Single-Gate, DG = Dual-Gate. \*\* for protein sensing. <sup>†</sup> Value extracted from graphs.

## 1.5 Summary

This chapter provides the theoretical basis for the work presented in this thesis. We discuss the concept of biosensors and explain why dermal interstitial fluid is an interesting biofluid for real-time biomarker detection in the human body. We also discuss the motivation behind our choice to use ion-sensitive field-effect transistors (ISFETs) as a key component of the biosensor system. ISFETs are easily miniaturized, offer low-power solutions, and can provide high sensitivity and selectivity when properly functionalized.

To enhance the sensitivity and stability of the system, we propose using high- $\kappa$  oxides as the sensitive gate oxide, and fully-depleted 1D structures (such as silicon nanowire arrays on silicon on insulator) as optimal candidates for high-sensitivity systems. Moreover, the use of antibody fragments as capturing probes, in the affinity-based detection mechanism of the biosensors, has been encouraged to overcome the Debye screening of charged analytes in ionic liquids.

In the next chapter, we introduce and provide a detailed presentation of the platform used during this work, with their fabrication process flow details and electrical characterization.



## 2 Silicon nanowires technology

*In the previous chapter, the fundamental theory of Field-Effect Transistor and Ion Sensitive FET has been introduced. Fully depleted silicon nanowire arrays on SOI substrates have been selected as the core technology of the biosensor, due to their high surface-to-volume ratio, and high subthreshold slope. Moreover, the use of high- $\kappa$  dielectric as gate oxide has proved to be the optimal choice for achieving high sensitivity and stability. This second chapter provides an overview of the fabrication technology chosen to implement a FET-based biosensor for rapid diagnostic and real-time protein detection. The focus is on two different implementations of SiNW arrays on SOI technology, namely wafer-scale fabricated chips produced by CEA-LETI in Grenoble, and chips fabricated at CMI in EPFL with a design that can fit with the microneedles array system needed to extract human interstitial fluid (ISF). Firstly, we present the most important steps of the CEA-LETI chips fabrication process flow, their DC electrical characterization, and performance in Section 2.2. Secondly, we report on the in-house fabricated nanowire arrays, where we provide an overview of the TCAD simulation used to select the best source and drain implantation parameters in Section 2.3.1. We then present the detailed fabrication process flow (Section 2.3.2) highlighting the most critical steps (Section 2.3.4) and the DC electrical characterization (Section 2.3.5).*

### 2.1 Introduction

As described in Chapter 1, 1D fully-depleted structures are optimal candidates for biochemical sensing in human bio-fluids [136]. In this work, horizontal silicon nanowires (SiNWs) on Silicon-on-Insulator (SOI) substrates have been exploited as the core platform for the fabrication of miniaturized biosensors. Over the full length of this work, two platforms will be exploited:

- A wafer-scale fabricated chip made of more than a hundred independent SiNW arrays, designed and fabricated at CEA-LETI in Grenoble.
- An optimized SiNW arrays chip on SOI, designed and fabricated at EPFL, able to be

integrated with the ISF extraction solution developed within the frame of the European Digipredict project.

The first platform was entirely designed and fabricated at CEA-LETI, and it was intended as a multi-purpose and projects chip. In Section 2.2, we report the fabrication details together with the DC electrical characterization of the SiNW arrays. The results obtained by using this platform as pH sensor and biosensor for protein detection are presented and commented on in section 4.1, and 5.1, respectively. Since this platform was not designed within the frame of the Digipredict project, compatibility with the other parts, such as the microneedles extractor or the electronic read-out circuit, is not ensured. Moreover, the limited availability of chips, lead to the decision to in-house fabrication of the second listed solution. The fabrication process of the latter is reported in section 2.3, the electrical characterization in section 2.3.5, while the obtained results for pH and CRP sensing are reported in section 4.1.3 and 5.1.

## 2.2 CEA-LETI silicon nanowire arrays

### 2.2.1 Chip description and fabrication process flow

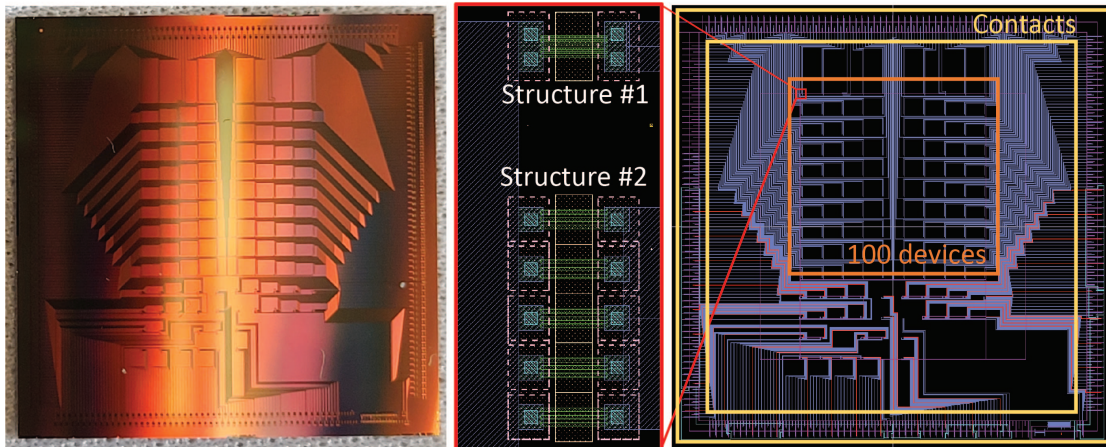


**Figure 2.1:** CEA-LETI chip: picture and layout. Each device is made of two separate structures, one made of 5 parallel nanowires, and the second with 15 parallel nanowires. In this work, we report the results obtained only with arrays of the second type. The orange box highlights the position of 100 identical devices.

The chips provided by CEA-LETI [137] are squared chips with a side length of 2 cm, as shown in Figure 2.1. They are based on SOI technology, and the main steps of the fabrication process are described in Figure 2.2: the fabrication starts from a (100)-oriented SOI wafer, with a SiO<sub>2</sub> box thickness of 120 nm. The top silicon layer is thinned down by oxidation and etching steps, to reach a final thickness of 30 nm. The NWs are patterned by electron beam lithography, followed by deep reactive ion etching of Si. A standard lithography step is then employed to define source and drain regions, that are created by phosphorous ion implantation. A first

layer of 3 nm thermal oxide is grown on the NWs surface, followed by atomic layer deposition (ALD) of 4 nm of high- $\kappa$  dielectric ( $\text{HfO}_2$ ). The nanowires are then encapsulated with a 50 nm SiN and 250 nm Tetraethyl Orthosilicate (TEOS) bilayer. After depositing ohmic metal contact and lines for source and drain regions, a 100nm thick silicon dioxide passivation layer is deposited. Finally, the  $\text{HfO}_2$  surface of the nanowires is exposed by selective etching of the passivation and encapsulation layers. Each chip possesses 100 identical devices, that are positioned in the top-center of the layout, within the orange square drawn in Figure 2.1.

Each device is split into two different structures, that can be operated independently: one structure (structure #1 in Figure 2.1) is made by five parallel nanowires, while the second structure (structure #2 in Figure 2.1) is made by five triplets of nanowires electrically connected in parallel. In the second structure, all the horizontal nanowires share the same source and drain contacts. At chip level, the 100 devices can be split into twenty lines: each line is composed of five sensors that possess common source and independent drain contacts. This particular design allows us to operate two sensors on the same line by using only five contacts, namely two drain contacts (one per each sensor), one source contact (shared by the two devices), a back-gate contact, and a liquid gate contact (shared by the two devices). As described in section 3.3.1, this will allow us to perform reference-compensated experiments.

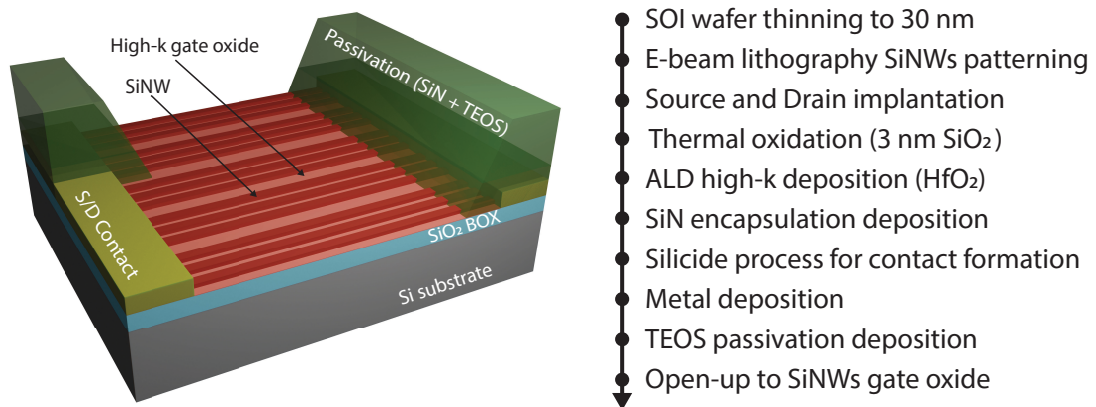


**Figure 2.2:** Schematic view of the complete device and summary of the fabrication process flow adapted from [137].

This specific chip layout has been developed in order to enable a microfluidic system integration to implement a multiplexed measurement of different bio-markers [137]. In our specific case, we developed a Polydimethylsiloxane (PDMS) microfluidic thanks to which we can specifically functionalize each sensor, with the liberty of immobilizing different probes on the surface of different SiNW arrays. We discuss this in detail in section 3.2. We report in Figure 2.3 the atomic force microscopy (AFM) surface topography of three parallel nanowires, a subgroup of the fifteen nanowires. Additionally, we provide a scanning electron microscopy (SEM) image, falsely colored for clarity. To acquire the AFM topography image we used a Cypher S AFM from Oxford Instruments in AC-tapping mode, a scan size of  $1 \mu\text{m}$ , and a scan rate of 1.95Hz. The used tip was a Tap300Al-G with aluminum reflective coating from



the source potential has been fixed at 0 V, thus in all the plots we consider the drain to source voltage  $V_{DS}$  equal to the voltage  $V_D$  applied on the drain contact. The front gate potential is applied through an external commercial Ag/AgCl reference electrode (from Micrux Technologies) immersed in the liquid-under-test (LUT) solution in contact with the gate oxide. We refer to this voltage as the reference voltage ( $V_{REF}$ ). The back-gate voltage is applied by biasing the Si bulk from the back of the chip while being in contact with the conductive chuck of the probe station, and we refer to it as  $V_{BG}$ . All the measurements are performed in normal environmental conditions and the LUT is always at room temperature. During the full DC electrical characterization, the employed liquid has been a not diluted phosphate saline buffer (PBS). One SiNW array is made of 15 parallel NWs, each with a length  $L = 1.4 \mu\text{m}$ , a width  $W = 140 \text{ nm}$ , and a thickness of 30 nm. First, we report the transfer characteristic  $I_D$ - $V_{REF}$  of one array on a semi-logarithmic plot in Figure 2.4a: the drain voltage is fixed at 0.3 V, and all the currents are measured thanks to the Source Measure units (SMUs) of the parameter analyzer, while the reference voltage is swept from -0.5 V to 1.0 V and vice-versa, to be able to measure the hysteresis between the forward and backward sweeps.

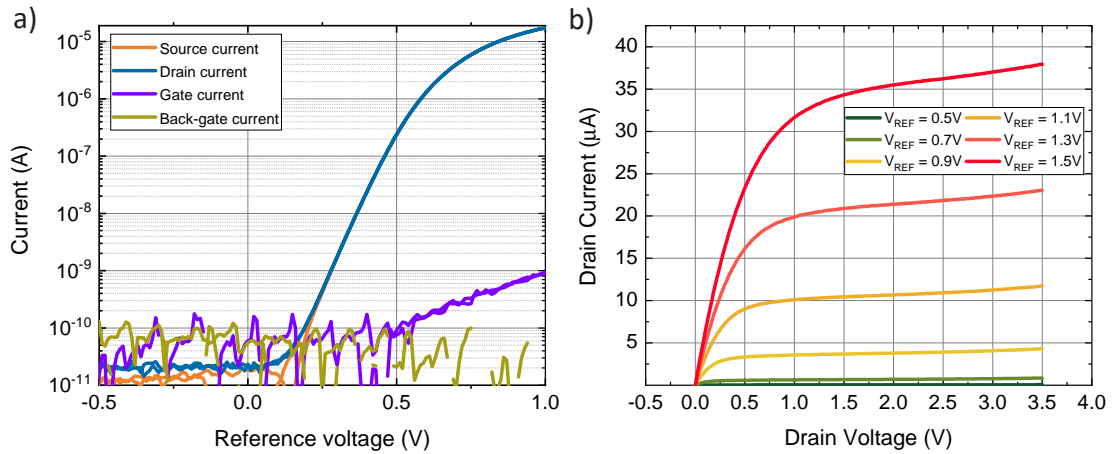


**Figure 2.4:** Transfer and output characteristics of a CEA-LETI SiNW array. a) Semi-logarithmic plot of the transfer characteristic of one SiNW array sensor. The drain current is hysteresis-free, with an ON-OFF ratio of six orders of magnitude. Leakage currents are lower than  $0.48 \text{ nA}/\mu\text{m}$  for the entire operating region. b) Output drain characteristic.

The SiNW array shows a drain  $I_{ON}$  to  $I_{OFF}$  ratio of six orders of magnitude, and a hysteresis between the forward and backward sweeps lower than 3 mV. Gate and back-gate leakages are lower than  $0.48 \text{ nA}/\mu\text{m}$  for the whole operating region, demonstrating the presence of a high-quality high- $\kappa$  dielectric. The transistor output characteristic is shown in Figure 2.4b, where  $V_{BG} = 0 \text{ V}$ . The plot shows the transistor response for different applied reference voltages, ranging from 0.5 V (weak inversion regime) to 1.5 V (strong inversion). In the saturation region, the transistor shows a slight channel length modulation effect, that does not affect the sensor capabilities.

Figure 2.5a shows the extracted sub-threshold slope of the device, for both backward and

Budget-Sensors. The scanning electron microscopy image has been acquired with a Zeiss Merlin microscope, equipped with a Gemini column. Our observations reveal that the SiNWs structure possesses an overall height of 42 nm, resulting from silicon dioxide box over-etching during fabrication. The SEM image further depicts two distinct structures with five and fifteen nanowires, respectively, which can be used independently. For this thesis, we solely report the results obtained from the second type of structure, consisting of five triplets of parallel nanowires.

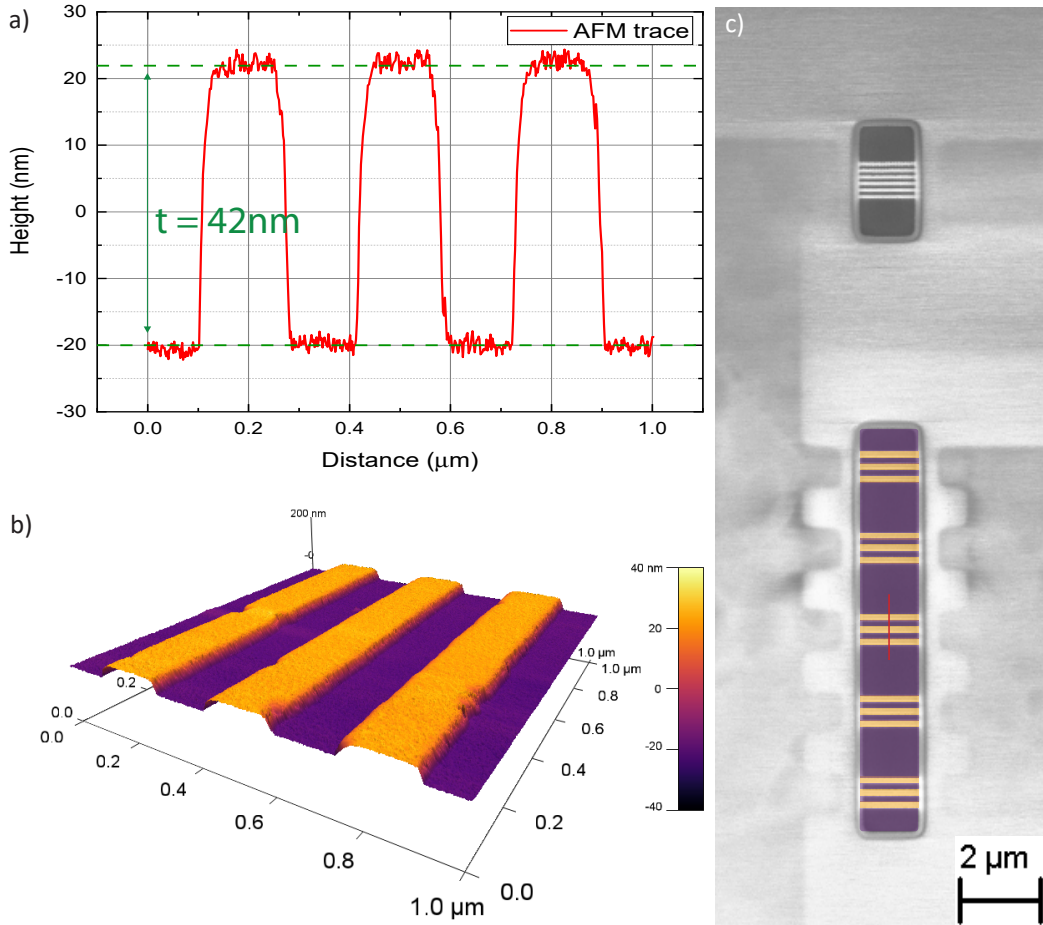


**Figure 2.3:** AFM and SEM images of the CEA-LETI SiNW array. a) Cut-line profile of the AFM topography image in figure (b). The total thickness of the SiNWs structure is 42nm, due to the thickness of the gate oxide and the over-etching of the silicon dioxide box. b) AFM topography image, highlighting three parallel nanowires. c) Falsely colored SEM image, to have a color correspondence with (b). We can notice on the top the smaller device, with only 5 parallel nanowires, and on the bottom trench the second type, with 15 parallel nanowires (in orange).

### 2.2.2 DC Electrical characterization

The DC electrical response of the SiNWs BioFET is measured using a Keithley 4200A Parameter Analyzer connected to a Cascade Microtech Probe Station. For all the reported measurements

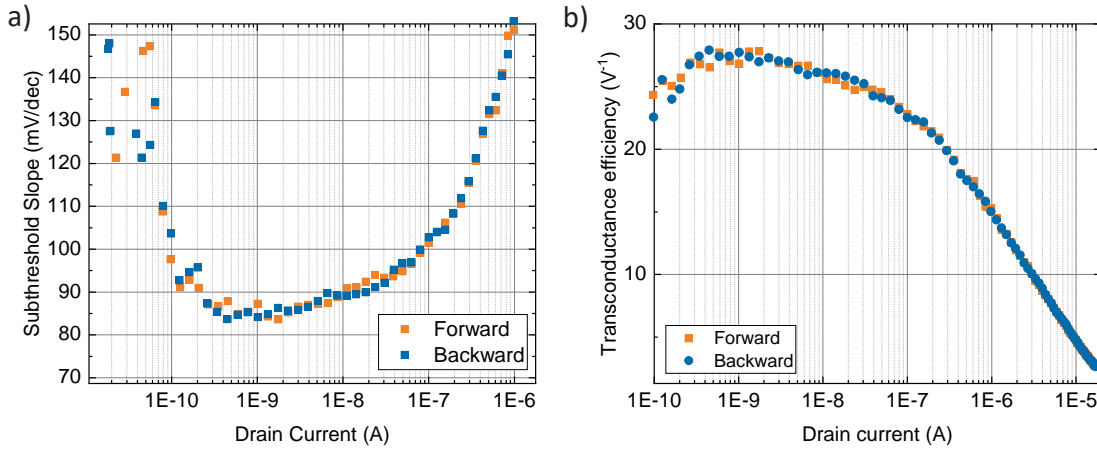


**Figure 2.5:** a) Transistor subthreshold slope for both forward and backward sweep of the reference voltage. b) Transconductance efficiency ( $g_m/I_D$ ). Higher values are found in sub-threshold working regime, as expected.

forward sweeps. The two curves overlap, highlighting once again the absence of hysteresis, and the sub-threshold slope remains lower than 90 mV/decade for almost two decades of the drain current. An abrupt switch-on mechanism is fundamental in a FET-based biosensor when operated in weak inversion regime. In fact, the current sensitivity is inversely proportional to the subthreshold slope value [138, 139, 140, 141, 142]. For the sake of completeness, we also report the transconductance efficiency of the transistor, a fundamental parameter in analog circuit design: it consists of the ratio between the transconductance  $g_m$ , and the drain current  $I_D$ , giving an immediate idea of the ratio between the amplifier gain and the power consumption. In weak inversion, our transistor demonstrated optimal capabilities, with a transconductance efficiency of  $28 \text{ V}^{-1}$ , comparable to those found in the literature for novel semiconductor devices [143], and standard bulk silicon Field Effect Transistors [144, 145, 146, 147, 148]. The transconductance efficiency is a key parameter for analog application and design [149], but it was also proven to be an important feature for the design and development of biosensors [150].

We also measure the transistor's back-gate transfer characteristic by applying a constant voltage to the Ag/AgCl reference electrode of  $V_{REF} = 0 \text{ V}$ , and a drain voltage  $V_D = 0.3 \text{ V}$ . The results are shown in Figure 2.6a, where we report the drain current together with the back-gate leakage. In this configuration, the back-gate leakage is always lower than  $0.14 \text{ nA}/\mu\text{m}$ , while the backward and forward sweep perfectly overlap, with no hysteresis. The ability to tune the transistor top-gate transfer characteristic is proven in Figure 2.6b, where different  $I_D$ - $V_{REF}$  curves at different back-gate constant voltage values are displayed. The transistor shows to be easily and reliably tunable, and this property allows to position the bias point in the desired working region: by tuning the back-gate voltage, it is possible to work in sub-threshold regime with a  $V_{REF} = 0 \text{ V}$ , an interesting working condition for a biosensor.

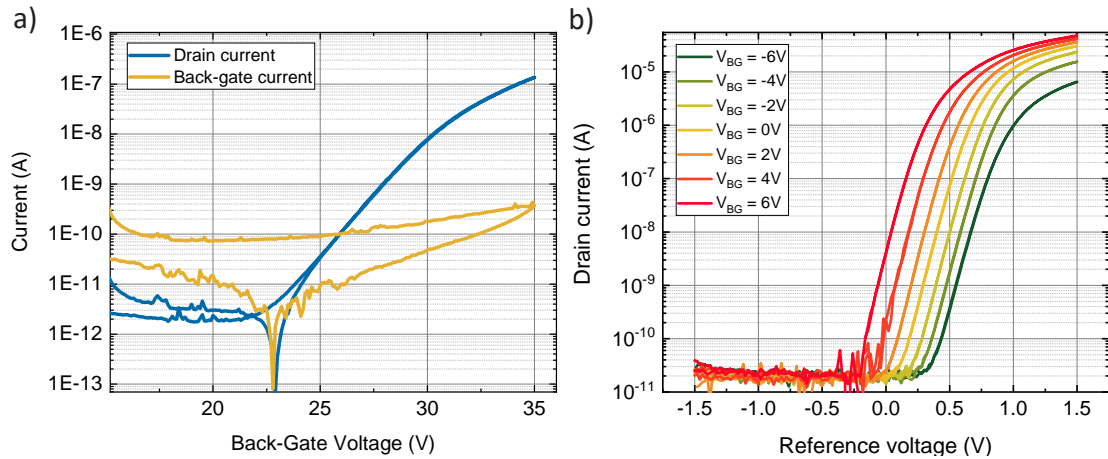


**Figure 2.6:** Back-gate influence on the transistor's performance. a) Back-gate transfer characteristic. b)  $I_D$ - $V_{REF}$  transfer characteristics for different applied back-gate voltages: the transistor shows to be easily tuned by changing the back-gate bias.

## 2.3 Fabrication and characterization of in-house SiNWs biosensors

In this section, we report the detailed fabrication of the SiNWs biosensors fully designed and produced in the cleanroom of the Center of MicroNanotechnology (CMi) on the EPFL campus. We first present the TCAD simulation used to tune the used parameters during the source and drain implantation step (section 2.3.1), followed by the complete fabrication process that eventually achieved the best performances (section 2.3.2), and the different trials of the fabrication process, describing the failed attempts in detail (section 2.3.4). Finally, we comment on the electrical performances of the chips in Section 2.3.5.

### 2.3.1 TCAD simulations for source and drain regions implantation

Dopants implantation in thin silicon layers of the SOI substrate presents many challenges that must be faced to obtain desired ohmic contacts, without damaging the SiO<sub>2</sub> box. In our work, the right ions' energy and implantation dose have been simulated using Sentaurus TCAD software, before shipping the substrates to IBS in France for the actual process. Three main parameters were taken into consideration during the simulations:

- the SiO<sub>2</sub> stopping layer thickness on top of the silicon layer, used to obtain the implantation peak at the Si surface;
- the implanted ions' energy;
- the implantation dose.

The three parameters have been tackled at the same time, but we report the results in the above-presented order.

To study the influence of the stopping layer, various thicknesses between 1nm and 10nm have been simulated. We can approximate the implantation doping profile as a Gaussian distribution [151], whose peak position and broadness are dependent on different parameters, mainly the implantation energy. To achieve a uniform and high concentration of dopants close to the gate oxide surface, the distribution peak position should fall near the top surface of the silicon layer. This can be accomplished by using a silicon oxide mask to physically stop the ions at the desired position. To obtain the best results, simulations have shown that a  $\text{SiO}_2$  mask thickness between 5nm and 7nm is ideal.

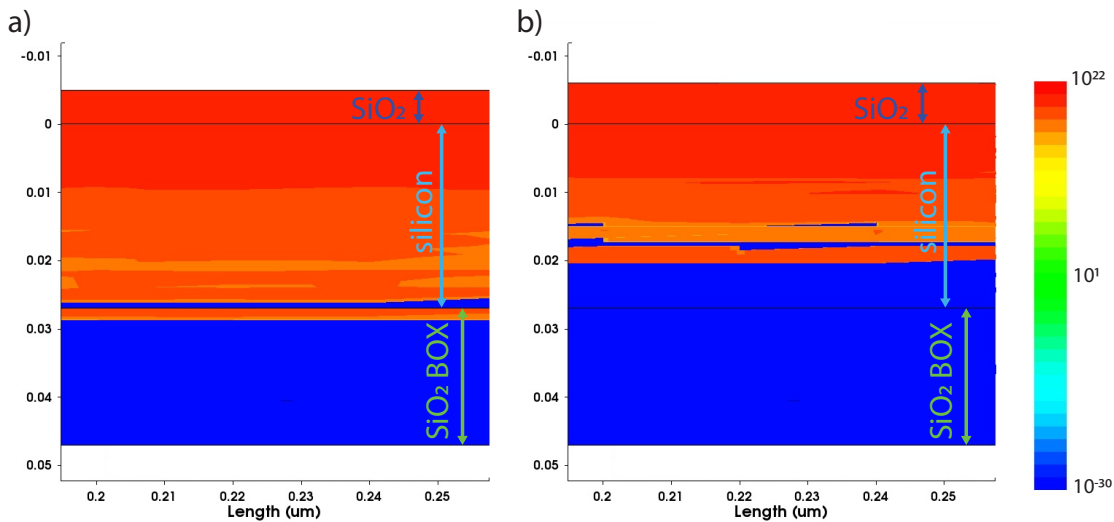


**Figure 2.7:** Stopping layer thickness TCAD simulation results. Channel cross-section when the top-oxide layer is a) 5 nm thick, and b) 6 nm thick. The implanted ions reach the  $\text{SiO}_2$  box for thicknesses of the stopping layer of 6 nm.

Figure 2.7 displays the results for 5nm and 6nm, where it can be observed that for a thickness below 6nm, the dopants reach the buried  $\text{SiO}_2$  box. However, this scenario should be avoided because a high-density concentration in the bottom oxide may increase leakage current, which can negatively impact the transistor's performance. Therefore, a thickness of 6nm was selected because it provides a high dopant concentration at the silicon surface while keeping the implanted ion relatively far from the buried oxide surface.

The second studied parameter has been the ions' energy. The highest their energy, the deeper the penetration depth of the ions. Since the silicon layer during the implantation process is only 27 nm thick, the tuning of this parameter is of great importance. We simulated 5 different implantation energies, at a fixed dose of  $3 \cdot 10^{19} \text{ cm}^{-2}$  and  $6 \cdot 10^{19} \text{ cm}^{-2}$ . The obtained results are depicted in Figure 2.9, considering the cross-section of the channel. To ensure the future presence of ohmic contacts, we arbitrarily impose a minimum active dopant concentration after the annealing above  $1 \cdot 10^{19} \text{ cm}^{-3}$  [65]. A second constraint is the absence of active dopants in the silicon oxide box, to avoid current leakage. As visible from the simulation results in Figure 2.8 for the phosphorous concentration, and in Figure 2.9 for the active dopant

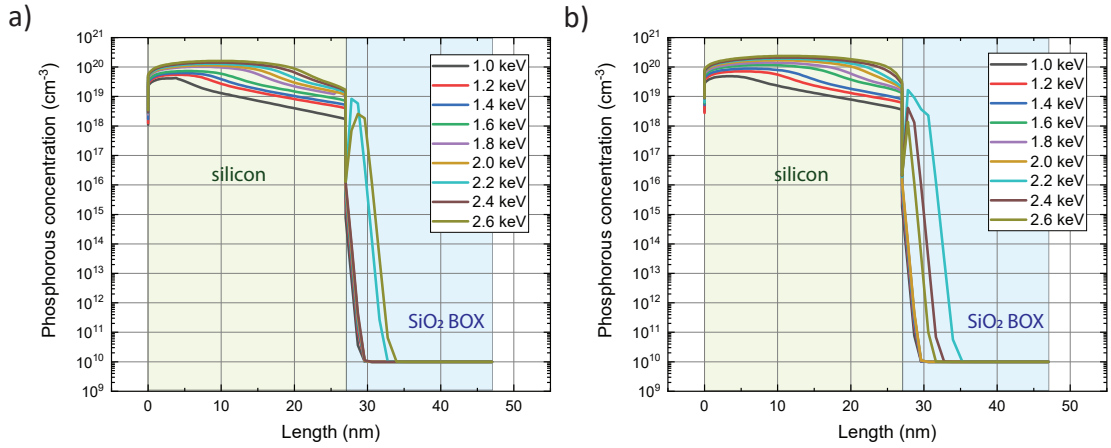


**Figure 2.8:** Source and drain simulated phosphorous concentration profiles at different implantation energy values after thermal annealing, at different implantation energies. a) Dose is fixed at  $3 \cdot 10^{15}$  atoms/cm<sup>-3</sup>. b) Dose is fixed at  $6 \cdot 10^{15}$  atoms/cm<sup>-3</sup>. We exclude energies that implant in the box.

profile, the energy values that satisfy both constraints are between 1.6 keV and 2.0 keV. Above 2.0 keV the presence of implanted ions in the box is clear, while under 1.6 keV the active dopants concentration in the Si channel is not satisfying the imposed conditions.

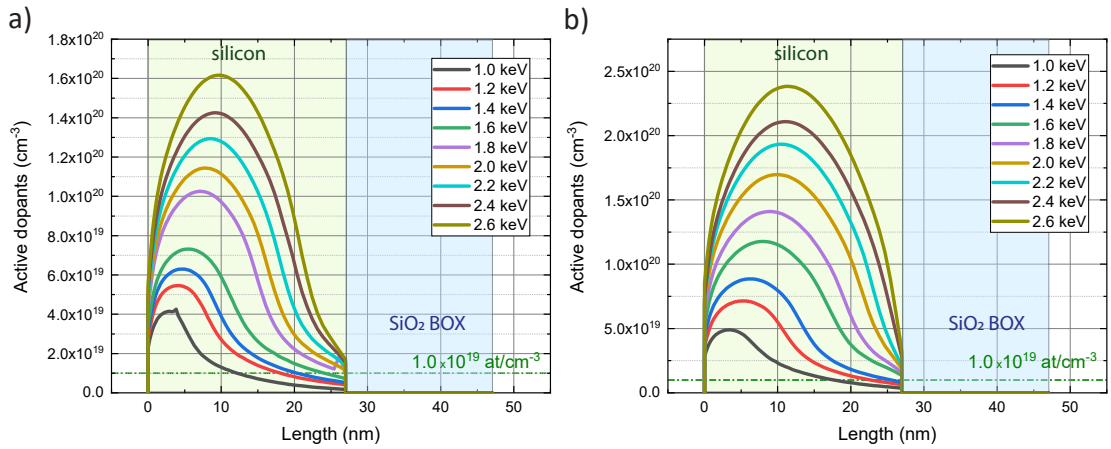
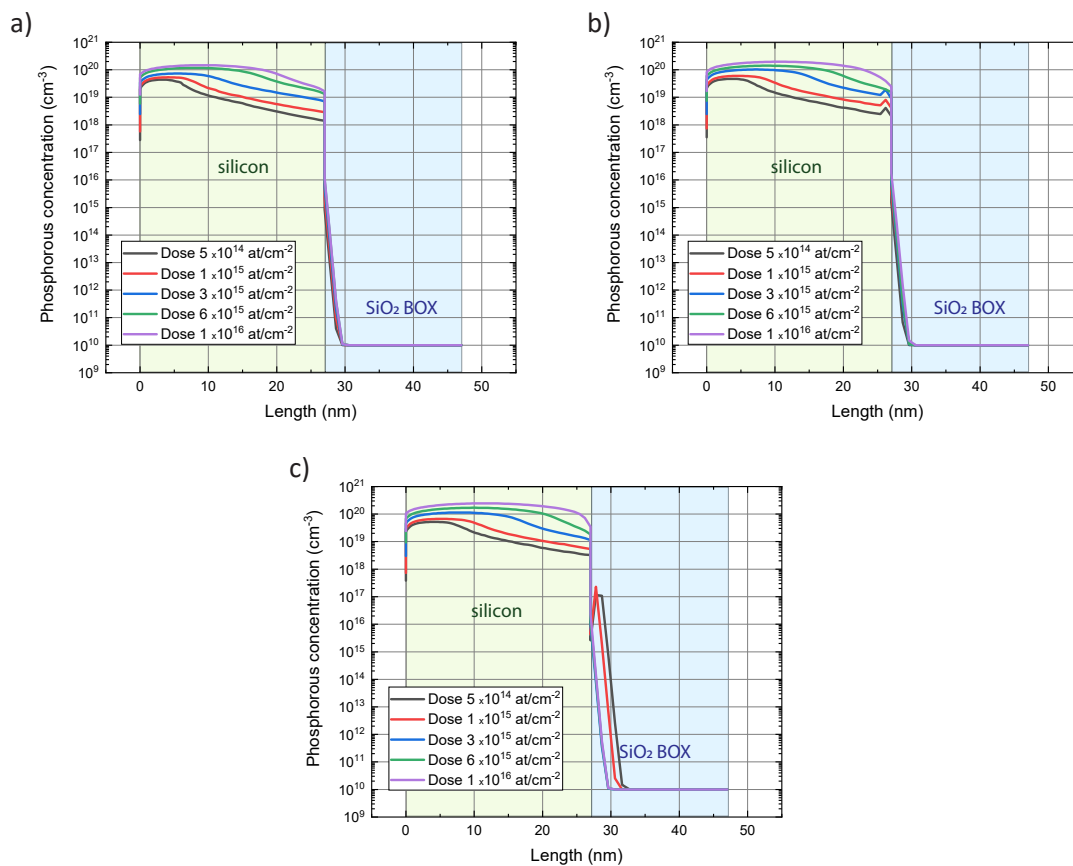


**Figure 2.9:** Source and drain simulated active dopants concentration at different implantation energy values after thermal annealing in the silicon layer (green) and silicon dioxide box (blue). Results for a)  $3 \cdot 10^{15}$  atoms/cm<sup>-3</sup> and b)  $6 \cdot 10^{15}$  atoms/cm<sup>-3</sup>. We arbitrarily choose a minimum dopants concentration of  $1 \cdot 10^{19}$  atoms/cm<sup>-3</sup> through the entire Si thickness.

For the three different implantation energies (1.6 keV, 1.8 keV, and 2.0 keV) we simulated five different dose values:  $5 \cdot 10^{14}$  cm<sup>-2</sup>,  $1 \cdot 10^{15}$  cm<sup>-2</sup>,  $3 \cdot 10^{15}$  cm<sup>-2</sup>,  $6 \cdot 10^{15}$  cm<sup>-2</sup>,  $1 \cdot 10^{16}$  cm<sup>-2</sup>, to fine-tune the best parameters and allow a final active dopant concentration higher than  $1 \cdot 10^{19}$  cm<sup>-3</sup> throughout the whole top silicon layer thickness, without having phosphorous atoms implanted in the SiO<sub>2</sub> box.

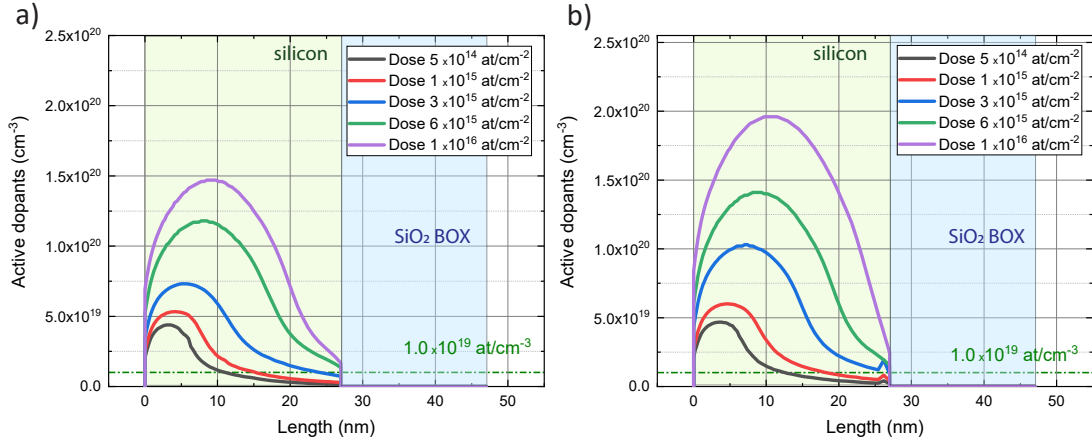
To check these requirements we report the phosphorous concentration along the thickness of the silicon layer and the net active dopant concentration after thermal annealing.

Figure 2.10 shows the dopant concentration across the silicon and the silicon dioxide box. We immediately notice that for both the implantation energy values of 1.6 keV and 1.8 keV the implanted phosphorous atoms do not penetrate the oxide box. Figure 2.10c highlights the simulation results concerning the implantation energy of 2.0 keV: we notice that for lower doses there is the presence of P atoms in the buried oxide, while for doses higher than  $3 \cdot 10^{15} \text{ cm}^{-2}$  the atoms do not penetrate in the box. Although strange, we can speculate that this result could be explained by the damage created to the silicon crystalline structure during implantation: at higher doses the damage is greater and happens faster, creating a more difficult path for the implanted P atoms that can not penetrate so deeply in the silicon as it happens for lower doses. Although simulation results seem to suggest that an implantation energy of 2 keV at higher doses would give the desired results, we opted to exclude this energy implantation value to avoid any possible damage to the silicon dioxide buried box.



**Figure 2.10:** Source and drain simulated phosphorous concentration at different implantation dose values after thermal annealing in the silicon layer (green) and silicon dioxide box (blue). Results for implantation energy of a) 1.6 keV, b) 1.8 keV, and c) 2.0 keV.

To reach the final decision about the employed implantation energy and dose, we finally compared the active dopants concentration for different doses at 1.6 keV and 1.8 keV. Figure 2.11 shows the obtained results for the mentioned conditions. For energy equal to 1.6 keV, the doses higher than  $6 \cdot 10^{15} \text{ cm}^{-2}$  would satisfy the imposed conditions: throughout the whole silicon layer the dopant concentration is higher than  $1 \cdot 10^{19} \text{ cm}^{-3}$ . This outcome is also guaranteed by the simulation for doses higher than  $3 \cdot 10^{15} \text{ cm}^{-2}$  at an implantation energy of 1.8 keV.



**Figure 2.11:** Source and drain simulated active dopants concentration at different implantation dose values after thermal annealing in the silicon layer (green) and silicon dioxide box (blue). Results for implantation energy of a) 1.6 keV, and b) 1.8 keV. We arbitrarily choose a minimum dopants concentration of  $1 \cdot 10^{19} \text{ atoms/cm}^{-3}$  through the entire Si thickness.

After careful consideration, we decided to use an energy level of 1.6 keV to avoid any potential damage to the box underneath, and a dose of  $6 \cdot 10^{15} \text{ atoms/cm}^{-2}$  since it provided the optimal balance of results and cost-effectiveness.

### 2.3.2 Cleanroom process flow for SiNWs-FET fabrication

The complete fabrication process flow is made of 24 steps as presented in the following section, and in the detailed runcard in Appendix A. The starting substrate is a silicon-on-insulator (SOI) wafer, with a  $\langle 100 \rangle$  silicon layer of 70 nm, a p-type doping concentration of  $10^{15} \text{ cm}^{-3}$ , and a SiO<sub>2</sub> BOX of 20 nm thickness (Figure 2.12a). To ensure full depletion in the silicon layer, the first step consists of the thinning of the silicon layer down to 35 nm, as explained by Bellando in [152]. The silicon layer undergoes a thermal oxidation growth of 86 nm SiO<sub>2</sub> in forming gas, using a Centrotherm furnace. During this step a silicon oxide growth and silicon consumption ratio of 0.44 has been considered (Figure 2.12b). After the growth of 86 nm of oxide, the substrate is immersed in buffered HF solution ( $\text{NH}_4\text{F}$  40% + HF 50%, 7:1) in order to etch the silicon oxide and obtain a 30 nm thick silicon layer (Figure 2.12c). The actual achieved final thickness is 32 nm.



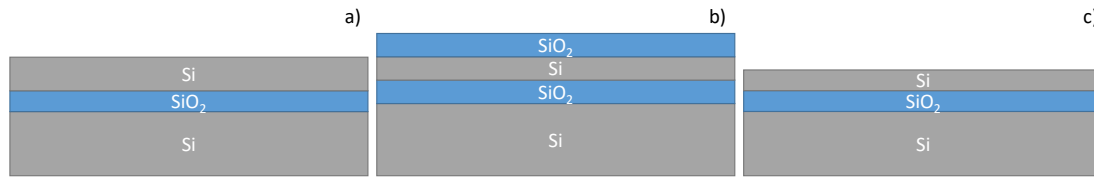


**Figure 2.12:** Fabrication step: top Si layer thinning. a) pristine substrate, b) thermal oxide growth, c) oxide etching to thin down the Si layer to 30 nm.

After the thinning of the Si layer, the implantation-stopping mask is created by repeating the thermal oxidation described above, but only growing 6 nm of SiO<sub>2</sub> (Figure 2.13a). Due to the nanometric dimensions of the silicon nanowires, any alignment step is critical in the fabrication process. Thus, the alignment markers are created by means of electron beam lithography, using a Raith EBPG5000+ system. The substrate is coated with CSAR62, a positive tone e-beam resist, and appropriate alignment markers are patterned on the resist surface (Figure 2.13b). Finally, the markers are etched into the wafer thanks to a silicon dry etching technique, by means of an Alcatel AMS 200 SE system, as shown in Figure 2.13c.

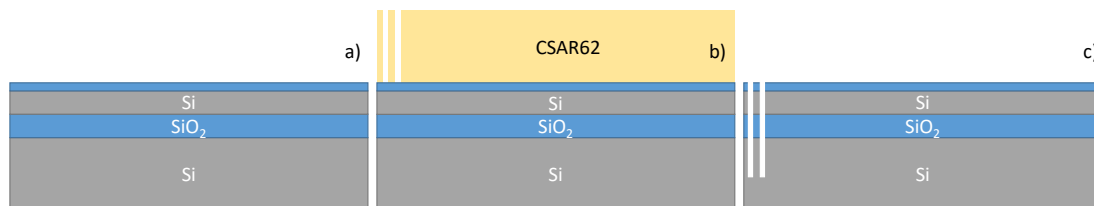


**Figure 2.13:** Fabrication step: electron beam markers creation. a) 6 nm thick implantation stopping layer growth, b) e-beam lithography, c) markers creation by deep reactive ion etching of Si/SiO<sub>2</sub> layers.

After the thinning of the top Si layer and the creation of the electron beam lithography markers, the highly doped source and drain regions must be defined and created. To do so, a first photolithography step occurs: we coat the substrate with 1  $\mu\text{m}$  of AZECI 3007, a photoresist designed to have high resistance for dry etching and implantation processes. Subsequently, the substrate is exposed by maskless lithography (Figure 2.14a) using the Heidelberg Instruments MLA150 to define the source and drain implantation regions. After the resist development step, the chips were shipped for implantation to IBS in France, where the highly doped regions were created using beam line implantation at 1.6 keV and a dose of  $6 \cdot 10^{15} \text{ cm}^{-2}$ , as simulated and discussed in subsection 2.3.1.

Once the source and drain implantation process has been completed, the remaining resist on the surface has been removed by a 30-second high-power oxygen plasma etching (600W, 400 sccm O<sub>2</sub> flow), followed by an overnight soaking in Microposit<sup>TM</sup> Remover1165 at 70°C. Following the resist removal, the thin oxide stopping layer is no longer needed. It could be kept as a high-quality thermally grown gate oxide, but the use of hydrogen silsesquioxane 2%

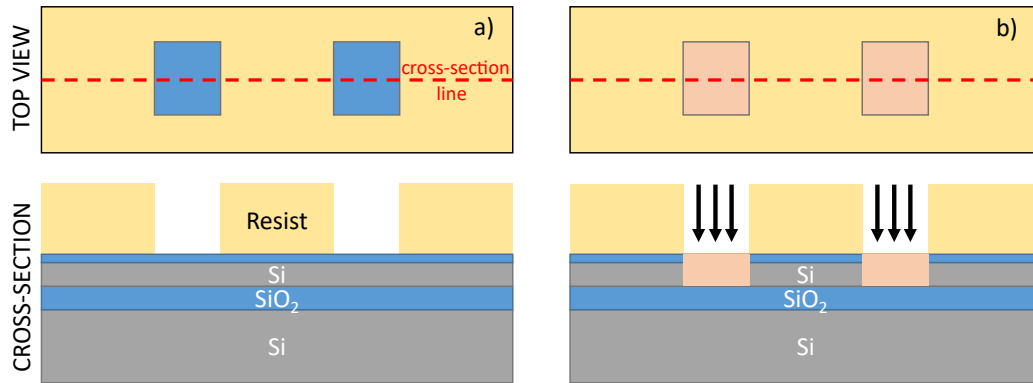


**Figure 2.14:** Fabrication step: source and drain regions implantation. a) Photolithography to define source and drain regions, b) ions implantation at energy 1.6 keV and a dose of  $6 \cdot 10^{15}$  atoms/cm<sup>-2</sup>.

(HSQ, commercialized by Dupont as XR-1541-002) would irreversibly affect its quality upon HSQ stripping. Thus, the oxide is removed by immersing the chips in BHF solution for 30 seconds.

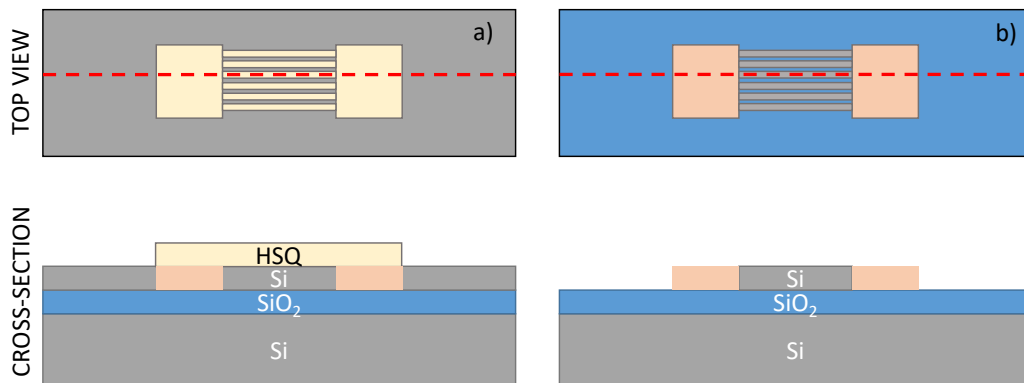


**Figure 2.15:** Fabrication step: silicon nanowires creation by electron beam lithography. a) HSQ patterning by e-beam exposure. b) DRIE to remove the excess of silicon, and define the nanowires.

To define the SiNWs' geometry, we employed electron beam lithography. 30 nm of HSQ 2% are coated on the chips, and exposed with a dose of  $2000 \mu\text{C}/\text{cm}^2$ . After resist development in 25% TMAH solution for 35 seconds, the SiNWs are formed by dry etching, exploiting an Alcatel AMS 200 SE, to etch the excess Si, as shown in Figure 2.15.

Before depositing the high- $\kappa$  gate oxide, two metallic stopping layers made of 5 nm Ti - 35 nm Pt - 2 nm Ti are deposited, to guarantee a successful ion beam etching step (details in 2.3.4). These stopping layers are deposited using lift-off technique, as shown in Figure 2.16. The second Ti layer is fundamental to guarantee uniform oxide growth by ALD technique during

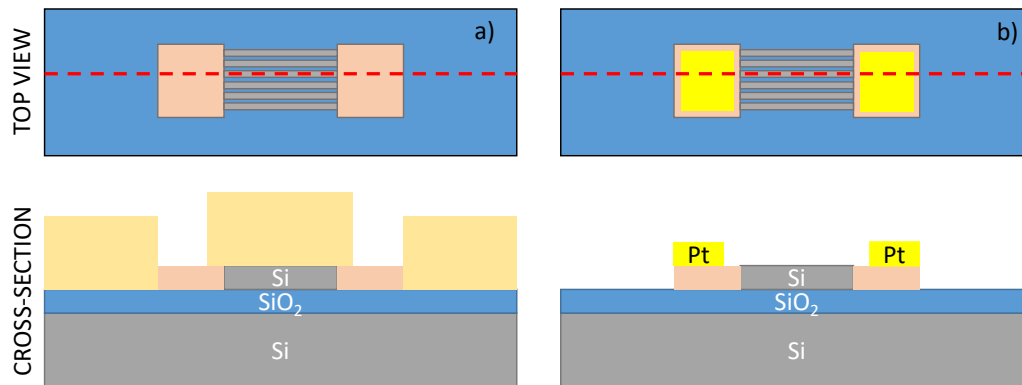


**Figure 2.16:** Fabrication step: metallic stopping layers deposition for the next Ion Beam Etching step. a) Standard photolithography to open source and drain regions. b) Ti-Pt-Ti tri-layer lift-off step.

the next step.

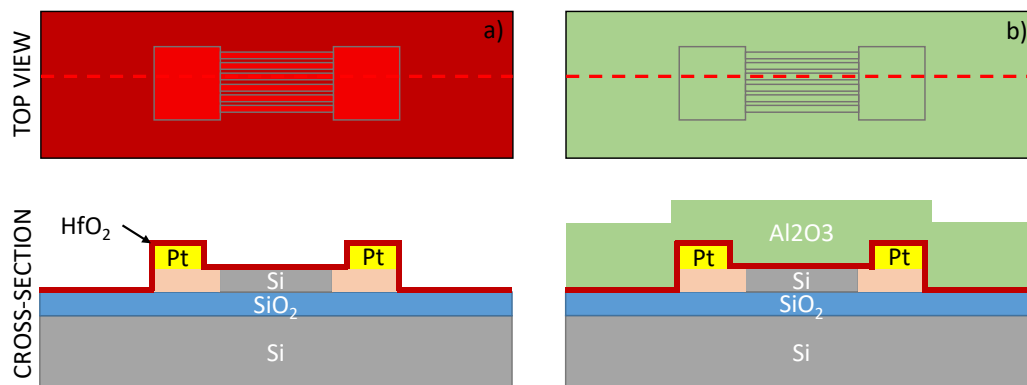


**Figure 2.17:** Fabrication step: gate and field oxide deposition. a) 7 nm high- $\kappa$  (HfO<sub>2</sub>) gate oxide deposition. b) 50 nm Al<sub>2</sub>O<sub>3</sub> field oxide deposition. Both layers are created by Atomic Layer Deposition.

To achieve a high-quality gate oxide, a 7 nm HfO<sub>2</sub> layer was deposited using atomic layer deposition [153]. Since the metallic lines that would be deposited later cover a significant area of the chip, ensuring electrical isolation from the silicon bulk was crucial. To address this issue, a 50 nm field oxide layer of Al<sub>2</sub>O<sub>3</sub> was deposited using ALD. These deposition techniques were carefully chosen to guarantee the quality and effectiveness of the gate oxide and field oxide layers, which are vital components in the fabrication of high-performance microchips. (Figure 2.17).

The final stage of the fabrication process involves creating the necessary metallic contacts to bias the device and exposing the gate oxide to enable contact with the liquid under test, thereby producing an ISFET-like device. This step is divided into three photolithographic

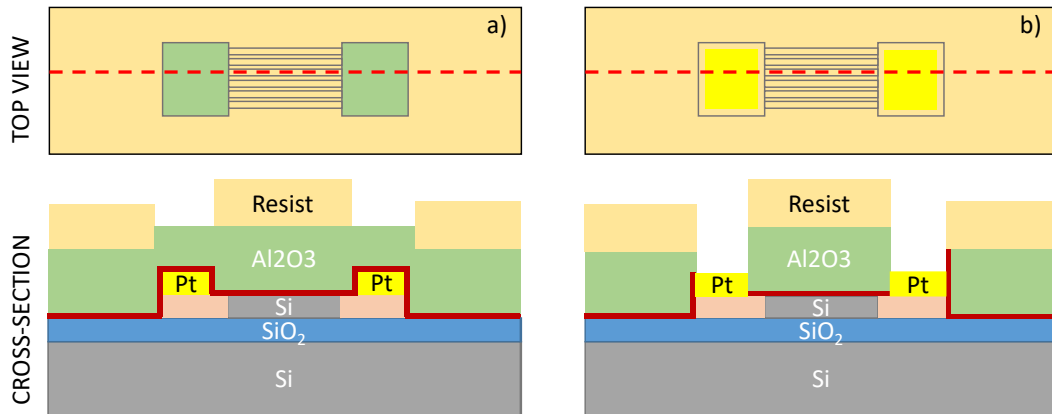


**Figure 2.18:** Fabrication step: source and drain region opening by ion beam etching. a) Photolithography to define source and drain contact. b) Al<sub>2</sub>O<sub>3</sub> and HfO<sub>2</sub> dry etching. The Pt layer is used as a stopping layer to tune the etching duration.

steps. The first step involves opening the source and drain contacts, as depicted in Figure 2.18. We explored two different techniques for this stage, namely BHF wet etching and ion beam dry etching. A detailed comparison of these two techniques is presented in the forthcoming subsection (2.3.4).

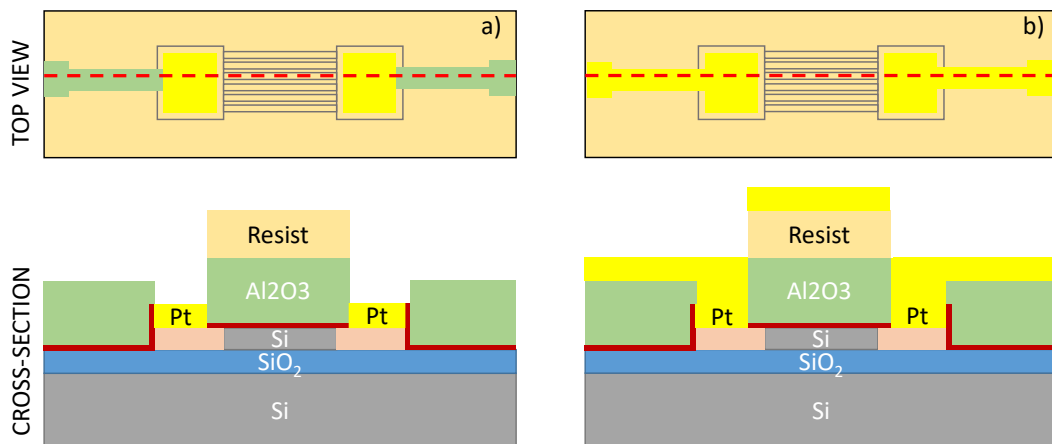


**Figure 2.19:** Fabrication step: metallic lines deposition. a) Standard photolithography for metal line deposition by lift-off. b) Top view and cross-section showing the deposition of metallic lines.

Ultimately, the second technique was found to produce more reliable results and was therefore preferred. During this step, the previously deposited Pt layer onto the highly doped source and drain regions is crucial as it serves as a stopping layer.

Subsequently, the metal lines that allow to contact the source and drain regions from the side of the chip are deposited by lift-off technique, using a new photolithography mask. The deposition process involves a 5 nm thick Ti layer used as an adhesion layer, onto which 65 nm

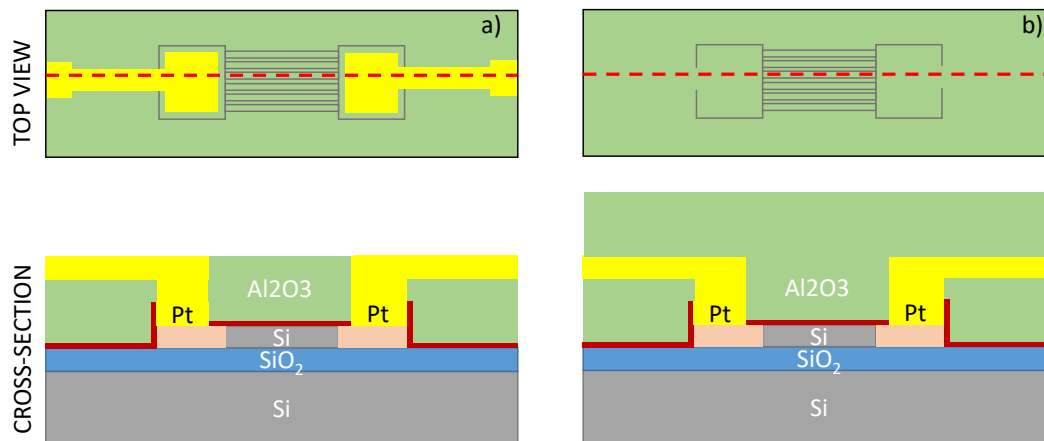


**Figure 2.20:** Fabrication step: passivation layer deposition. 100 nm  $\text{Al}_2\text{O}_3$  encapsulation layer deposited by atomic layer deposition.

of Pt is deposited (Figure 2.19).

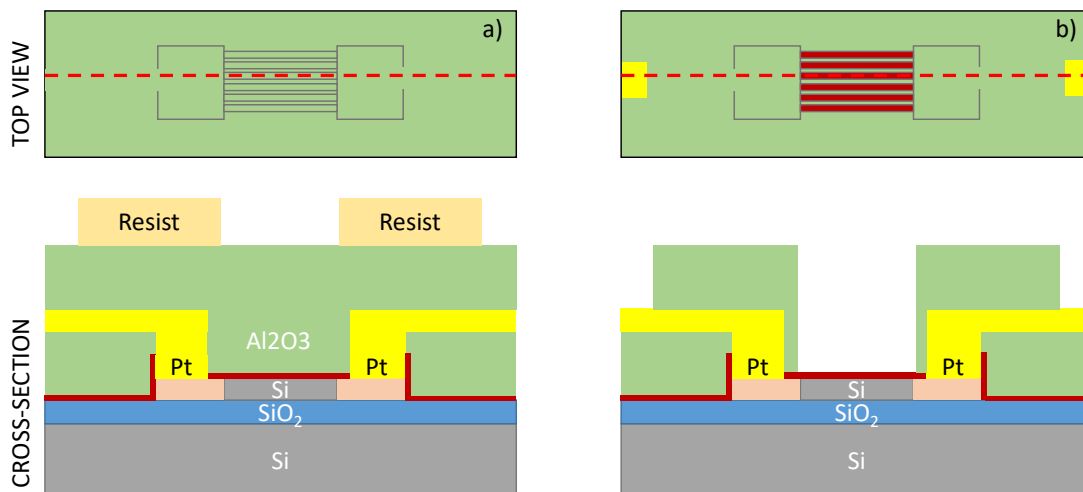


**Figure 2.21:** Fabrication step: opening-up of the passivation layer to reach SiNWs surface. a) Standard photolithography step for b) selective etching of  $\text{Al}_2\text{O}_3$  layer by means of  $\text{H}_3\text{PO}_4$  wet etching.

To conclude an encapsulation and passivation layer of 100 nm  $\text{Al}_2\text{O}_3$  is deposited by ALD technique (Figure 2.20). The last photolithographic mask is then used to expose the metal pads for contacts, and the gate oxide. This last step is performed by selectively etching the aluminum oxide layer with 85%  $\text{H}_3\text{PO}_4$  for two minutes (Figure 2.21).

The chip layout and an optical picture of the final chip are shown in Figure 2.22. Each chip possesses ten pairs of identical SiNWs arrays, that can be differently functionalized, and one on-chip reference electrode. The chip is a square of 1 cm side length.

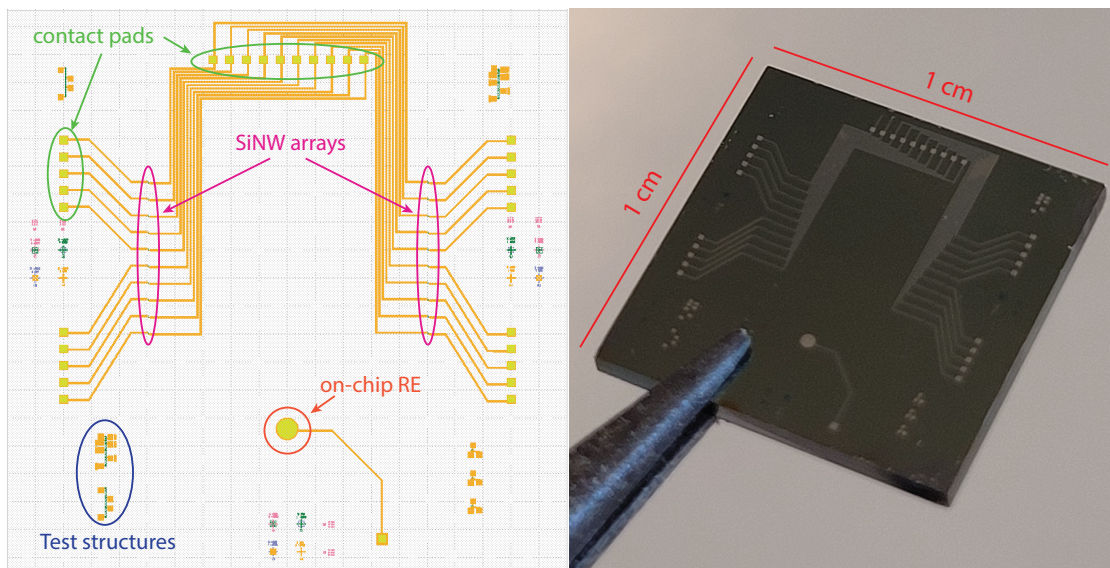


**Figure 2.22:** Fabricated SiNWs chip. a) Design layout, highlighting the different structures on the chip. Each chip contains 10 pairs of SiNW arrays, an on-chip reference electrode, and test structures to measure the actual source and drain doping level. b) Optical picture of the finished chip.

### Transmission Electron Microscopy

To confirm that the correct fabrication process has been pursued, Transmission Electron Microscopy characterization has been performed on a chip with SiNW arrays that have been successfully electrically characterized. The main goal of this step is to ensure the presence of a uniform  $\text{HfO}_2$  that would ensure high sensitivity and stability to the sensor. Moreover, there is the necessity to check the absence of over-etching effects, and the layers' thicknesses.

Figure 2.23 reports the main results of the study. The complete lamella preparation and more detailed images are reported in the Annex B, for the sake of completeness. In Figure 2.23a we report the TEM cross-section of a single NW, highlighting the different layers' thickness. As expected, the  $\text{SiO}_2$  box has an overall thickness of 20 nm, with a thinning down where the layer is not protected by the Si nanowire, due to the dry etching step and the use of BHF for HSQ removal. The real SiNW thickness stands at 25 nm, a small deviation from the measured 27 nm with ellipsometer techniques. Finally, the high- $\kappa$   $\text{HfO}_2$  layer has a thickness of 8nm, close to the expected one. The blur effect on the side of the nanowire is an artifact due to the not perfect alignment of the lamella. A better representation of the real uniformity of the  $\text{HfO}_2$  layer is shown in Figure 2.23b: it is a scanning TEM (STEM), and the bright layer is the gate oxide. To confirm the presence of the correct stack of materials, the Energy-dispersive X-ray spectroscopy (EDS) characterization of one nanowire has been performed. Figure 2.23c shows the high-angle annular dark-field image, while Figures 2.23d-f show the map elemental analysis of the nanowire's cross-section. As expected Hf is prevalent in the gate oxide layer, being uniform all over the surface. Moreover, the analysis of Si and O signal confirm the correct

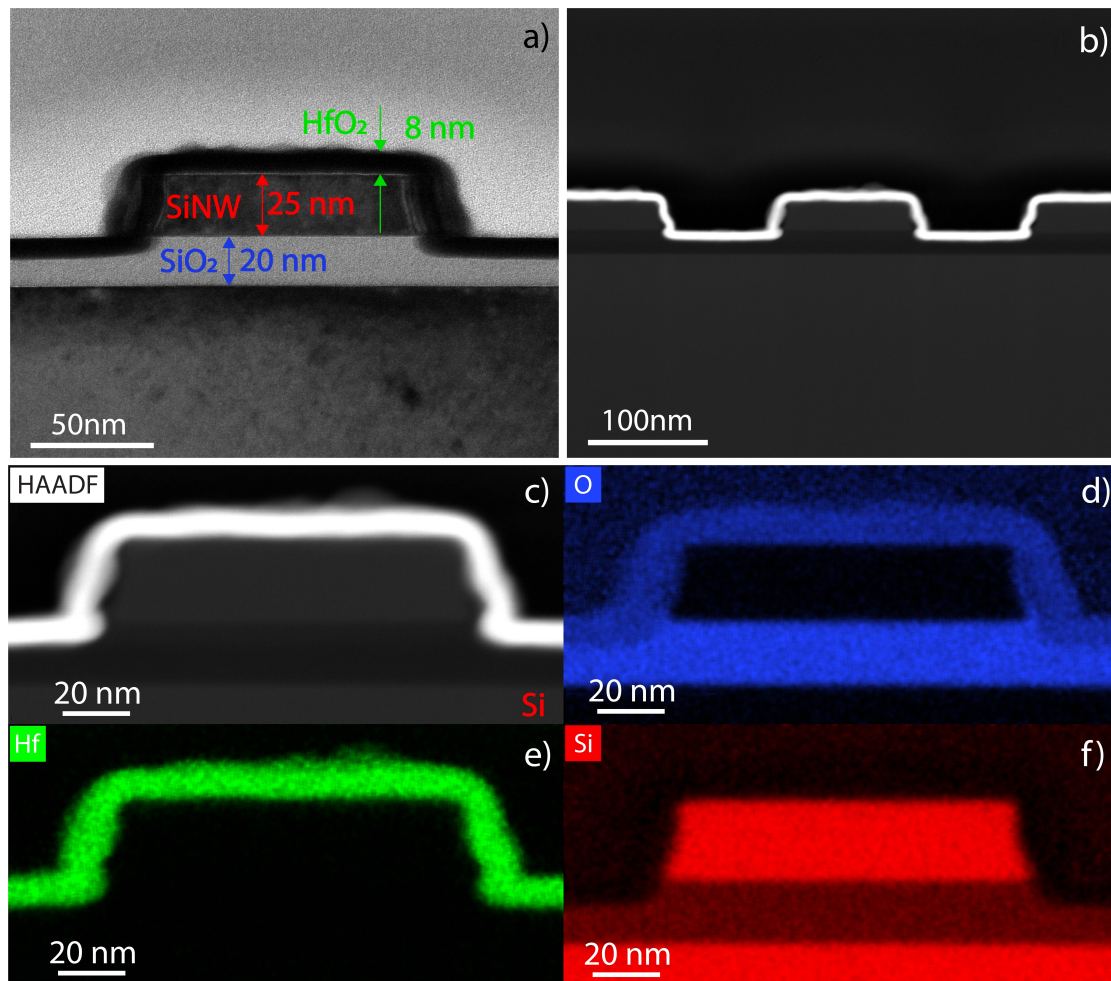


**Figure 2.23:** TEM, STEM, and EDS characterization of the in-house fabricated SiNWs. a) TEM cross-section of one SiNW. The thicknesses of the different layers are pointed out, and they agree with the expected ones. b) STEM cross-section image of three nanowires, to show the uniformity of the  $\text{HfO}_2$  layer. c)-d) EDS characterization, and elemental analysis for the STEM cross-section of one NW. c) High-angle annular dark field detector image, d) oxygen signal, e) hafnium signal, and f) silicon signal.

fabrication process.

### 2.3.3 Ohmic contacts on thin silicon and doping level test

To ensure a proper function of the SiNWs FET, we need to create ohmic source and drain contacts on a 27 nm thin silicon layer. This requires the tuning of different parameters, such as the implantation energy and dose to avoid the penetration of the dopants in the buried  $\text{SiO}_2$  box, while keeping a high doping level. The parameters for the phosphorous implantation have been chosen after carefully simulating the process with Sentaurus TCAD, as previously described in section 2.3.1. To verify the correct occurrence of the silicon doping process and to

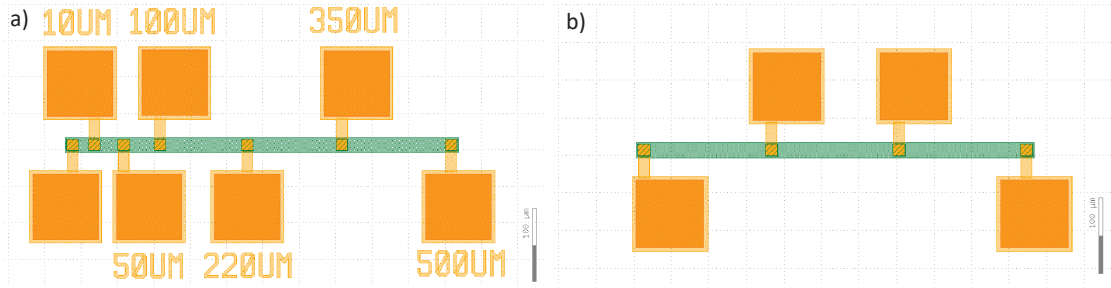


**Figure 2.24:** On-chip test structures to measure source and drain doping level: a) TLM method, b) 4-probes point method.

measure the actual doping level, various test structures (Figure 2.24) specifically incorporated into the chip layout were used. The first structure is based on a simple *transmission line model* (TLM), to study both the sheet resistance and the contact resistance [154].

I-V curves are recorded between contacts placed at an increasing distance on a doped line of silicon, and plotted in Figure 2.25a. The contacts between the deposited metal and the doped Si are ohmic, resulting in linear I-V curves. Resistance values are extracted from the slope of each curve: the intercept with the y-axis corresponds to twice the value of the contact resistance, while the slope is the sheet resistance divided by the line width. From the extracted parameters it is noteworthy to obtain the Si doping level through the equations:

$$\rho_{Si} = R_{sheet} \cdot t \quad (2.1)$$

and

$$N_D = \frac{1}{q\mu_n\rho_{Si}} \quad (2.2)$$

using the empirical relation for the electron mobility as a function of the doping concentration [155]:

$$\mu_n = 88 \left( \frac{T}{300} \right)^{-0.57} + \frac{7.4 \times 10^8 T^{-2.33}}{1 + 0.88 \left( \frac{T}{300} \right)^{-0.146} \left[ \frac{N_D}{1.26 \times 10^{17} \left( \frac{T}{300} \right)^{2.4}} \right]} \text{ cm}^2 \text{ V}^{-1} \text{ s}^{-1} \quad (2.3)$$

The extracted sheet resistance was found to be  $152.10 \, \Omega$ , which corresponds to a resistivity of



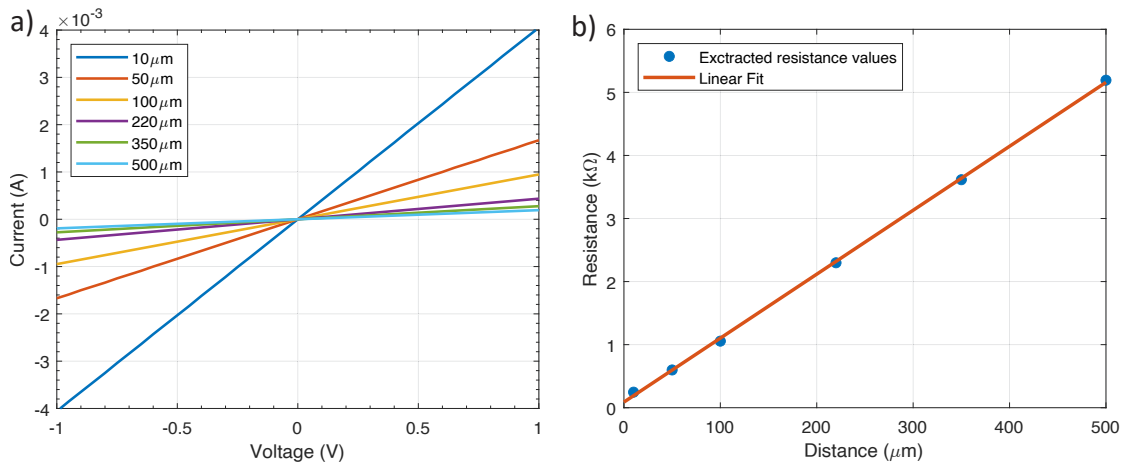


**Figure 2.25:** Linear I-V curves between two contacts placed at an increasing distance on a doped Si line. b) Extracted resistance values. The intercept with the y-axis is equivalent to twice the contact resistance value, while the slope is proportional to the sheet resistance.

0.410 m $\Omega\text{cm}$ . Thus, we obtain a measured doping concentration of  $1.71 \cdot 10^{20} \text{cm}^{-3}$ , confirming the simulated results. To further validate this finding, we conducted a four-point probes measurement on the test structures shown in Figure 2.24b. Following a similar calculation process, the extracted sheet resistance is 150.02  $\Omega$ , equivalent to a resistivity of 0.405 m $\Omega\text{cm}$ , resulting in a measured doping level of  $9.35 \cdot 10^{19} \text{cm}^{-3}$ . This demonstrates good consistency with the predicted doping concentration.

### 2.3.4 Critical steps in the fabrication process flow

The detailed process flow described above represents the very final version, which was arrived at after numerous attempts and modifications to the original design. Through an iterative approach of trial and error, we were able to optimize the fabrication process to achieve the desired results. The final process flow was carefully developed to ensure the highest quality and reliability of the fabricated microchips. One of the most critical steps has been the opening of the source and drain regions after the gate and field oxide deposition. The first attempts were made by using selective wet etching with buffered HF: a protective photoresist mask was created with standard photolithography, and the  $\text{Al}_2\text{O}_3$  and  $\text{HfO}_2$  layers were etched by immersing the chips in BHF. The nominal values for etching rates at CMi are 70 nm/min and 1.5 nm/min for  $\text{Al}_2\text{O}_3$  and  $\text{HfO}_2$ , respectively.

The huge difference between the two etching rates [156], created many problems, leading to unwanted electrical paths for the current flowing in the devices. In particular, a long etching time is required, due to the very slow etching of  $\text{HfO}_2$  in BHF, resulting in a very large lateral etching of the aluminum oxide layer, as shown in Figure 2.26: both in the test structures and in the real SiNWs device, it is possible to notice halos around the etched structures. These circles extend for various micrometers, indicating possible damage to the oxide layers.

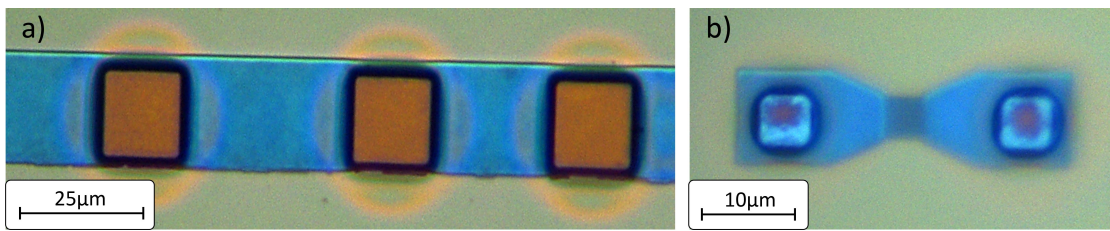


**Figure 2.26:** Optical microscope pictures highlighting the lateral over-etching. Phenomenon happening in a) test structures and b) real devices. Glowing halos are clearly visible around the structures, indicating an oxide over-etching during the wet-etching step.

Measuring the current flowing between two random contacts on the chip, we obtain Schottky conduction like in Figure 2.27a, indicating an unwanted leakage, probably created by the lateral over-etching, described above. To solve this issue the wet-etching step has been replaced by a dry ion beam etching one. Nevertheless, this technique would create another problem: in fact, the silicon layer is very thin (only 27 nm), and precisely stopping the etching on the Si without damaging it resulted to be nearly impossible. The Veeco IBE350 at CMi is equipped with a secondary ions mass spectroscopy (SIMS) detection system, that collects and counts the ejected secondary ions during the etching in real-time. The counts are displayed in real-time, thus the user has the faculty to follow the elements that are being etched, and to stop the etching step whenever the desired signal appears.

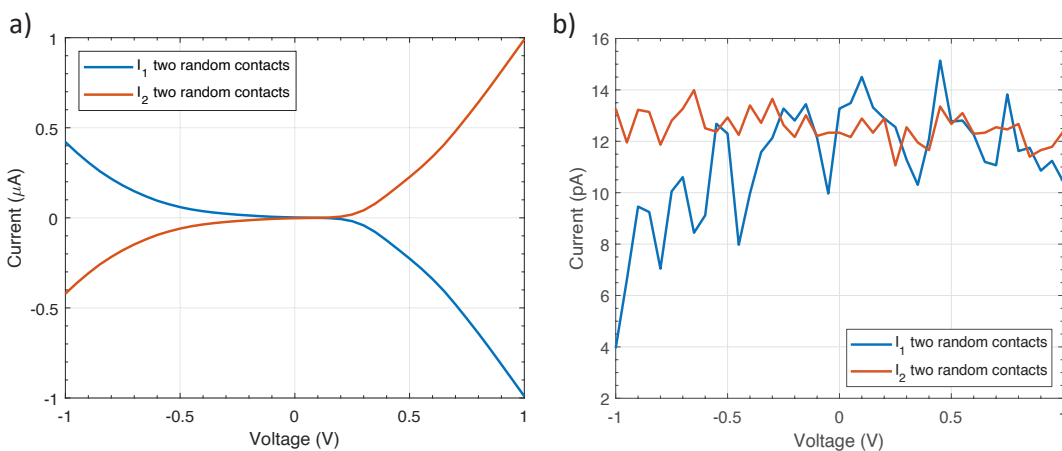


**Figure 2.27:** Flowing current between two random contacts on the chip. a) Chip with lateral over-etching, showing unwanted electrical current conduction, and b) chip after the solved issue, showing pA current levels between two random contacts on the chip.

Unfortunately, silicon can not be detected easily by this tool, introducing a further difficulty that we solved by depositing a platinum stopping layer prior to growing the gate and field oxides. In this way, the ion beam etching would be stopped when the Pt signal was detected by the SIMS system, indicating the complete etching of the oxides on top. Figure 2.27b shows the current flowing through two random contacts on a perfectly working chip: it is clear that the measured current corresponds to the instrumentation noise level, indicating the absence

of unwanted leakage.

### 2.3.5 Electrical characterization of the fabricated SiNWs

After the completion of the fabrication process flow, the chips were electrically characterized. All the electrical measurements presented in the following have been performed at room temperature and ambient conditions, employing a Keithley 4200A parameter analyzer. The reported results concern a device made of 20 parallel NWs, each of them is  $1.6 \mu\text{m}$  long, and  $120 \text{ nm}$  wide, spaced by  $100 \text{ nm}$  from the neighbor nanowires.

In order to study the impact of the liquid top gate and the back-gate on the conduction mechanism we measured both the top and back-gate transfer characteristics, constantly applying a drain to source voltage bias of  $0.5 \text{ V}$ . In all cases, the controlling voltage has been swept from low to high values (forwards sweep) and vice-versa (backward sweep) to measure the hysteresis.

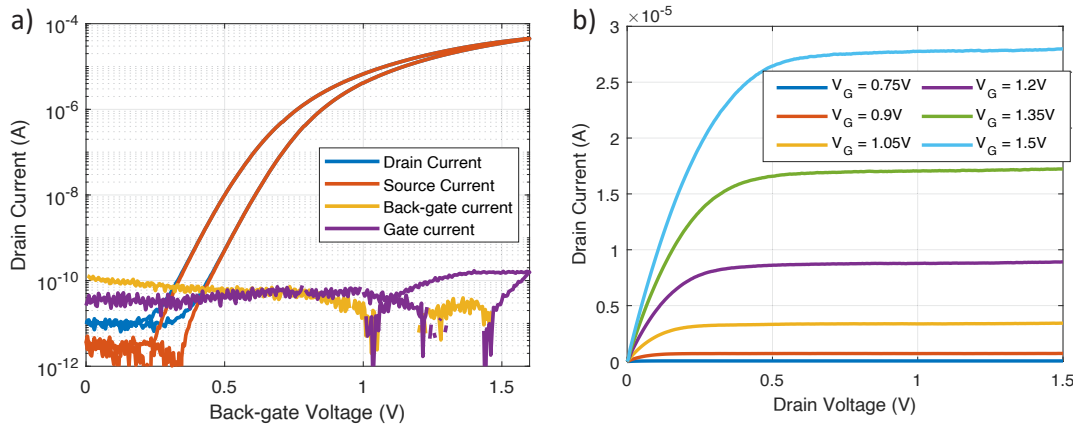


**Figure 2.28:** Transfer and output characteristics of the in-house fabricated SiNW array with 20 parallel nanowires, each of them has a width of  $120 \text{ nm}$  and a length of  $1.6 \mu\text{m}$ . a) Dual-sweep transfer characteristic of one SiNW array on the fabricated chip.  $V_{DS} = 0.5 \text{ V}$ , and  $V_{BG} = 0 \text{ V}$ . b) Output characteristic obtained sweeping  $V_{DS}$  between  $0 \text{ V}$  and  $1.5 \text{ V}$ , and keeping  $V_{BG} = 0 \text{ V}$ .

The device exhibits n-type conduction, as illustrated by the semilogarithmic plot of the transfer characteristic in Figure 2.28a. The applied  $V_{DS}$  is  $0.5 \text{ V}$ , the back-gate is held at  $0 \text{ V}$ , and the reference voltage is applied through a Micrux Technologies Ag/AgCl bulk reference electrode immersed in the liquid under test in contact with the exposed gate oxide. The  $I_{ON}/I_{OFF}$  current ratio is found to exceed 7 orders of magnitude, indicative of the high-quality transistor behavior. The gate and back-gate leakages remain consistently lower than  $100 \text{ pA}/\mu\text{m}$ , which is noteworthy given that the back-gate contact is connected to the Si bulk, collecting leakage contributions from the entire chip. The calculated hysteresis between the forward and backward sweep is  $110 \text{ mV}$ . The transistor output characteristic is shown in Figure 2.28b, which demonstrates a low channel length modulation effect. Specifically, we present the output curves generated by varying the gate voltage (in this case, we assume that the gate and

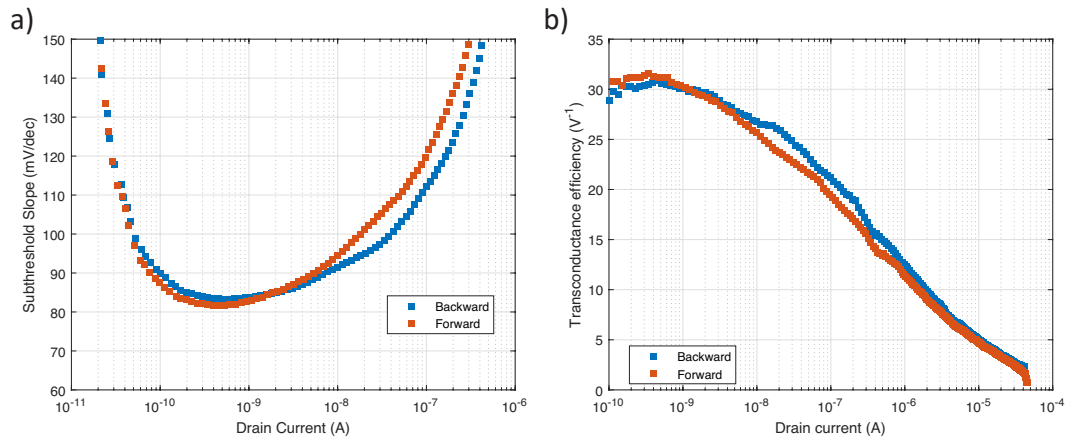


**Figure 2.29:** a) Subthreshold swing and b) transconductance efficiency of the in-house fabricated SiNW array.

reference voltage are equivalent) between 0.75 V and 1.5 V, while the back-gate and source voltages are maintained at 0 V.

Figure 2.29a shows the subthreshold swing as a function of the transistor's output current. The extracted minimum value is 80 mV/decade, while we obtain values lower than 90 mV/decade over a current range of two orders of magnitude. Similar behavior can be observed in the reverse sweep of the reference voltage, although a hysteresis value of 110 mV between the forward and backward sweep, similar subthreshold swing values show that the device can be exploited in both sweep directions, with similar performance. Figure 2.29a represent the transistor transconductance efficiency, a key parameter for selecting the best operating region to obtain high sensitivity in biosensors application and low power consumption to satisfy the constraints imposed by the wearable application of our system.

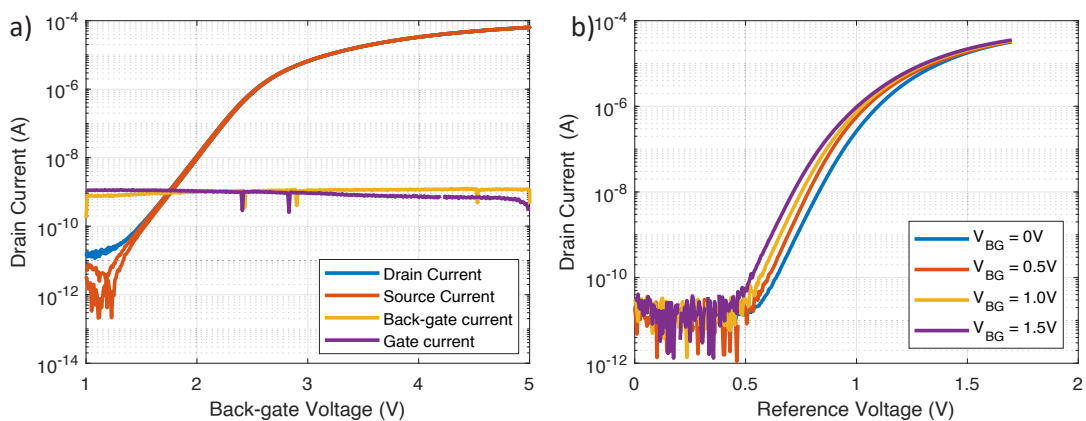


**Figure 2.30:** Back-gate control capabilities for the in-house fabricated SiNW array. a) Back-gate transfer characteristic, with  $V_{REF} = V_S = 0$  V, and  $V_D = 0.5$  V. b) Transfer characteristic shift due to different applied back-gate bias values.

In Figure 2.30 we demonstrate the ability of our sensor to be controlled by the back-gate contact, provided through the bulk of the chip. In particular Figure 2.30a shows the back-gate transfer characteristic of our system: the ON/OFF ratio is more than six orders of magnitude, while the leakage current remains always lower than 2 nA. We will show how we exploit the capability of our sensor to work in back-gate configuration in Chapter 4 and 5, by demonstrating an intrinsic signal amplification during pH and protein sensing. Figure 2.30b reports different  $I_D-V_{REF}$  curves at different applied back-gate voltage values, demonstrating the ability of this second gate to control the position of the transfer characteristic, in order to place our bias point in the optimal conditions.

### 2.3.6 On-chip Ag/AgCl quasi reference electrode

As shown in Figure 2.22, the in-house fabricated chips possess a platinum pad with an area of  $0.2 \text{ mm}^2$  that can serve as an on-chip quasi-reference electrode (QRE) if properly covered with Ag/AgCl ink. Platinum was chosen as a pad material due to its low reactivity and for its high surface charge density, and SunChemical (C2130809D5) Ag/AgCl (60/40) paste was chosen as ink material. To study the performance of such QRE, multiple Ag/AgCl on-chip reference electrodes have been tested against a double-junction Ag/AgCl commercial electrode in ISF-like solutions (composition in Table 2.1).

Compounds	Concentration (mM)
<b>Na<sup>+</sup></b>	133
<b>K<sup>+</sup></b>	4
<b>Ca<sup>2+</sup></b>	1.2
<b>Mg<sup>2+</sup></b>	0.7
<b>Cl<sup>-</sup></b>	112.2
<b>HCO<sub>3</sub><sup>-</sup></b>	28.3
<b>BSA</b>	0.19
<b>Creatinine</b>	61.9
<b>Phosphate</b>	0.61

**Table 2.1:** ISF-like solution composition.

In Figure 2.31 we report the performance results for different QREs, with a surface area between  $0.1 \text{ mm}^2$  and  $0.5 \text{ mm}^2$ , both in terms of voltage and temporal drift against double-junction reference electrodes. Moreover, in the figure, we compare these performances with commercially available Ag/AgCl reference electrodes.

The observed time drift for QREs ranging in size from  $0.1 \text{ mm}^2$  to  $0.25 \text{ mm}^2$  is comparable to the drift observed in commercial reference electrodes, both falling within the range of 0 to  $\pm 2 \text{ mV/h}$  (with the exception of one chip displaying an outlier value). Additionally, the stabilization voltage values of the QRE exhibit minimal dispersion, as depicted in Figure 2.31a, with a maximum voltage mismatch of 80 mV compared to the commercial double-junction Ag/AgCl electrode.

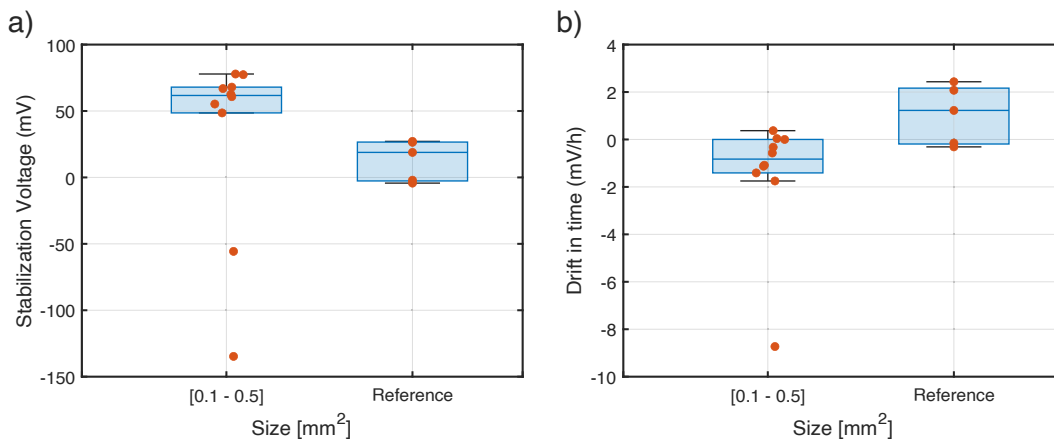


**Figure 2.31:** Quasi reference electrode stability study in ISF-like solutions. a) Stabilization voltage statistics of different on-chip Ag/AgCl QREs vs double-junction reference electrodes compared to commercial reference electrodes. b) Temporal drift statistics of different on-chip Ag/AgCl QREs vs double-junction reference electrodes compared to commercial reference electrodes.

This study validates the feasibility of utilizing on-chip QREs based on Ag/AgCl ink deposition on a 0.2 mm<sup>2</sup> platinum metal pad for the in-house fabricated SiNW chip, offering an additional capability for system miniaturization.

## 2.4 Summary

This chapter presents the fabrication process flow of two similar platforms based on Fully-Depleted SOI technology. The first platform is a wafer-scale chip consisting of 100 identical SiNW arrays suitable for use as biosensors based on FETs, fabricated by CEA-LETI in Grenoble. The second platform, designed and fabricated in-house at EPFL, Lausanne, features 10 couples of identical SiNW arrays, enabling reference-compensated configuration.

For each platform, the chapter provides a detailed description of the fabrication steps and DC electrical characterization. In particular, the critical fabrication steps for the in-house fabricated chip are highlighted, and the strategies employed to overcome difficulties are discussed.

The CEA-LETI chip allows for the operation of 100 identical devices, providing redundancy in sensor response and the capability to target multiple analytes with the same platform. The DC electrical characterization of the chip shows a high drain current ON/OFF ratio (> 6 orders of magnitude), very low hysteresis (< 3 mV), and low gate and back-gate leakage currents (< 0.5 nA/ $\mu$ m). The capability of the sensor to tune the threshold voltage through back-gate biasing is also demonstrated, which is crucial for the detection of C-Reactive protein as discussed in Section 5.1.

The in-house fabricated chip provides 10 couples of identical devices, facilitating reference-compensated configuration. TCAD simulation is employed to select the best parameters for source and drain implantation, leading to ohmic contacts on thin silicon. The fabricated system shows excellent ohmic contacts with the thin silicon layer (contact resistance of 30  $\Omega$ ), a high drain current ON/OFF ratio ( $> 7$  orders of magnitude), low gate and back-gate leakage currents ( $< 100$  pA/ $\mu\text{m}$ ), and a threshold voltage that can be easily modulated through back-gate biasing. The optimal back-gate transfer characteristics are also demonstrated.

Table 2.2 provides a comprehensive comparison of the performance between the two different platforms discussed in this chapter. The table highlights the key parameters and highlights the differences and similarities between the platforms. The in-house fabricated devices exhibit superior performance compared to the CEA-LETI device, particularly in terms of the ON/OFF ratio, which is a crucial factor in achieving a wide range of detected concentrations in biosensors. Additionally, the chips fabricated in CMI offer the advantage of depositing an Ag/AgCl ink to create a quasi-reference electrode, eliminating the need for an external and cumbersome reference electrode required by the CEA-LETI chip. Furthermore, the geometry of the in-house fabricated chips is specifically designed for seamless integration with the microneedles extractor system developed by our partner institution.

	<b>CEA-LETI</b>	<b>In-House</b>
<b># of NWs</b>	15	20
<b># of arrays</b>	100	10
<b>Length</b>	1.4 $\mu\text{m}$	1.6 $\mu\text{m}$
<b>Width 1 NW</b>	140 nm	120 nm
<b>NW pitch</b>	120 nm	100 nm
<b>Gate oxide</b>	3 nm SiO <sub>2</sub> + 4 nm HfO <sub>2</sub>	7 nm HfO <sub>2</sub>
<b>SiO<sub>2</sub> box thickness</b>	120 nm	20 nm
<b>OFF current</b>	10 pA	$< 10$ pA
<b>ON current (@V<sub>REF</sub> = 1 V, V<sub>D</sub> = 0.3 V)</b>	10 $\mu\text{A}$	10 $\mu\text{A}$
<b>ON/OFF ratio</b>	$> 10^6$	$> 10^7$
<b>Front-gate leakage</b>	0.48 nA/ $\mu\text{m}$	0.083 nA/ $\mu\text{m}$
<b>Back-gate leakage</b>	0.14 nA/ $\mu\text{m}$	0.083 nA/ $\mu\text{m}$
<b>SS<sub>min</sub></b>	85 mV/decade	81 mV/decade
<b>SS<sub>average</sub> (over 3 decades of I<sub>D</sub>)</b>	89 mV/decade	90 mV/decade
<b>Max g<sub>m</sub>/I<sub>D</sub></b>	28 V <sup>-1</sup>	30 V <sup>-1</sup>
<b>Front-gate hysteresis</b>	3 mV	110 mV
<b>Back-gate hysteresis</b>	$< 300$ mV	$< 10$ mV
<b>On-chip reference electrode</b>	NO	YES
<b>Microneedles chip compatibility</b>	NO	YES
<b>Back-gate operating voltage window</b>	20-35 V	1-4 V

**Table 2.2:** CEA-LETI and in-house fabricated SiNW platforms performance comparison.

Overall, this chapter provides a comprehensive overview of the fabrication process and DC electrical characterization of two similar platforms based on Fully-Depleted SOI technology,

highlighting their potential applications in biosensing and providing insights into the critical steps of their fabrication.





## 3 Surface functionalization and methods

*In the previous chapters, we provided an overview of the technology selected for the fabrication of our biosensor system, the complete microfabrication process flow, and the DC electrical performances of the exploited SiNW arrays. In this chapter, we delve into the crucial steps of the implemented functionalization protocol used to covalently immobilize anti-CRP Fab fragments on the HfO<sub>2</sub> gate oxide surface (Section 3.1). To detect C-Reactive proteins, a functionalization layer is essential to enable selective detection of the desired antigen, and it is crucial to ensure that the layer is sufficiently short to overcome the Debye screening of charged molecules in ionic bio-fluids. We present various methods used to confirm the correct immobilization of antibody fragments. Surface plasmon resonance (Section 3.1.3) verifies that the selected antibody fragments provide selective recognition of CRP in the desired concentration range. X-ray spectroscopy confirms that the chosen immobilization protocol ensures the proper immobilization of fragments on high-oxide surfaces (Section 3.1.4), while Quartz Microbalance measurements demonstrate the necessity of a good APTES layer for stability and low drift. We then describe our measurement setup in Section 3.2. Our setup utilizes a microfluidic chip to detect biomarkers in low sample volumes, and a printed circuit board interfaces the chip with multiple electrical cables. The final three sections of this chapter detail the different electrical characterization methods we used to measure the targeted biomarkers. Section 3.3.2 explains the classical method we employed, called front-gate operation. In Section 3.3.3, we describe the internal amplification obtained by sweeping the back-gate voltage of our transistors, thus exploiting the double gate structure of the device. Lastly, we introduce a method called drain constant-current amplification in Section 3.3.4, with which we could achieve a tunable amplification of the signal, depending on the operation region of the transistor.*

### 3.1 Surface functionalization study

#### 3.1.1 Materials

In this subsection, we report all the materials employed during this work for the experiments. All reagents and solvents were used as received, without further purification. DI

water was obtained through a Millipore Milli-Q lab water system, and 99% ethanol was purchased by Sigma-Aldrich. 11-Mercaptoundecanoic acid 95%, MES buffer, 1M ethanolamine, (3-Aminopropyl)triethoxysilane (APTES 99%), Di(N-succinimidyl) glutarate, glutaraldehyde solution 25%, were purchased from Sigma-Aldrich. 0.01M HEPES buffer was prepared by diluting 1M stock solution purchased from ThermoFisher. EDC (1-ethyl-3-(3-dimethylaminopropyl) carbodiimide hydrochloride), Sulfo-NHS (N-hydroxysulfosuccinimide), StartingBlock<sup>TM</sup> Blocking Buffer were purchased from ThermoFisher. BR228-D4A3 CRP recombinant monoclonal antibody fragments (Fab), human C-Reactive Protein, and human C-Reactive Protein depleted serum were purchased from BBI Solutions. Anti-cardiac troponin I F(ab)<sub>2</sub> fragments were purchased from Absolute Antibody. Bovine Serum Albumin was purchased from Sigma-Aldrich.

### 3.1.2 Employed functionalization for antibody fragments immobilization on high- $\kappa$ oxide surfaces

The most commonly used chemistry in the literature to immobilize antibodies on silicon dioxide involves (3-Aminopropyl)triethoxysilane (APTES) molecules [98, 116, 118, 159, 160, 161, 162, 163, 164, 157, 158]. APTES is an amino silane that possesses triethoxysilyl groups, which can react with hydroxyl groups on the silicon dioxide surface [165], and can act as the first layer of a self-assembled monolayer functionalization structure [166, 167, 168]. The other termination of the molecule is an amino group, which can be used in conjunction with an amine-reactive homobifunctional cross-linker, such as di-(N-succinimidyl) glutarate (DSG), to link the antibody fragments to the surface via free amine groups present on the lysine residues of the antibody structure [169]. We chose to use DSG crosslinker due to its short carbon chain between the NHS ester groups, which is critical to avoid the Debye screening effect that may occur to the electrical charges carried by the proteins [110]. Below, we present a detailed description of the functionalization protocol, outlining each step in detail.

To create a specific CRP capture layer, anti-CRP fragments (Fab) were immobilized on the HfO<sub>2</sub> surface of the NWs (Figure 3.1). Initially, the surface was thoroughly rinsed with 99% ethanol and dried with N<sub>2</sub>. To ensure effective surface coverage of the hydroxyl-terminated oxide surface, the SiNWs were exposed to UV ozone curing for 1 minute [170, 171], then immediately incubated in a 2% APTES solution in 99% ethanol for 1 hour. Following this incubation, the chip was extensively rinsed with ethanol and dried with N<sub>2</sub>. To obtain an ordered monolayer, the SiNWs were annealed at 120°C, as described in [165, 133]. Next, the APTES-modified surface was immersed in a 1 mM DSG crosslinker aqueous solution (1X PBS) for 15 minutes to create an amine-reactive surface. The amine-reactive homobifunctional crosslinker was then utilized to immobilize the CRP Fab (active channel) or the cTnI F(ab)<sub>2</sub> (reference channel) by immersing the NWs in a 20 μg/mL antibody fragments solution diluted in 1X PBS for 1 hour. The unbound antibodies were removed by carefully washing the surface with a 1X PBS solution. To prevent nonspecific surface binding, the surface was blocked with StartingBlock<sup>TM</sup> blocking buffer (ThermoFisher), and the unreacted sites were quenched with 1M ethanolamine.

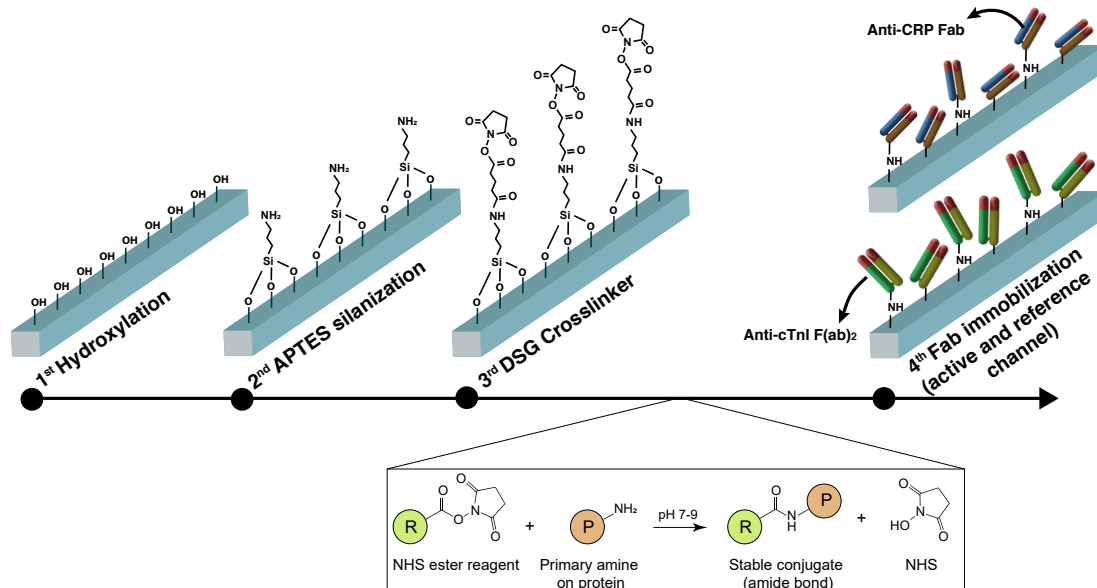


**Figure 3.1:** Schematic showing the employed high- $\kappa$  oxide surface functionalization process. The first step consists of the hydroxylation of the oxide surface by means of UV ozone treatment. Then, the hydroxyl groups react with the ethoxy groups of the APTES molecules, creating an amino reactive surface. The selected DSG cross-linker molecules possess two amino-reactive ester groups: one side reacts with the amine groups of the APTES molecules, and the other is used to covalently bind the primary amine on the antibody fragments to the surface.

### 3.1.3 Surface Plasmon Resonance (SPR)

To prove the capability of the purchased anti-CRP Fab to selectively capture CRP in the physiological range, and to study their binding kinetic, we exploited surface plasmon resonance (SPR) [172], both in buffer and ISF-like solutions. SPR is a powerful label-free optical detection technique that employs surface plasmons (SPs) and changes in the refractive index upon biomolecular interactions to measure the analyte concentration in solution [173, 174]. The SPR technique employs a metal-dielectric interface where coherent electron oscillations (SPs) are created upon interaction with a light source, and which shift in propagation constant is measured after the biomolecular recognition elements capture the specific analyte in the liquid. The binding event creates a shift in the refractive index proportional to the amount of captured analyte, which can be measured using intensity modulation.

In our case, we employed a Biacore<sup>TM</sup> 8K+ high-throughput and high-sensitivity SPR system with gold sensor chips to create user-defined surface chemistries. Our goal was to confirm the functionality of the anti-CRP Fab fragments, rather than to study the functionalization process on the dielectric surface of the SiNWs. The employed SPR system performs high-sensitivity analysis using an Au electrode, thus the antibody probes are immobilized on the metallic surface by means of thiol-chemistry. In the employed SPR system, each chip enables the

parallel execution of eight distinct experiments, facilitated by eight independent channels, each accompanied by a corresponding reference channel. The functionalization steps for the primary channels are replicated in their respective reference channels, with the sole distinction being the omission of the selected probes (i.e., antibodies) in the latter, leading to a blocked surface devoid of specific probes. The reference channels are exploited to remove bulk and temperature effects from the active channel response. The study utilized four independent channels, assigned as follows: two channels were dedicated to buffer measurements, while the remaining two were utilized for measurements conducted in ISF-like solutions. In each set of channels, one was functionalized with anti-CRP Fab fragments (active channel), while the other was functionalized with anti-cTnI F(ab)<sub>2</sub> fragments (reference channel). The channels functionalized with cardiac troponin antibodies served as negative controls throughout the entire experiment. Both the active, negative control, and reference channels undergo the same dose-response analysis. The experimental design and channel descriptions are provided in Table 3.1 for experiments conducted in buffer solutions and in Table 5.1 for experiments in ISF.

Matrix	Buffer			
Name	Reference - Active	Active	Reference - Negative	Negative
Channel #	CH-1 ref	CH-1	CH-2 ref	CH-2
Probes	Blocked surface	anti-CRP	Blocked surface	anti-cTnI

**Table 3.1:** Experimental design and channel attribution for the experiments carried out in buffer solutions.

Matrix	ISF-like			
Name	Reference - Active	Active	Reference - Negative	Negative
Channel #	CH-3 ref	CH-3	CH-4 ref	CH-4
Probes	Blocked surface	anti-CRP	Blocked surface	anti-cTnI

**Table 3.2:** Experimental design and channel attribution for the experiments carried out in ISF-like solutions.

A consistent functionalization protocol has been employed to immobilize both types of antibody fragments. Initially, the chip was incubated overnight in a 1mM solution of 11-Mercaptoundecanoic acid (MUA) in ethanol. This step facilitated the attachment of the molecules to the bare gold chip through the thiol group located at the molecule's end. Subsequently, the chip underwent thorough rinsing alternating between ethanol and DI water. Next, the chip was inserted into the Biakore™8K+ system to finalize the immobilization process and assess the dose response of CRP. The carboxylic terminations of the MUA molecules were activated using EDC/NHS, after which a solution of 10 mM 2-(N-morpholino) ethane sulfonic acid (MES) buffer at pH 6.0, enriched with 20 µg/mL of CRP antibody fragments for the active channels (CH-1 and CH3 in Tables 3.1 and 5.1) or anti-cTnI F(ab)<sub>2</sub> for the reference channel (CH-2 and CH-4 in Tables 3.1 and 5.1), was flushed onto the gold chips. To minimize the non-specific absorption of biomolecules on the surface, any unreacted MUA sites were quenched using a 1M ethanolamine solution. Finally, the surface was further blocked by

flushing it with StartingBlock<sup>TM</sup> solution by Thermofisher.

Before conducting the CRP dose response, the functionalized chip was washed with assay diluent for 1 hour. After the completion of the functionalization process, the different channels were exposed to consecutive injections of the liquid under test.

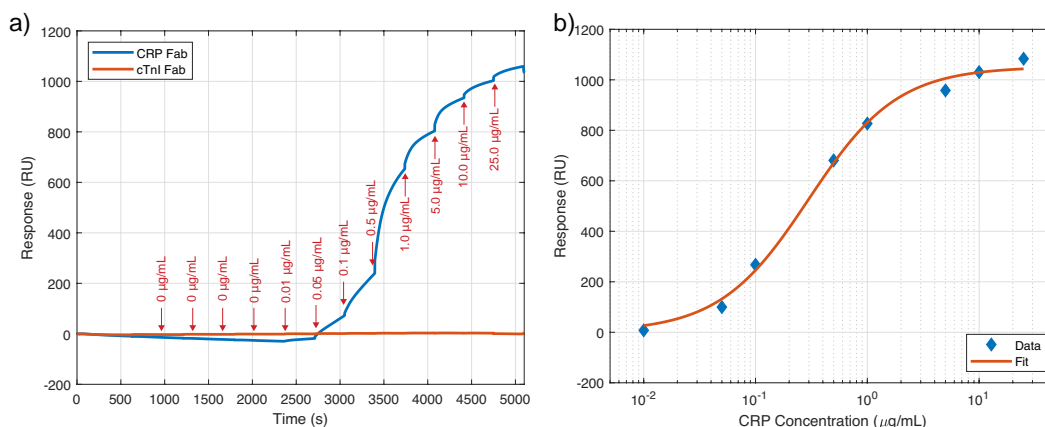


**Figure 3.2:** Surface Plasmon resonance anti-CRP Fab study in buffer solutions. a) Reference subtracted SPR real-time traces for the channels functionalized with anti-CRP Fab and anti-cTnI F(ab)<sub>2</sub>. The latter does not show any response to CRP injections with increasing concentrations. b) Calibration curve showing the dose-response to CRP injection of the anti-CRP Fab fragments in buffer.

All the reported results are obtained by subtracting the active signal from the reference one (signals of CH-i reference channels are subtracted from signals of CH-i channels). Figure 3.2a shows the real-time reference subtracted SPR response in buffer for the channels functionalized with anti-CRP Fab and anti-cTnI F(ab)<sub>2</sub>. We notice a completely flat response of the troponin antibodies to consecutive CRP injections, while the channel with anti-CRP fragments responds with a classical stabilization curve that depends on the CRP concentration in solution. The flat response of the troponin antibodies demonstrates a good quenching of the unreacted sites, minimizing the effect of undesired unspecific absorption of proteins. To better visualize the CRP dose-response, the average values for each injection are extracted from the real-time response and plotted against the CRP concentration in a semi-logarithmic plot in Figure 3.2b. A 4-parameter logistic (4PL) regression is used to fit the obtained data, to extract information on the binding kinetics of the antibody fragments. We conclude that in buffer, the half maximal effective concentration (EC<sub>50</sub>) is approximately 1 µg/mL.

The same data analysis is performed with the real-time SPR response in an ISF-like solution. For this case, it is essential to subtract the reference channel response to obtain meaningful results. The reference subtracted real-time traces for both the channels with anti-CRP and anti-cTnI antibodies are shown in Figure 3.3a. Figure 3.3b reports the CRP dose response of the properly functionalized channel, and the relative fit performed with a 4PL regression. It is worth noting that the absolute response to the same concentrations of CRP is lower than

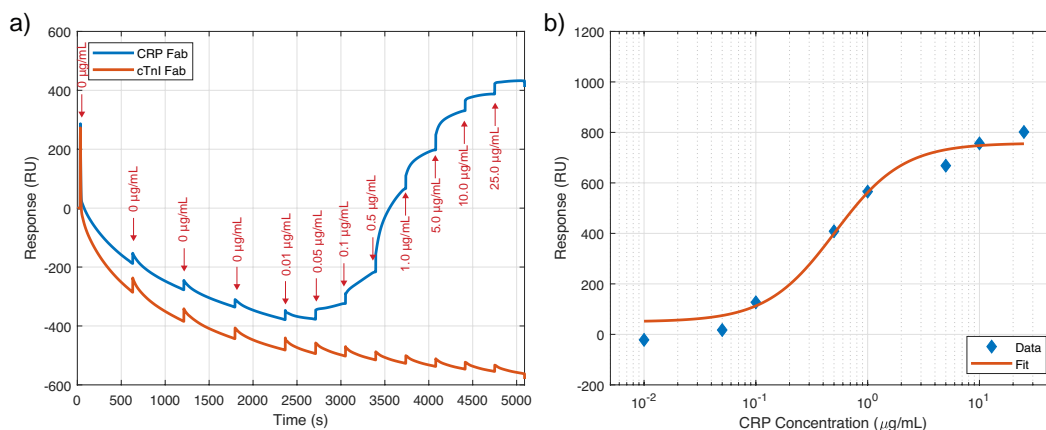


**Figure 3.3:** Surface Plasmon resonance anti-CRP Fab study in ISF solutions. a) Reference subtracted SPR real-time traces for the channels functionalized with anti-CRP Fab and anti-cTnI  $F(ab)_2$ . The latter does not show any response to CRP injections with increasing concentrations. b) Calibration curve showing the dose-response to CRP injection of the anti-CRP Fab fragments in ISF.

the one obtained in buffer. This result is precious since it would probably be reflected in FET-based detection. The regression model outputs a half maximal effective concentration (EC50) of  $1.5 \mu\text{g}/\text{mL}$ , slightly higher than the one obtained in buffer.

The above-described experiments are conclusive, indicating the good performance of the chosen anti-CRP Fab fragments in the concentration range of interest. Moreover, these probes can well perform both in buffer and in more complex matrices, such as ISF.

### 3.1.4 X-Ray Spectroscopy (XPS)

After confirming that the selected antibodies respond correctly to CRP in the desired range, the immobilization protocol on the  $\text{HfO}_2$  surface has to be tested and studied. X-Ray Spectroscopy (XPS) is a method of characterizing surfaces that provides insight into the microstructural composition of a material's surface [175]. This technique uses the photoelectric effect, in which photons, specifically X-rays, are directed at the surface of interest, causing the emission of secondary electrons that carry characteristic energy. The energy of these electrons depends on the material's composition and the chemical bonding of its elements. Since the photons' penetration depth is usually greater than that of electrons, the excited volume in this method is not limited to the surface of the sample. The short escaping length of electrons enables the collection of information that pertains solely to the surface of the sample, making this technique interesting for our study. We used a PHI VersaProbe II scanning XPS microprobe by Physical Instruments AG with an  $\text{Al K}\alpha$  X-ray source of 24.8 W power, and  $100 \mu\text{m}$  size. The spherical capacitor analyzer was set at  $45^\circ$  take-off angle with respect to the sample surface. The pass energy was 46.95 eV yielding a full width at half maximum of 0.91 eV for the Ag 3d

5/2 peak. Curve fitting was performed using the PHI Multipak software.

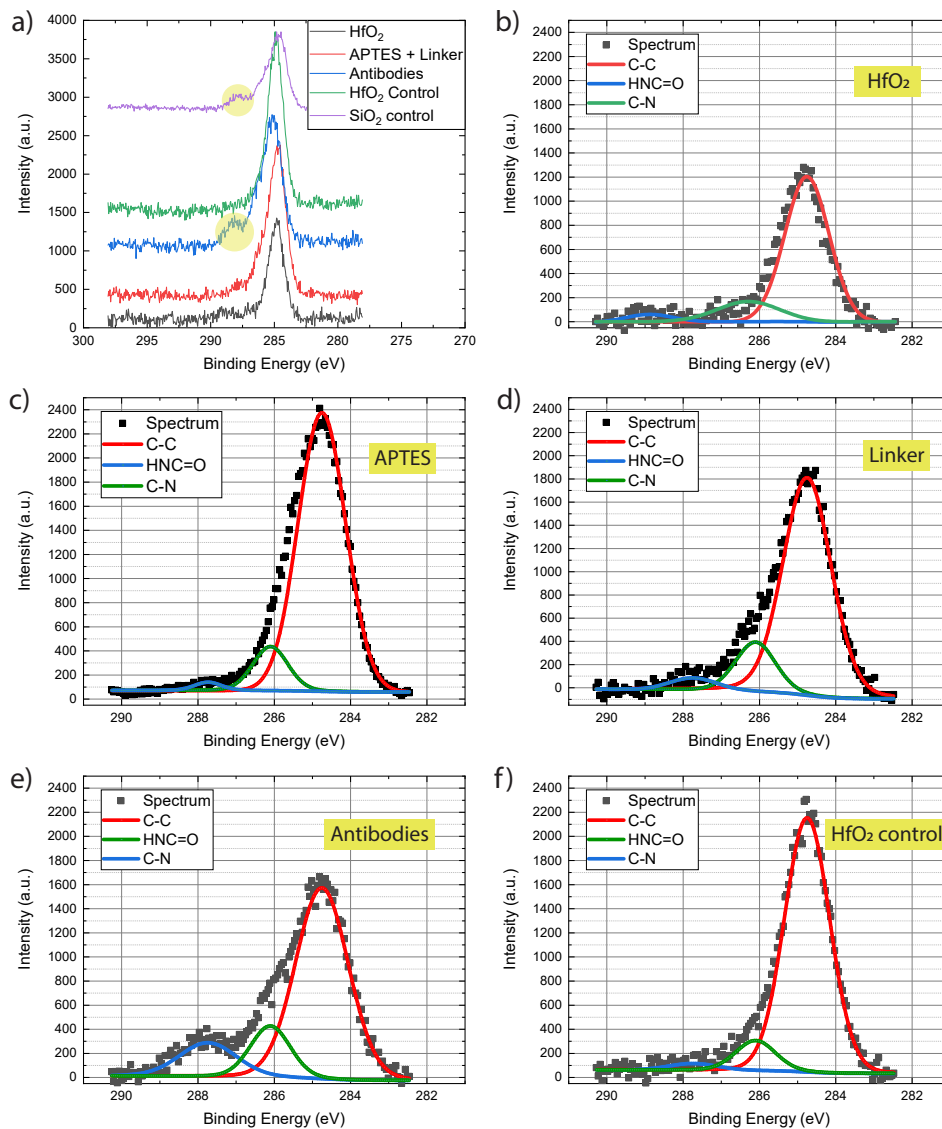


**Figure 3.4:** X-ray spectroscopy carbon peak modulation after each functionalization step. a) Comparison between the different spectra at every step of the functionalization and two control chips. The hafnium oxide control is immersed in an antibodies solution without undergoing the previous functionalization steps. The silicon dioxide control chip undergoes the same functionalization process as the properly functionalized hafnium dioxide chip. We can notice the presence of the secondary peak at 288.3 eV for the fully functionalized HfO<sub>2</sub> and SiO<sub>2</sub> chips, indicating a correct antibodies immobilization, while this peak does not show up for the HfO<sub>2</sub> control chip, indicating the necessity of a proper functionalization layer to ensure a correct antibodies immobilization. b-e) Detailed carbon peak evolution at every functionalization step, with peaks fitting. f) Carbon peak with peaks fitting for the HfO<sub>2</sub> control chip.

To demonstrate the successful functionalization of high- $\kappa$  dielectric with specific antibodies,



we conducted XPS analysis on 20 nm HfO<sub>2</sub> grown by ALD on Si substrate, as well as on a thermally grown 200 nm layer of SiO<sub>2</sub> on Si substrate, which we utilized as a control experiment. The functionalization of silicon dioxide with the proposed chemistry has been extensively documented in the literature [176, 177, 178]. Our primary focus was on the C and N peaks in the acquired spectra, as they provide the most valuable qualitative information regarding the presence of covalently bonded antibodies on the two surfaces [133]. By examining these peaks, we were able to determine the efficacy of our antibody functionalization method on both HfO<sub>2</sub> and SiO<sub>2</sub> surfaces.

The evolution of the C1s peak for the different steps of the functionalization protocol presented in Section 3.1.2 is shown in Figure 3.4a: the bare HfO<sub>2</sub> surface shows a peak at 285 eV, corresponding to a C-C bonding and indicating normal surface contamination [179]. This peak varies in intensity throughout the functionalization process, as shown in Figure 3.4a and in greater detail in Figure 3.4b-e, where the spectrum is fit with various peaks representing different molecular bonds. Upon covalent bonding of APTES molecules to the oxide surface, the C-C peak at 284.8 eV intensifies due to the carbon backbone of the molecules [180]. Additionally, a peak at 286 eV appears, indicating the presence of C-N bonds at the amine termination of the molecule [180, 181]. The relative contribution of the C-N peak increases upon the reaction of the glutarate linker with the amino termination of the APTES, as depicted in Figure 3.4d. Finally, the antibodies are covalently immobilized on the surface and an additional shoulder peak at 288.3 eV emerges (Figure 3.4e), clearly indicating the presence of a peptide bond (NHC=O) in the functionalization stack [182, 183, 184], and confirming successful functionalization of our high- $\kappa$  dielectric surface. We can compare the final spectrum with two control experiments. The XPS spectrum of an HfO<sub>2</sub> surface that was merely immersed in antibody solution but did not undergo the full functionalization process is presented in Figure 3.4f: it lacks the shoulder peak at 288.3 eV, confirming the absence of correctly immobilized antibodies on the surface. Furthermore, we present the spectrum of a 200 nm silicon dioxide surface that underwent the same functionalization approach (Figure 3.4a), showing a similar XPS spectrum to that of the HfO<sub>2</sub> surface.

A similar description can be carried on by focusing attention on the modulation of the nitrogen peak. In our study, the peak showed a relatively low intensity, but useful information can still be extracted by a careful peak fitting, as shown in Figure 3.5. The comparison of the spectra at different functionalization steps is reported in Figure 3.5a, where we can immediately recognize a strong similitude between the fully functionalized HfO<sub>2</sub> surface and the control SiO<sub>2</sub> with the same functionalization. In Figures 3.5b-d the fitting of the more relevant spectra is reported: after the addition of the APTES molecule a strong intensity contribution of the C-NH<sub>2</sub> peak at 399.6 eV is clearly visible [185, 184, 183], most probably related to the amino terminations of the molecule. We assigned the peak at 400 eV to the HNC=O peptide bonds, which increases in intensity when the antibodies are covalently bonded to the linker molecules.

We can confidently conclude that the silanization chemistry perfectly serves the necessary role of immobilizing the chosen anti-CRP Fab fragments on our high- $\kappa$  dielectric surface, having

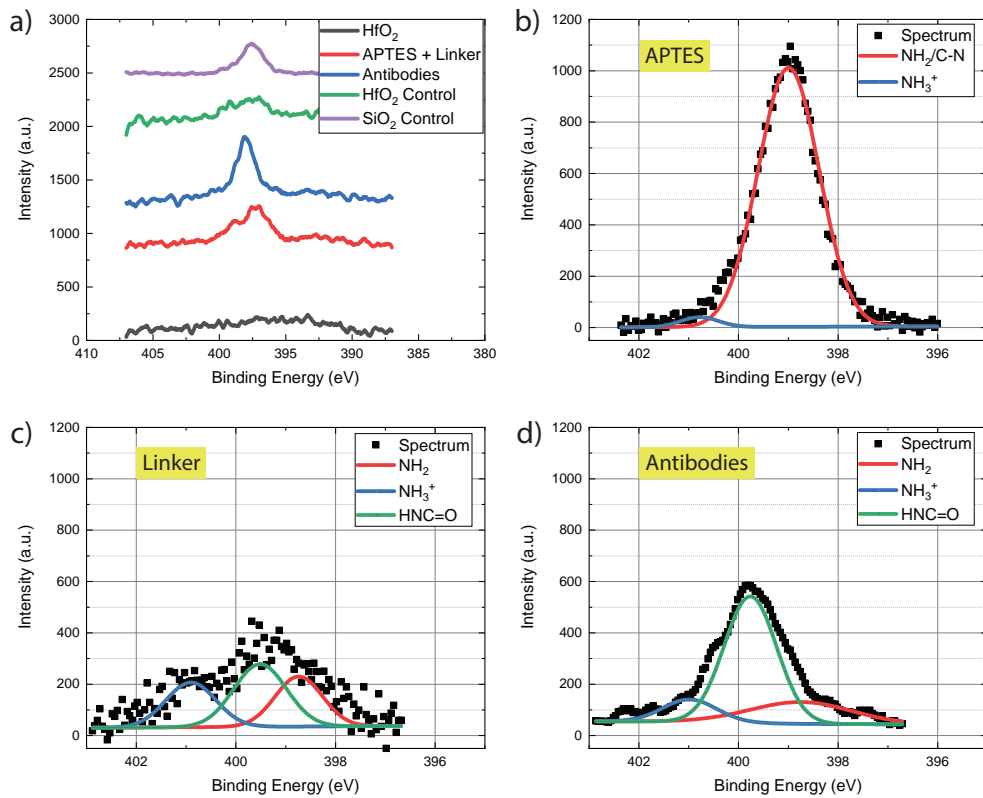


**Figure 3.5:** X-ray spectroscopy nitrogen peak modulation after each functionalization step. a) Comparison between the different spectra at every step of the functionalization and two control chips. The hafnium oxide control is immersed in an antibodies solution without undergoing the previous functionalization steps. The silicon dioxide control chip undergoes the same functionalization process as the properly functionalized hafnium dioxide chip. We can notice the presence of a pronounced peak at 400 eV for the fully functionalized HfO<sub>2</sub> and SiO<sub>2</sub> chips, indicating a correct antibodies immobilization, while this peak does not show up for the HfO<sub>2</sub> control chip, indicating the necessity of a proper functionalization layer to ensure a correct antibodies immobilization. b-d) Detailed nitrogen peak evolution at every functionalization step, with peaks fitting.

compared the results with a standard SiO<sub>2</sub> functionalized one.

### 3.1.5 Quartz Crystal Microbalance (QCM)

Quartz Crystal Microbalance with dissipation monitoring (QCM-D) measurements have been employed to prove the good quality of the functionalization layer and to highlight the importance of a uniform APTES layer. QCM-D is a highly sensitive mass balance that exploits a resonating quartz crystal to detect nanogram changes in mass per unit area. QCM-D is based on a resonating body, that shifts its resonant frequency based on the amount of analyte adsorbed on the surface. It is part of the acoustic wave sensors family, based on piezoelectric materials that can be oscillated with the application of an alternating electrical voltage via metal electrodes. The resonant frequency of the oscillation is related to the added mass at the crystal surface [186], with the following equation [187]:

$$\Delta f = \left( \frac{-2f_0}{A\sqrt{\rho G}} \right) \Delta m \quad (3.1)$$

where  $\Delta f$  represents the resonance frequency shift due to the mass change  $\Delta m$ ,  $f_0$  is the resonance frequency of the quartz crystal,  $A$  is the surface area, and  $\rho$  and  $G$  are the density and the shear modulus of the quartz, respectively. This technique proves to be interestingly useful to study our functionalization layer since it can be exploited in a liquid environment [188], by taking into consideration the dissipation contributions due to viscoelastic interaction of the absorbed analyte with the liquid environment [189]. The information extracted from the viscoelastic interaction of the experiment can result in interesting information about the nature of the absorbed analyte, its thickness, or its density. For the scope of our work, we are only interested in confirming the ability of our functionalization layer to selectively recognize and detect specific antigens in the solution. We will not apply a data analysis model such as the Voight-based viscoelastic one to extract the absorbed concentration, since we used this method only to obtain qualitative information on our functionalization protocol. Further analysis could be carried out with the use of our data, but this is out of the scope of this work.

For our study, we used a Q-Sense Analyzer from Biolin Scientific, with three available parallel measurement modules. We exploited custom-made quartz crystals with a deposited layer of  $\text{HfO}_2$  on top, to mimic the SiNWs gate oxide surface and study the effectiveness of our functionalization protocol on high- $\kappa$  dielectric surfaces. The first step of our experiment is to create a dense monolayer of APTES molecules onto the surface: this step is done in static mode, not exploiting the Q-Sense chamber, since APTES solutions can be very contaminant and usually are not allowed in those systems. After immobilizing the APTES molecules with the process described in section 3.1.2 on two out of three hafnium oxide discs, we proceed by loading the three discs in the available modules. Each microbalance undergoes a slightly different functionalization process, in fact, only one of them will be properly functionalized with the described protocol, and the other two will be used as control experiments. The control experiments are based as such:

- one microbalance has not been immersed in the APTES solution, thus it does not possess the first silanized layer. Apart from this modification, the rest of the functionalization protocol is maintained. This control serves as proof of the utility of the APTES layer;
- one microbalance undergoes the complete functionalization protocol, but instead of using anti-CRP Fab fragments as capture layer, we employ cardiac troponin I (cTnI) F(ab)<sub>2</sub> fragments. We expect this microbalance to not respond to CRP injections in the tested solution. Thus, we use this sensor as the negative control.

For the entirety of the dose-response experiment with the Q-Sense Analyzer, we flush the same solutions through the three modules with the three microbalances, with the help of a peristaltic pump, that keeps a constant flow of 50  $\mu\text{L}/\text{minute}$ . The first part of the experiment involves completing the functionalization protocol, and it is reported by showing the 5th harmonic frequency shifts in Figure 3.6a: after injecting 0.1xPBS buffer until we reach a stable response, we introduce a 1 mM DSG aqueous solution that acts as a linker between the APTES molecules and the antibodies. After the injection of the linker, the three microbalances are exposed to different solutions (steps indicated with 'probes' in the graph): the main sensor and the sensor with no APTES layer are functionalized with a solution of 20  $\mu\text{g}/\text{mL}$  of anti-CRP Fab fragments, while the negative control is shown to a solution of 20  $\mu\text{g}/\text{mL}$  anti-cTnI F(ab)<sub>2</sub> antibodies fragments. As expected the three sensors experience a negative shift in the frequency: the two sensors functionalized with anti-CRP fragments show a similar shift, while the resonator functionalized with cardiac troponin antibodies fragments experiences a larger shift. Since the QCM technique is a mass-sensitive measurement, we expected the latter sensor to show a larger change in frequency, since the F(ab)<sub>2</sub> fragments are double in size with respect to Fab fragments. Indeed, the total change is almost two times larger than the one for the quartz functionalized with anti-CRP Fab.

After the immobilization of antibodies on the microbalances' surface, we flush in the modules the washing buffer to remove the unbound probes. Both the negative control and the microbalance without the APTES layer show a positive shift of the frequency, indicating that part of the antibodies was not covalently bonded to the surface. On the other hand, the properly functionalized sensor does not show such a positive shift, suggesting that the antibodies were correctly immobilized on the hafnium dioxide surface with a strong binding mechanism. To passivate not functionalized areas we proceed with two steps: we flush StartingBlock<sup>TM</sup> Blocking Buffer from Thermofisher and 1 M ethanolamine to quench amino terminations that did not react. We have presented the extracted frequency shifts from the real-time trace shown in from 3.6a in Figure 3.6b to better visualize what is happening on the resonators' surfaces. We can notice that antibodies are either absorbed or immobilized on all surfaces. Comparing the two sensors with anti-CRP Fab, the one without the APTES layer seems to undergo only physical absorption of antibodies and not covalent bonding, as the probes are washed away with buffer injection, indicating a weaker bonding to the surface.

After completing the functionalization process, we tested the three sensors with the same

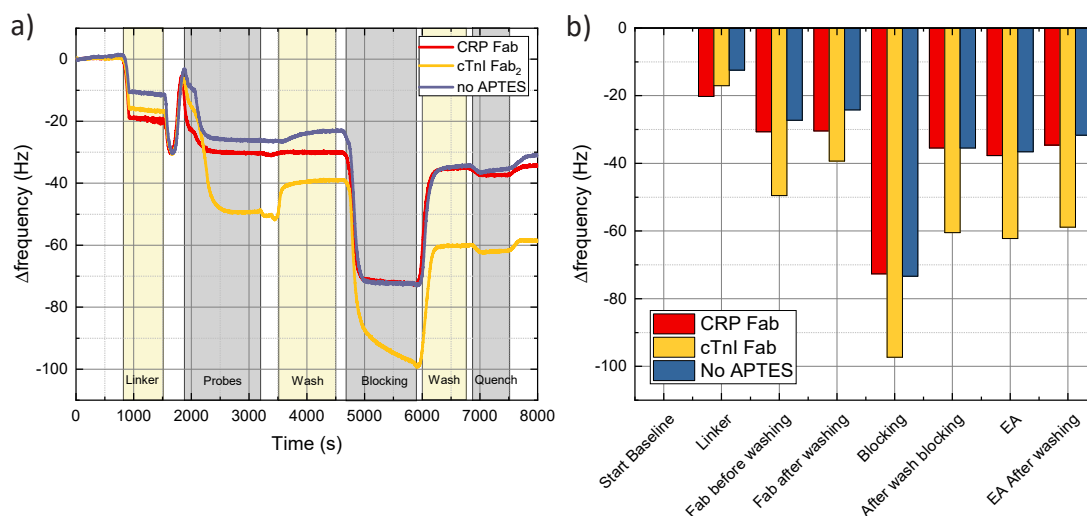


**Figure 3.6:** QCM frequency shift of the 5th harmonic for three different sensors. The first sensor (red) undergoes a complete functionalization process, the second one (yellow) is similarly functionalized with the only difference that anti-cardiac troponin I antibodies fragments are used as a replacement for the CRP ones, and finally, the third curve (blue) undergoes a full functionalization with anti-CRP fragments, but skipping the first step of APTES monolayer deposition. a) Real-time sensors' response during the functionalization process. Each functionalization step is highlighted at the bottom of the plot. The used linker is 5% DSG, while the blocking and the quenching are performed with StartingBlock<sup>TM</sup> blocking buffer by Thermofisher and 1 M ethanolamine solution, respectively. b) Average values extracted for each curve at every step of the functionalization.

solutions injections. First, we injected increasing concentrations of Bovine Serum Albumin (BSA) to test the unspecific response of the functionalization layer. During this step, the three sensors respond in different ways. The negative control exhibited a small negative frequency shift, with a maximum shift of -0.5 Hz when tested with a high BSA concentration of 25  $\mu$ g/mL. The negative shift can be associated with a very slight temporal drift, as visible in the plot of figure 3.7a. Similar behavior is shown by the sensor with the full functionalization layer (labeled in the figures as "CRP Fab"): the sensor shows a maximum positive response of BSA of 0.75 Hz Figure 3.7b, also clearly traceable to a minimal temporal drift. The only sensor that shows a (small) response to BSA injection is the one without the APTES layer: for the highest BSA concentration, this sensor shows a frequency shift of 2 Hz, either signaling an unspecific response to proteins or a large temporal shift. The origin of this shift is associated with the absence of the silane molecules, thus to the poor bonding of the probes to the surface.

After the unspecific binding test, the sensors' specific dose response is tested with different concentrations of C-Reactive protein, from 0.1  $\mu$ g/mL to 25  $\mu$ g/mL. The negative control sensor, functionalized with anti-cTnI antibodies does not show any response as expected, indicating good passivation and quenching procedure. The two sensors with anti-CRP fragments show a specific response to CRP injections, even if the capturing probes on the sensor without

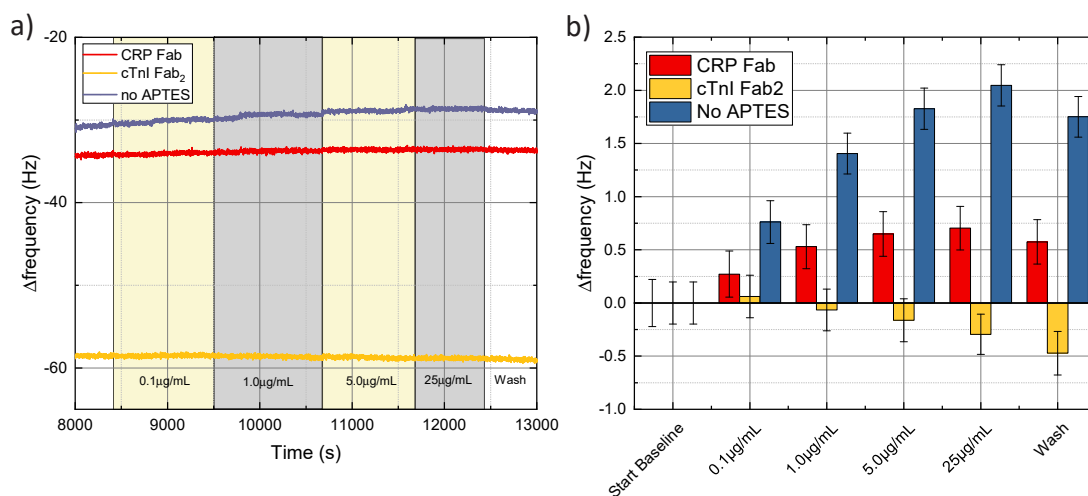


**Figure 3.7:** QCM frequency shift of the 5th harmonic when the three sensors are exposed to different concentrations of Bovine Serum Albumin in 0.1xPBS buffer. a) Real-time frequency shift, the different BSA injections are highlighted with alternating background colors, and the absolute values are indicated at the bottom of the plot. b) Average values extracted from a). A higher unspecific response (or temporal drift) for the sensor with the anti-CRP Fab but without APTES monolayer is present. Proper functionalization is necessary to achieve sufficient sensor stability and lower unspecific response.

APTES are only physically absorbed on the surface and not covalently bonded. The necessity of the APTES layer in the functionalization stack is demonstrated by a higher sensitivity for a larger concentration range, as shown in Figure 3.8a-b. The red bars in the plot show a higher frequency shift for the entire tested concentration range. Moreover, after the CRP injections, the sensors are washed with 0.1xPBS buffer, and they do not show an unwanted unbinding of the captured analytes.

We can conclude that our functionalization protocol is stable and reliable, providing a specific response, with low temporal drift and an unspecific response towards different proteins other than CRP.

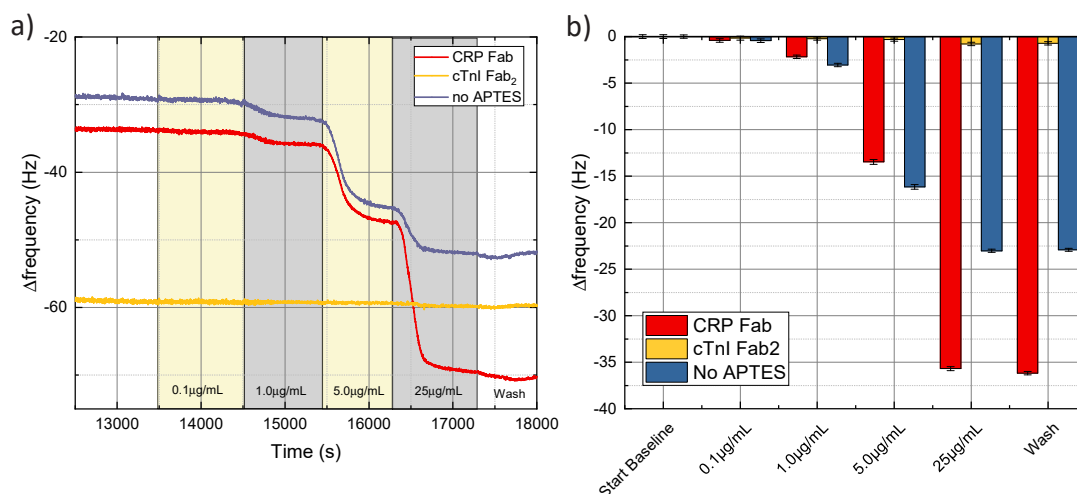


**Figure 3.8:** QCM frequency shift of the 5th harmonic for when the three sensors are exposed to different concentrations of C-Reactive Protein in 0.1xPBS buffer. a) Real-time frequency shift. Consecutive CRP injections are highlighted with alternate background colors, and the absolute value of the concentrations is indicated at the bottom of the plot. b) Average values extracted from a). We first notice that the sensor functionalized with anti-cTnI fragments does not show an unspecific response, being a good candidate as a reference sensor in a reference-compensated system. The fully functionalized sensor (red) shows a higher sensitivity over a larger concentration range compared to the sensor missing the APTES layer, proving once more the necessity of proper functionalization.

## 3.2 Measurement setup

### 3.2.1 Low-volume microfluidic

To ensure the distinct functionalization of different sensors, we developed a customized microfluidic stamp using polydimethylsiloxane (PDMS) for both SiNWs platforms. The fabrication is based on standard soft lithography techniques, as illustrated in Figure 3.9. Firstly, we designed a silicon mold with the precise negative imprint of the desired microfluidic channels using standard photolithography. Next, we poured liquid PDMS (with a ratio of 15:1 of base PDMS and cross-linker) onto the silicon mold and used a vacuum chamber to fill the empty cavities. The PDMS was then cured at 80°C for at least an hour, and the resulting PDMS stamp was gently removed from the silicon mold. Finally, we bonded the PDMS stamp to the SiNWs chip using UV curing and thermal treatment [190, 191, 192], as explained below.

In standard PDMS processing, to bond the fabricated PDMS to a silicon or silicon dioxide surface, a plasma oxygen treatment is required. In our case, when trying to transfer the fabricated PDMS microfluidic to the SiNW chips the process was irreversibly damaging the transistors' performance. As shown in Figure 3.10, after the oxygen plasma treatment used to bond the PDMS stamp to the oxide top surface of our chip the transfer characteristic was

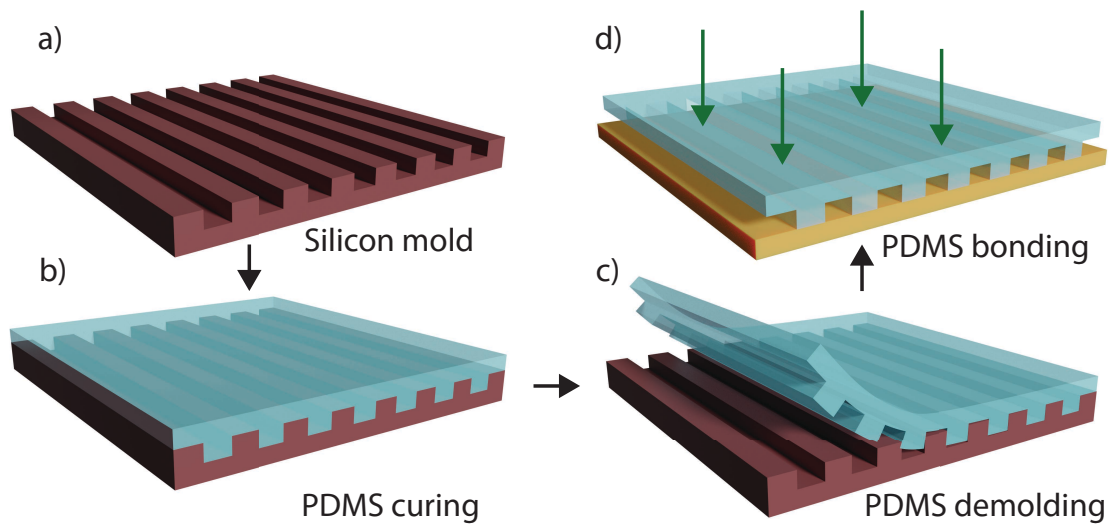


**Figure 3.9:** Soft lithography process for PDMS microfluidic stamps fabrication: a) a silicon mold is fabricated through a standard photolithography process, to obtain the negative replica of the microfluidic stamp. Before PDMS pouring the mold surface is conditioned with Trimethylchlorosilane (TMCS) to prevent PDMS sticking and help the de-molding process. b) Liquid PDMS with a PDMS primer to cross-linker ratio of 15:1 is poured onto the Si mold surface. Before curing the PDMS to obtain a solid stamp, the mold with the liquid PDMS is degassed in a vacuum desiccator for at least 15 minutes, to avoid the presence of bubbles in the PDMS matrix. The PDMS is then cured at 80° C for at least 2 hours. c) After PDMS curing, the microfluidic stamps are cut and gently de-molded from the Si substrate. The inlet and outlet are created by means of a manual puncher. d) The PDMS microfluidic stamp is bonded to the surface of the chip after 5 minutes of ozone UV treatment. To enhance and ensure a good bonding, the chip with the stamp on top is beaked for 30 minutes at 120° C.

unpredictably changing: some transistors stopped working, such as the one reported in Figure 3.10a, while others experienced a deterioration of the sub-threshold slope and an increase of the hysteresis (Figure 3.10b-d).

The issue originated from the charge trapping phenomenon in the gate oxide during oxygen plasma exposure of the chip before PDMS transfer. The metal contacts were also adversely affected by this process, leading to an irreversible deterioration in the transistors' overall performance. Following numerous trials, we established a reliable recipe that would not damage the SiNWs electrical performance and would allow a strong bond between the chip's surface and the PDMS. We discovered that for our application, which did not involve high pressure in the microfluidic channels that could detach the PDMS from the sensor surface and cause undesired leakage, a 5-minute UV ozone chamber exposure of the PDMS alone was sufficient to create adequate -OH groups on its surface for bonding to the chip. A subsequent 30-minute baking step at 80°C of the chip and PDMS ensured a robust bond without harming the transistors.

For both the CEA-LETI nanowires chip and the one designed in-house we used the same



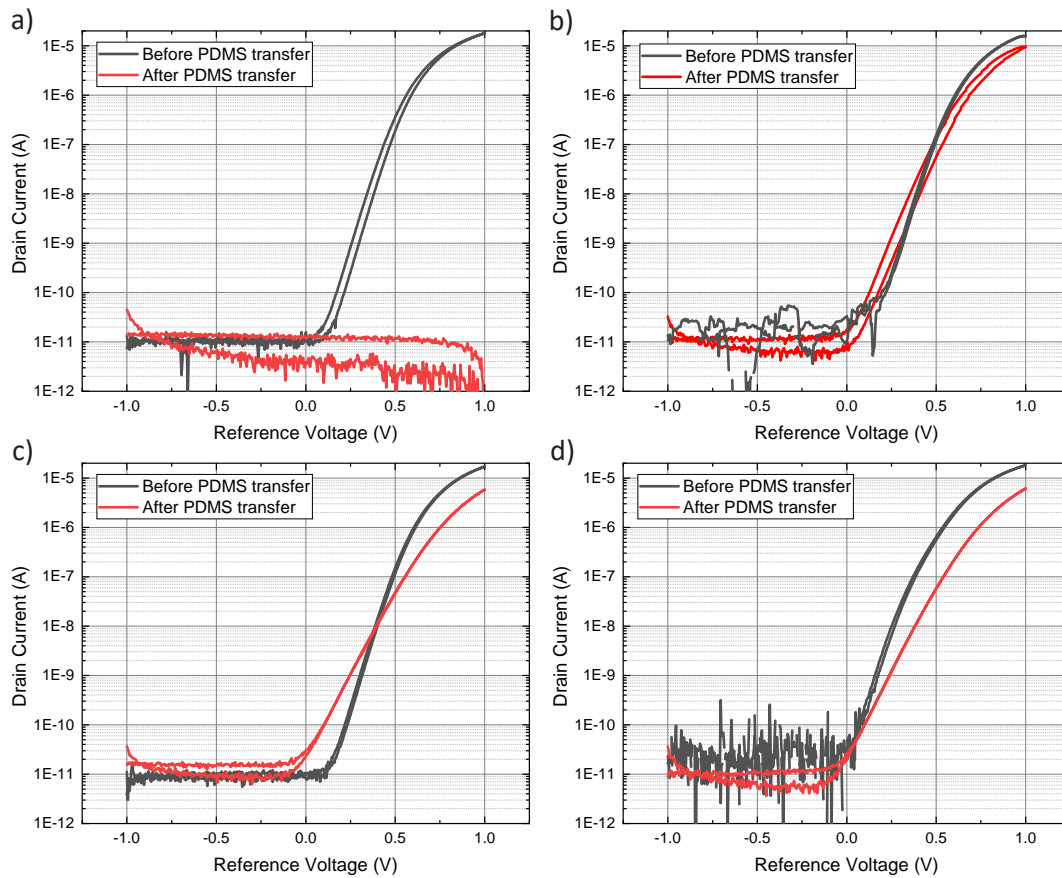


**Figure 3.10:** Various transfer characteristics of four different SiNW arrays before (black curves) and after (red curves) PDMS microfluidic stamp transfer. The plasma oxygen surface activation step irreversibly damages the transistors' functionality. (a) In some cases, the transistor completely stops working, while (b) in others we experience an increased hysteresis or (c) a deterioration of the OFF to ON switching capabilities of the arrays.

technique for the fabrication of the PDMS stamp, and the bonding to the chip's surface. Two pictures of the two chips with the respective PDMS stamp bonded on the surface are shown in Figure 3.11.

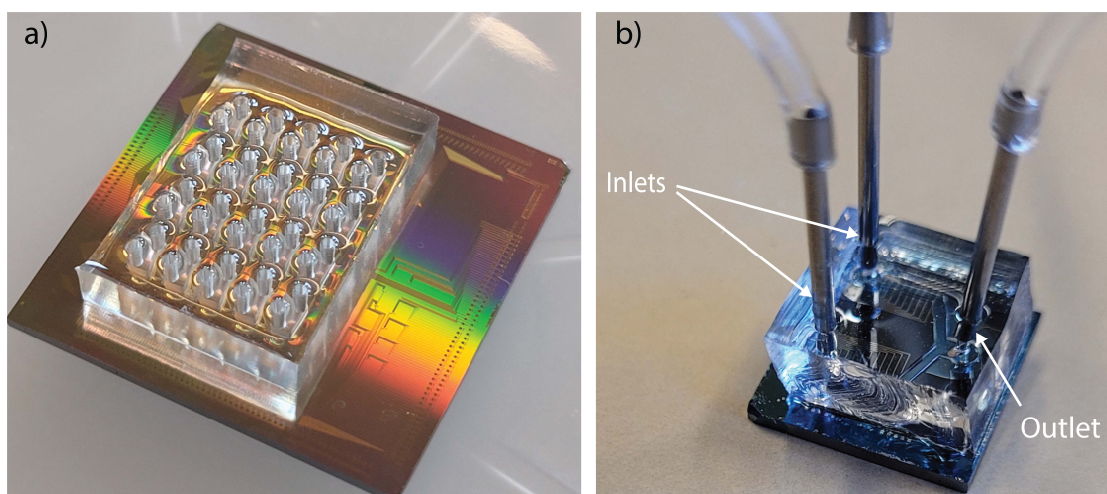


**Figure 3.11:** a) CEA-LETI and b) in-house fabricated silicon nanowire arrays chips with their respective microfluidic stamps.

### 3.2.2 Printed-Circuit-Board

To streamline our measurement process, we designed and built a printed circuit board (PCB) to replace the traditional probe station setup. The probe station requires constant probe positioning, which can be cumbersome and time-consuming while having numerous microfluidic tubes hanging from the PDMS stamps going from the liquid source to the waste. The PCB is comprised of two parts: one part where we attach the chip using conductive glue to ensure a back-gate contact through the chip body (Figure 3.12b), and the other part where we plug in the first PCB to select the sensor we want to work with using mechanical multiplexers (Figure 3.12a). The second part of the PCB includes SMB connectors to easily interface with the parameter analyzer. By using the PCB, we can eliminate the need for manual probe positioning, which improves accuracy and saves time. Furthermore, the mechanical multiplexers allow for quick and easy switching between sensors, making it a more versatile and efficient method for repetitive measurements. The conductive glue used to attach the chip ensures good electrical contact between the back-gate and the PCB, leading to more reliable and consistent measurements. The PCB also provides a more stable and controlled environment for measurements, minimizing external interference and enhancing accuracy. Overall, the use of the PCB has greatly improved our measurement process, allowing us to obtain more precise and reliable data more efficiently.

## 3.3 Electrical characterization methods

In this section, we present the different characterization methods exploited to measure pH and CRP with the SiNWs biosensor.

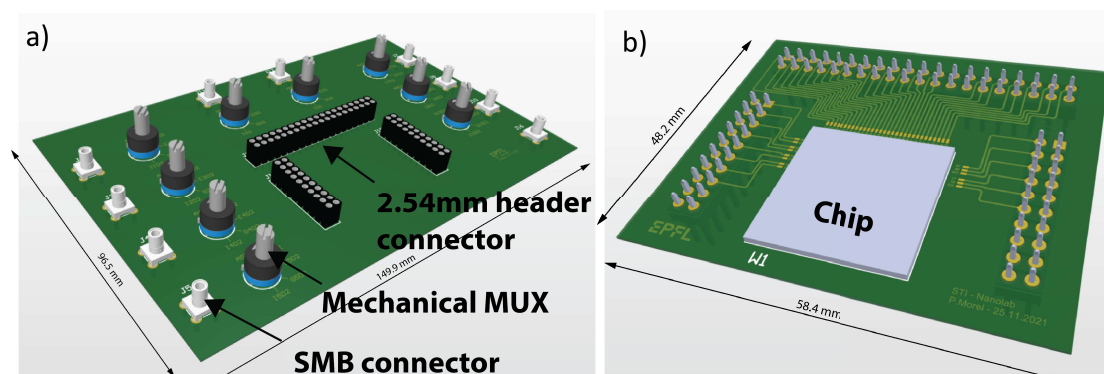


**Figure 3.12:** Printed circuit boards used to facilitate the SiNWs chips measurement. a) PCB with SMB connectors to connect the board with the parameter analyzer and with mechanical multiplexers to easily switch between different sensors for repetitive measurements. b) PCB for the support of the SiNW arrays chip. The chip is glued with a conductive glue to the board, to ensure the possibility to bias the back-gate through the chip body. The edge contact pads on the chip are wire-bonded to the PCB. This second PCB is plugged into the one in figure a).

### 3.3.1 Reference-compensated response

Label-free biosensors are vulnerable to various factors that may result in the false detection of target analytes. Temperature changes, temporal drift, external environmental influences, and unspecific responses can all cause a shift in the biosensor's response, mimicking and obscuring an accurate analyte detection. While batch calibration is typically employed to mitigate this effect, it can not entirely solve the problem. In this work, we utilized a reference-compensated method, which has been previously employed in other biosensor applications, including optical biosensors [193, 194, 195]. This technique involves treating the reference sensor with the same immobilization conditions used for the primary sensor but with a different immobilized antibody, ensuring that the common mode response is adequately subtracted [193]. In our study, we implemented the reference compensation method during the data analysis stage. However, our next objective is to develop and design a circuitry solution to enable reference compensation in practical applications.

Thanks to the design of our SiNW arrays chips, both for the CEA-LETI and the in-house fabricated one, we have access to identical copies of the same transistor on the same chip, accurately positioned in a manner that allows us to differently functionalize them with the help of the customized PDMS microfluidic stamps described in section 3.2.1. The functionalization protocol is identical for the active and reference sensors' gate oxide but differs only for the immobilized capturing probes: we immobilize specific anti-CRP Fab antibodies fragments on the surface of our active sensor, while we use unspecific F(ab)<sub>2</sub> fragments (either anti-fluorescein or anti-cTnI) on the surface of the reference sensor. We have already proved the absence of an unspecific response towards CRP with the anti-cTnI capturing layer using QCM analysis in section 3.1.5, thus making this a perfect candidate for the reference surface role.

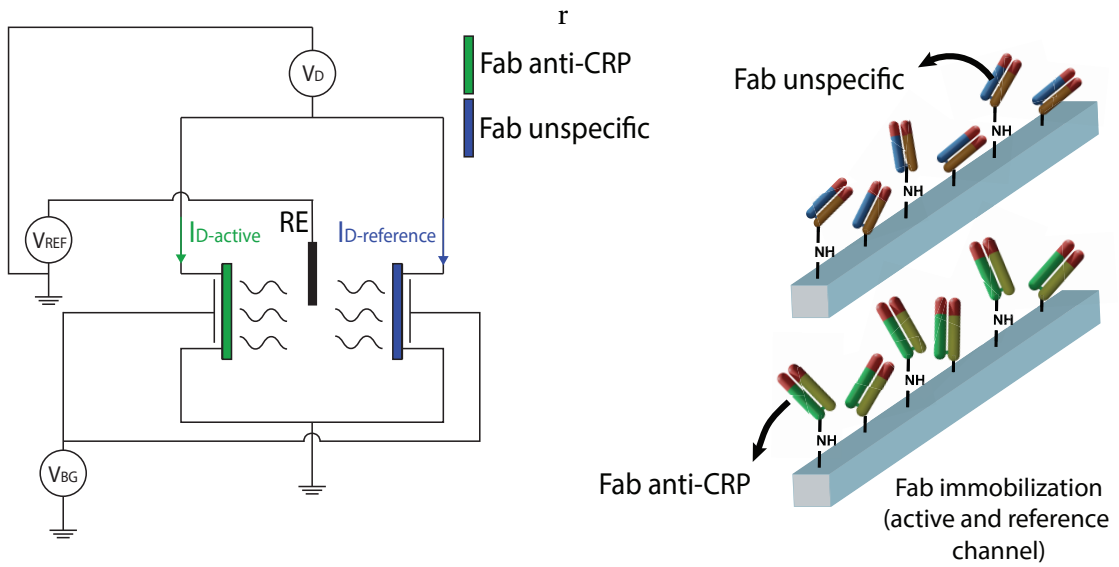


**Figure 3.13:** Reference compensated circuit schematic, representing the bias conditions for the two identical SiNWs arrays, functionalized with different antibody types. The gate oxides of the two transistors are immersed in the same liquid under test, biased by one external or on-chip Ag/AgCl reference electrode.

### 3.3.2 Front-Gate operation

We can consider one single SiNW array as a four-terminal transistor, with a source and drain contact, a back-gate (body) contact, and a liquid gate that is biased either through an external reference electrode immersed in the liquid under test, or an on-chip reference electrode. There are many different ways to bias our sensors, the most common one is what we call *front-gate operation*. In this method, we ground the source contact, while we apply a fixed voltage to the drain and the back-gate contacts, and we sweep the reference voltage in a defined voltage range, as shown in the schematic in Figure 3.14a. By imposing those bias conditions we can record the transfer characteristic  $I_D-V_{REF}$  while the sensor gate is in contact with different liquids under test (LUTs). The composition of the liquid, i.e. ions' concentration, pH, proteins' concentrations, or its physical properties, i.e. temperature, can change the surface equilibrium of the oxide surface, which can be translated in the equations as a threshold voltage change. This change brings a measurable shift in the transfer characteristic curves, which can be related to a specific analyte concentration in solution if the surface is properly functionalized. In the simplest case study of pH variations, it is possible to link the threshold voltage shift ( $\Delta V_T$ ) with the pH change ( $\Delta pH$ ) through the equation [196]:

$$\Delta V_T = 2.3 \frac{k_B T}{q} \Delta pH \quad (3.2)$$

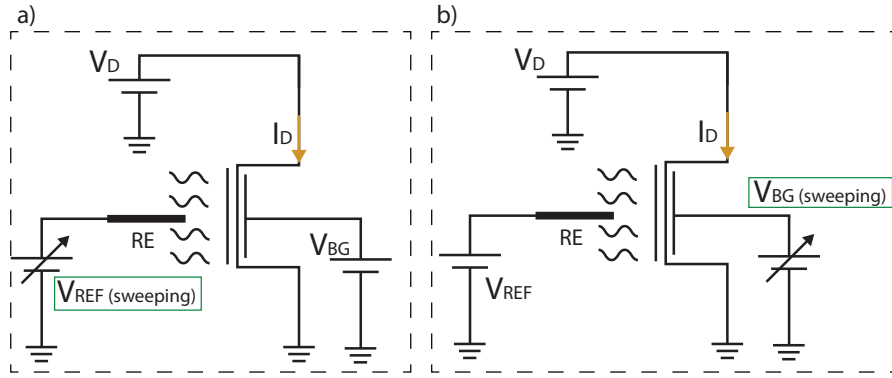


**Figure 3.14:** a) Front-gate and b) back-gate operation schematics.

where  $k_B$  is the Boltzmann constant,  $T$  is the temperature expressed in Kelvin, and  $q$  is the elementary charge. According to theory, and the previous equation, the maximum theoretical voltage shift with an ISFET system is 59mV/pH.

A similar sensor's characterization technique is achieved by applying a fixed reference voltage, and not sweeping it between two values, to record the drain current over time. When the chemical or physical conditions of the liquid under test change, the output drain current changes accordingly to the input stimulus. By recording the current change it is possible to measure the intensity of the stimulus at the input, whether it is a change in the analyte concentrations or a temperature change. In the case of pH monitoring, the current shift ( $\Delta I_D$ ) is related to the pH change ( $\Delta pH$ ) by the following equation [139]:

$$\Delta I_D = g_m 2.3 \frac{k_B T}{q} \Delta pH \quad (3.3)$$

where  $g_m$  is the transconductance of the transistor. We can immediately notice that the output current shift strongly depends on the working regime of the transistor. In our experiments, we exploited both the explained methods in front-gate operation: an example of the monitoring of threshold voltage shift is shown in Figure 4.1, while real-time current monitoring with applied constant bias is shown in Figure 4.3, with the correlated calibration curves.

### 3.3.3 Double-gate operation

Field Effect Transistors fabricated on SOI substrates have the intrinsic property to offer a second mechanism to control the carriers density in the conductive channel: in fact, the presence of a  $\text{SiO}_2$  BOX offers access to a second MOS capacitor structure, that can be gated by a voltage applied to the bulk of the transistor, as shown in Figure 3.15. We can consider the silicon body as a fourth terminal, where we could apply a voltage to modulate the channel

electrical properties thanks to the  $\text{SiO}_2$  back-oxide to channel capacitive coupling. Thanks to this structure we can gain a signal enhancement in the sensor's response. Indeed, the electron carrier density in the transistor's channel can be modulated by both the top and bottom gates. As we have previously defined, we can perform a quantitative analysis of a sensor's pH response by analyzing the voltage shift needed on one of the two gates to restore the drain current value upon a unit change of pH in the solution. Since both gates in a double-gate structure can influence the current flowing in the channel, we can define two different pH responsivities, one for the top gate and one for the bottom gate. In this paragraph, we explain why these two differ from each other.

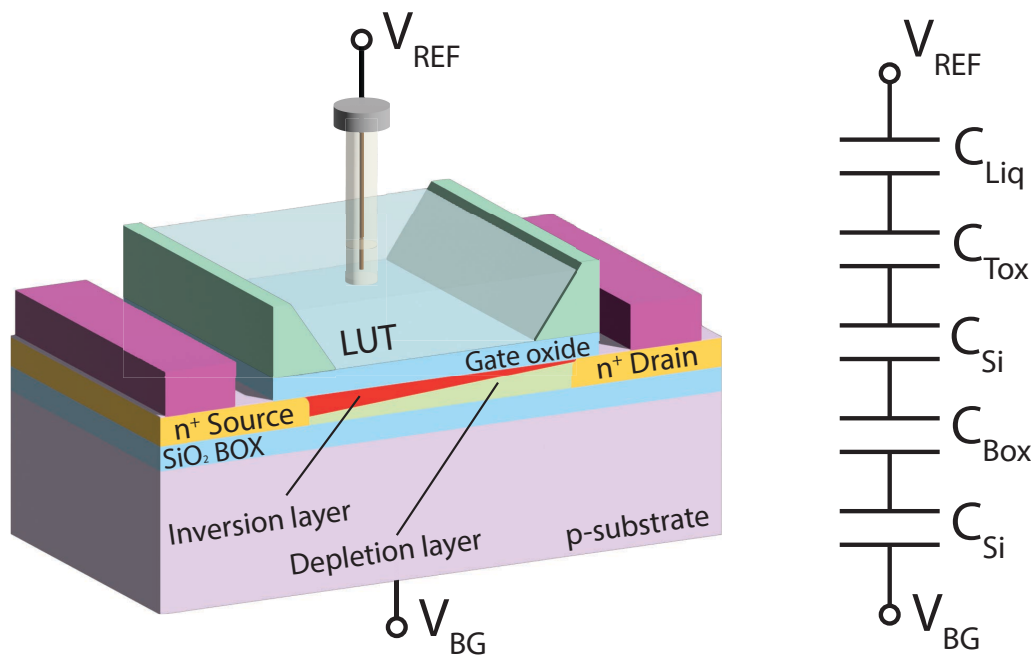


**Figure 3.15:** Dual-gate Silicon on Insulator Fully-Depleted Transistor schematic and capacitive stack representation.

The dual-gate field-effect transistor (DG-FET) typically utilizes the secondary gate as a biasing or supporting gate. However, in our application, we take advantage of it to overcome the Nernst limitation in ion-sensitive field-effect transistors. Let's consider the example of pH sensing: when the top gate oxide is exposed to a liquid with varying pH, the shift in the liquid's acidity can be measured by monitoring the threshold voltage shift during the transfer characteristic recording while sweeping the top gate. During this operation, the back-gate voltage remains constant to optimally bias the transistor in the desired operating region, which supports the top gate's operation.

We can also swap the gate roles by maintaining the voltage on the reference electrode constant (which biases the liquid on top of the top gate) and sweeping the back gate to record the bottom transfer characteristic. The biasing conditions are reported in the schematic in Figure

3.14b: the reference voltage, such as the source and drain voltages are kept constant, while the back-gate voltage is swept between two values, to record the  $I_D$ - $V_{BG}$  back-gate transfer characteristic. A change in pH or any desired analyte concentration in the liquid under test would cause a threshold voltage shift that could be detected during the back-gate voltage sweep characteristics. The interesting outcome is that the threshold voltage shift for the top and bottom gate sweeps is different due to the differences between the top-gate oxide and the bottom-gate oxide.

This concept has been demonstrated and described in previous works, such as [197, 198, 128, 129, 199, 125, 200]. Ahn et al. [139] used a theoretical approach to explain the nature of this amplification by simulating the occurring amplification in dual-gate FET-based biosensors, while [201] performed simulations to confirm the origin of the amplification effect, and specified the transistor working regimes where the dual gate configuration would bring the best advantages in terms of sensitivity and signal to noise ratio enhancement.

When we operate the double gate FET by sweeping the front gate (through the reference electrode immersed in the solution in contact with the gate oxide) and we fix the voltage on the back-gate, we can define the corresponding pH sensitivity as the change in gate voltage ( $\Delta V_G$ ) necessary to maintain a constant drain current after a change in pH ( $\Delta pH$ ). While the reference voltage (and thus the liquid potential) is kept constant by applying a constant reference voltage, and we sweep the back-gate voltage to acquire the back-gate transfer characteristic, any pH variation at the level of the sensing top oxide would create a current change in the transistor. Since the current is kept constant, there should be compensation on the bottom gate side, to maintain the total channel conductance change equal to zero. The back-gate voltage shift ( $\Delta V_{BG}$ ) necessary to keep a constant drain current after a pH shift  $\Delta pH$  defines the back-gate sensitivity of our DG-FET operated in back-gate configuration.

The sensitivity boost in back-gate sweeping derives from the asymmetry of the two gate oxides. More precisely, as already demonstrated in previous works [201, 139], we can write:

$$\frac{\Delta V_{BG}}{\Delta pH} = \gamma \frac{\Delta V_{REF}}{\Delta pH} \frac{C_{Tox}}{C_{Box}} \quad (3.4)$$

where  $\gamma$  is a multiplication factor that depends on the operating region of the transistor,  $C_{Tox}$  and  $C_{Box}$  are respectively the top and bottom gate oxide capacitances. The detailed description of the role of the parameter  $\gamma$  is extensively discussed in previous works [201, 139]. The signal-to-noise ratio (SNR) could be easily enhanced while operating the transistor in back-gate configuration, and after proving the ability of our system to overcome the Nernstian limit for pH sensitivity (section 4.1.1), we exploit the dual gate configuration to successfully detect CRP concentration shift in 0.1xPBS buffer, as described later in section 5.1.

We summarize the methods described so far in Table 3.3, together with the amplification

Method	Sensing parameter	Equation	Amplification factor
Front Gate sweeping	$\Delta V_{T,FG}$	$\Delta V_{T,FG} = 2.3 \frac{k_B T}{q} \Delta pH$	-
Constant Voltage	$\Delta I_D$	$\Delta I_D = g_{m,LG} \Delta V_{T,BG}$	$g_{m,LG}$
Back-gate sweeping	$\Delta V_{T,BG}$	$\Delta V_{T,BG} = \gamma \frac{C_{Tox}}{C_{Box}} \Delta V_{T,FG}$	$\gamma C_{Tox} / C_{Box}$

**Table 3.3:** Different electrical methods employed for pH and CRP sensing. For each method, we indicate the sensing parameter, the involved equation, and the amplification factor.

factors (in the case of pH sensing for the sake of simplicity).

### 3.3.4 Constant Drain current operation

In this section, we will describe the third method that we utilized to detect pH and CRP with our system. This technique is referred to as *constant drain current operation* because it involves injecting a constant current into the drain of the field-effect transistor, while both the front gate and the back gate are biased with a constant voltage. The drain voltage is taken as the output of the system, and its evolution is monitored over time. The bias conditions of the system are shown in Figure 3.16: the reference voltage is kept constant through an Ag/AgCl reference electrode immersed in the solution under test in contact with the transistor's gate oxide, while the source and the bulk are grounded and a constant current is injected in the drain. The voltage output is read at the drain terminal of the transistor, and its value is measured over time.

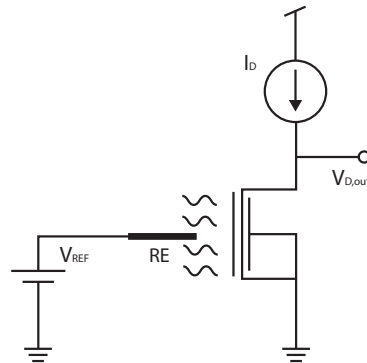


**Figure 3.16:** Constant drain current operation schematic: the liquid potential is fixed through a reference electrode immersed in the solution, as well as the source and back-gate voltages. The drain current is forced to be constant at a selected value, and the drain voltage is taken as the output signal.

As already extensively discussed, the value of the applied reference voltage controls the amount of inversion charge in the nanowires' silicon channels, thus dictating the working regime, i.e. weak, moderate, or strong inversion. Similarly, the operation region of the transistor is controlled by the drain to source voltage drop and can be linear, triode, or saturation. As discussed below, the behavior of the sensor, including its sensitivity, stability, and power consumption, is greatly influenced by the channel inversion conditions and the operation region. By operating the sensors in constant current mode, we can vary the applied reference voltage and drain current to reproduce various sensor behaviors within a single system. This allows us to create either a threshold sensor that can detect even minimal changes in analyte



concentration, as well as a highly sensitive sensor that can operate over a broad concentration range.

In the following section, we will present a step-by-step analysis of the study we conducted to understand the capabilities of this method, by using our system as a pH sensor. It is well-established that the gate (and back-gate) voltage modulates the density of carriers in the transistor's channel, which in turn affects the current flowing through it. When the applied gate voltage is lower than the transistor's threshold voltage ( $V_G < V_T$ ), the MOSFET operates in the subthreshold regime (or weak inversion). By increasing the voltage applied to the gate, we can transition from weak to moderate inversion and then to strong inversion. We will show that the calibration curves obtained with this method can significantly vary depending on the applied bias. Moving from weak to moderate or strong inversion or from the triode to saturation operation region can transform our sensor from a threshold sensor to a highly sensitive continuous detector of analyte concentration shifts in the solution under test. It is important to note that the drain current has an exponential dependence on the gate voltage while working in the subthreshold regime and a quadratic behavior when moving to strong inversion. Another crucial bias voltage that regulates the current flowing through the channel is the drain voltage. There are two working regions when it comes to drain voltage: the triode region (when  $V_G - V_T < V_{DS}$ ) and saturation one ( $V_G - V_T > V_{DS}$ ). The behavior of the output signal when operating our sensor in constant drain current mode depends heavily on which region the transistor is operating in. At times, after a pH change or a shift in analyte concentration, the sensor can shift from one working regime to another, resulting in a significant non-linearity in the sensor's readings.

To overcome this limitation, we calibrate the sensor with calibration solutions, which we then use to create a look-up table for future readings. In the following section, we present the preliminary results obtained while studying this method exploiting our system as a pH sensor, by testing the sensor with five pH solutions, ranging from 6.6 to 7.8. We aim to explain the system and demonstrate how to better utilize it.

### Weak Inversion

By analyzing the sensor's behavior in weak inversion, we concluded that we can utilize the sensor mainly as a threshold detector, or as a highly sensitive system in a very short concentration range. We bias the sensor with a reference voltage  $V_{REF} = 0.2$  V,  $V_S = V_{BG} = 0$  V, and a drain current of 1 nA. The bias point corresponds to the red dot on the  $I_D$ - $V_D$  output characteristic in Figure 3.17a.

The different output current regions of the sensor are highlighted with various background colors: in red we highlight the triode region, in white the saturation region, and in green the region of breakdown. Five different pH solutions are presented to the sensor's gate oxide, with small values steps. The real-time trace is reported in Figure 3.17b, where we can follow the output drain voltage over time. The sensor responds with relatively small and non-linearly

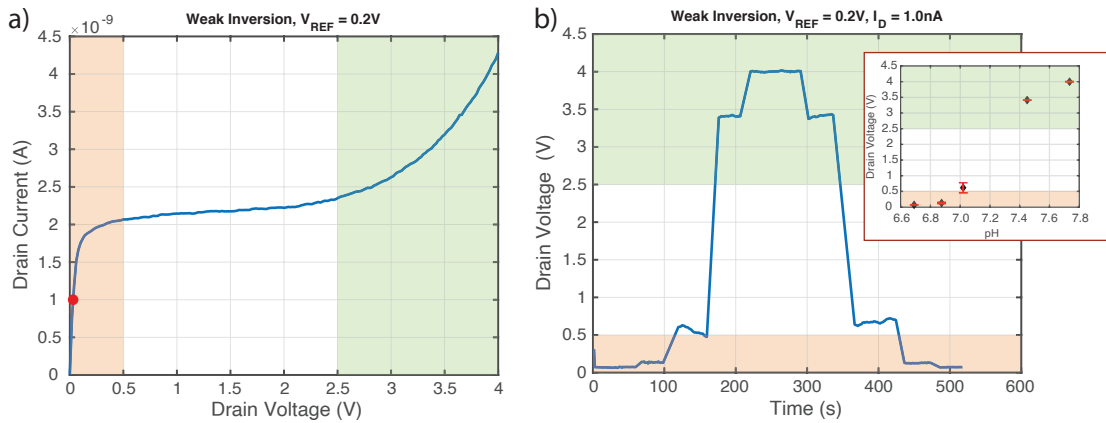


**Figure 3.17:** a)  $I_D$ - $V_D$  output curve recorded at the lowest tested pH while applying  $V_{REF} = 0.2$  V,  $V_S = V_{BG} = 0$  V, thus in weak inversion condition. The red marker indicates the starting bias point of  $I_D = 1$  nA for the constant drain current operation. b) Output drain voltage variation over time upon different pH injections. The inset shows the calibration curves extracted from the real-time trace.

spaced voltage steps for the first three pH values, but there is a significant change in the output drain voltage of more than 2 V when moving to the fourth pH value. This indicates that while working in weak inversion and with a fixed drain current of 1 nA, only a small pH variation is required to move from the triode region to the saturation region. When the drain voltage 'lands' in the breakdown region, the change in pH creates a lower shift in drain voltage, thanks to the ability of the sensor to compensate for it with a lower drain voltage shift. Indeed, the saturation region extends only from  $V_D = 0.5$  V to 2.5 V (Figure 3.17a). This brings the sensor to operate in the saturation region for a very narrow pH range, which we were not able to capture with our standard solutions, as seen in Figure 3.17b. The inset of Figure 3.17b reports the calibration curve after the drift correction of the real-time trace. In summary, the sensor operating in weak inversion mode exhibits high sensitivity as it approaches the saturation region, making it suitable for use as a threshold sensor in most applications.

### Moderate Inversion

The next analyzed region is the so-called moderate inversion. We fix the carriers concentration in the channel by biasing the liquid gate with a  $V_{REF} = 0.5$  V, a source voltage, and a back-gate voltage of 0 V. We studied three different constant drain currents: 700 nA, 800 nA and 870 nA. As we will shortly explain, in the first case we can exploit our sensor as a threshold detector, very similar to the weak inversion case, while when we apply 800 nA or 870 nA we place our starting point on the edge of the saturation region. The results obtained in the first case are shown in Figure 3.18: after the first three pH values the output drain voltage experiences a large shift (as in the weak inversion case). This case shows a similar behavior to the weak inversion one, but we obtain a more stable and repeatable response, affected by a lower variability.

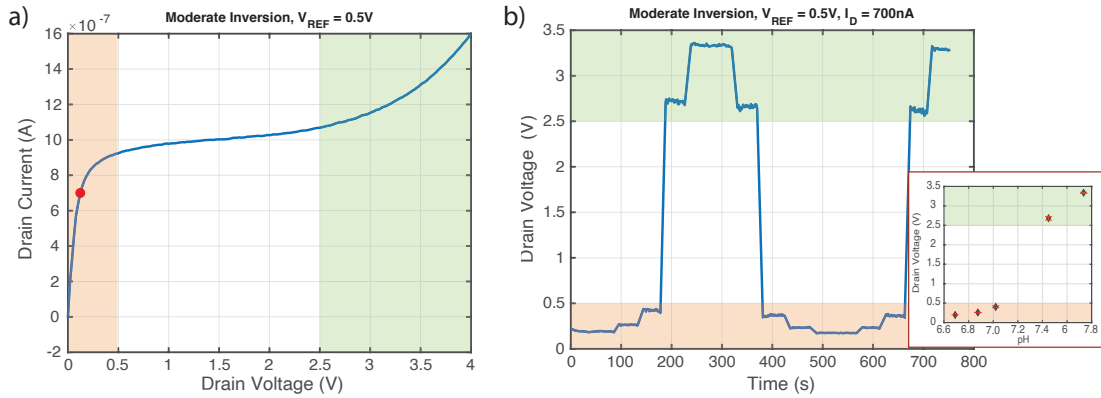


**Figure 3.18:** a)  $I_D$ - $V_D$  output curve recorded at the lowest tested pH while applying  $V_{REF} = 0.5$  V,  $V_S = V_{BG} = 0$  V, thus in moderate inversion condition. The red marker indicates the starting bias point of  $I_D = 700$  nA for the constant drain current operation. b) Output drain voltage variation over time upon different pH injections. The inset shows the calibration curves extracted from the real-time trace.

When we increase the forced drain current to 800 nA (for the lowest pH value), we place the starting point close to the edge saturation window (Figure 3.19a). This allows us to exploit the saturation region for the first pH values, obtaining a huge sensitivity for this pH range. As shown in the inset of Figure 3.19b the sensor response is highly non-linear, but with a linear region when the values of the drain voltage land in the saturation operation regime.

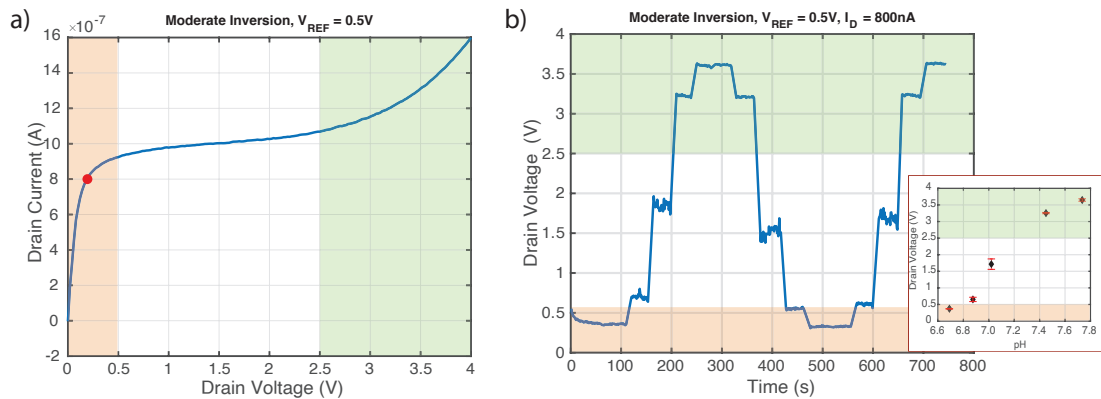


**Figure 3.19:** a)  $I_D$ - $V_D$  output curve recorded at the lowest tested pH while applying  $V_{REF} = 0.5$  V,  $V_S = V_{BG} = 0$  V, thus in moderate inversion condition. The red marker indicates the starting bias point of  $I_D = 800$  nA for the constant drain current operation. b) Output drain voltage variation over time upon different pH injections. The inset shows the calibration curves extracted from the real-time trace.

By applying a current of 870 nA to bias the sensor, we can utilize it primarily in the breakdown region, which is illustrated in Figure 3.20. Although the shift in drain voltage remains substantial, the absolute values are greater than they were previously. It is important to note that the sensor's behavior depicted in the figure is limited to five specific pH values, and the optimal

working region can be determined for each of these values. In an actual sensor, multiple look-up tables for each working condition and various pH ranges would be required. One interesting concept is to combine this sensor with a less sensitive pH sensor to first determine the pH of the liquid being tested with low accuracy, then proceed to a more precise real-time measurement using the more sensitive system.

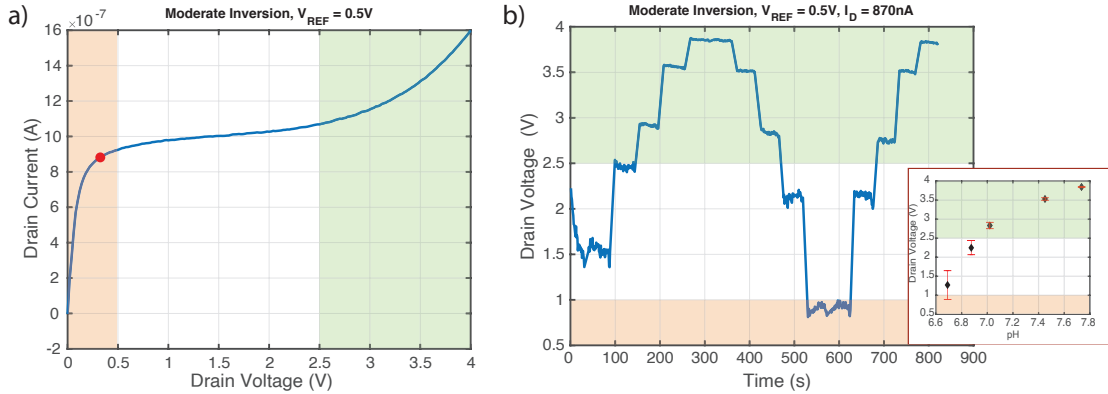


**Figure 3.20:** a)  $I_D$ - $V_D$  output curve recorded at the lowest tested pH while applying  $V_{REF} = 0.5$  V,  $V_S = V_{BG} = 0$  V, thus in moderate inversion condition. The red marker indicates the starting bias point of  $I_D = 870$  nA for the constant drain current operation. b) Output drain voltage variation over time upon different pH injections. The inset shows the calibration curves extracted from the real-time trace.

### Strong Inversion

When the sensor is biased in strong inversion conditions, it produces a quasi-linear calibration curve in the largest pH range. As shown in Figure 3.21a, the different regions possess the largest drain voltage ranges in the  $I_D$ - $V_D$  output characteristic. Furthermore, the breakdown region is not prominent in the examined drain voltage range, allowing us to utilize the triode region or saturation region to the fullest extent.

By utilizing a drain current of  $2 \mu A$ , a  $V_S = V_{BG} = 0$  V, and a reference voltage of  $V_{REF} = 1.0$  V, we can entirely exploit the triode region (Figure 3.21b). Throughout the entire pH range variation, we stay within this region, resulting in a quadratic calibration curve (inset of 3.21b). This configuration yields a lower relative drain voltage change compared to the aforementioned cases, but ensures the most reliable response for a broader pH range, preventing response saturation. This setup could be utilized as the initial measurement stage before proceeding to a more accurate pH measurement using one of the above-mentioned configurations.

Modifying the drain bias from  $20 \mu A$  to  $22.5 \mu A$  causes a complete alteration in the sensor's response to the identical pH range. In this situation, the saturation region is fully utilized, as demonstrated in Figure 3.22b, resulting in a nearly linear calibration curve with a  $2$  V/pH sensitivity. The sensor's response in this region is also the most straightforward to model. When operating in saturation the transistor's channel experience the so-called channel length

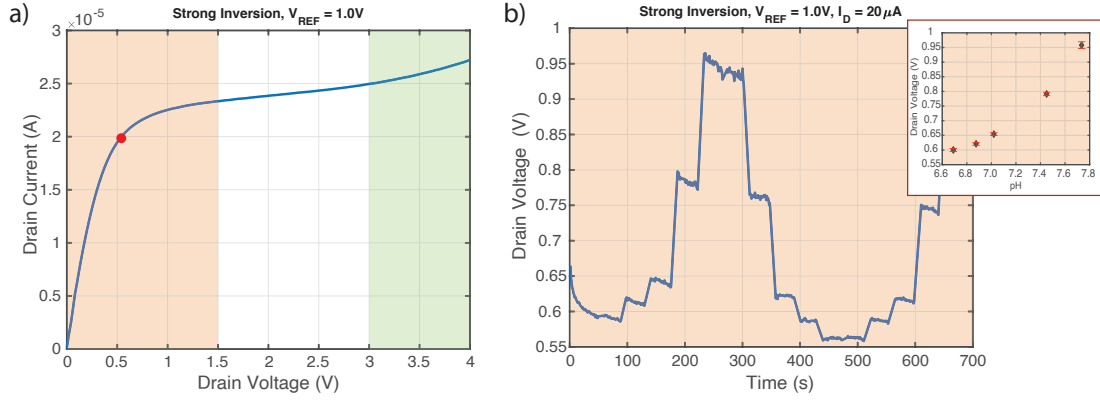


**Figure 3.21:** a)  $I_D$ - $V_D$  output curve recorded at the lowest tested pH while applying  $V_{REF} = 1.0$  V,  $V_S = V_{BG} = 0$  V, thus in moderate inversion condition. The red marker indicates the starting bias point of  $I_D = 20$   $\mu$ A for the constant drain current operation. b) Output drain voltage variation over time upon different pH injections. The inset shows the calibration curves extracted from the real-time trace.

modulation (CLM) effect: by increasing the drain voltage the effective channel length shortens, causing a current increase following the equation [202]:

$$I_D = \mu_n \frac{1}{2} C_{ox} \left( \frac{W}{L - \Delta L} \right) (V_G - V_T)^2 \quad (3.5)$$

where  $\Delta L$  is the change in channel length. Considering  $\Delta L \ll L$ , by reorganizing the equation and exploiting the first-order Taylor expansion we can write:

$$I_D = \mu_n \frac{1}{2} C_{ox} \left( \frac{W}{L} \right) (V_G - V_T)^2 (1 + \lambda V_{DS}) \quad (3.6)$$

where  $\lambda$  is a technology parameter expressed in  $V^{-1}$  that indicates the strength of the channel modulation effect.

In the presence of a pH shift in a solution ( $\Delta pH$ ), the perturbation on the oxide surface is compensated by a modification in channel conductance (or carrier density). In our specific use case, the drain current flowing in the channel is kept constant, therefore, to compensate for the change in conductance, the drain voltage automatically adjusts itself. If we want to relate the drain voltage shift as a consequence of a pH change in solution, we can write the following equation:

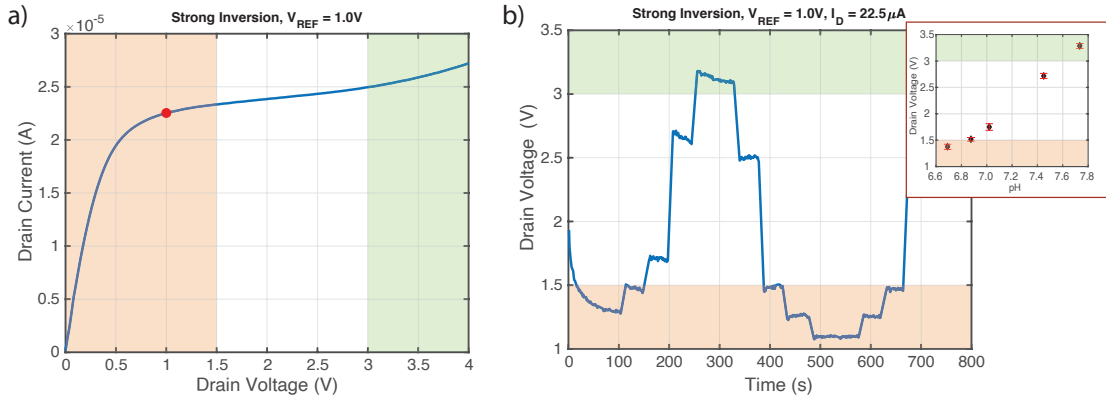


**Figure 3.22:** a)  $I_D$ - $V_D$  output curve recorded at the lowest tested pH while applying  $V_{REF} = 1.0$  V,  $V_S = V_{BG} = 0$  V, thus in moderate inversion condition. The red marker indicates the starting bias point of  $I_D = 22.5 \mu\text{A}$  for the constant drain current operation. b) Output drain voltage variation over time upon different pH injections. The inset shows the calibration curves extracted from the real-time trace.

$$\frac{\Delta V_D}{\Delta pH} = \frac{\Delta V_G}{\Delta pH} \frac{\Delta I_D}{\Delta V_G} \frac{\Delta V_D}{\Delta I_D} \quad (3.7)$$

In the ideal case, the first factor of the right half of the equation corresponds to the threshold shift due to a pH variation, and we already know this corresponds to 59.5 mV/pH. The second term can be related to the transistor's transconductance: by biasing the transistor with a fixed reference voltage, we can approximate  $g_m$  as a constant value. Any pH change would create a small signal perturbation on the gate oxide. The last term of the equation is more complicated. In the case of small signal analysis, this would reduce to the well-known transistor output resistance  $r_0 = (\lambda I_D)^{-1}$ , but here the change of drain voltage is too large to be considered as a small signal. In the case of strong inversion and saturation, we can still consider this parameter as a constant, since the  $I_D$ - $V_D$  has a linear behavior (thus the slope is constant) and we force a constant drain current. The previous equation can be written as:

$$\frac{\Delta V_D}{\Delta pH} = \beta g_m \frac{1}{\lambda I_D} \quad (3.8)$$

corresponding to the sensitivity of our sensor while working in strong inversion and saturation.  $\beta$  corresponds to the top-gate pH sensitivity (59.5 mV/pH in the ideal case). The last four data points collected in saturation and strong inversion are plotted in Figure 3.23, together with a linear model extracted by using the previous equation as the slope of the line. The good fit of the model with the data point indicates the correctness of our findings.

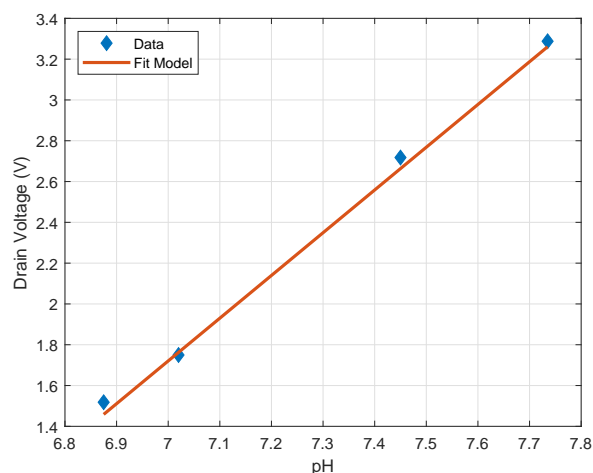


**Figure 3.23:** Obtained results in constant current operation and strong inversion regime with proposed model fit. Data points represent the four drain voltage values obtained for the four highest pH while operating the transistor in strong inversion and biasing with a drain current of  $22.5 \mu\text{A}$ . The continuous line represents the proposed model valid only for this working regime.

We achieved a good agreement between the fit and the model. For other working regions, the modeling results are more complicated since the third term of the equation can not be considered constant, but it is very dependent on the same output voltage  $V_D$ .

### Comparison of the working regimes

To select the working regime that best suits the necessity of high sensitivity and low limit of detection of our protein biosensor, we challenged a sensor with a higher number of pH solutions, with a finer step between two consecutive values. To carry out this study we selected the saturation region for all the working regimes (weak, moderate, and strong inversion) because it intuitively offers higher sensitivity, as demonstrated in Figure 3.24a. In this plot, five different  $I_D$ - $V_D$  curves are reported at different pH, when the same source, back-gate, and reference voltage are applied: fixing a drain current, we could intersect the reported curve and extract the corresponding drain voltage values. It is clear that the biggest shifts are obtained when working in saturation, and that is the reason behind our choice.

To study the different behaviors of the sensors in saturation and in the three different channel inversion regimes, we exploited 11 solutions, with a pH between 6.6 and 8, as reported in Figure 3.24b.

From the obtained results we can conclude that the weak inversion regime offers the highest sensitivity in a narrower pH range, while the strong inversion shows the lowest drain voltage shift, but for the largest pH range. The moderate inversion is a good trade-off between the two

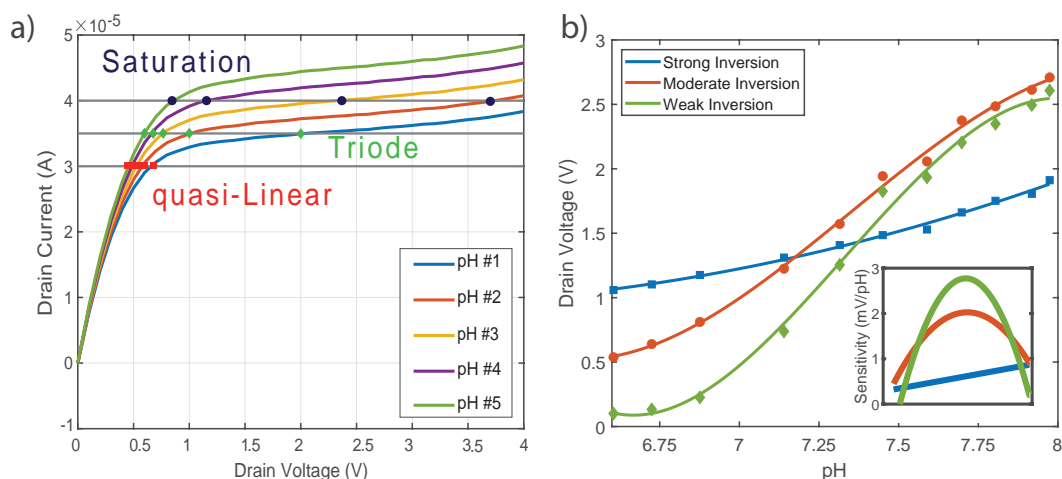


**Figure 3.24:** Constant-current method sensitivity in different working regimes. a) Different drain voltage shifts at different constant current values, for various pH levels. b) pH response in constant-current bias in the three different working regimes.

other regimes: it offers a quasi-linear sensitivity for a useful concentration range. Moreover, we repeatedly experience a lower sensor's stability while operating in weak inversion regime, thus for the experiment presented in Chapter 4 and Chapter 5 we will mainly exploit a sensor working in moderate inversion regime because it offers the best trade-off between sensitivity, linearity, and stability.

### 3.4 Summary

This chapter lays the foundation for the introduction of the next chapter by presenting the results of a proposed protocol for the functionalization of the gate hafnium dioxide surface of SiNW arrays sensors to detect C-Reactive Protein (CRP) in ionic solutions. Additionally, various methods used for the electrical detection of these species are introduced.

Our research demonstrates the successful use of silanization chemistry on high- $\kappa$  oxides, such as  $\text{HfO}_2$ , for the covalent immobilization of chosen anti-CRP Fab fragments. Through SPR analysis, we were able to show that these fragments can selectively detect CRP in both buffer and ISF-like solutions within a physiological concentration range of  $0.05 \mu\text{g/mL}$  to  $25 \mu\text{g/mL}$ . We also used XPS to prove that our protocol can immobilize antibody fragments on  $\text{HfO}_2$  surfaces, as has been demonstrated previously on  $\text{SiO}_2$ . Additionally, we used QCM analysis to demonstrate the importance of the APTES layer in our functionalization, which reduces the temporal drift in our sensor and extends the detected concentration range. Moreover, QCM analysis proved that anti-cTnI F(ab)<sub>2</sub> fragments are a good candidate for the functionalization of the reference sensor in a reference-compensated configuration. We described the implementation of the latter, along with its advantages, before moving to the detailed description of the three electrical detection methods implemented in the next chapter to monitor pH and



detect CRP.

In the second part of this chapter, we have introduced the electrical characterization methods that will be employed for pH and CRP monitoring, in Chapter 4 and Chapter 5, respectively. We detailed the necessary bias conditions for each method, and we will explore their capabilities in the next sections. The standard front-gate operation offers an easy option to monitor analyte changes in solution, but it is limited to a maximum sensitivity of 59.5 mV/decade when the threshold voltage shift is taken as output quantity. Instead, when the bias reference voltage is kept constant, the drain current could be monitored over time, and the maximum shift in the output current upon analyte concentration change in solution is strictly linked to the transconductance of the transducer. The double-gate intrinsic structure of the SOI system allows operating the transistor by sweeping the back-gate voltage and recording the back-gate threshold voltage shift as output quantity. Thanks to the asymmetry between the top and bottom gate oxides, an internal amplification factor (proportional to the ratio between the two capacitance values) can enhance the threshold shift upon changes in the analyte concentration. This effect will be exploited both for pH and CRP sensing in the following chapters. The main drawback of this configuration is the more complicated necessary read-out. Lastly, we introduced a novel method called "constant current operation" that holds great potential for achieving significant sensitivity in protein detection. This method offers the advantage of providing a pure voltage output, exhibiting substantial voltage changes within the millivolt range in response to even very small concentration changes. The utilization of this configuration could lead to the development of a simpler read-out circuit, along with a higher amplification factor and an improved signal-to-noise ratio. Notably, the sensitivity of the system can be easily controlled by adjusting the bias conditions. Operating in the weak inversion regime offers high sensitivity but within a limited concentration range, while strong inversion reduces sensitivity but expands the detectable concentration range. By operating in the moderate inversion regime, an optimal trade-off can be achieved, striking a balance between the two.

A performance comparison in CRP detection capabilities of the three different methods will be provided in Chapter 5.

## 4 pH sensing

*In the previous chapter the employed microfluidics and PCB, together with the electrical methods employed in this work are explained in detail to understand the advantages of each. In this chapter, we present the main results of our research on monitoring pH using the developed SiNWs sensor platforms described in Chapter 2. Section 4.1.1 showcases the outcomes of our pH monitoring experiments conducted in both static conditions and real-time employing PBS buffer and CEA-LETI chips. Furthermore, in Section 4.1.3, we present the results achieved with chips fabricated in-house for pH monitoring under similar conditions. This section provides insights into the performance and characteristics of the in-house fabricated chips about pH monitoring. Additionally, in Section 4.1.2, we explore the capabilities of our sensor platform to measure pH values in ISF-like solutions, following careful calibration using human serum samples. This section highlights the potential of our sensor in real-world applications involving ISF analysis. Finally, in Section 4.2, we discuss the initial attempts to interface our pH sensor with the multi-modal on-chip read-out system developed by imec, Belgium. We present a detailed description of the measurement setup and the interfacing board, along with the primary experimental findings and conclusions derived from this exploration.*

### 4.1 pH monitoring

In this study, we have utilized pH measurement in various fluids to showcase the potential of our system before transitioning to protein detection. The significance of maintaining a balanced pH in the interstitial fluid cannot be overstated, as evidenced by numerous medical studies. In situations of poor oxygen supply, intracellular fluid environments tend to exhibit higher levels of acidity, resulting in lower pH values [41]. To maintain an optimal intracellular metabolism, it is crucial to maintain an optimal pH value. Consequently, any acid produced in the intracellular space is extruded into the interstitial fluid. Monitoring pH levels in ISF is thus critical for detecting various illnesses. Furthermore, it is important to note that monitoring pH values in other fluids such as blood and urine can also provide useful insights into the overall health and potential diseases of a patient.

We can divide the performed experiments for pH monitoring and the obtained results into three groups, based on three families of tested sensors:

- A first batch of SiNW arrays fabricated by CEA-LETI;
- A second batch of SiNW arrays fabricated by CEA-LETI;
- A batch of SiNW arrays fabricated at EPFL.

Initially, we conducted experiments by measuring significant pH shifts in buffers with predetermined pH levels. These experiments were conducted to demonstrate the efficacy of our system in detecting pH changes. Following this, we transitioned to monitoring smaller pH changes in both buffers and more complex matrices, such as 3-fold diluted human serum collected from diverse individuals. This approach allowed us to assess the performance of our system under more realistic conditions, and it proved successful in detecting pH variations in complex biological fluids. In the following paragraphs, we present the different performed studies and the related results.

#### 4.1.1 pH monitoring in buffer

The first experiments are carried out in front-gate operation, as described in 3.3.2. Figures 4.1-4.3 show the results obtained with the first batch of CEA-LETI's chips. We tested five different pH values, ranging from a minimum value of 6.9 to a maximum of 8 (a range similar to the physiological one). Figure 4.1 shows the obtained results while the sensor is operated in front gate configuration: source and back-gate contact are maintained at 0 V, while a potential of 0.3 V is applied to the drain contact. The solution potential is swept from 0.5 V to 1.5 V through an Ag/AgCl electrode immersed in the solution under test in contact with the SiNWs gate oxide. In particular, Figure 4.1a shows the transfer characteristics recorded at different pH levels: to a pH increase corresponds a right-shift of the curve, indicating a positive shift of the threshold voltage ( $\Delta V_T > 0$ ). To quantify this shift, we arbitrarily fix a drain current in the weak inversion regime of the transistor, e.g. 80 pA, and we extract the correspondent reference voltage for the different curves at different pH values. The obtained data are plotted in Figure 4.1b: each data point represents the average of three measurements performed at the same pH value, while the error bars represent the standard deviation. As expected, the voltage shift shows a linear relation with the pH values, we thus perform a linear fit, to extract the sensitivity of the sensor in front-gate configuration, defined as

$$S = \frac{\delta V_{REF}}{\delta pH} \quad (4.1)$$

In our experiment, we obtain a sensitivity of 63 mV/pH, indicating a good quality of our sensor

that shows Nernstian pH sensitivity, thanks to the high- $\kappa$  HfO<sub>2</sub> gate oxide.

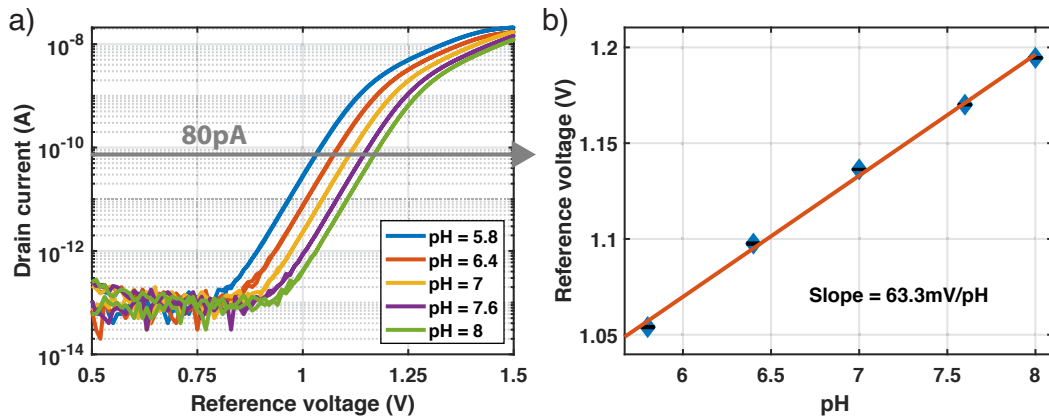


**Figure 4.1:** pH sensing in top-gate configuration with the first batch of CEA-LETI chips. Applied voltages are  $V_D = 0.3$  V,  $V_S = V_{BG} = 0$  V. The reference voltage is swept between 0.5 V and 1.5 V through an external Ag/AgCl reference electrode. a) Transfer characteristic curves acquired at different pH levels. It is possible to notice a right shift with the increase in pH. b) pH dose response extracted from (a) at  $I_D = 80$  pA. The obtained sensitivity reaches the Nernstian limit.

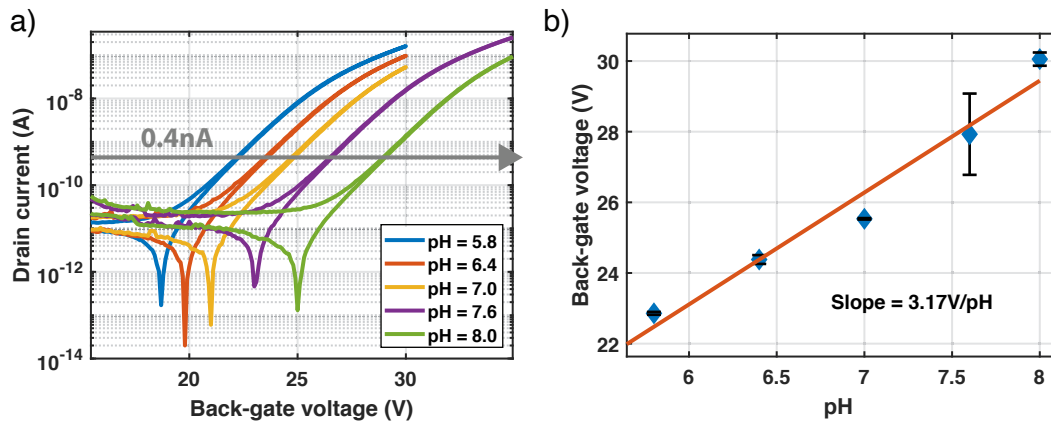


**Figure 4.2:** pH sensing in back-gate configuration with the first batch of CEA-LETI chips. Applied voltages are  $V_D = 0.3$ ,  $V_S = V_{REF} = 0$  V. The back-gate voltage is swept between 15 V and 35 V through the bulk silicon of the chip. a) Transfer characteristic curves acquired at different pH levels. It is possible to notice a right shift with the increase in pH. b) pH dose response extracted from (a) at  $I_D = 0.4$  nA. The obtained sensitivity is fifty times higher than the one in top-gate configuration.

The same sensor has been used in back-gate configuration, as explained in section 3.3.3, by exploiting the double gate structure of our system. The potential of the solution is kept constant by applying a fixed voltage to the Ag/AgCl reference electrode of 0 V, while  $V_{DS} = 0.3$  V. The back-gate voltage is swept through the silicon bulk between 15 V and 35 V. The high voltages are necessary due to the thick bottom silicon dioxide layer of the SOI structure. As in

the first experiment, the sensor top gate dielectric is put in contact with solutions with different pH, ranging from 5.8 to 8. Each pH value is measured three times, and Figure 4.2a reports one back-gate transfer characteristic for each pH value. During the data analysis process, we arbitrarily fix a drain current value of 0.4 nA, to extract the correspondent back-gate voltage values. The results are then reported against the pH level in Figure 4.2b, where each data point represents the average of three measurements, and the reported error bars represent the standard deviations. Also in this case we linearly fit the results, to obtain a sensitivity of 3.17 V/pH. This value exceeds the theoretical Nernst limit of 59.5 mV/pH, indicating an internal amplification mechanism that can achieve gain values higher than 50. A detailed explanation of the origin of this amplification is reported in Section 3.3.3.

The last experiment run with the first batch of CEA-LETI chips proves the ability of our sensor to measure pH change in buffer in real-time. Figure 4.3 shows the sensor response to pH changes in buffer while the SiNW array is biased with  $V_{BG} = V_S = 0$  V and  $V_{REF} = V_D = 0$  V. The sensor proves to be reliable and the expected reversed pyramid behavior (Figure 4.3a) for increasing and decreasing pH is obtained. The sensor shows a temporal drift, that can easily be subtracted in post-processing. By averaging the current values at different pH levels we obtained the linear calibration curve in Figure 4.3b: in these bias conditions the sensor shows a current sensitivity of -438 pA/pH.

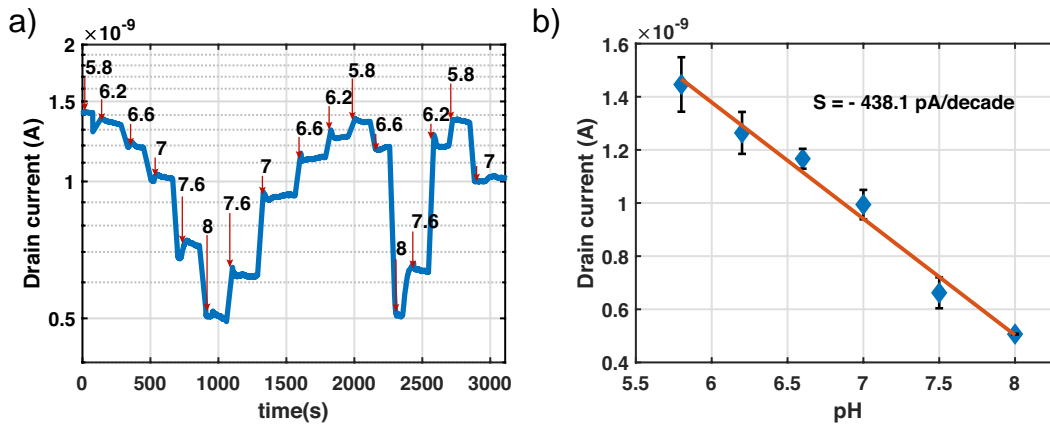


**Figure 4.3:** Real-time pH sensing in top-gate configuration with the first batch of CEA-LETI chips. Applied voltages are  $V_{REF} = V_D = 0.3$ ,  $V_S = V_{BG} = 0$  V. a) Real-time output drain current. The drain current shifts upon injections of different pH solutions. b) Drain current pH dose response extracted from (a).

#### 4.1.2 pH monitoring in ISF-like solutions

To study the behavior of our sensors in interstitial fluid we decided to exploit collected human serum and dilute the samples 3 times, in order to match protein concentrations similar to the one found in human ISF. For this round of experiments, chips from the second batch of the CEA-LETI chips have been utilized. Unfortunately, those chips do not show Nernstian sensitivity to pH changes, as shown later in this paragraph, but we were able to achieve a

maximum pH sensitivity of 45 mV/pH while working in front-gate configuration. This 'loss' of sensitivity compared to the first batch of sensors can be reconducted to the lower high- $\kappa$  front gate dielectric layer uniformity, as shown in the TEM cross-section image in Figure 4.4.

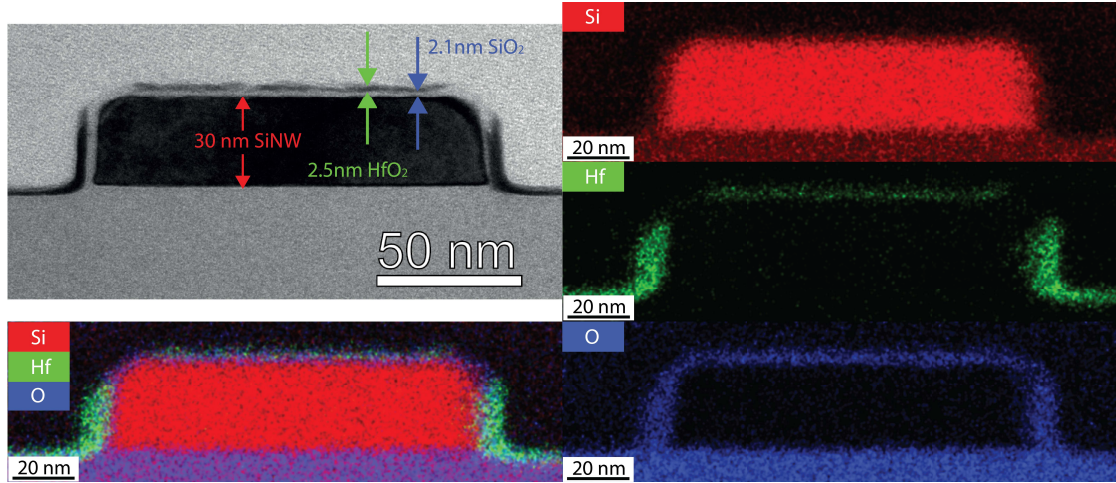


**Figure 4.4:** TEM image of one SiNW cross-section on the second batch of CEA-LETI chips. We notice a non-perfectly uniform  $\text{HfO}_2$  layer, that decreases the overall pH sensitivity of the system.

Moreover, with this second batch, we have not been able to perform measurements by sweeping the back-gate voltage in dual-gate configuration. All the tested chips were not properly responding to the sweeping of the voltage, making the reproduction of the previously obtained results impossible. This was one of the reasons that pushed our work to move towards our own designed and fabricated silicon nanowire arrays chip, described in detail in Section 2.3.

To study the pH response of our sensors in ISF solutions, we proceeded by comparing the experimental output of two main experiments: small pH variations ( $< 0.5$ ) were monitored both in buffer and in ISF-like solutions, to compare the sensitivity in different matrices. Moreover, the sensor has been calibrated with a serum matrix with adjusted pH and then tested with unknown samples. The readings of our sensor have been compared with the ones of a standard table pH meter.

Figure 4.5 reports the transfer characteristic curves of one nanowire array for different pH values, in 1xPBS buffer and MES buffer for the most acidic pH value. The solution potential is swept between -0.5 V and 1.5 V by applying a voltage to the external reference electrode immersed in the liquid under test. Source and back-gate voltage are kept constant at 0 V, while on the drain we applied a voltage of 0.5 V. In Figure 4.5a we show the transfer characteristics for five different pH values in a semi-logarithmic scale, to enhance the details of the weak inversion working regime. In the inset, it is possible to appreciate the very low sensor's hysteresis, since we reported both the forward and backward sweeps. Figure 4.5b represents the same curves, but on a linear scale, to enhance the strong inversion working regime. Also, in this case, the low hysteresis can be appreciated in the small plot inset. The same sensor is

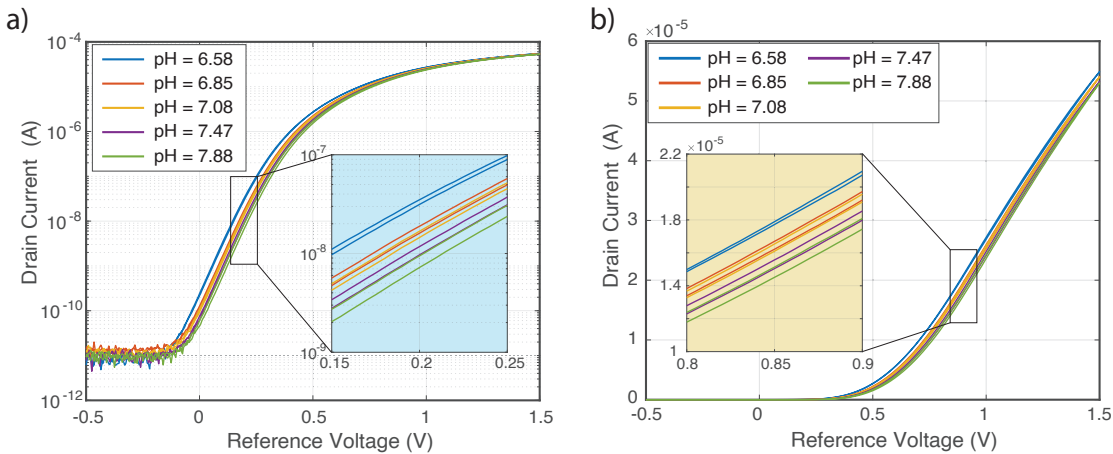


**Figure 4.5:** pH sensing in buffer solutions and in top-gate configuration with the second batch of CEA-LETI chips. Applied voltages are  $V_D = 0.5$ ,  $V_S = V_{BG} = 0$  V. The reference voltage is swept between  $-0.5$  V and  $1.5$  V through an external Ag/AgCl reference electrode. a) Transfer characteristic curves (in a semi-logarithmic scale to highlight the subthreshold region) acquired at different pH levels. It is possible to notice a right shift with the increase in pH. The zoomed inset shows low hysteresis between forward and backward traces. b) Transfer characteristic curves (in linear scale to highlight the strong inversion region) acquired at different pH levels. It is possible to notice a right shift with the increase in pH. The zoomed inset shows low hysteresis between forward and backward traces.

used for the second part of the experiment: a human serum matrix is diluted 3 times to mimic human ISF, and its pH is adjusted to five different values in a range similar to the one used in the first part of the experiment performed with buffer solutions. The sensor is then exposed to those five different ISF-like solutions, to measure the transfer characteristic of the transistor and the threshold voltage shift linked to the pH variations.

The results are reported in Figure 4.6a and 4.6b, in a semi-logarithmic and linear plot, respectively. It is immediately possible to notice some differences between these two plots and the ones obtained by measuring pH variation in buffer (Figure 4.5). The transistor's drain current ON/OFF ratio remains identical, with a value higher than five orders of magnitude, but when exposed to complex matrices as the used ISF-like solutions, the transistor shows a degraded subthreshold slope. This effect could be explained by the complex nature of the solutions under test: in human serum, there is an abundance of different species than ions, such as proteins and hormones. These components have a complex structure and can carry charges, or they can be polarized. These characteristics bring the formation of an additional capacitor on top of the gate dielectric, thus changing the coupling capabilities of the reference electrode in solution with the transistor's channel. As a consequence, the turn-on mechanism is affected, and a higher reference voltage change is needed to obtain the same drain current variation in the inverted channel of the transistor. It is worth noting that the hysteresis between the forward and the backward sweeps is not affected by the nature of the solutions under test. To compare the pH response in buffer and ISF, an arbitrary current of 10 nA is selected to extract

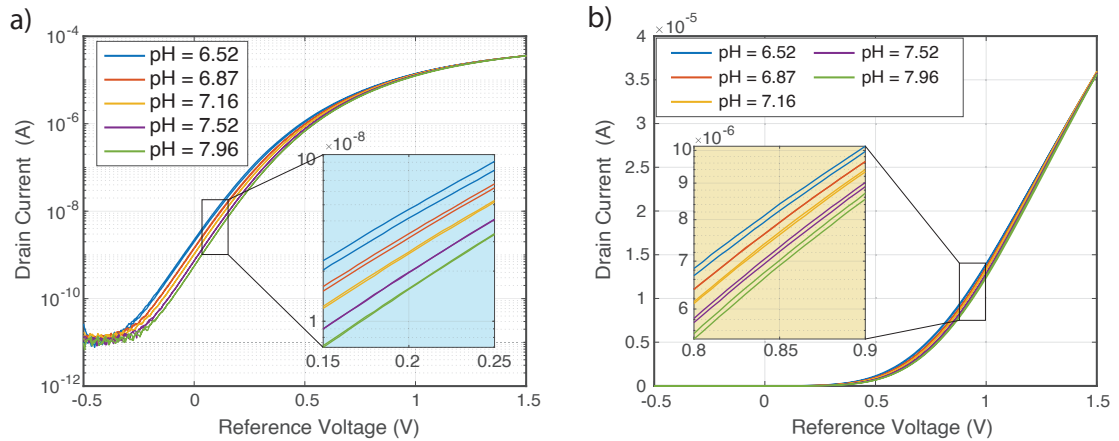


**Figure 4.6:** pH sensing in ISF-like solutions and in top-gate configuration with the second batch of CEA-LETI chips. Applied voltages are  $V_D = 0.5$ ,  $V_S = V_{BG} = 0$  V. The reference voltage is swept between  $-0.5$  V and  $1.5$  V through an external Ag/AgCl reference electrode. a) Transfer characteristic curves (in semi-logarithmic scale to highlight the subthreshold region) acquired at different pH levels. It is possible to notice a right shift with the increase in pH. The zoomed inset shows low hysteresis between forward and backward traces. b) Transfer characteristic curves (in linear scale to highlight the strong inversion region) acquired at different pH levels. It is possible to notice a right shift with the increase in pH. The zoomed inset shows low hysteresis between forward and backward traces.

the corresponding reference voltage values. This process is carried out for both experiments, the curves obtained in buffer and the ones in ISF-like solutions. The respective results are shown in Figure 4.7a and 4.7b. In both cases, the sensor shows a responsivity to pH variations: when operated in buffer the pH sensitivity is  $42$  mV/pH, while this value increases up to  $54$  mV/pH in human ISF-like solution (3-fold diluted human serum). The possible explanation for this sensitivity increase relies on the presence of complex structures in solution, that can enhance the pH variation, by changing the carried charges and increasing the variation of carrier concentration in the channel. Apart from the sensitivity difference, in both cases, the sensor shows huge reliability in measuring pH variations, with a linear relationship between the pH value and the reference voltage shift. To ensure the capabilities of our sensor, we need to prove that a different matrix, i.e. a human serum sample from a different patient, would not affect the pH response of our sensor.

To prove this claim we calibrated our sensor with the same serum matrix we used for the previous experiment, with adjusted pH. In particular, we run a pyramid calibration by cycling at least four times the same pH solution, while we keep the bias conditions constant: reference voltage is kept at  $0.1$  V, while  $V_{DS} = 0.5$  V and the back-gate is fixed at  $0$  V. We monitored the drain current variations in time, while different solutions with known pH were consecutively injected. The obtained results are shown in Figure 4.8a: the pyramidal behavior is clearly visible and repeatable, while it is possible to notice a slight temporal drift that can be corrected. Figure 4.8b shows the extracted average values plotted both against time (low x-axis) and



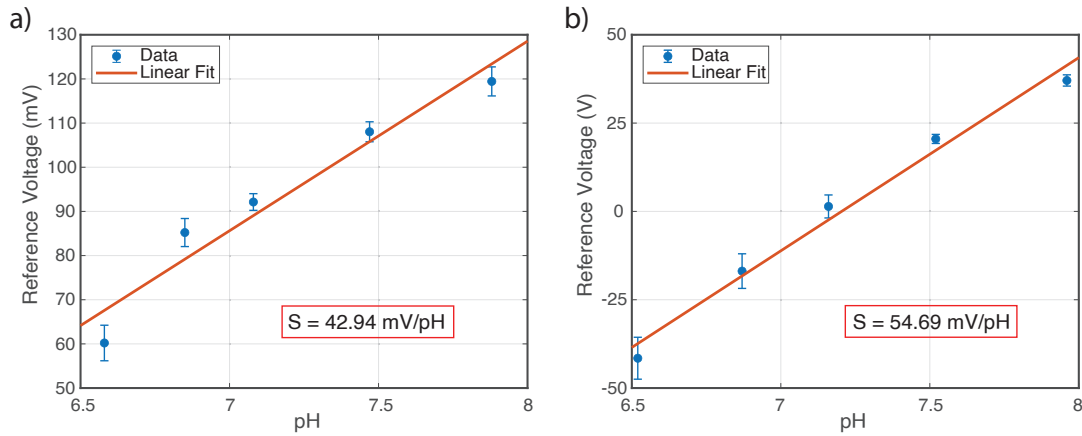


**Figure 4.7:** Comparison between pH response in buffer and ISF-like solutions with the second batch of CEA-LETI chips. a) pH calibration curve in buffer extracted from Figure 4.5 at  $I_D = 1 \text{ nA}$ . Extracted sensitivity is around  $42 \text{ mV/pH}$ . b) pH calibration curve in ISF-like solution extracted from 4.6 at  $I_D = 1 \text{ nA}$ . Extracted sensitivity is around  $54 \text{ mV/pH}$ .

pH values (top x-axis) after subtracting the linear trend-line. From this data the calibration curve of Figure 4.11a is obtained, and the linear model highlighted in the figure describes the prediction model that can be used to measure pH values in unknown solutions, like different human sera characterized by a different matrix. Figure 4.11b exactly represents this experiment: after the sensor calibration, we showed to the sensor 5 different serum samples that were not in the batch used for the calibration.

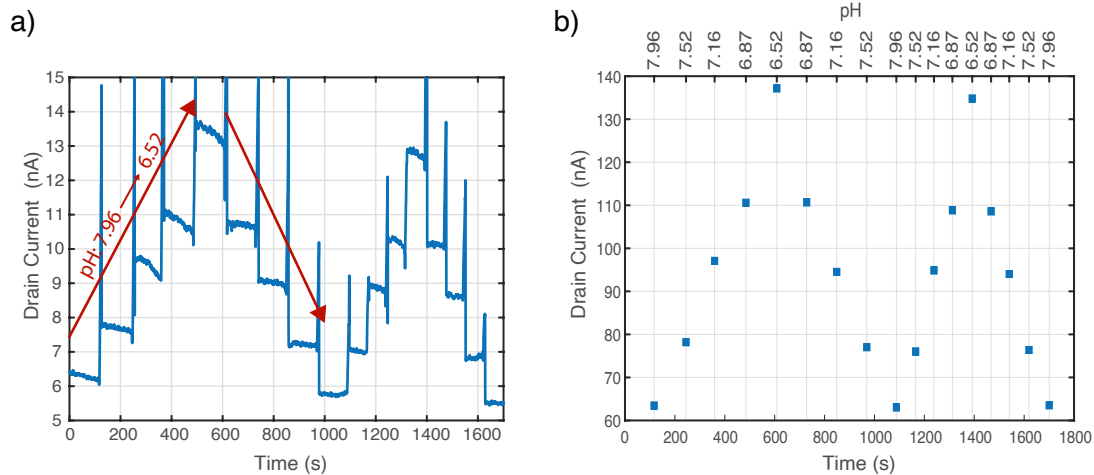


**Figure 4.8:** Real-time pH sensing in top-gate configuration in ISF-like solution with the second batch of CEA-LETI chips. Applied voltages are  $V_{REF} = 0.2 \text{ V}$ ,  $V_D = 0.5 \text{ V}$ ,  $V_S = V_{BG} = 0 \text{ V}$ . a) Real-time output drain current. The drain current shifts upon injections of different pH solutions. b) Average values extracted from (a) after baseline removal. The bottom x-axis represents the time, and the top one the pH values.

These serum samples belong to different people and thus are characterized by a different composition. In particular, we used the serum samples from three different people (S1, S2, and S3), and for the third serum, we injected two arbitrary amounts of Bovine Serum Albumin protein, to check the effect of large protein concentration variation on the pH readings capabilities of our sensor. We need to take into consideration that the presence of BSA changes the pH level of the solutions. After showing the serum samples to our sensor, we back-calculate the measured pH level thanks to the calibrated prediction model, and we compare our sensor's readings with the ones of a standard pH meter.

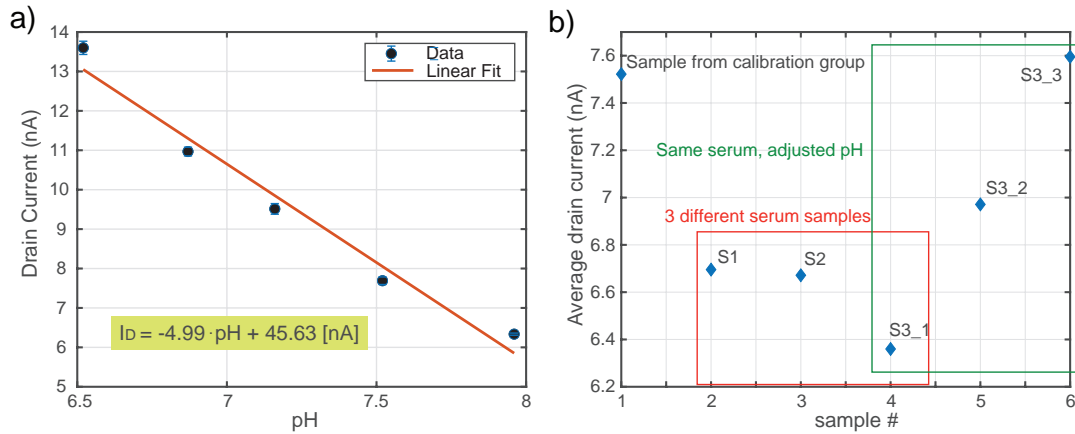


**Figure 4.9:** a) Calibration curve was obtained by creating a linear regression model from the data extracted in 4.8. b) Calibrated sensor reading of pH values of unknown ISF-like samples. The system can correctly measure the pH values with a maximum error of 1.65%.

The compared readings are summarized in the table 4.1: we report the two readings (the first with the use of the pH meter, and the second with our sensor), together with the relative error between the two measurements. The SiNW sensor shows great accuracy in the measurement of the pH levels of the unknown samples of the three people with no added BSA, with a maximum error of 1.65%, but also the reading with the BSA modified samples show sufficient accuracy, with a maximum relative error of 3.43% from the real pH value (assessed with the use of the commercial pH meter).

Label	Sample description	pH meter reading	pH SiNWs reading	error %
$S_{cal}$	Sample from calibration batch	7.52	7.51	0.09
S1	Person 1	7.61	7.68	0.90
S2	Person 2	7.59	7.67	1.23
S3-1	Person 3	7.62	7.75	1.65
S3-2	Person 3 + 10mg/mL BSA	7.42	7.62	2.74
S3-3	Person 3 + 25mg/mL BSA	7.25	7.50	3.43

**Table 4.1:** Comparison of pH readings in ISF-like solution by the SiNWs in top-gate configuration and a commercial pH meter.

The last experiment performed with the second batch of CEA-LETI chips to evaluate pH levels of biofluids was done with the same ISF-like solution used in the previous experiment. In this case, we used the constant current operation mode, described in detail in 3.3.4 to compare the accuracy of this method with the previous ones. We decided to operate the transistor in moderate inversion and saturation regime because as previously discussed it is the region with the best trade-off between sensitivity and linearity. The SiNW array transistor is biased with a constant drain current of  $2 \mu\text{A}$ , a source and back-gate voltage of  $0 \text{ V}$ , and a reference voltage of  $0.6 \text{ V}$ . While operated in constant current mode we keep track of the drain voltage variations in time. The first part of the experiment consists of the sensor calibration, by cycling the five calibration serum solutions previously used. The obtained curve is shown in Figure 4.10a, while in Figure 4.10b it is possible to appreciate the extracted average values. These data are later used to find the best curve fit. In this case, we decided to use an exponential fit with two terms.

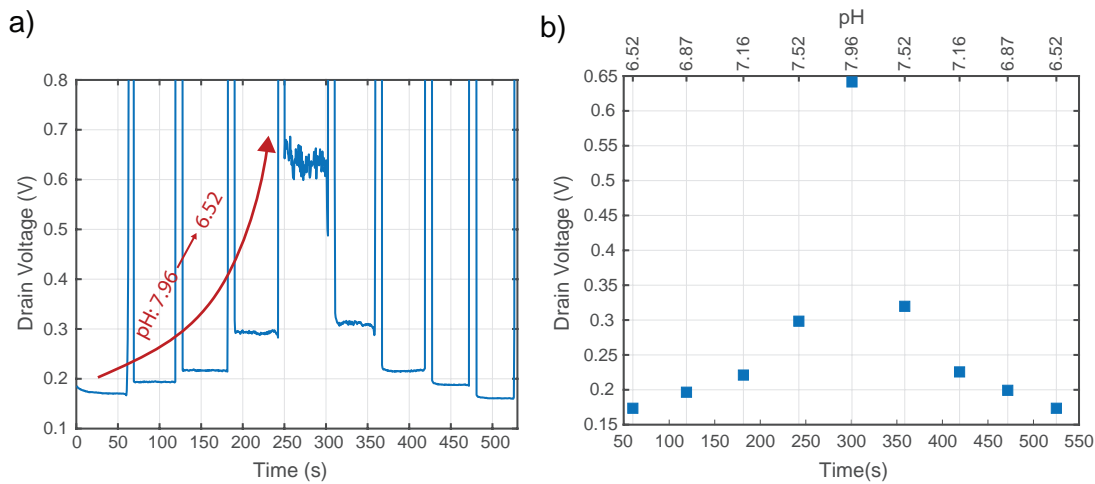


**Figure 4.10:** Real-time pH sensing in drain constant current configuration in ISF-like solution with the second batch of CEA-LETI chips. Applied bias point has  $V_{REF} = 0.56 \text{ V}$ ,  $I_D = 2 \mu\text{A}$ ,  $V_S = V_{BG} = 0 \text{ V}$ . a) Real-time output drain voltage. The drain voltage shifts upon injections of different pH solutions. b) Average values extracted from (a) after baseline removal. The bottom x-axis represents the time, and the top one the pH values.

After the sensor calibration in constant current mode, we show the sensor five serum samples that are unknown to the SiNWs sensor, as already done with the previous experiment. By applying the experimental calibrated model we can back-calculate the pH values of the unknown solutions, in order to compare them with the commercial pH meter readings and calculate the relative error.

The obtained results are summarized in 4.2: the obtained pH values strongly agree with the ones measured with the commercial system. Moreover, the relative errors are comparable with the previous method. The main advantage consists of a direct voltage read-out with voltage variations that are larger than  $100 \text{ mV/pH}$  in the worst case and can reach  $800 \text{ mV/pH}$  in the largest sensitivity region. The voltage read-out would sensibly increase the simplicity of the

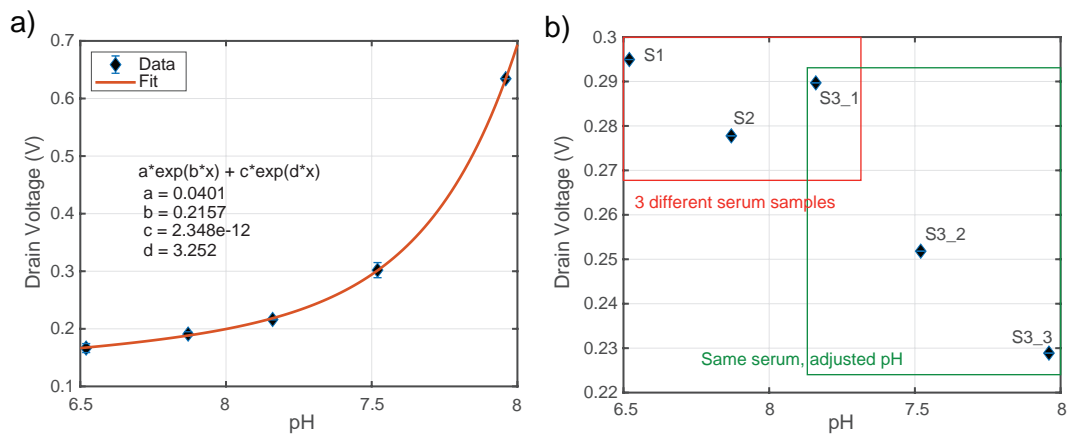


**Figure 4.11:** a) Calibration curve was obtained by creating a non-linear regression model from the data extracted in 4.10. b) Calibrated sensor reading of pH values of unknown ISF-like samples. The system can correctly measure the pH values with a maximum error of 0.52%.

system, avoiding the necessity of reading current changes of the order of pA.

Label	Sample description	pH meter reading	pH SiNWs reading	error %
S1	Person 1	7.61	7.68	0.90
S2	Person 2	7.59	7.62	0.42
S3-1	Person 3	7.62	7.66	0.52
S3-2	Person 3 + 10mg/mL BSA	7.42	7.52	1.37
S3-3	Person 3 + 25mg/mL BSA	7.25	7.40	2.11

**Table 4.2:** Comparison of pH readings in ISF-like solution by the SiNWs in constant drain current configuration and a commercial pH meter.

### 4.1.3 In-house pH sensing

Until now we have shown the results obtained with the SiNW array chips from CEA-LETI. As previously discussed, the second batch of those chips did not show Nernstian sensitivity towards pH in front-gate operation and did not have a stable response when operated in double-gate mode, by sweeping the back-gate voltage. We explained the lower pH sensitivity with the low quality of the high-k dielectric  $\text{HfO}_2$  layer, as shown in the scanning transmission electron microscopy images in Figure 4.4. This lowered the sensitivity down to 45 mV/pH and did not allow the reproduction of the obtained C-Reactive Protein detection results described in the next section. Those were among the reasons behind the decision of designing and fabricating our own SiNW arrays, with a more suitable form factor for the integration with a microneedles extractor and other types of sensors developed within the frame of the Digipredict project, such as a miniaturized amperometric sensor for lactate detection.

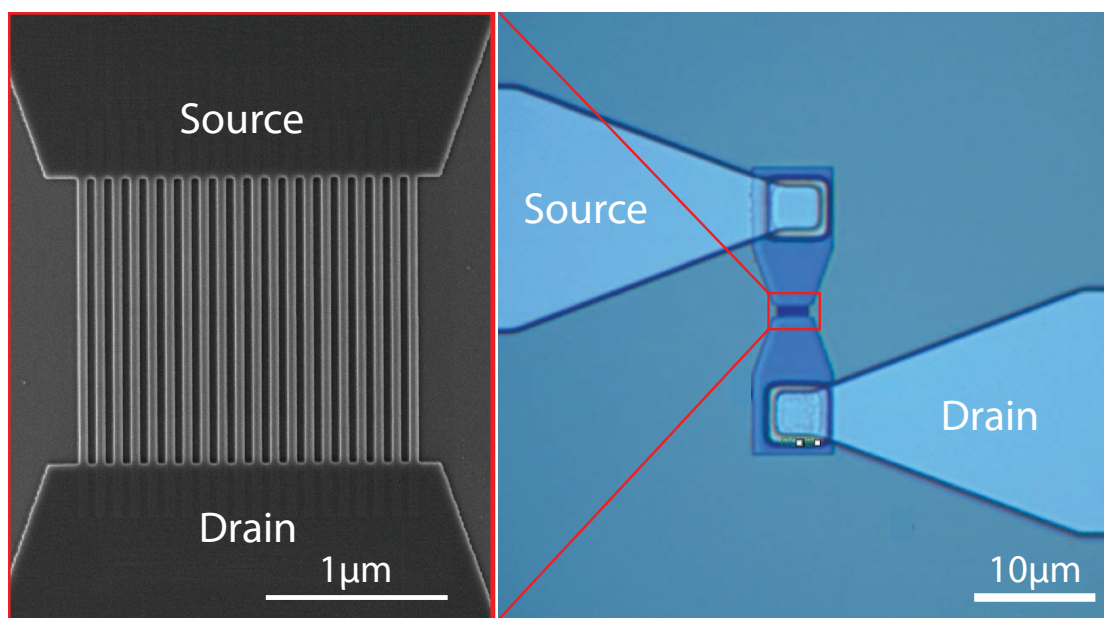


**Figure 4.12:** SEM and optical images of one of the SiNW arrays fabricated at CMi: the parallel silicon nanowires are in between the source and drain regions. Two metallic lines depart in opposite directions from the source and drain.

After the complete fabrication of our custom-designed chips, we characterized the different designs of the nanowire arrays. The highest performances in terms of ON-OFF ratio, hysteresis, and leakage current were achieved by the design featuring an array of 20 parallel nanowires, each of them with a length of 1.6 μm, a width of 120 nm, and a distance between each other of 100 nm. Figure 4.12 shows the scanning transmission electron microscopy image of the nanowire arrays after the deep reactive ion etching step and the optical microscope image of the final device.

This device has been electrically characterized, and its performances are reported in section 2.3.5. In this section, we report the sensing performance toward pH variations (in buffer) of the

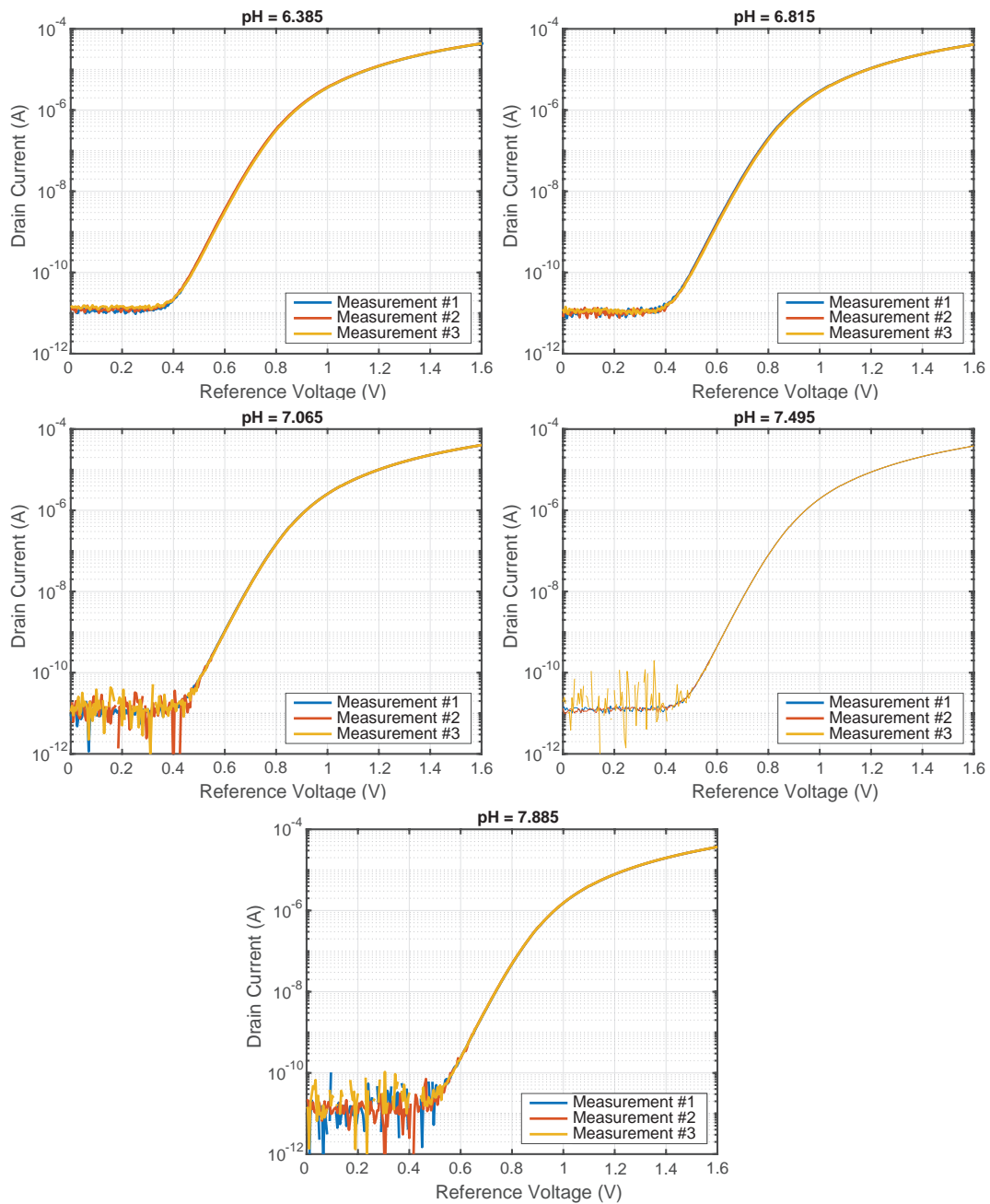


**Figure 4.13:** Repeated measurement at different pH in top-gate configuration with an in-house fabricated SiNW array chip. For each pH solution, we repeated three measurements of the transfer characteristic. Each plot represents the three measurements, and the pH level is indicated on top of each figure. We notice optimal stability and measurement repeatability.

same transistor. To measure its performance, we used five different buffers with adjusted pH between 6.385 and 7.885. We decided to use a PDMS cell that contains the liquid volume on a defined region of the chip surface and to manually dispense and exchange the liquids with the

help of manual micropipettes. The volume of the liquid under test was  $50 \mu\text{L}$ . To apply the necessary bias conditions and to measure the transfer characteristics of the device we used a Microtech Cascade prober station and a Keithley 4200A semiconductor parameter analyzer. Each solution has been injected three times, to have a statistical relevance of the obtained results and to study the variability of the sensor's response towards the same pH value. We started our study by operating our sensor in front gate operation, by applying a source and back-gate voltage of  $0 \text{ V}$ , a drain voltage of  $0.5 \text{ V}$ , and sweeping the reference voltage between  $0 \text{ V}$  and  $1.5 \text{ V}$  through an external Ag/AgCl reference electrode. The repeated measurements of the transfer characteristic for each pH value are reported in Figure 4.13 as semi-logarithmic plots: we can appreciate the low variability of the sensor response for repeated tests in the same liquid, indicating a good reproducibility and reliability of our sensor.

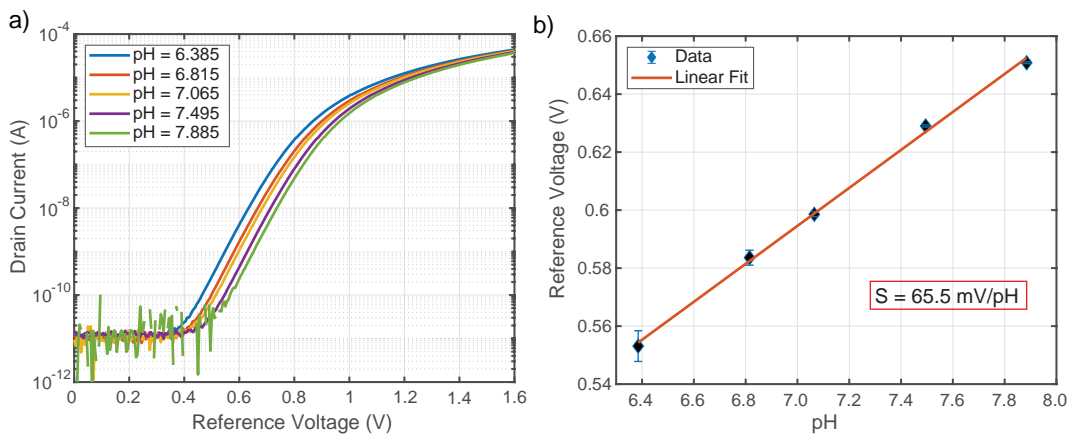


**Figure 4.14:** pH sensing in top-gate configuration with the in-house fabricated chips. Applied voltages are  $V_D = 0.5$ ,  $V_S = V_{BG} = 0 \text{ V}$ . The reference voltage is swept between  $0 \text{ V}$  and  $1.5 \text{ V}$  through an external Ag/AgCl reference electrode. a) Transfer characteristic curves acquired at different pH levels. It is possible to notice a right shift with the increase in pH. b) pH dose response extracted from (a) at  $I_D = 1 \text{ nA}$ . The obtained sensitivity reaches the Nernstian limit.

To appreciate the pH response we report one transfer characteristic per pH value in the plot in Figure 4.14a: also in this case, we obtain a threshold voltage positive shift ( $\Delta V_T > 0$ ) for increasing value of pH in solution. To study the sensitivity we decide to arbitrarily fix a drain current of  $1 \text{ nA}$  to extract the correspondent reference voltage values for each measurement, and we plot the obtained data as a function of the pH value in Figure 4.14b. By performing a linear interpolation of the data we can obtain the sensitivity as the slope of the linear fit, obtaining a value of  $63 \text{ mV/pH}$ . The value is slightly above the theoretical Nernstian limit, probably given a user error during the solutions' preparation. The important conclusion is that the custom fabricated sensors at EPFL satisfy the necessary conditions by showing a Nernstian sensitivity towards pH in buffer, thanks to a restored high quality of the gate oxide layer, as shown in the TEM picture in Figure 2.23, and described in details in Section 2.3.2.

The second reason that pushed us to fabricate our customized devices was the inability of reproducing the CRP detection results in back-gate configuration, due to the instability and

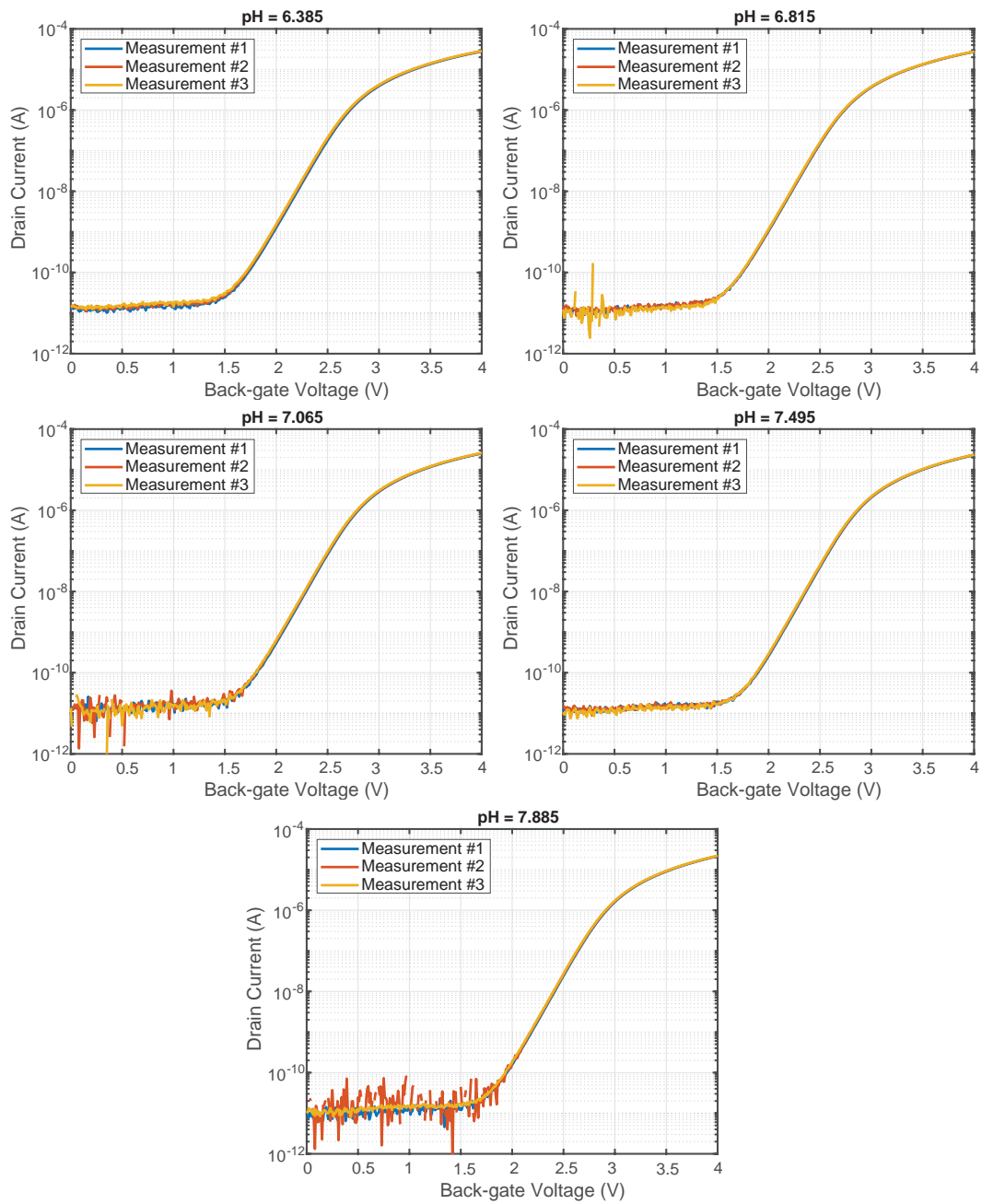


**Figure 4.15:** Repeated measurement at different pH in back-gate configuration with an in-house fabricated SiNW array chip. For each pH solution, we repeated three measurements of the back-gate transfer characteristic. Each plot represents the three measurements, and the pH level is indicated on top of each figure. We notice optimal stability and measurement repeatability.

the poor response of the second batch of CEA-LETI chips while sweeping the back-gate voltage through the Si bulk contact. With this fabrication, we wanted to prove the ability to amplify



the detection signal by using the sensor in dual gate configuration, thanks to the intrinsic amplification given by the ratio of the two capacitive couplings between front and bottom gate, as described in detail in the Methods Chapter, Section 3.3.3. To prove the ability of our sensor to amplify detection signals when operated in back-gate configuration, we repeated the same experiment performed in top-gate, by sweeping the back-gate voltage between 0 V and 4 V while keeping the solution potential constant at 0 V, and the drain to source voltage constant at 0.5 V. Also in this case, we repeated the measurement in each solution three times, and we report the transfer characteristic curves in a semi-logarithmic fashion in Figure 4.15. Also in this case we can greatly appreciate the stability of our sensor when shown with the same solution: the three curves for each pH values perfectly overlap, originating a very small deviation from the average value.

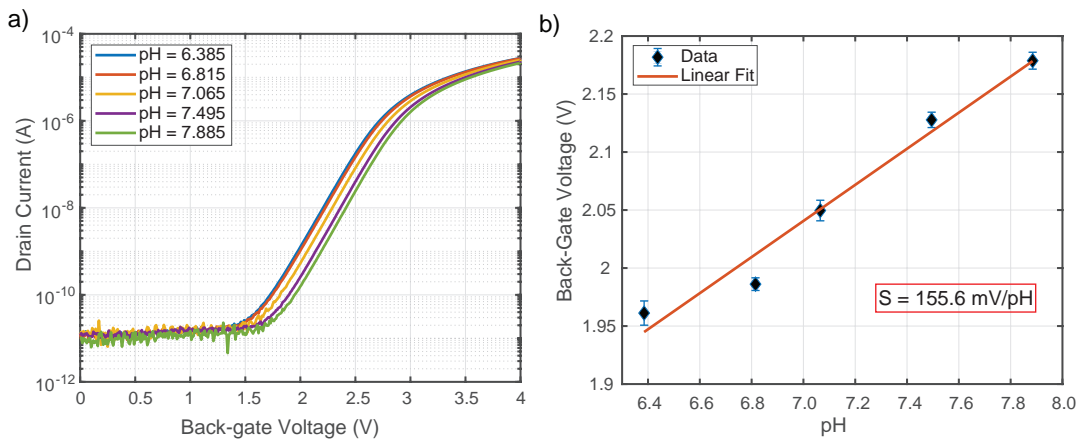


**Figure 4.16:** pH sensing in back-gate configuration with the in-house fabricated chips. Applied voltages are  $V_D = 0.5$ ,  $V_S = V_{BG} = 0$  V. The back-gate voltage is swept between 0 V and 4 V through the bulk silicon of the chip. a) Transfer characteristic curves acquired at different pH levels. It is possible to notice a right shift with the increase in pH. b) pH dose response extracted from (a) at  $I_D = 1$  nA. The obtained sensitivity is 155 mV/pH.

Once again we want to study the sensor's sensitivity, to prove the presence of internal amplification and to reinforce our claim. In Figure 4.16a one transfer characteristic curve per each pH value is reported to appreciate the positive threshold voltage shift with the increase of the protons concentration in the liquid under test. We arbitrarily fix a drain current value of 1 nA, to extract the correspondent reference voltage, and we report the obtained data in Figure 4.16b. We perform linear interpolation, and we report the linear fit in the same figure. The slope of the linear curves is around 155 mV/pH, indicating a three times amplified sensitivity toward pH when the sensor is operated in back-gate configuration. This result supports our claim and proves the great quality of the fabricated arrays, that can be used in future experiments to measure CRP variation in complex matrices, such as human interstitial fluid.

### 4.2 Integration and Compatibility Demonstration of the pH Sensor with On-Chip Read-Out through an Intermediary Board

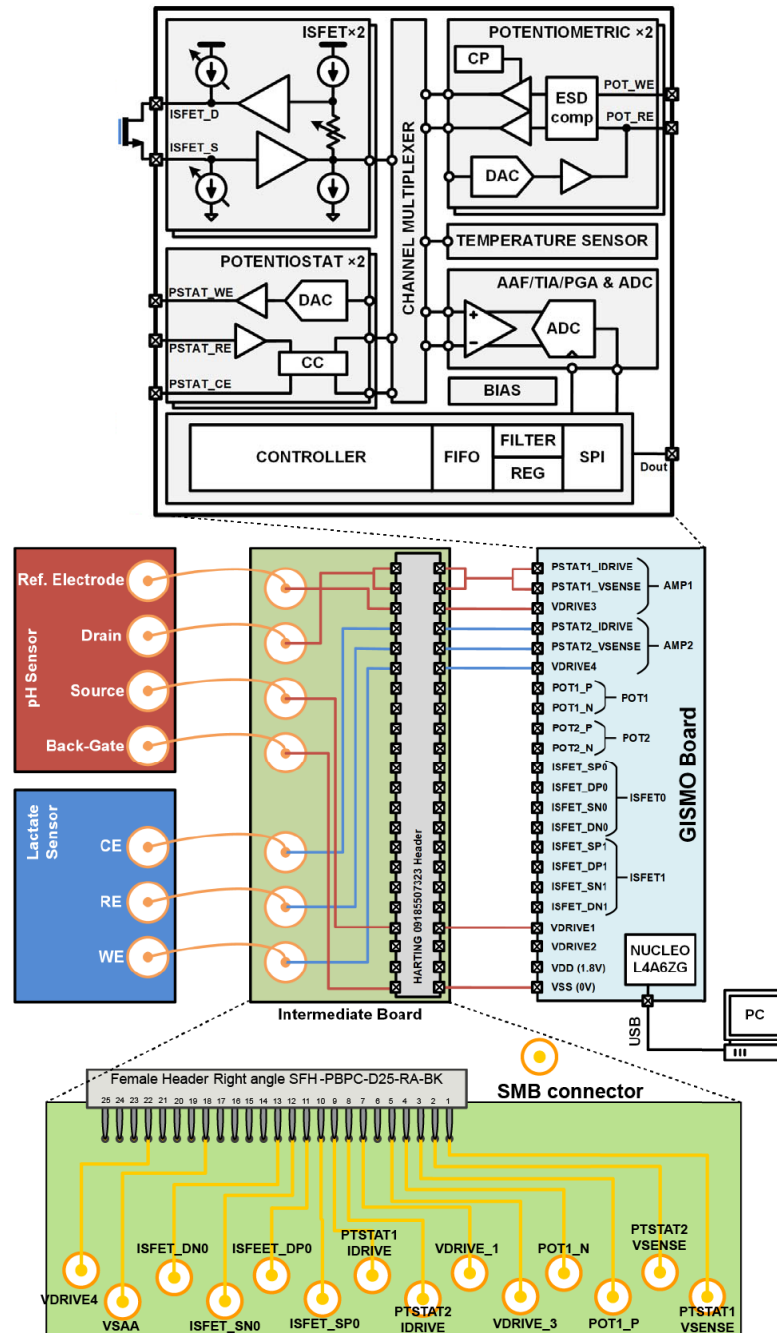


**Figure 4.17:** Schematic representing the interface system between pH and lactate sensors with the on-chip read-out. On the top part, the block diagram of the ASIC developed by imec [203], and on the bottom the intermediate PCB is used to interface the read-out chip and the sensors.

As previously mentioned in the introductory chapter (Chapter 1), the objective of this project is to fabricate a biosensor system capable of selectively monitoring different biomarker concentrations in human interstitial fluid (ISF). This biosensor system is intended to be integrated into a wearable setup, which includes an on-skin microneedle extractor system, a microfluidic interposer for passive fluid pumping, the biosensor itself, and a read-out system for driving and collecting data on the detected biomarkers. It is essential to emphasize the importance of designing and fabricating a low-power electronic read-out that can be seamlessly integrated with the sensor technology, considering the wearable nature of the system. Furthermore, the aim is not limited to ISFET-based sensors described in this work but also extends to the detection of various biomarker species using amperometric systems (e.g. lactate detection based on lactate oxidation) or potentiometric systems.

The development of the microneedle extractor and the read-out electronics involved external collaborations. The design of the fabricated SiNWs chips was specifically tailored to integrate with these two systems. Notably, the read-out system was designed and developed by imec (Leuven, Belgium). To serve as a low-power electrochemical sensor interface integrated circuit (IC), a multi-modal ASIC was designed and fabricated using 0.18  $\mu\text{m}$  node technology [203] (GISMO chip). The read-out system offers versatile capabilities for multi-modal electrochemical sensing read-out channels, accommodating ISFETs, amperometric, and potentiometric sensors. It specifically includes two distinct ISFET channels and two separate potentiostat channels. The top portion of Figure 4.17 illustrates the block diagram of the ASIC, which was designed and independently developed by imec.

In collaboration with imec, this research conducted joint experiments to assess the compatibility between the developed SiNWs sensors (as part of this work), an amperometric lactate sensor (developed at Nanolab, EPFL), and the GISMO read-out (imec, Belgium).

During the first demonstration, the three sensors were mounted on separate printed circuit boards (PCBs) and required proper interfacing. To address this requirement, an intermediate PCB was designed to serve as an interface between a male 2.54mm spacing pin header mounted on the read-out board and the SMB connectors on the two sensor boards (Figure D.1). The interfacing system is depicted in the lower section of Figure 4.17. In the conducted tests, both sensors were biased using the two independent potentiostats of the read-out system.

The first experiment targeted the two sensors separately, in this manuscript we report only the results for the pH sensor. The setup images are reported in the Annex section D.

In the first experiment, a SiNW array chip from CEA-LETI was used to test three different pH values (4, 7, and 10) in phosphate buffer. The sensor was biased through a potentiostat channel of the read-out chip, providing an output range of  $\pm 5 \mu\text{A}$ . The voltage settings used were  $V_{REF} = 1 \text{ V}$ ,  $V_S = V_{BG} = 0 \text{ V}$ , and  $V_D = 0.5\text{V}$ .

An external Ag/AgCl Micrux electrode was utilized, by inserting it into the microfluidic inlet tube, as illustrated in Figure D.1. A customized microfluidic system (as described in Section

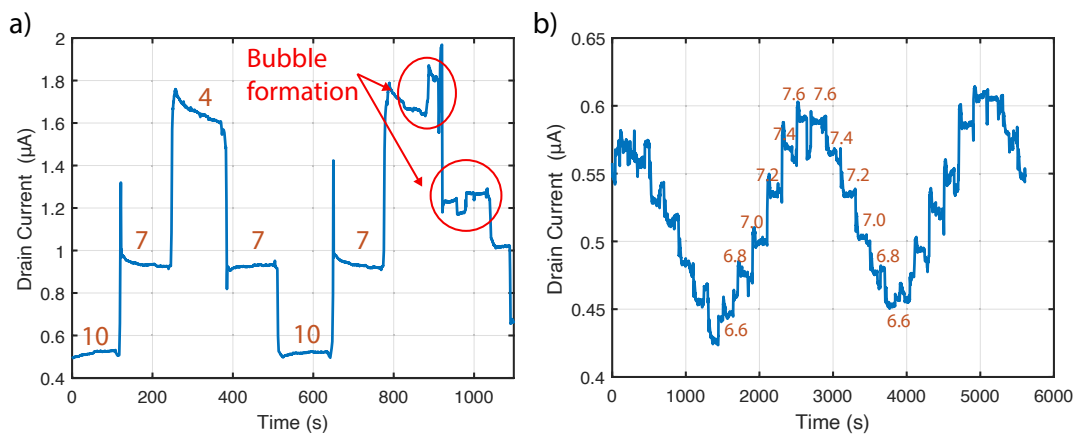


**Figure 4.18:** pH measurements conducted using the on-chip readout system developed by imec. a) Large pH variations monitored using the potentiostat channel of the GISMO chip. The system demonstrates reliable pH monitoring until the formation of a bubble near the sensor's surface, resulting in signal disruption. b) Small pH variations measured using the potentiostat channel of the GISMO chip. The experiment was repeated without the bubble trap in the microfluidic system. Although the sensor exhibits higher noise and lower current, a discernible pH response is still observable.

3.2.1) was employed to deliver the different solutions automatically to the sensor's surface. Additionally, a bubble trap was incorporated into the inlet tubing line to prevent any interference. The experimental results are depicted in Figure 4.18a. The system demonstrates its capability to continuously and reliably record the shift in current response for the three different pH levels, maintaining accuracy until the formation of a bubble near the sensor's surface within the microfluidic system. Additionally, an attempt was made to achieve finer pH monitoring within the range of 6.6 to 7.6, with 0.2 pH steps, using the same bias conditions but without the bubble trap system (Figure 4.18b). Unexpectedly, the sensor response displayed decreased current amplitude and increased noise levels, despite the presence of a discernible pyramidal step-like response pattern. This behavior can be attributed to two potential factors: the sub-optimal design of the microfluidic delivery system and the placement of the external reference electrode. The non-integrated nature of the solution led to the formation of multiple air bubbles in the T-junction used for inserting the reference electrode. Furthermore, the usage of a cumbersome external reference electrode may have contributed to the elevated noise levels and susceptibility to electromagnetic interference experienced during multiple experimental attempts.

A second experiment was conducted to simultaneously measure pH and lactate variations in a solution using the read-out chip and two different sensors placed in separate chambers but exposed to the same solution. For this experiment, the two potentiostat channels were utilized in parallel. The bias conditions for the pH sensor remained the same as described above, while the lactate sensor was subjected to a constant potential bias of 0.5 V and an output range of  $\pm 1 \mu\text{A}$ .

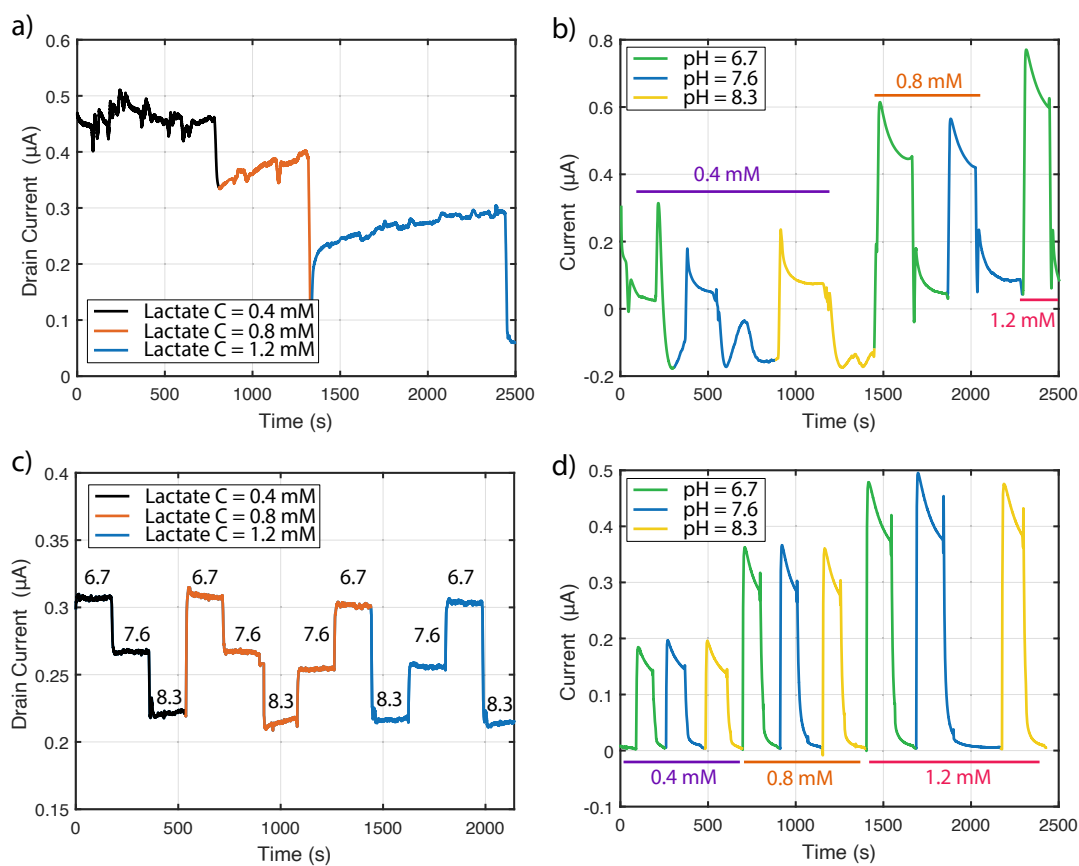


**Figure 4.19:** Figure 4.19: Simultaneous pH and lactate sensing. a) pH sensor response using the imec read-out system, with variations in pH and lactate levels. Surprisingly, the sensor exhibits cross-sensitivity to lactate. b) Lactate sensor amperometric response with  $E = 0.5$  V (developed at EPFL, not part of this work) using the imec read-out system, with variations in pH and lactate levels. The sensor does not provide a reliable response. c) pH sensor response using a standard Keithley 4200A readout system, with variations in pH and lactate levels. As expected, the sensor exhibits correct behavior, responding solely to pH variation without lactate cross-sensitivity. d) Lactate sensor response using a standard PalmSens potentiostat, with variations in pH and lactate levels. As expected, the sensor exhibits correct behavior, responding exclusively to lactate variation without pH cross-sensitivity. The issues encountered in a) and b) are attributed to a non-ideal switching mechanism during the biasing of the respective reference electrodes.

To enable simultaneous sensing, a switch mechanism was employed to bias the reference electrodes of the two systems. The switching frequency of the mechanism was set to 2 Hz. In total, nine different solutions were tested, comprising all possible combinations of three distinct pH levels (6.7, 7.6, 8.3) and three different lactate concentrations in phosphate buffers (0.4 mM, 0.8 mM, and 1.2 mM).

The results obtained for the pH and lactate sensors are presented in Figure 4.19a and 4.19b, respectively. Unfortunately, the implemented switching mechanism did not provide suitable bias conditions, leading to disruptions in the accurate measurement of the respective analytes by the two sensors. Notably, the pH sensor's response appeared to be susceptible to changes in lactate concentration in the solution, indicating a high level of cross-sensitivity. To address this issue, the same experiment was repeated using standard equipment, specifically the Keithley 4200A for the pH sensor and a PalmSens potentiostat for the lactate sensor. The results of this alternative setup are illustrated in Figure 4.19c and 4.19d for pH and lactate sensing, respectively. As expected, neither the varying lactate concentrations influenced the pH sensor's response nor did the pH levels affect the lactate sensor's response. These results confirm that the difficulties encountered during the experiments utilizing the on-chip read-out system were indeed caused by the inadequate biasing mechanism.

In conclusion, the preliminary experiments conducted have demonstrated the compatibility of the SiNWs sensors with the read-out circuit developed by imec. These initial findings provide promising evidence of the potential for integrating the SiNWs sensors into the wearable biosensor system. However, it is important to note that further experiments need to be conducted to validate the feasibility of simultaneous measurements. Specifically, additional investigations are required to address the challenges associated with the switching mechanism and cross-sensitivity observed in the pH and lactate sensors. By building upon these preliminary results, future experiments can provide valuable insights and pave the way for the successful realization of simultaneous measurements in the biosensor system.

### 4.3 Summary

In this chapter, we have demonstrated the ability of our Bio-FET platform to continuously monitor pH variation both in buffer and human ISF-like solution, covering the concentration range of interest. We have achieved Nernstian sensitivity of 60 mV/pH while operating the sensor in top-gate configuration, with low temporal drift and high reliability. Furthermore, by employing a back-gate configuration and leveraging the asymmetrical structure between the top and bottom gate oxides, we have surpassed the Nernst sensitivity limit with our sensor. Specifically, the CEA-LETI platform achieved super-Nernstian sensitivity exceeding 3 V/pH, while the in-house fabricated SiNW arrays achieved sensitivity greater than 150 mV/pH. Operating the sensor in constant drain current mode has yielded an improved signal-to-noise ratio, resulting in a significant increase in sensitivity for pH monitoring. We benchmarked the developed SiNWs sensor with a standard pH meter, both exploiting the system in top-gate

and constant drain current configuration. We achieved a pH resolution of 0.07 pH unit in a physiopathological range from 6.5 to 8, with a maximal error of 0.92%.

Moreover, we conducted the first experiment to assess the compatibility of our developed pH sensor with an on-chip multi-modal read-out system developed by imec, Belgium. This experiment successfully demonstrated the integration capabilities between the two systems, serving as a foundation for future experiments aiming to achieve higher levels of integration.

## 5 C-Reactive Protein sensing

*In Chapter 3, we introduced the functionalization approach employed to selectively detect C-Reactive Proteins (CRP) using the SiNWs sensor. In this chapter, we describe the results of our experiments on detecting CRP in buffer. Initially, we operated our sensor in the top-gate configuration to assess its performance under varying ionic strengths. However, we found that it was impossible to detect CRP in this configuration with undiluted buffers. To overcome this limitation, we implemented a back-gate signal amplification method, which proved to be effective in monitoring changes in CRP concentration in 0.1xPBS buffer with high sensitivity in the desired concentration range. We also report the results of our study on sensor stability against blank injections, which is a fundamental condition to ensure the quality of the obtained CRP detection. Lastly, we introduce preliminary results obtained while operating the sensor in constant drain current mode. This novel method holds great promise for achieving enhanced sensitivities and lower limits of detection. We discuss the potential advantages of this approach and its implications for future CRP detection applications.*

### 5.1 C-Reactive Protein sensing

In Section 1.2 of the introduction chapter, we extensively covered the significance of monitoring CRP levels in ISF or blood. The following section is focused on the experiments conducted and the results obtained using both CEA-LETI chips and the one fabricated in CMi at EPFL while monitoring CRP levels through the three different methods elaborated in Section 3.3. The results are presented in the same order as the methods used. We begin by describing the outcomes obtained through top-gate configuration, including both successful and unsuccessful conditions of our system. Next, we discuss the results of the back-gate operation, which allowed us to monitor CRP levels in the human physiological concentration range in 0.1xPBS buffer. Finally, we describe the initial outcomes of employing our sensor in constant drain current mode, which demonstrated to be an interesting method to achieve high sensitivities in protein detection.

For all the experiments reported in the following sections, we followed the same surface



functionalization protocol described and confirmed in Section 3.1. Moreover, when possible, we employed the reference-compensated method. For specific probes, we used the anti-CRP Fab fragments previously described, while for unspecific functionalization, we used anti-cTnI F(ab)<sub>2</sub> fragments, which proved to be resilient to CRP binding in the QCM-D experiments reported in 3.1.5.

The initial set of experiments was carried out using the top-gate configuration, beginning with CRP detection in a 0.01xPBS buffer. This dilution of the matrix increased the Debye screening length, making the detection process easier and enhancing the sensor's response [133].

### 5.1.1 Front-Gate operation

To work in the front-gate operation, we set  $V_{DS}$  to 0.1 V, back-gate voltage at 0 V, and swept the reference voltage from -0.4 V to 0.8 V. In this section, we only report the extracted reference voltage required to maintain a 10 nA current in the channel since we have explained the extraction method in detail before. Before injecting CRP into the liquid under test, we recorded multiple transfer characteristic curves in the buffer solution to establish the sensor's stability. We obtained a maximum dispersion of 6 mV in the reference voltage values at  $I_D = 10$  nA. We averaged the last five responses recorded during the stability tests to establish an initial reference value. The sensor's response is represented by the reference voltage shift concerning the response to buffer injections in Figure 5.1a. The figure shows two sets of data: one (blue markers) represents the response of the sensor whose gate oxide is functionalized with specific anti-CRP antibodies, while the other (orange markers) shows the response obtained from the reference sensor, which is functionalized with unspecific antibodies. The specific sensor showed a clear reference voltage shift after an injection of 1  $\mu\text{g}/\text{mL}$  of CRP, while the reference sensor did not experience a threshold voltage shift, even at concentrations as high as 100  $\mu\text{g}/\text{mL}$ . Figure 5.1b displays the average response of four different sensors functionalized with specific anti-CRP antibodies in comparison with the unspecific response.

The experiment is repeated in a 0.1xPBS buffer, where the ionic concentration is ten times greater than in the previous case. This results in a decrease in the Debye length from 7.3 nm to 2.3 nm [133]. The decrease in the Debye length implies that the ions in the solution provide greater electrostatic screening to the charges carried by the proteins. Consequently, the perturbation created on the transistor's channel conductance by the proteins binding to the antibodies on the oxide surface is significantly reduced. This is evident in Figure 5.2a, which shows the response of two sensors used to record specific and unspecific responses, respectively. The reference voltage shift is reported for both sensors at a fixed drain current of 10 nA. In this case, both sensors show a similar shift in response to increasing concentrations of CRP, making it impossible to establish any useful correlation between the sensor voltage shift and the protein concentration in solution. Figure 5.2b compares the specific sensor's response in 0.1xPBS and 0.01xPBS. The higher ionic strength of the former solution 'masks' the charges carried by the proteins to the oxide surface and does not allow any detection by

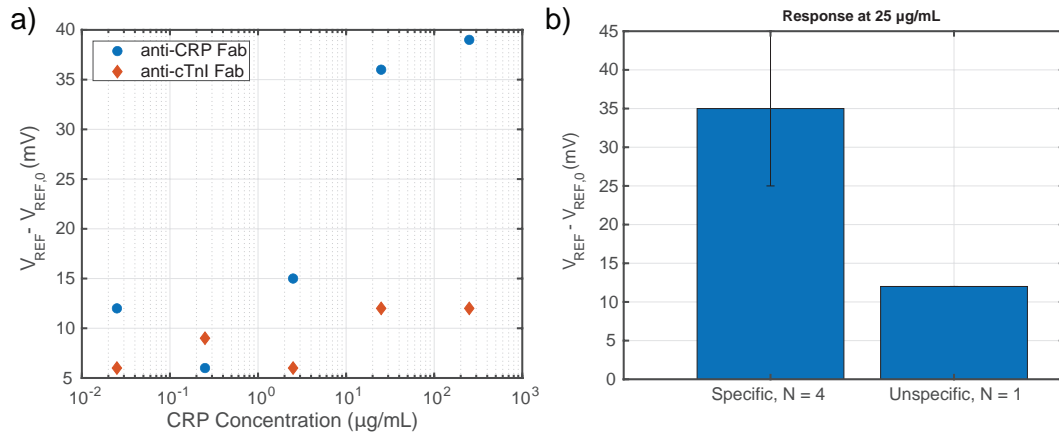


**Figure 5.1:** CRP monitoring in 0.01xPBS in top-gate configuration with the second batch of CEA-LETI chips. a) Extracted reference voltages at a fixed  $I_D = 10$  nA for different CRP concentrations in 0.01xPBS. The values are obtained by subtracting the response in blank buffer from the response at a certain CRP concentration. In blue the response of the sensor functionalized with specific anti-CRP Fab, and in orange the response of the sensor functionalized with unspecific anti-cTnI  $F(ab)_2$ . b) Bar plot showing the average response to an injection of 25  $\mu\text{g/mL}$  CRP of four correctly functionalized sensors and one sensor functionalized with unspecific antibodies.

tracking the threshold voltage shifts.

These findings were unexpected, considering that prior literature has reported successful protein detection in 0.1xPBS using full antibodies and at lower concentrations. However, the objective of this thesis is to establish a robust foundation of knowledge for designing and producing protein sensors that are reliable and yield repeatable results, ultimately leading toward real-life applications and wearable sensing. It is crucial that our sensors exhibit stability, reliability, and miniaturization as fundamental properties, rather than relying solely on isolated successful experiments. This purpose leads us to implement other methods to obtain a more reliable and stable response in higher ionic strength solutions.

### 5.1.2 Back-gate configuration

The next step in our study has been to detect CRP in 0.1xPBS buffer by exploiting the internal amplification obtainable by operating the sensor in back-gate configuration, as described in previous sections and proved to work with pH monitoring in 4.1.1.

For all the following experiments we set  $V_S = V_{REF} = 0$  V,  $V_D = 0.3$  V and we sweep the back-gate voltage between 0 V and 25 V. Also in this case, we study the sensor stability while injecting blank buffers before starting the study of the CRP response. To do so we repeat five times the measurement of the back-gate transfer characteristic curves in different blank buffers, for both the active and the reference sensors. The results for the active specific sensor are

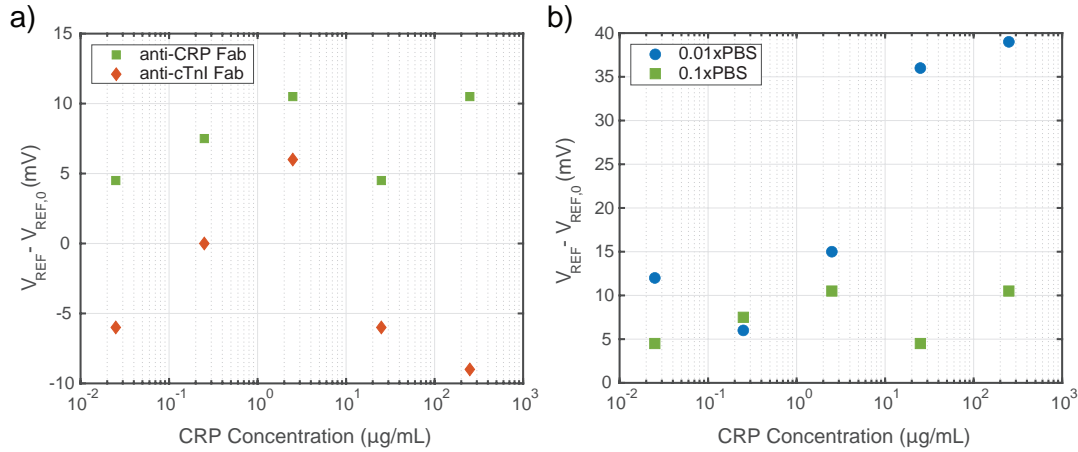


**Figure 5.2:** a) Extracted reference voltages at a fixed  $I_D = 10$  nA for different CRP concentrations in 0.1xPBS. The values are obtained by subtracting the response in blank buffer from the response at a certain CRP concentration. In blue the response of the sensor functionalized with specific anti-CRP Fab, and in orange the response of the sensor functionalized with unspecific anti-cTnI  $F(ab)_2$ . b) Comparison between the dose-response obtained in 0.01xPBS and 0.1xPBS. The Debye charge-screening does not allow any CRP detection in high-ionic strength solutions, while the sensor is operated in top-gate configuration.

reported in Figure 5.3a, both in semilogarithmic scale (left axis) and linear scale (right axis). In the inset of the same plot, we zoomed in on the curves to highlight two important aspects of our sensor: the sweeping of the back-gate voltage is carried on both in forward mode and backward mode, to study the hysteresis between the two. The sweeps possess a hysteresis lower than 300 mV, for all the buffer injections. Moreover, we can get a glance at the drift between each curve. It is important to underline that in between the recording of two curves, there is a stabilization time of 10 minutes. To better visualize the temporal drift we analyze the drain current evolution at different fixed back-gate voltages. We extract these values for both the active and the reference sensor, and we calculate the difference ( $\Delta$  Drain current, in the plots) between the response of the sensor functionalized with the specific probes and the one functionalized with the troponin-specific antibodies. The results are shown in Figure 5.3b, for different selected back-gate voltages.

The highest drift (-19 pA/minute) is obtained at high back-gate voltages ( $V_{BG} = 23$  V), but to have a fully-comprehensive picture we need to compare those values with the sensitivity values extracted in the full experiment.

To study the sensor's response to CRP we inject seven CRP concentrations between 0.06  $\mu\text{g/mL}$  (500 pM) and 100  $\mu\text{g/mL}$  (833 nM), each every 15 minutes. To record the response we measure the back-gate transfer characteristics for both the active and the reference sensors, we then fix a back-gate voltage to extract the equivalent current, and we subtract the reference response from the active. We repeat this process for four different back-gate voltages, and we report the obtained results in Figure 5.4. The extracted data are then fit with a four-parameter logistic

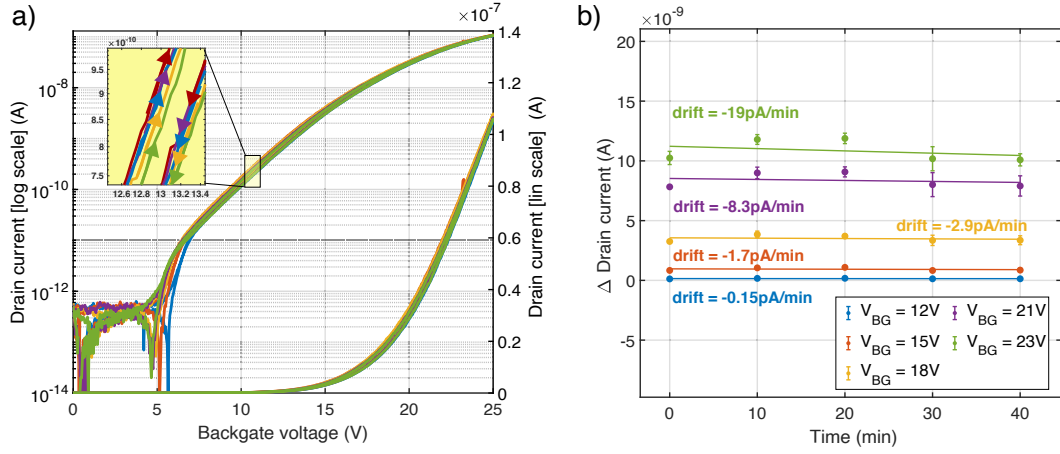


**Figure 5.3:** Drift and hysteresis are studied with repeated injections of the blank buffer. a) Back-gate transfer characteristic curves collected every ten minutes after repeated injections of blank buffer. Applied bias:  $V_D = 0.3$  V,  $V_S = V_{REF} = 0$  V. The small inset shows a zoom of the curves, to highlight the minimal drift between each measurement, and a hysteresis lower than 300 mV. b) Extracted reference-compensated (response of the reference sensor is subtracted to the one of the active sensor) drain current shifts over time (e.g. different blank injection every ten minutes). The time drift at different fixed back-gate voltages is reported.

(4PL) regression expressed as:

$$f(x) = d + \frac{a - d}{1 + \left(\frac{x}{c}\right)^2} \quad (5.1)$$

The best fit is given at a fixed back-gate voltage of 15V, while increasing the back-gate voltage the sensor shows a high current shift at low concentrations, but a quick signal saturation. Comparing the absolute current shift (we remind that each injection is performed every 15 minutes) with the temporal drift shown in Figure 5.3b, we have a signal-to-drift ratio in the linear response region higher than 40 for  $V_{BG} = 15$  V. Also the signal to noise ratio is lower at low back-gate voltages, as shown by the error bars present in the plots. The main drawback of working at lower back-gate voltages is the smaller absolute shift obtained at the output current.

If we want to compare the responses of the sensor in different working regions, we could plot the relative response shift in percentage, defined as:

$$S_I = 100x \left| \frac{\Delta I_D - \Delta I_{D,0}}{\Delta I_{D,0}} \right| \quad (5.2)$$

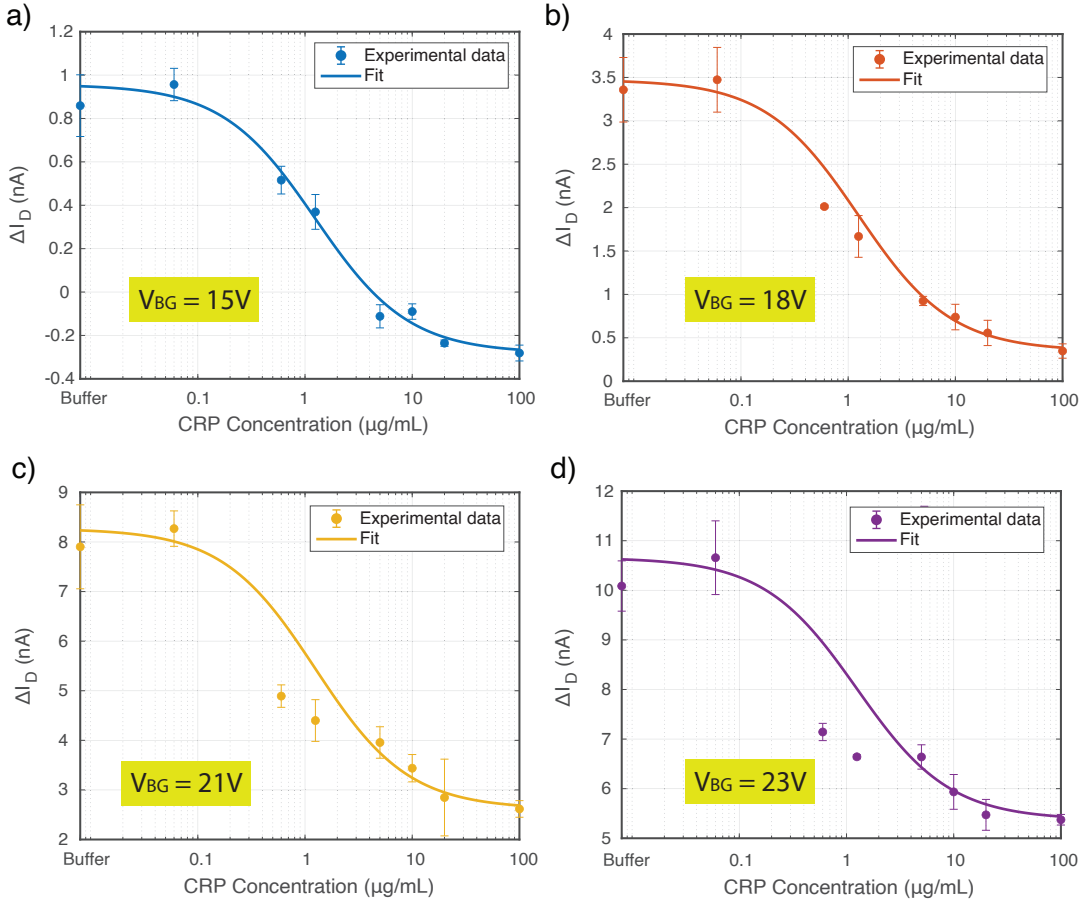


**Figure 5.4:** Extracted reference-compensated (response of the reference sensor is subtracted to the one of the active sensor) drain current shifts for increasing concentration of CRP in 0.1xPBS (each injection of CRP is performed every 15 minutes). Applied bias:  $V_D = 0.3$  V,  $V_S = V_{REF} = 0$  V. The dose-response is extracted for four different back-gate voltage values.

where  $\Delta I_D = I_{D,active} - I_{D,reference}$  at a specific concentration, and  $\Delta I_{D,0} = I_{D,0-active} - I_{D,0-reference}$ , where the 0 stands for the value of the drain current when blank buffer is shown to the sensor. By applying this equation to the data of Figure 5.4, we obtain the plot of Figure 5.5. Even if the absolute value shift between one concentration and the other is higher for higher back-gate voltages, this plot confirms that we obtain a higher relative sensitivity for lower  $V_{BG}$ .

We can conclude that the most interesting region is the one at lower back-gate voltages, but we need to be able to measure low absolute changes of current, resulting in a more sensitive and low-noise read-out circuit and interface.

Considering the results obtained at  $V_{BG} = 15$  V, we can calculate a signal-to-noise ratio (SNR) at 20  $\mu\text{g/mL}$  of 24.22 dB, and an average SNR of 15.72 dB. By considering the sensitivity as the slope of the linear part of the response ( $S_{lin}$ ), we can calculate the limit of detection offered in

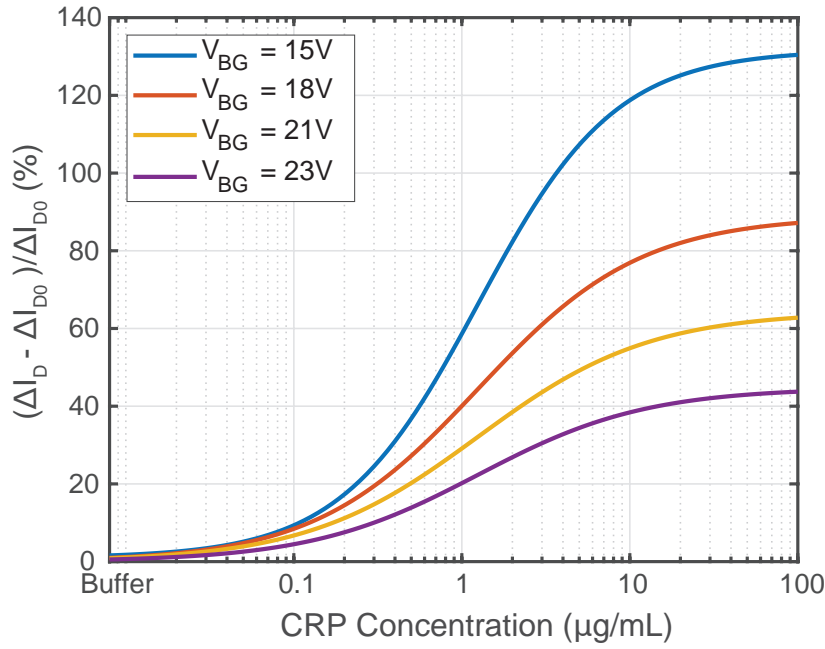


**Figure 5.5:** Relative current shift values defined as in Equation 5.2 for different back-gate voltage values. Current relative sensitivity results to be higher in weak inversion regime.

this configuration as:

$$LoD = \frac{3 \cdot \sigma_0}{S_{lin}} = 0.8645 \mu\text{g} \cdot \text{mL}^{-1} \quad (5.3)$$

The main limitation of the back-gate operation method is the complicated read-out circuit required to operate it [204]. In a real system, we would not be able to sweep the back-gate voltage for such big ranges, and the only solution would consist in exploiting a feedback loop that adjusts the  $V_{BG}$  to keep an output current constant.

In a wearable system, such high voltages impose a critical limitation. For this reason, we explored other reading methods, such as the constant drain current operation described in Section 3.3.4, and proved with pH measurement in Section 4.1.1.

### 5.1.3 Constant drain current operation

The constant current method presented in Section 3.3.4 employed to monitor pH levels in ISF (Section 4.1.2) has also been employed for the detection of CRP in 0.1xPBS solutions in the preliminary experiment reported below. While the reported results are only preliminary and require further investigation, they demonstrate a promising path towards a read-out method

that is both highly sensitive and low-power, making it suitable for detecting very low protein concentrations.

In the reported experiment below, we functionalized with anti-CRP Fab a CEA-LETI SiNW array transistor employing the immobilization protocol presented in Section 3.1.2. We employed a Keithley 4200A parameter analyzer to characterize the system. The system was biased in constant drain current mode, imposing a reference voltage of 0.5 V to ensure the transistor worked in moderate inversion, while the back-gate and source were grounded, forcing a drain current of 100 nA in the channel, and measuring the drain voltage as output.

As already mentioned in the previous section, before testing the detection capabilities of the sensor we proceed with multiple injections of blank buffer (0.1xPBS) to ensure the stability of the sensor. After six buffer injections, the sensor output signal stabilized adequately (Figure 5.6a), and we began injecting CRP concentrations ranging from 0.04  $\mu\text{g}/\text{mL}$  (333 pM) to 100  $\mu\text{g}/\text{mL}$  (833 nM). Each concentration was left on the oxide surface for ten minutes before injecting the next one.

The real-time trace in Figure 5.6a already shows the technique to be highly promising. For each injection, we calculated the average value and standard deviation by taking the real-time response between 70% and 90% after the injection time. To determine the zero response, we averaged the values obtained from the last three blank injections. This value served as the zero reference for calculating the relative responses at different concentrations, which we plotted in a semi-logarithmic plot in Figure 5.6b.

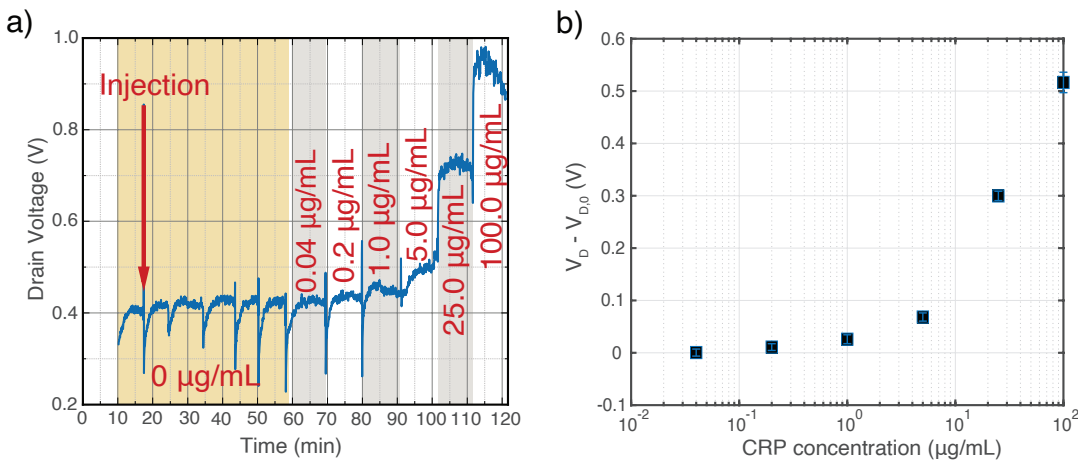


**Figure 5.6:** CRP detection in 0.1xPBS performed with the constant drain current configuration. Applied bias:  $V_{REF} = 0.5$  V,  $V_S = V_{BG} = 0$  V, and forced drain current  $I_D = 100$  nA. a) Output drain voltage evolution over time upon multiple injections of blank buffer and increasing CRP concentration. b) Dose-response extracted by averaging the values as highlighted in (a). The sensor in this configuration shows a non-linear response, with high drain voltage shifts in the interesting CRP concentration range.

The response signal shows astonishing sensing capabilities: we can clearly distinguish 0.2

$\mu\text{g/mL}$  (1.67 nM) concentration of CRP in 0.1xPBS buffer, with a signal-to-noise ratio calculated at 25  $\mu\text{g/mL}$  of 30.55 dB, and an average SNR of 18.43 dB. Moreover, the sensor response covers the necessary physiological range. We can estimate the limit of detection by considering a "small-signal" linear sensitivity extracted from the interpolation of the first three concentrations' response of  $S^* = 62.5 \text{ mV}/(\mu\text{g} \cdot \text{mL}^{-1})$ , thus obtaining:

$$LoD = \frac{3 \cdot \sigma_0}{S^*} = 0.16 \mu\text{g} \cdot \text{mL}^{-1} \quad (5.4)$$

where  $\sigma_0$  is the standard deviation upon blank injections. We define a voltage sensitivity parameter similar to the relative current sensitivity of Equation 5.2, obtaining Equation 5.5:

$$S_V = 100 \cdot \frac{V_{D,i} - V_{D,0}}{V_{D,0}} \quad (5.5)$$

where  $V_{D,i}$  is the measured drain voltage for the  $i$ -th concentration, and  $V_{D,0}$  is the average drain voltage upon blank buffer injections. The obtained value can be visualized in Figure 5.7. If we take for example the relative voltage sensitivity at the reference CRP concentration of 25  $\mu\text{g/mL}$  we obtain a relative change of 70%, a value comparable with the current sensitivities obtained while operating the sensor in back-gate configuration.

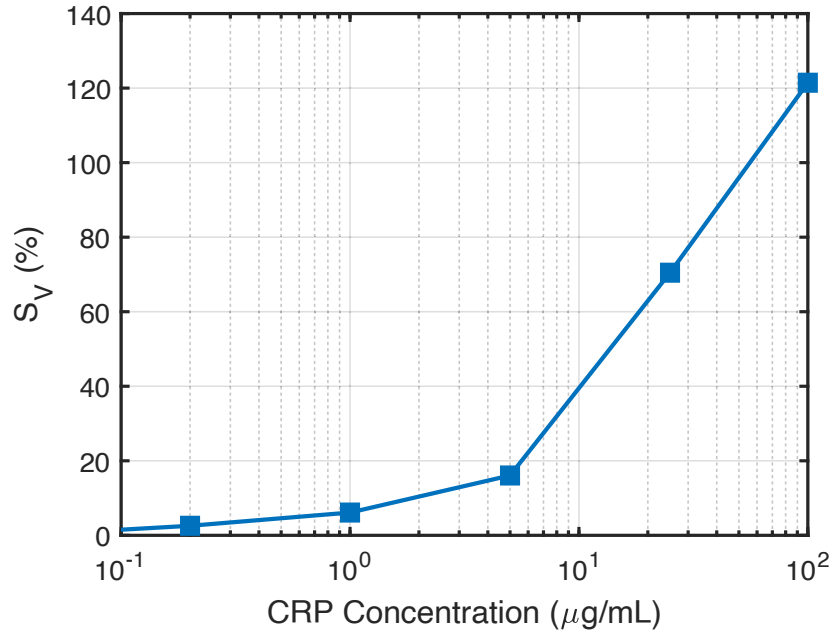


**Figure 5.7:** Relative voltage shift values defined as in Equation 5.5.



Other than achieving large sensitivities, large concentration range, and low limit of detection, this method could significantly simplify the readout electronics by enabling the measurement of voltage changes in the mV range, as opposed to the sub-nanoampere sub-nA range of current like in the standard read-out methods.

	<b>Top-Gate</b>	<b>Back-Gate (<math>V_{BG} = 15V</math>)</b>	<b>Constant Current</b>
<b>Buffer dilution</b>	10-fold	10-fold	10-fold
<b>Detected Concentration range (<math>\mu\text{g/mL}</math>)</b>	No detection	0.06 - 100	0.04 - 100
<b>LoD (<math>\mu\text{g/mL}</math>)</b>	NA	0.86	0.16
<b>Maximum quantity shift (0 - 100 <math>\mu\text{g/mL}</math>)</b>	NA	$\approx 1.2$ nA	$\approx 500$ mV
<b>Relative sensitivity @ 25 <math>\mu\text{g/mL}</math></b>	NA	125%	70%
<b>SNR @ 25 <math>\mu\text{g/mL}</math> (dB)</b>	NA	24.21	30.55
<b>Average SNR (dB)</b>	NA	18.15	18.43

**Table 5.1:** CRP electrical detection methods performance comparison in 0.1xPBS.

## 5.2 Summary

In this chapter, we characterized the response of our properly functionalized sensors toward C-Reactive protein in 0.1xPBS buffer. We found that a standard top-gate configuration could not achieve protein sensing in buffer with high ionic strength due to the Debye screening effect. However, we amplified the signal response by exploiting the back-gate configuration of our system, and the asymmetrical geometry of the back-gate and gate oxide. By exploiting a reference-compensated configuration and back-gate read-out, we demonstrated great stability during blank buffer injections, with a rate as low as 0.19 pA/minute, and CRP response in the physiological range of interest (0.06  $\mu\text{g/mL}$  to 100  $\mu\text{g/mL}$ ). We found relative drain current shifts higher than 120 % for CRP concentration of 10  $\mu\text{g/mL}$  when the sensor is operated in a back-gate configuration and weak inversion regime.

Lastly, we reported preliminary results on the constant current method while detecting CRP in 0.1xPBS buffer. These results showed tremendous capabilities, with output voltage change higher than 400 mV for specific CRP concentration ranges, relative voltage sensitivity up to 80%, and a high signal-to-noise ratio.

A comparison table to compare the C-Reactive sensing performance of the SiNW arrays in 0.1x buffer while operating the sensor in different configurations is reported below.

We reported successful CRP detection, providing both current and voltage output, with a low limit of detection ( $< 0.9$   $\mu\text{g/mL}$ ), low temporal drift, and high signal-to-noise ratios.



## 6 Conclusions and future perspective

*In this final chapter, the main achievements presented in this manuscript are summarized in the first section, to highlight the most important contributions. In the second section, the future perspective is presented to the reader, together with the possible improvements and future steps.*

### 6.1 Main achievements

#### 1. High-performance SiNW array FETs biosensing platform

The top-down fabrication of SiNW arrays posed a difficult task due to the many technological challenges. The resulting chip possesses identical copies of SiNW arrays, that can be separately functionalized to achieve multi-markers detection and/or reference compensated measurements. The design of the chip allows the presence of an on-chip Ag/AgCl reference electrode and the integration with a microfluidic system that dispenses low volumes ( $< 10 \mu\text{L}$ ) of the liquid under test. The double-gate structure of the SiNWs FETs enables an internal signal amplification: the in-house fabricated chips ensure an amplification factor of 3. The fabricated SiNWs FETs are characterized by an optimal subthreshold slope of 80 mV/decade, an ON/OFF ratio larger than 6 orders of magnitude, and a maximum transconductance of  $30 \text{ V}^{-1}$ . Doping parameters were accurately extracted through simulation-based techniques, resulting in optimal ohmic contacts for the source and drain regions on thin Si on SOI.

#### 2. High- $\kappa$ surface functionalization protocol assessment

A complete study of the antibody fragments immobilization protocol on the  $\text{HfO}_2$  surface has been carried out to demonstrate the high-quality functionalization layer essential to obtain a stable and selective response to C-Reactive protein in complex biofluids. Standard silanization chemistry has been transferred from silicon dioxide surfaces to high- $\kappa$  dielectrics. By means of characterization techniques such as X-Ray Spectroscopy and Quartz Crystal Microbalance study, the adopted functionalization layer has demonstrated low temporal drift, the absence of unspecific binding, and the ability to be used in reference-compensated techniques. The

chosen anti-CRP fragments have been tested by means of surface plasmon resonance, to prove their capability of selectively detecting CRP in ISF-like solution in the desired physiological range between 0.1  $\mu\text{g}/\text{mL}$  and 100  $\mu\text{g}/\text{mL}$ .

### 3. pH monitoring in buffer and human biofluids

The Fully-Depleted SiNW FETs have proven to be excellent candidates for real-time pH monitoring. This technology platform has demonstrated exceptional performance in both buffers and ISF-like solutions (3-fold diluted human serum), exhibiting quasi-Nernstian sensitivity in both cases. pH monitoring has been successfully demonstrated in both static and real-time modes, showing low temporal drift and high reproducibility. After calibration in human serum, these sensors have shown remarkable accuracy in measuring pH in collected serum from different individuals, with an error as small as 0.9% and a low dependence on the tested matrix. Repeated measurements using the sensors fabricated at CEA-LETI and CMi (EPFL) have consistently shown Nernstian sensitivity. In the case of CEA-LETI sensors, sweeping the back-gate voltage has allowed for an amplification factor as high as 50 times, whereas in-house fabricated sensors achieved a more limited amplification factor of 3. Conversely, the CMi sensors employ a smaller back-gate voltage, striking an optimal trade-off between power consumption and amplification.

### 4. CRP detection in the human physiological range

C-Reactive Protein (CRP) detection has been successfully conducted in static mode under various conditions. The monitoring of CRP within the range of 0.1  $\mu\text{g}/\text{mL}$  to 100  $\mu\text{g}/\text{mL}$  has been repeatedly demonstrated using a 100-time diluted PBS buffer in a top-gate configuration, yielding a sensitivity of up to 20 mV/decade. However, it should be noted that protein detection in this configuration has been limited to 0.01xPBS due to the presence of higher ionic strength, which prevents the detection of proteins by causing Debye screening effects. To overcome this limitation, the sensors have been operated in a back-gate configuration, leveraging the high amplification factor and signal-to-noise improvements. In this mode, the detection of CRP within the physiological range has been successfully demonstrated using 10-time diluted buffers. The stability of the sensor has been confirmed through repeated injections of blank buffers. Notably, the sensitivity of the sensor was dependent on the operational bias, with the highest sensitivity achieved in the weak inversion regime.

### 5. Preliminary results on a novel read-out constant current method

A novel approach based on the injection of a constant current on the transistor channel has been proposed and experimentally demonstrated, showing that the appropriate selection of constant-current bias mode and inversion region of silicon nanowire FETs leads to significant signal output amplification and improved sensitivity in biosensing. This approach not only

simplifies the readout circuit and reduces power consumption but also enables continuous pH sensing in human interstitial fluid-like solutions. The pH sensing results exhibited a sensitivity exceeding 400 mV/pH and an error lower than 1% when compared to a pH benchtop system. Furthermore, a proof of concept was developed to demonstrate the potential benefits of signal amplification in protein sensing, specifically highlighting enhanced performance in the detection of CRP in 0.1X PBS compared to the top-gate configuration. However, further investigations are required to quantitatively evaluate the amplification mechanism, and additional characterizations are needed to assess the long-term performance of the pH and CRP sensors. The findings of this study emphasize that utilizing the constant current method with optimized current levels and control of non-linear response can offer remarkable trade-offs, including improved sensitivity, stability, and low power consumption, for real-time continuous sensing of pH and CRP in human interstitial fluids.

## 6.2 Future Perspective

This section presents a few suggestions for further exploration and continuation of the research presented in this thesis.

### 1. Cross-sensitivity and temperature dependence

Thanks to the utilization of the same NWs structure for pH and CRP sensing, integrating both sensors simultaneously becomes a straightforward task for future research. An essential test to conduct would be investigating the influence of pH changes on the CRP detection response across all the utilized electrical configurations. The pH response in ISF-like solutions has been demonstrated in Chapter 4, and the influence on the pH response of various protein concentrations has been excluded. In the performed experiment involving CRP detection, the pH level has been kept constant. Therefore, to comprehensively examine the potential variations in performance, it is important to conduct an in-depth investigation of the possible changes in performance due to pH variations.

Another crucial parameter in biosensing is temperature. Different temperatures can alter the kinetics of the affinity-based detection system and affect transducer performance. Therefore, integrating an on-chip temperature sensor becomes paramount for future endeavors and should be regarded as a primary task.

### 2. On-chip readout integration

As described at the beginning of this manuscript, this project is part of a large European Consortium involving different partners, whose objective is to deliver an Edge-AI-based Digital Twin system. The goal of this work was to develop a biosensor system that could monitor different biomarkers in ISF, while other partners develop the read-out circuit and the

microneedles extractor systems.

Preliminary experiments have been carried out to ensure the compatibility of the read-out chip developed at imec, [203], Belgium, with the SiNW FET sensors, as described in Chapter 4, Section 4.2. Figure D.1 shows the setup of the first trial of joint experiments. The obtained results have shown compatibility between the two systems while measuring pH in a buffer, but further demonstrations have to be carried out to enhance the integration of the two systems, and the use of an on-chip reference electrode.

### **3. Simultaneous pH and lactate monitoring, and multiplexed biomarkers monitoring**

Preliminary experiments were conducted to simultaneously measure pH and lactate variations using in-house designed and fabricated sensors, along with an externally provided read-out circuit. However, issues arose due to the incompatible simultaneous measurements offered by the read-out chip. An important future step involves implementing continuous and simultaneous pH and lactate measurements. This presents an additional challenge as the amperometric detection process of lactate oxidation can locally alter the pH of the solution. Consequently, the pH and lactate measurements should be carried out in separate ISF volumes. Achieving this would require the implementation of a passive microfluidic system capable of splitting the extracted ISF into two chambers. While numerous challenges lie ahead for the implementation of this dual sensor, the necessary sensor technology already exists within the team, and continuous efforts are being made to achieve this objective.

The proposed sensor aims to monitor C-Reactive Protein (CRP) within the physiological range. This biomarker has been selected for several reasons, including its relatively higher concentrations compared to other relevant biomarkers. Additionally, various physical parameters, proteins, molecules, or hormones can offer crucial information for developing a Digital Twin. The flexible SiNWs platform allows for the detection of different proteins, thereby enabling multiplexed biomarker monitoring. Future investigations should focus on modifying the functionalization layer to accommodate the affinity-based detection of additional proteins. Different antibodies and aptamers can be utilized as specific probes for other proteins, such as cortisol. Therefore, the CRP sensor designed and proposed in this study can be adapted for the detection of various proteins.

### **4. Sensors integration on microneedles extractor**

The integrated sensor system, illustrated in Figure 1.6, aims to combine the sensing platform with the silicon microneedles system, which is responsible for ISF extraction and is designed and fabricated by consortium partners. The in-house fabricated SiNWs chips have been specifically designed to be compatible with the microneedles chip, but the development of a suitable intermediate layer is necessary. The microfluidic interposer must transport the liquid from the back of the microneedles chip to the sensor surface, enabling a passive and

continuous flow of fresh ISF. Since ISF does not clot, the sensor chip can be plugged into a wearable patch and replaced with a new sensor when required. Designing the integrated system presents several challenges, with the primary one being the handling of low-volume extraction. The microfluidic component must be capable of accommodating small volumes, ranging from 1 to 5  $\mu\text{L}$ , in order to align with the microneedles chip's extraction capabilities.

### 5. Constant current method investigation

The previous chapter of this work presented preliminary results on real-time C-Reactive Protein (CRP) monitoring using the constant-current method. However, further investigations are required to optimize and validate this method, particularly in terms of its ability to measure CRP in undiluted buffers and complex matrices. Another crucial step involves designing, fabricating, and testing the on-chip read-out circuit necessary for the CRP monitoring system. Furthermore, it is essential to conduct an in-depth study on the reproducibility and device-to-device variability of this method, considering that it relies on a non-ideal mechanism like the channel modulation effect in field-effect transistors. Such analysis will provide valuable insights into the performance consistency of the system.

### 6. Non-equilibrium methods

The previous chapter's results have demonstrated the limitations of sensing C-Reactive Protein (CRP) in undiluted buffers using the top-gate configuration, thus further exploration of alternative methods is necessary. In this regard, non-equilibrium methods hold promising potential. While the presented work focused solely on DC detection, the application of an AC signal could enhance the sensor response by overcoming Debye screening in high ionic strength solutions. Therefore, investigating the use of AC signals is an avenue that should be pursued to improve CRP sensing capabilities.

## 6.3 Concluding remarks

The implementation of Edge-AI technologies plays a crucial role in collecting data for the development of a Digital Twin. Undoubtedly, biosensors hold immense significance in this regard. This thesis has laid the groundwork for the realization of multiplexed biosensors that are highly selective and sensitive. These biosensors are based on Fully-Depleted silicon nanowires field-effect transistors, offering exceptional integration capabilities and low-power sensing.

In conclusion, the results obtained and summarized in Section 6.1 serve as a solid starting point for the development of a sensing integrated circuit. This circuit can seamlessly integrate with wearable sensing devices and low-invasive technologies, enabling a wide range of applications in the field of biosensing.





# A Runcard of SiNWs fabrication

No	Process	Equipment	Recipe	Target
<b>1</b>	<b>RCA cleaning</b>			
1.1	RCA1	RCA baths	H <sub>2</sub> O:NH <sub>4</sub> OH:H <sub>2</sub> O <sub>2</sub> 5:1:1 / 5 min, T = 75°C	
1.2	Oxide removal	RCA baths	HF:H <sub>2</sub> O 1:10 / 15 s, T = 20°C	
1.3	RCA2	RCA baths	H <sub>2</sub> O:HCl:H <sub>2</sub> O <sub>2</sub> 6:1:1 / 5 min, T = 75°C	
<b>2</b>	<b>Si thinning</b>			
2.1	Thermal oxidation	Centrotherm furnace	Si/SiO <sub>2</sub> consumption 0.44	86 nm of SiO <sub>2</sub>
2.2	Oxide etching	Plade Oxide wetbench	BHF 7:1	2 min
<b>3</b>	<b>Oxide stop layer</b>			
3.1	Thermal oxidation	Centrotherm furnace	Si/SiO <sub>2</sub> consumption 0.44	6 nm of SiO <sub>2</sub>
<b>4</b>	<b>Dicing</b>			
4.1	Surface treatment	Thermal dehydration	120°C - 300s	
4.2	Coating	Sawatec SM-200	AZ 1512 - 5000 RPM	1.1 μm
4.3	Soft-bake	Hot-plate	100°C - 1 min 5 s	1.1 μm
4.4	Dicing			
4.5	Photoresist clearing	UFT resist	Remover 1165 - 70°C 5 min	
<b>5</b>	<b>Markers creation</b>			
5.1	Surface treatment	Thermal dehydration	180°C - 300 s	
5.2	Coating	ATMsse OPTIspin SB20	CSAR - 2000RPM	600 nm
5.3	Soft-bake	Hot-plate	180°C - 300 s	1.1 μm
5.4	Exposure	Raith EPBG5000+	Dose 2000 μC/cm <sup>2</sup>	CD = 20 μm
5.5	Development	Amyl-Acetate	1 min 50 s (stir)	
5.6	Rinse	90:10 MiBK:IPA	1 min	

The runcard continues on next page.

No	Process	Zone/Equipment	Recipe	Target
<b>6</b>	<b>Markers etching</b>			
6.1	SiO <sub>2</sub> /Si etching	AMS200	CHECK LOG	2 μm depth
<b>7</b>	<b>Resist clearing</b>			
7.1	Plasma oxygen	Tepla GiGAbatch	30 s, 600 W, O <sub>2</sub> flow 400sccm	
7.2	Photoresist clearing	UFT resist	Remover 1165 - 70°C 5 min	
<b>8</b>	<b>Implantation</b>			
8.1	HMDS priming	SSE VB20	HMDS standard - 135°C	
8.2	Coating	Sawatec SM-200	AZECI 3007 - 2000RPM	1.0 μm
8.3	Soft-bake	Hot-plate	90°C - 60 s	
8.4	Exposure	Heidelberg MLA2	Dose 155 mJ/cm <sup>2</sup> , defoc 0	Laser 405 nm
8.5	Post-exposure bake	Hotplate	100°C - 60 s	
8.6	Development	AZ 726 MIF	30 s	
8.7	Shipment to IBS			
8.8	Implantation	standard P	1.6 keV, N <sub>D</sub> = 6 × 10 <sup>15</sup>	
<b>9</b>	<b>Resist clearing</b>			
9.1	Plasma oxygen	Tepla GiGAbatch	60 s, 600 W, O <sub>2</sub> flow 400sccm	
9.2	Photoresist clearing	UFT resist	Remover 1165 - 70°C 2 h	
<b>10</b>	<b>Dopant Activation</b>			
10.1	Rapid Thermal Annealing	Jetfirst200	7 s above 900°C forming gas	
<b>11</b>	<b>Stop Oxide removal</b>			
11.1	Oxide etching	Plade Oxide wetbench	BHF 7:1	30s
<b>12</b>	<b>SiNWs formation</b>			
12.1	Surface treatment	Thermal dehydration	180°C - 300 s	
12.2	Coating	ATMsse OPTIspin SB20	HSQ 2% - 6000RPM	30 nm
12.3	Exposure	Raith EPBG5000+	Dose 2000 μC/cm <sup>2</sup>	CD = 100 nm
12.5	Development	TMAH 25%	40 s	
<b>13</b>	<b>Silicon etching</b>			
13.1	Excess Si etching	AMS200	Si-opto-HR-20deg 28 s	SiO <sub>2</sub> carrier
<b>14</b>	<b>HSQ clearing</b>			
14.1	HSQ removal	Arias Acid wetbench	HF 1%, 45 s	
14.2	HSQ removal	Plade Oxide wetbench	Quick dip in BHF	

The runcard continues on next page.

No	Process	Zone/Equipment	Recipe	Target
<b>15</b>	<b>S and D opening</b>			
15.1	HMDS priming	SSE VB20	HMDS standard - 135°C	
15.2	Coating	Sawatec SM-200	AZ1512 - 5000RPM	1.1 $\mu\text{m}$
15.3	Soft-bake	Hot-plate	100°C - 65 s	
15.4	Exposure	Heidelberg MLA2	Dose 50 mJ/cm <sup>2</sup> , defoc -2	Laser 405 nm
15.5	Development	AZ 726 MIF	30 s	
15.6	Descum	Tepla GiGAbatch	20 s, 200 W, O <sub>2</sub> flow 200sccm	
15.7	Native Oxide removal	Plade Oxide wetbench	Quick dip in BHF	
<b>16</b>	<b>Stop layer deposition</b>			
16.1	Metal deposition	LAB600	Ti-Pt-Ti 5-35-3 nm	
16.2	Lift-off	Remover 1175	overnight	
<b>17</b>	<b>Gate oxide</b>			
17.1	HfO <sub>2</sub> gate oxide	ALD 1	70 cycles	7 nm
<b>18</b>	<b>Field oxide</b>			
18.1	Al <sub>2</sub> O <sub>3</sub> encapsulation	ALD 1	460 cycles	50 nm
<b>19</b>	<b>S and D opening</b>			
19.1	Surface treatment	Thermal dehydration	120°C - 300 s	
19.2	Coating	Sawatec SM-200	AZ1512 - 5000RPM	1.1 $\mu\text{m}$
19.3	Soft-bake	Hot-plate	100°C - 65 s	
19.4	Exposure	Heidelberg MLA2	Dose 50 mJ/cm <sup>2</sup> , defoc -2	Laser 405 nm
19.5	Development	AZ 726 MIF	30 s	
19.6	Descum	Tepla GiGAbatch	20 s, 200 W, O <sub>2</sub> flow 200sccm	
<b>20</b>	<b>S and D opening</b>			
20.1	Ion Beam Etching	Veeco IBE	Low IBE - 162 s	
20.2	Plasma oxygen	Tepla GiGAbatch	30 s, 600 W, O <sub>2</sub> flow 400sccm	
20.3	Resist clearing	Remover 1175	overnight	
<b>21</b>	<b>Metal lines mask</b>			
21.1	Surface treatment	Thermal dehydration	120°C - 300 s	
21.2	Coating	Sawatec SM-200	AZ1512 - 5000RPM	1.1 $\mu\text{m}$
21.3	Soft-bake	Hot-plate	100°C - 65 s	
21.4	Exposure	Heidelberg MLA2	Dose 50 mJ/cm <sup>2</sup> , defoc -2	Laser 405 nm
21.5	Development	AZ 726 MIF	30 s	
21.6	Descum	Tepla GiGAbatch	20 s, 200 W, O <sub>2</sub> flow 200sccm	

The runcard continues on next page.

No	Process	Zone/Equipment	Recipe	Target
<b>22</b>	<b>Metal deposition</b>			
22.1	Metal deposition	LAB600	Ti-Pt-Ti 5-65 nm	
22.2	Lift-off	Remover 1175	overnight	
<b>23</b>	<b>Passivation</b>			
23.1	Al <sub>2</sub> O <sub>3</sub> encapsulation	ALD 1	720 cycles	100 nm
<b>24</b>	<b>Passivation opening</b>			
24.1	HMDS priming	SSE VB20	HMDS standard - 135°C	
24.2	Coating	Sawatec SM-200	AZ1512 - 5000RPM	1.1 μm
24.3	Soft-bake	Hot-plate	100°C - 65 s	
24.4	Exposure	Heidelberg MLA2	Dose 55 mJ/cm <sup>2</sup> , defoc -2	Laser 405 nm
24.5	Development	AZ 726 MIF	30 s	
24.6	Descum	Tepla GiGAbatch	20 s, 200 W, O <sub>2</sub> flow 200sccm	
25.6	Al <sub>2</sub> O <sub>3</sub> etching	Arias Acid wetbench	H <sub>3</sub> PO <sub>4</sub> 60°C, 2 min	
20.3	Resist clearing	Remover 1175	overnight	

## B TEM lamella preparation

In this Annex, additional images (Figure B.1) about the lamella preparation are reported. The TEM lamella has been prepared with a Zeiss CrossBeam 540, a combined FIB and SEM system. The Lamella preparation has been performed at the EPFL Interdisciplinary Centre for Electron Microscopy (CiME), in Lausanne.

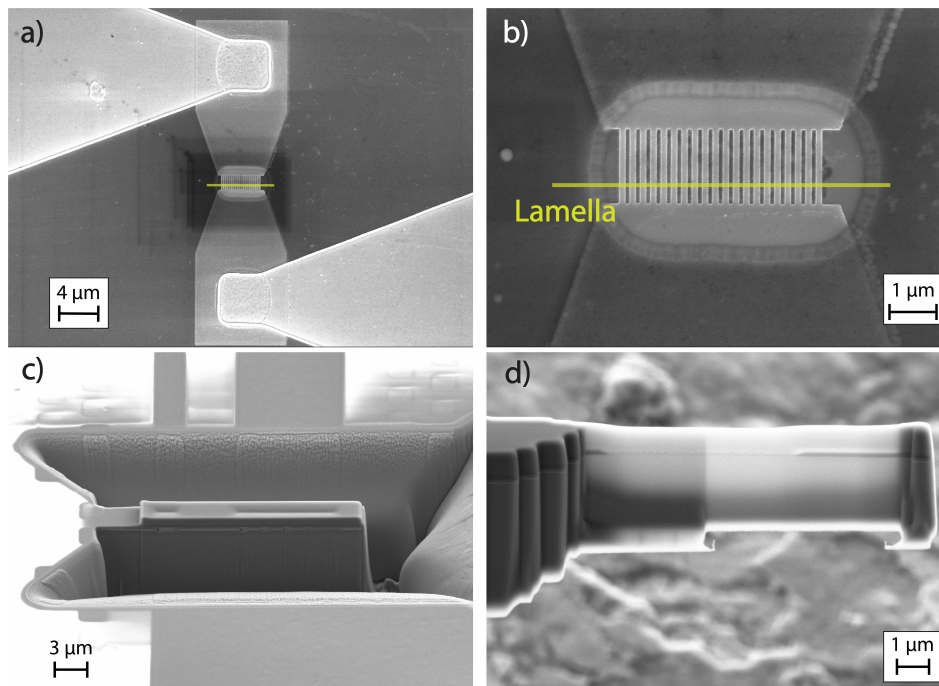


**Figure B.1:** TEM lamella preparation, performed at CiME. a) SEM image of the chosen device: 20 parallel SiNWs distanced by 100nm, each of them has a width of 100nm, and a length of 1.6  $\mu\text{m}$ . The yellow line indicates the position where the lamella is extracted. b) Magnified image of the selected SiNW array. It is possible to notice the passivation opening. The yellow line indicates the position where the lamella is extracted. c) Suspended lamella, before transferring to the TEM lamella support. Only one side is still linked to the chip. d) Finalized lamella. Two different thicknesses are visible for the two halves, according to the electron transparency.

Figure B.2 shows two diffraction patterns acquired during the TEM analysis of the lamella. The figure on the left represents the crystalline diffraction pattern of the bulk silicon, while the figure on the right represents the diffraction pattern of the thin silicon layer on the insulator. The two patterns can be perfectly overlapped, indicating the same crystal orientation. On the top part of the Figure on the right no pattern is visible, due to the amorphous hafnium dioxide gate oxide layer.

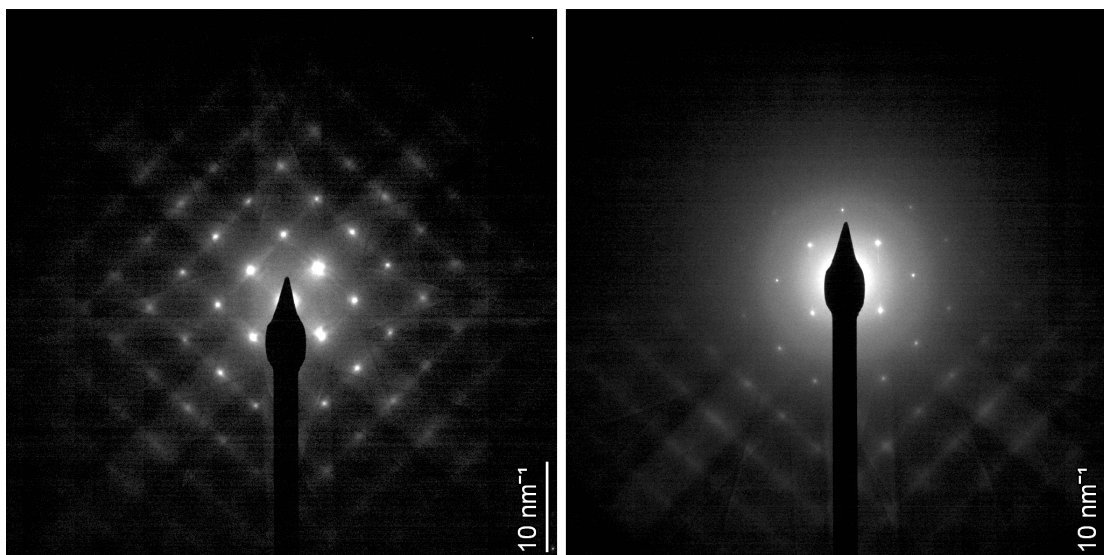


**Figure B.2:** TEM diffraction patterns for the silicon bulk and the thin silicon layer.

# C Script for source and drain implantation TCAD simulation

This appendix contains the scripts for the Ssprozess compiler used for the simulation of the source and drain phosphorous implantation.

```
set SDdose @dose@
set SDenergy @energy@
set oxmask @OxideMaskThickness@

AdvancedCalibration
AdvancedModels

pdbSet ImplantData MonteCarlo 1

pdbSet MCImplant model sentaurus.mc

#--- 2D Grid definition -----
line x location = 0.0 spacing = 0.2<nm> tag= SiliconTop
line x location = 27<nm> spacing = 0.8<nm> tag= SiliconBottom
line x location = 47<nm> spacing = 2<nm> tag = BOXBottom
line y location = 0.0 spacing = 20<nm> tag= BOXLeft
line y location = 1<um> spacing =20<nm> tag= BOXRight

#--- Initial simulation domain -----
region Silicon xlo= SiliconTop xhi=SiliconBottom ylo= BOXLeft yhi= BOXRight
region Oxide xlo= SiliconBottom xhi= BOXBottom ylo= BOXLeft yhi= BOXRight

#--- Initialize the simulation -----
init concentration = 1e15<cm-3> field = Boron wafer.orient = 100

#--- MGOALS settings for automatic meshing in newly generated layers -
mgoals min.normal.size = 1<nm> max.lateral.size = 0.2<um>
normal.growth.ratio = 1.4

# graphics configure = " xyshow = Phosphorous *"
```



```
# graphics on

#--- Mask Definition -----

mask name = implant_mask segments = { -1<nm> 500<nm> 1500<nm> 2001<nm> }
# deposit Si type = isotropic thickness =27<nm>
deposit oxide type = isotropic thickness = $oxmask
# deposit oxide type = isotropic thickness = $oxmask
# etch oxide type = anisotropic thickness = $oxmask mask = implant_mask
photo thickness=2<um> mask=implant_mask

#--- Implanting P -----

# Analytic implantation models use the simple Gaussian and Pearson as
# well as the advanced dual Pearson functions . The implantation damage with
# analytic models is calculated according to the Hobler model

implant Phosphorus energy = $SDenergy dose = $SDdose tilt = 7<degree>
rotation = 0<degree> ion.movie

# The MC method uses a statistical approach to the
# calculation of the penetration of implanted ions into the target and
# accumulation of crystal damage based on the binary collision approximation

#--- Plotting out the "As implanted " profile -----

struct tdr= n@node@_2Dimplant
SetPlxList

#--- Rapid Thermal Annealing -----

diffuse temperature = 180<C> time = 10.0<s> N2
diffuse temperature = 180<C> time = 5.0<s> N2 ramprate = 24<C/s>
diffuse temperature = 300<C> time = 20.0<s> N2
diffuse temperature = 300<C> time = 10.0<s> N2 ramprate = 70<C/s>
diffuse temperature = 1000<C> time = 5.0<s> N2

#--- Plotting out the " Annealed " profile -----

struct tdr= n@node@_2Danneal
SetPlxList { Damage }
```

## D Read-out circuit and sensor demonstrator: setup

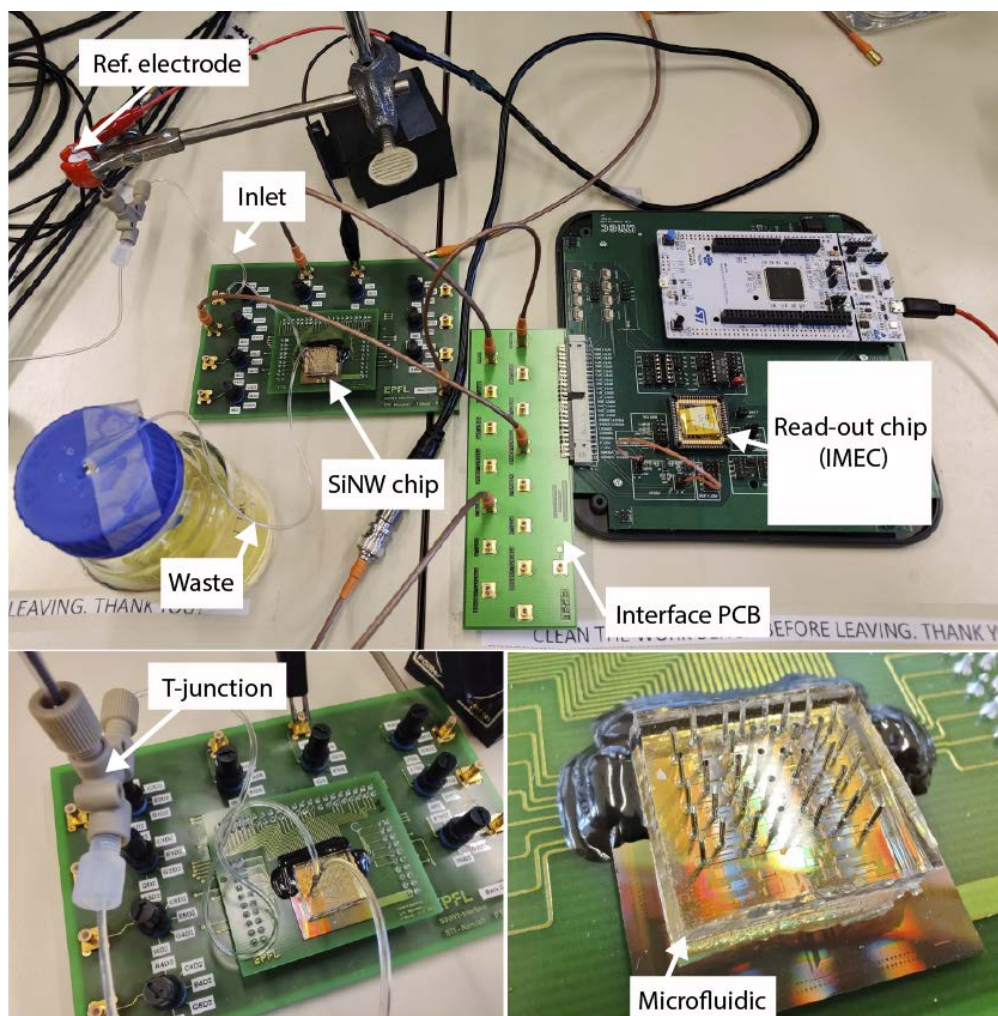


**Figure D.1:** Biosensor and chip-readout [203] system setup during the first demonstrator.



## Bibliography

- [1] *DIGIPREDICT Project*. My Website. URL: <https://www.digipredict.eu/> (visited on 05/13/2023).
- [2] Lieke Bakkerus and Peter Pickkers. “Personalized medicine in COVID-19”. In: *Intensive Care Medicine* 48.11 (Nov. 1, 2022), pp. 1607–1610. ISSN: 1432-1238. DOI: 10.1007/s00134-022-06908-6. URL: <https://doi.org/10.1007/s00134-022-06908-6> (visited on 04/02/2023).
- [3] Laura Teodori, Barbara Osimani, Ciro Isidoro, and Seeram Ramakrishna. “Mass versus personalized medicine against COVID-19 in the “system sciences” era”. In: *Cytometry Part A* 101.12 (2022), pp. 995–999. ISSN: 1552-4930. DOI: 10.1002/cyto.a.24662. URL: <https://onlinelibrary.wiley.com/doi/abs/10.1002/cyto.a.24662> (visited on 04/02/2023).
- [4] Bianca N. Valdés-Fernández, Jorge Duconge, Ana M. Espino, and Gualberto Rúaño. “Personalized health and the coronavirus vaccines—Do individual genetics matter?” In: *BioEssays* 43.9 (2021), p. 2100087. ISSN: 1521-1878. DOI: 10.1002/bies.202100087. URL: <https://onlinelibrary.wiley.com/doi/abs/10.1002/bies.202100087> (visited on 04/02/2023).
- [5] Joaquín Dopazo, Douglas Maya-Miles, Federico García, Nicola Lorusso, Miguel Ángel Calleja, María Jesús Pareja, José López-Miranda, Jesús Rodríguez-Baño, Javier Padillo, Isaac Túnez, and Manuel Romero-Gómez. “Implementing Personalized Medicine in COVID-19 in Andalusia: An Opportunity to Transform the Healthcare System”. In: *Journal of Personalized Medicine* 11.6 (May 26, 2021), p. 475. ISSN: 2075-4426. DOI: 10.3390/jpm11060475. URL: <https://www.ncbi.nlm.nih.gov/pmc/articles/PMC8226500/> (visited on 04/02/2023).
- [6] Mohd Arish and Farha Naz. “Personalized therapy: can it tame the COVID-19 monster?” In: *Personalized Medicine* 18.6 (Nov. 2021). Publisher: Future Medicine, pp. 583–593. ISSN: 1741-0541. DOI: 10.2217/pme-2021-0077. URL: <https://www.futuremedicine.com/doi/10.2217/pme-2021-0077> (visited on 04/02/2023).
- [7] Florinel-Gabriel Banica. *Chemical Sensors and Biosensors: Fundamentals and Applications*. Google-Books-ID: 3m3qaVQdK3sC. John Wiley & Sons, Aug. 15, 2012. 834 pp. ISBN: 978-1-118-35423-0.

- [8] N Fogh-Andersen, B M Altura, B T Altura, and O Siggaard-Andersen. "Composition of interstitial fluid". In: *Clinical Chemistry* 41.10 (Oct. 1, 1995), pp. 1522–1525. ISSN: 0009-9147. DOI: 10.1093/clinchem/41.10.1522. URL: <https://doi.org/10.1093/clinchem/41.10.1522> (visited on 04/04/2023).
- [9] *Interstitial fluid volume: local regulatory mechanisms*. DOI: 10.1152/physrev.1981.61.3.556. URL: <https://journals.physiology.org/doi/epdf/10.1152/physrev.1981.61.3.556?src=getftr> (visited on 04/04/2023).
- [10] *Interstitial fluid - Definition and Examples - Biology Online Dictionary*. Biology Articles, Tutorials & Dictionary Online. Oct. 7, 2019. URL: <https://www.biologyonline.com/dictionary/interstitial-fluid> (visited on 04/04/2023).
- [11] Pradnya P. Samant, Megan M. Niedzwiecki, Nicholas Raviele, Vilinh Tran, Juan Mena-Lapaix, Douglas I. Walker, Eric I. Felner, Dean P. Jones, Gary W. Miller, and Mark R. Prausnitz. "Sampling interstitial fluid from human skin using a microneedle patch". In: *Science Translational Medicine* 12.571 (Nov. 25, 2020). Publisher: American Association for the Advancement of Science, eaaw0285. DOI: 10.1126/scitranslmed.aaw0285. URL: <https://www.science.org/doi/10.1126/scitranslmed.aaw0285> (visited on 04/04/2023).
- [12] Philip R. Miller, Robert M. Taylor, Bao Quoc Tran, Gabrielle Boyd, Trevor Glaros, Victor H. Chavez, Raga Krishnakumar, Anupama Sinha, Kunal Poorey, Kelly P. Williams, Steven S. Branda, Justin T. Baca, and Ronen Polsky. "Extraction and biomolecular analysis of dermal interstitial fluid collected with hollow microneedles". In: *Communications Biology* 1.1 (Oct. 22, 2018). Number: 1 Publisher: Nature Publishing Group, pp. 1–11. ISSN: 2399-3642. DOI: 10.1038/s42003-018-0170-z. URL: <https://www.nature.com/articles/s42003-018-0170-z> (visited on 04/20/2023).
- [13] Bao Quoc Tran, Philip R. Miller, Robert M. Taylor, Gabrielle Boyd, Phillip M. Mach, C. Nicole Rosenzweig, Justin T. Baca, Ronen Polsky, and Trevor Glaros. "Proteomic Characterization of Dermal Interstitial Fluid Extracted Using a Novel Microneedle-Assisted Technique". In: *Journal of Proteome Research* 17.1 (Jan. 5, 2018). Publisher: American Chemical Society, pp. 479–485. ISSN: 1535-3893. DOI: 10.1021/acs.jproteome.7b00642. URL: <https://doi.org/10.1021/acs.jproteome.7b00642> (visited on 04/20/2023).
- [14] *Skin Anatomy: Image Details - NCI Visuals Online*. URL: <https://visualsonline.cancer.gov/details.cfm?imageid=4604> (visited on 04/04/2023).
- [15] Farshad Tehrani, Hazhir Teymourian, Brian Wuerstle, Jonathan Kavner, Ravi Patel, Allison Furmidge, Reza Aghavali, Hamed Hosseini-Toudeshki, Christopher Brown, Fangyu Zhang, Kuldeep Mahato, Zhengxing Li, Abbas Barfidokht, Lu Yin, Paul Warren, Nickey Huang, Zina Patel, Patrick P. Mercier, and Joseph Wang. "An integrated wearable microneedle array for the continuous monitoring of multiple biomarkers in interstitial fluid". In: *Nature Biomedical Engineering* 6.11 (Nov. 2022). Number: 11 Publisher: Nature Publishing Group, pp. 1214–1224. ISSN: 2157-846X. DOI: 10.1038/s41551-022-00887-1. URL: <https://www.nature.com/articles/s41551-022-00887-1> (visited on 04/04/2023).

## BIBLIOGRAPHY

---

- [16] Federico Ribet, Annika Bendes, Claudia Fredolini, Mikolaj Dobielewski, Michael Böttcher, Olof Beck, Jochen M. Schwenk, Göran Stemme, and Niclas Roxhed. “Microneedle Patch for Painless Intradermal Collection of Interstitial Fluid Enabling Multianalyte Measurement of Small Molecules, SARS-CoV-2 Antibodies, and Protein Profiling”. In: *Advanced Healthcare Materials* n/a (n/a), p. 2202564. ISSN: 2192-2659. DOI: 10.1002/adhm.202202564. URL: <https://onlinelibrary.wiley.com/doi/abs/10.1002/adhm.202202564> (visited on 04/20/2023).
- [17] Maria T. Arévalo, Gabrielle M. Rizzo, Ronen Polsky, Trevor Glaros, and Phillip M. Mach. “Proteomic Characterization of Immunoglobulin Content in Dermal Interstitial Fluid”. In: *Journal of Proteome Research* 18.6 (June 7, 2019). Publisher: American Chemical Society, pp. 2381–2384. ISSN: 1535-3893. DOI: 10.1021/acs.jproteome.9b00155. URL: <https://doi.org/10.1021/acs.jproteome.9b00155> (visited on 04/20/2023).
- [18] Elise Laszlo, Gregory De Crescenzo, Alfonso Nieto-Argüello, Xavier Banquy, and Davide Brambilla. “Superswelling Microneedle Arrays for Dermal Interstitial Fluid (Prote)Omics”. In: *Advanced Functional Materials* 31.46 (2021), p. 2106061. ISSN: 1616-3028. DOI: 10.1002/adfm.202106061. URL: <https://onlinelibrary.wiley.com/doi/abs/10.1002/adfm.202106061> (visited on 04/20/2023).
- [19] Mark Friedel, Ian A. P. Thompson, Gerald Kasting, Ronen Polsky, David Cunningham, Hyongsok Tom Soh, and Jason Heikenfeld. “Opportunities and challenges in the diagnostic utility of dermal interstitial fluid”. In: *Nature Biomedical Engineering* (Jan. 19, 2023). Publisher: Nature Publishing Group, pp. 1–15. ISSN: 2157-846X. DOI: 10.1038/s41551-022-00998-9. URL: <https://www.nature.com/articles/s41551-022-00998-9> (visited on 04/20/2023).
- [20] John P Bantle and William Thomas. “Glucose measurement in patients with diabetes mellitus with dermal interstitial fluid”. In: *Journal of Laboratory and Clinical Medicine* 130.4 (Oct. 1, 1997), pp. 436–441. ISSN: 0022-2143. DOI: 10.1016/S0022-2143(97)90044-5. URL: <https://www.sciencedirect.com/science/article/pii/S0022214397900445> (visited on 04/21/2023).
- [21] P. Parini, L. Johansson, A. Bröijersén, B. Angelin, and M. Rudling. “Lipoprotein profiles in plasma and interstitial fluid analyzed with an automated gel-filtration system”. In: *European Journal of Clinical Investigation* 36.2 (2006), pp. 98–104. ISSN: 1365-2362. DOI: 10.1111/j.1365-2362.2006.01597.x. URL: <https://onlinelibrary.wiley.com/doi/abs/10.1111/j.1365-2362.2006.01597.x> (visited on 04/21/2023).
- [22] Manju Venugopal, Sunil K. Arya, Ganna Chornokur, and Shekhar Bhansali. “A real-time and continuous assessment of cortisol in ISF using electrochemical impedance spectroscopy”. In: *Sensors and Actuators A: Physical*. Euroensors XXIV, Linz, Austria, 5-8 September 2010 172.1 (Dec. 1, 2011), pp. 154–160. ISSN: 0924-4247. DOI: 10.1016/j.sna.2011.04.028. URL: <https://www.sciencedirect.com/science/article/pii/S0924424711002755> (visited on 04/21/2023).

- [23] Damien K. Ming, Saylee Jangam, Sally A. N. Gowers, Richard Wilson, David M. E. Freeman, Martyn G. Boutelle, Anthony E. G. Cass, Danny O'Hare, and Alison H. Holmes. "Real-time continuous measurement of lactate through a minimally invasive microneedle patch: a phase I clinical study". In: *BMJ Innovations* 8.2 (Apr. 1, 2022). Publisher: BMJ Specialist Journals Section: Medical devices. ISSN: 2055-8074, 2055-642X. DOI: 10.1136/bmjinnov-2021-000864. URL: <https://innovations.bmj.com/content/8/2/87> (visited on 04/25/2023).
- [24] Julia Madden, Conor O'Mahony, Michael Thompson, Alan O'Riordan, and Paul Galvin. "Biosensing in dermal interstitial fluid using microneedle based electrochemical devices". In: *Sensing and Bio-Sensing Research* 29 (Aug. 1, 2020), p. 100348. ISSN: 2214-1804. DOI: 10.1016/j.sbsr.2020.100348. URL: <https://www.sciencedirect.com/science/article/pii/S2214180420300064> (visited on 04/21/2023).
- [25] A.K. Nilsson, U. Sjöbom, K. Christenson, and A. Hellström. "Lipid profiling of suction blister fluid: Comparison of lipids in interstitial fluid and plasma". In: *Lipids in Health and Disease* 18.1 (2019). ISSN: 1476-511X. DOI: 10.1186/s12944-019-1107-3.
- [26] David Rodbard. "Continuous Glucose Monitoring: A Review of Successes, Challenges, and Opportunities". In: *Diabetes Technology & Therapeutics* 18 (S2 Feb. 2016). Num Pages: S2-13 Publisher: Mary Ann Liebert, Inc., publishers, S2-3. ISSN: 1520-9156. DOI: 10.1089/dia.2015.0417. URL: <https://www.liebertpub.com/doi/full/10.1089/dia.2015.0417> (visited on 04/04/2023).
- [27] Christer Svedman, Bing B. Yu, Terence J. Ryan, and Henry Svensson. "Plasma proteins in a standardised skin mini-erosion (II): effects of extraction pressure". In: *BMC Dermatology* 2.1 (Feb. 11, 2002), p. 4. ISSN: 1471-5945. DOI: 10.1186/1471-5945-2-4. URL: <https://doi.org/10.1186/1471-5945-2-4> (visited on 04/21/2023).
- [28] Christer Svedman, Bing B. Yu, Terence J. Ryan, and Henry Svensson. "Plasma proteins in a standardised skin mini-erosion (I): permeability changes as a function of time". In: *BMC Dermatology* 2.1 (Feb. 11, 2002), p. 3. ISSN: 1471-5945. DOI: 10.1186/1471-5945-2-3. URL: <https://doi.org/10.1186/1471-5945-2-3> (visited on 04/21/2023).
- [29] Arvind Jina, Michael J. Tierney, Janet A. Tamada, Scott McGill, Shashi Desai, Beelee Chua, Anna Chang, and Mark Christiansen. "Design, Development, and Evaluation of a Novel Microneedle Array-based Continuous Glucose Monitor". In: *Journal of Diabetes Science and Technology* 8.3 (May 1, 2014). Publisher: SAGE Publications Inc, pp. 483-487. ISSN: 1932-2968. DOI: 10.1177/1932296814526191. URL: <https://doi.org/10.1177/1932296814526191> (visited on 04/25/2023).
- [30] Zheyu Wang, Jingyi Luan, Anushree Seth, Lin Liu, Minli You, Prashant Gupta, Priya Rathi, Yixuan Wang, Sisi Cao, Qisheng Jiang, Xiao Zhang, Rohit Gupta, Qingjun Zhou, Jeremiah J. Morrissey, Erica L. Scheller, Jai S. Rudra, and Srikanth Singamaneni. "Microneedle patch for the ultrasensitive quantification of protein biomarkers in interstitial fluid". In: *Nature Biomedical Engineering* 5.1 (Jan. 2021). Number: 1 Publisher:

## BIBLIOGRAPHY

---

- Nature Publishing Group, pp. 64–76. ISSN: 2157-846X. DOI: 10.1038/s41551-020-00672-y. URL: <https://www.nature.com/articles/s41551-020-00672-y> (visited on 04/04/2023).
- [31] Hanjia Zheng, Amin GhavamiNejad, Peyman GhavamiNejad, Melisa Samarikhalaj, Adria Giacca, and Mahla Poudineh. “Hydrogel Microneedle-Assisted Assay Integrating Aptamer Probes and Fluorescence Detection for Reagentless Biomarker Quantification”. In: *ACS Sensors* 7.8 (Aug. 26, 2022). Publisher: American Chemical Society, pp. 2387–2399. DOI: 10.1021/acssensors.2c01033. URL: <https://doi.org/10.1021/acssensors.2c01033> (visited on 04/25/2023).
- [32] Muamer Dervisevic, Esmā Dervisevic, Lars Esser, Christopher D. Easton, Victor J. Cadarso, and Nicolas H. Voelcker. “Wearable microneedle array-based sensor for transdermal monitoring of pH levels in interstitial fluid”. In: *Biosensors and Bioelectronics* 222 (Feb. 15, 2023), p. 114955. ISSN: 0956-5663. DOI: 10.1016/j.bios.2022.114955. URL: <https://www.sciencedirect.com/science/article/pii/S0956566322009952> (visited on 04/20/2023).
- [33] Erin Hopkins, Terrence Sanvictores, and Sandeep Sharma. “Physiology, Acid Base Balance”. In: *StatPearls*. Treasure Island (FL): StatPearls Publishing, 2023. URL: <http://www.ncbi.nlm.nih.gov/books/NBK507807/> (visited on 05/11/2023).
- [34] Sujay Samanta, Ratender Kumar Singh, Arvind K. Baronia, Prabhaker Mishra, Banani Poddar, Afzal Azim, and Mohan Gurjar. “Early pH Change Predicts Intensive Care Unit Mortality”. In: *Indian Journal of Critical Care Medicine: Peer-Reviewed, Official Publication of Indian Society of Critical Care Medicine* 22.10 (Oct. 2018), pp. 697–705. ISSN: 0972-5229. DOI: 10.4103/ijccm.IJCCM\_129\_18.
- [35] I. Smith, P. Kumar, S. Molloy, A. Rhodes, P. J. Newman, R. M. Grounds, and E. D. Bennett. “Base excess and lactate as prognostic indicators for patients admitted to intensive care”. In: *Intensive Care Medicine* 27.1 (Jan. 1, 2001), pp. 74–83. ISSN: 1432-1238. DOI: 10.1007/s001340051352. URL: <https://doi.org/10.1007/s001340051352> (visited on 05/11/2023).
- [36] Yoshinori Marunaka. “Roles of interstitial fluid pH and weak organic acids in development and amelioration of insulin resistance”. In: *Biochemical Society Transactions* 49.2 (Mar. 26, 2021), pp. 715–726. ISSN: 0300-5127. DOI: 10.1042/BST20200667. URL: <https://doi.org/10.1042/BST20200667> (visited on 05/11/2023).
- [37] Dongun Lee and Jeong Hee Hong. “The Fundamental Role of Bicarbonate Transporters and Associated Carbonic Anhydrase Enzymes in Maintaining Ion and pH Homeostasis in Non-Secretory Organs”. In: *International Journal of Molecular Sciences* 21.1 (Jan. 2020). Number: 1 Publisher: Multidisciplinary Digital Publishing Institute, p. 339. ISSN: 1422-0067. DOI: 10.3390/ijms21010339. URL: <https://www.mdpi.com/1422-0067/21/1/339> (visited on 05/11/2023).



- [38] Cassandra A. A. Locatelli and Erin E. Mulvihill. “Islet Health, Hormone Secretion, and Insulin Responsivity with Low-Carbohydrate Feeding in Diabetes”. In: *Metabolites* 10.11 (Nov. 2020). Number: 11 Publisher: Multidisciplinary Digital Publishing Institute, p. 455. ISSN: 2218-1989. DOI: 10.3390/metabo10110455. URL: <https://www.mdpi.com/2218-1989/10/11/455> (visited on 05/11/2023).
- [39] Yoshinori Marunaka. “The Proposal of Molecular Mechanisms of Weak Organic Acids Intake-Induced Improvement of Insulin Resistance in Diabetes Mellitus via Elevation of Interstitial Fluid pH”. In: *International Journal of Molecular Sciences* 19.10 (Oct. 2018). Number: 10 Publisher: Multidisciplinary Digital Publishing Institute, p. 3244. ISSN: 1422-0067. DOI: 10.3390/ijms19103244. URL: <https://www.mdpi.com/1422-0067/19/10/3244> (visited on 05/11/2023).
- [40] Yoshinori Marunaka, Naomi Niisato, Xiaobo Zou, Jian Bo Xiao, and Takashi Nakahari. “Food intake targeting and improving acidity in diabetes and cancer”. In: *Food Frontiers* 1.1 (2020). \_eprint: <https://onlinelibrary.wiley.com/doi/pdf/10.1002/fft2.5>, pp. 9–12. ISSN: 2643-8429. DOI: 10.1002/fft2.5. URL: <https://onlinelibrary.wiley.com/doi/abs/10.1002/fft2.5> (visited on 05/11/2023).
- [41] Wataru Aoi, Xiaobo Zou, Jian Bo Xiao, and Yoshinori Marunaka. “Body Fluid pH Balance in Metabolic Health and Possible Benefits of Dietary Alkaline Foods”. In: *eFood* 1.1 (2020). \_eprint: <https://onlinelibrary.wiley.com/doi/pdf/10.2991/efood.k.190924.001>, pp. 12–23. ISSN: 2666-3066. DOI: 10.2991/efood.k.190924.001. URL: <https://onlinelibrary.wiley.com/doi/abs/10.2991/efood.k.190924.001> (visited on 05/11/2023).
- [42] J Sheldon, P Riches, R Gooding, N Soni, and J R Hobbs. “C-reactive protein and its cytokine mediators in intensive-care patients”. In: *Clinical Chemistry* 39.1 (Jan. 1, 1993), pp. 147–150. ISSN: 0009-9147. DOI: 10.1093/clinchem/39.1.147. URL: <https://doi.org/10.1093/clinchem/39.1.147> (visited on 05/10/2023).
- [43] Lorraine Marnell, Carolyn Mold, and Terry W. Du Clos. “C-reactive protein: Ligands, receptors and role in inflammation”. In: *Clinical Immunology* 117.2 (Nov. 1, 2005), pp. 104–111. ISSN: 1521-6616. DOI: 10.1016/j.clim.2005.08.004. URL: <https://www.sciencedirect.com/science/article/pii/S1521661605002809> (visited on 05/11/2023).
- [44] Nicola R. Sproston and Jason J. Ashworth. “Role of C-Reactive Protein at Sites of Inflammation and Infection”. In: *Frontiers in Immunology* 9 (Apr. 13, 2018), p. 754. ISSN: 1664-3224. DOI: 10.3389/fimmu.2018.00754. URL: <https://www.ncbi.nlm.nih.gov/pmc/articles/PMC5908901/> (visited on 05/11/2023).
- [45] Peter C. Hart, Ibraheem M. Rajab, May Alebraheem, and Lawrence A. Potempa. “C-Reactive Protein and Cancer—Diagnostic and Therapeutic Insights”. In: *Frontiers in Immunology* 11 (Nov. 19, 2020), p. 595835. ISSN: 1664-3224. DOI: 10.3389/fimmu.2020.595835. URL: <https://www.ncbi.nlm.nih.gov/pmc/articles/PMC7727277/> (visited on 05/11/2023).

## BIBLIOGRAPHY

---

- [46] Paul M Ridker. “Clinical Application of C-Reactive Protein for Cardiovascular Disease Detection and Prevention”. In: *Circulation* 107.3 (Jan. 28, 2003). Publisher: American Heart Association, pp. 363–369. DOI: 10.1161/01.CIR.0000053730.47739.3C. URL: <https://www.ahajournals.org/doi/10.1161/01.CIR.0000053730.47739.3C> (visited on 05/10/2023).
- [47] Pamela Sakkinen, Robert D. Abbott, J. David Curb, Beatriz L. Rodriguez, Katsuhiko Yano, and Russell P. Tracy. “C-reactive protein and myocardial infarction”. In: *Journal of Clinical Epidemiology* 55.5 (May 1, 2002), pp. 445–451. ISSN: 0895-4356. DOI: 10.1016/S0895-4356(01)00502-9. URL: <https://www.sciencedirect.com/science/article/pii/S0895435601005029> (visited on 05/10/2023).
- [48] Erik M. Stuvelling, Hans L. Hillege, Stephan J. L. Bakker, Reinold O. B. Gans, Paul E. de Jong, and Dick de Zeeuw. “C-reactive protein is associated with renal function abnormalities in a non-diabetic population”. In: *Kidney International* 63.2 (Feb. 1, 2003), pp. 654–661. ISSN: 0085-2538. DOI: 10.1046/j.1523-1755.2003.00762.x. URL: <https://www.sciencedirect.com/science/article/pii/S0085253815489197> (visited on 05/11/2023).
- [49] Martha Rodriguez-Moran and Fernando Guerrero-Romero. “Increased Levels of C-Reactive Protein in Noncontrolled Type II Diabetic Subjects”. In: *Journal of Diabetes and its Complications* 13.4 (July 1, 1999), pp. 211–215. ISSN: 1056-8727. DOI: 10.1016/S1056-8727(99)00047-1. URL: <https://www.sciencedirect.com/science/article/pii/S1056872799000471> (visited on 05/11/2023).
- [50] Martin A. Crook, Peter Tutt, Helen Simpson, and John C. Pickup. “Serum sialic acid and acute phase proteins in type 1 and type 2 diabetes mellitus”. In: *Clinica Chimica Acta* 219.1 (Oct. 15, 1993), pp. 131–138. ISSN: 0009-8981. DOI: 10.1016/0009-8981(93)90204-H. URL: <https://www.sciencedirect.com/science/article/pii/000989819390204H> (visited on 05/11/2023).
- [51] Milad Sharifpour, Srikant Rangaraju, Michael Liu, Darwish Alabyad, Fadi B. Nahab, Christina M. Creel-Bulos, Craig S. Jabaley, and on behalf of the Emory COVID-19 Quality {and} Clinical Research Collaborative. “C-Reactive protein as a prognostic indicator in hospitalized patients with COVID-19”. In: *PLOS ONE* 15.11 (Nov. 20, 2020). Publisher: Public Library of Science, e0242400. ISSN: 1932-6203. DOI: 10.1371/journal.pone.0242400. URL: <https://journals.plos.org/plosone/article?id=10.1371/journal.pone.0242400> (visited on 05/10/2023).
- [52] Jean-Remi Lavillegrand, Marc Garnier, Agathe Spaeth, Nathalie Mario, Geofroy Hariri, Antoine Pilon, Enora Berti, Fabienne Fieux, Sara Thietart, Tomas Urbina, Matthieu Turpin, Lucie Darrivere, Muriel Fartoukh, Franck Verdonk, Guillaume Dumas, Alain Tedgui, Bertrand Guidet, Eric Maury, Yannick Chantran, Guillaume Voiriot, and Hafid Ait-Oufella. “Correction to: Elevated plasma IL-6 and CRP levels are associated with adverse clinical outcomes and death in critically ill SARS-CoV-2 patients: inflammatory response of SARS-CoV-2 patients”. In: *Annals of Intensive Care* 11.1 (June 9, 2021), p. 93.

- ISSN: 2110-5820. DOI: 10.1186/s13613-021-00879-5. URL: <https://doi.org/10.1186/s13613-021-00879-5> (visited on 05/11/2023).
- [53] Nurshad Ali. “Elevated level of C-reactive protein may be an early marker to predict risk for severity of COVID-19”. In: *Journal of Medical Virology* 92.11 (2020). \_eprint: <https://onlinelibrary.wiley.com/doi/pdf/10.1002/jmv.26097>, pp. 2409–2411. ISSN: 1096-9071. DOI: 10.1002/jmv.26097. URL: <https://onlinelibrary.wiley.com/doi/abs/10.1002/jmv.26097> (visited on 05/11/2023).
- [54] Paul M Ridker, Julie E. Buring, Nancy R. Cook, and Nader Rifai. “C-Reactive Protein, the Metabolic Syndrome, and Risk of Incident Cardiovascular Events”. In: *Circulation* 107.3 (Jan. 28, 2003). Publisher: American Heart Association, pp. 391–397. DOI: 10.1161/01.CIR.0000055014.62083.05. URL: <https://www.ahajournals.org/doi/10.1161/01.CIR.0000055014.62083.05> (visited on 05/11/2023).
- [55] Paul M. Ridker, Nader Rifai, Lynda Rose, Julie E. Buring, and Nancy R. Cook. “Comparison of C-Reactive Protein and Low-Density Lipoprotein Cholesterol Levels in the Prediction of First Cardiovascular Events”. In: *New England Journal of Medicine* 347.20 (Nov. 14, 2002), pp. 1557–1565. ISSN: 0028-4793. DOI: 10.1056/NEJMoa021993. URL: <https://doi.org/10.1056/NEJMoa021993> (visited on 05/11/2023).
- [56] Chang-Hoon Kim, Jae-Hyuk Ahn, Jee-Yeon Kim, Ji-Min Choi, Kyung-Choon Lim, Tae Jung Park, Nam Su Heo, Hee Gu Lee, Jong-Wan Kim, and Yang-Kyu Choi. “CRP detection from serum for chip-based point-of-care testing system”. In: *Biosensors and Bioelectronics* 41 (Mar. 15, 2013), pp. 322–327. ISSN: 0956-5663. DOI: 10.1016/j.bios.2012.08.047. URL: <https://www.sciencedirect.com/science/article/pii/S0956566312005714> (visited on 07/26/2023).
- [57] Hee Ho Lee, Myunghan Bae, Sung-Hyun Jo, Jang-Kyoo Shin, Dong Hyeok Son, Chul-Ho Won, Hyun-Min Jeong, Jung-Hee Lee, and Shin-Won Kang. “AlGaIn/GaN High Electron Mobility Transistor-Based Biosensor for the Detection of C-Reactive Protein”. In: *Sensors* 15.8 (Aug. 2015). Number: 8 Publisher: Multidisciplinary Digital Publishing Institute, pp. 18416–18426. ISSN: 1424-8220. DOI: 10.3390/s150818416. URL: <https://www.mdpi.com/1424-8220/15/8/18416> (visited on 07/26/2023).
- [58] Gulam Rabbani, Mohammad Ehtisham Khan, Ejaz Ahmad, Mohsin Vahid Khan, Abrar Ahmad, Anwar Ulla Khan, Wahid Ali, Mazin A. Zamzami, Abdulateef H. Bashiri, and Waleed Zakri. “Serum CRP biomarker detection by using carbon nanotube field-effect transistor (CNT-FET) immunosensor”. In: *Bioelectrochemistry* 153 (Oct. 1, 2023), p. 108493. ISSN: 1567-5394. DOI: 10.1016/j.bioelechem.2023.108493. URL: <https://www.sciencedirect.com/science/article/pii/S1567539423001305> (visited on 07/26/2023).
- [59] Min-Ho Lee, Kooknyung Lee, and Suk Won Jung. “Multiplexed detection of protein markers with silicon nanowire FET and sol-gel matrix”. In: *2012 Annual International Conference of the IEEE Engineering in Medicine and Biology Society*. 2012 Annual

## BIBLIOGRAPHY

---

- International Conference of the IEEE Engineering in Medicine and Biology Society. ISSN: 1558-4615. Aug. 2012, pp. 570–573. DOI: 10.1109/EMBC.2012.6345995.
- [60] Chia-Ho Chu, Wen-Hsin Chang, Wei-Jer Kao, Chih-Lin Lin, Ko-Wei Chang, Yu-Lin Wang, and Gwo-Bin Lee. “An integrated microfluidic system with field-effect-transistor-based biosensors for automatic highly-sensitive C-reactive protein measurement”. In: *2015 28th IEEE International Conference on Micro Electro Mechanical Systems (MEMS)*. 2015 28th IEEE International Conference on Micro Electro Mechanical Systems (MEMS). ISSN: 1084-6999. Jan. 2015, pp. 581–584. DOI: 10.1109/MEMSYS.2015.7051022.
- [61] Jiaobing Tu, Jihong Min, Yu Song, Changhao Xu, Jiahong Li, Jeff Moore, Justin Hanson, Erin Hu, Tanyalak Parimon, Ting-Yu Wang, Elham Davoodi, Tsui-Fen Chou, Peter Chen, Jeffrey J. Hsu, Harry B. Rossiter, and Wei Gao. “A wireless patch for the monitoring of C-reactive protein in sweat”. In: *Nature Biomedical Engineering* (June 22, 2023). Publisher: Nature Publishing Group, pp. 1–14. ISSN: 2157-846X. DOI: 10.1038/s41551-023-01059-5. URL: <https://www.nature.com/articles/s41551-023-01059-5> (visited on 07/26/2023).
- [62] Yannis Tsididis and Colin McAndrew. *Operation and Modeling of the MOS Transistor*. Google-Books-ID: oYmYPwAACAAJ. Oxford University Press, 2011. 723 pp. ISBN: 978-0-19-517015-3.
- [63] M. M. Atalla, E. Tannenbaum, and E. J. Scheibner. “Stabilization of Silicon Surfaces by Thermally Grown Oxides\*”. In: *Bell System Technical Journal* 38.3 (1959). \_eprint: <https://onlinelibrary.wiley.com/doi/pdf/10.1002/j.1538-7305.1959.tb03907.x>, pp. 749–783. ISSN: 1538-7305. DOI: 10.1002/j.1538-7305.1959.tb03907.x. URL: <https://onlinelibrary.wiley.com/doi/abs/10.1002/j.1538-7305.1959.tb03907.x> (visited on 04/08/2023).
- [64] Kahng Dawon. “Electric field controlled semiconductor device”. U.S. pat. 3102230A. Bell Telephone Laboratories Inc. Aug. 27, 1963. URL: <https://patents.google.com/patent/US3102230A/en> (visited on 04/08/2023).
- [65] Simon M. Sze and Kwok K. Ng. *Physics of Semiconductor Devices*. Google-Books-ID: o4unkmHBHb8C. John Wiley & Sons, Dec. 13, 2006. 828 pp. ISBN: 978-0-470-06830-4.
- [66] Francesco Bellando. “Sweat monitoring with CMOS compatible technology: ISFETS and beyond”. PhD thesis. Lausanne: EPFL, 2020. 182 pp. DOI: 10.5075/epfl-thesis-7464.
- [67] Luigi Colombo, Jim Chambers, and Hiroaki “Hiro” Niimi. “Gate Dielectric Process Technology for the Sub-1 nm Equivalent Oxide Thickness (EOT) Era”. In: *The Electrochemical Society Interface* 16.3 (Sept. 1, 2007). Publisher: IOP Publishing, p. 51. ISSN: 1944-8783. DOI: 10.1149/2.F07073IF. URL: <https://iopscience.iop.org/article/10.1149/2.F07073IF/meta> (visited on 04/12/2023).
- [68] *Intel’s Fundamental Advance in Transistor Design Extends Moore’s Law, Computing Performance*. URL: <https://www.intel.com/pressroom/archive/releases/2007/20071111comp.htm> (visited on 04/12/2023).

- [69] Joo-Won Kang and Won-Ju Cho. “Achieving enhanced pH sensitivity using capacitive coupling in extended gate FET sensors with various high-K sensing films”. In: *Solid-State Electronics* 152 (Feb. 1, 2019), pp. 29–32. ISSN: 0038-1101. DOI: 10.1016/j.sse.2018.11.008. URL: <https://www.sciencedirect.com/science/article/pii/S0038110118303368> (visited on 04/16/2023).
- [70] D.J. Wouters, J.-P. Colinge, and H.E. Maes. “Subthreshold slope in thin-film SOI MOS-FETs”. In: *IEEE Transactions on Electron Devices* 37.9 (Sept. 1990). Conference Name: IEEE Transactions on Electron Devices, pp. 2022–2033. ISSN: 1557-9646. DOI: 10.1109/16.57165.
- [71] J.-P. Colinge. *Silicon-on-Insulator Technology: Materials to VLSI*. Google-Books-ID: 6yZH3lmXa6EC. Springer Science & Business Media, Sept. 30, 1997. 294 pp. ISBN: 978-0-7923-8007-8.
- [72] P. Francis, A. Terao, D. Flandre, and F. Van de Wiele. “Modeling of ultrathin double-gate nMOS/SOI transistors”. In: *IEEE Transactions on Electron Devices* 41.5 (May 1994). Conference Name: IEEE Transactions on Electron Devices, pp. 715–720. ISSN: 1557-9646. DOI: 10.1109/16.285022.
- [73] F. Balestra, S. Cristoloveanu, M. Benachir, J. Brini, and T. Elewa. “Double-gate silicon-on-insulator transistor with volume inversion: A new device with greatly enhanced performance”. In: *IEEE Electron Device Letters* 8.9 (Sept. 1987). Conference Name: IEEE Electron Device Letters, pp. 410–412. ISSN: 1558-0563. DOI: 10.1109/EDL.1987.26677.
- [74] F. Gamiz and M. V. Fischetti. “Monte Carlo simulation of double-gate silicon-on-insulator inversion layers: The role of volume inversion”. In: *Journal of Applied Physics* 89.10 (May 15, 2001). Publisher: American Institute of Physics, pp. 5478–5487. ISSN: 0021-8979. DOI: 10.1063/1.1358321. URL: <https://aip.scitation.org/doi/10.1063/1.1358321> (visited on 04/14/2023).
- [75] H. Helmholtz. “Ueber einige Gesetze der Vertheilung elektrischer Ströme in körperlichen Leitern, mit Anwendung auf die thierisch-elektrischen Versuche (Schluss.)” In: *Annalen der Physik* 165.7 (1853), pp. 353–377. ISSN: 1521-3889. DOI: 10.1002/andp.18531650702. URL: <https://onlinelibrary.wiley.com/doi/abs/10.1002/andp.18531650702> (visited on 04/15/2023).
- [76] M. Gouy. “Sur la constitution de la charge électrique à la surface d’un électrolyte”. In: *Journal de Physique Théorique et Appliquée* 9.1 (1910), pp. 457–468. ISSN: 0368-3893. DOI: 10.1051/jphysap:019100090045700. URL: <http://www.edpsciences.org/10.1051/jphysap:019100090045700> (visited on 04/15/2023).
- [77] David Leonard Chapman. “LI. A contribution to the theory of electrocapillarity”. In: *The London, Edinburgh, and Dublin Philosophical Magazine and Journal of Science* 25.148 (Apr. 1, 1913), pp. 475–481. ISSN: 1941-5982. DOI: 10.1080/14786440408634187. URL: <https://doi.org/10.1080/14786440408634187> (visited on 04/15/2023).

## BIBLIOGRAPHY

---

- [78] Otto Stern. “Zur Theorie Der Elektrolytischen Doppelschicht”. In: *Zeitschrift für Elektrochemie und angewandte physikalische Chemie* 30.21 (1924), pp. 508–516. ISSN: 0005-9021. DOI: 10.1002/bbpc.192400182. URL: <https://onlinelibrary.wiley.com/doi/abs/10.1002/bbpc.192400182> (visited on 04/15/2023).
- [79] P. Bergveld. “Development of an Ion-Sensitive Solid-State Device for Neurophysiological Measurements”. In: *IEEE Transactions on Biomedical Engineering* BME-17.1 (Jan. 1970). Conference Name: IEEE Transactions on Biomedical Engineering, pp. 70–71. ISSN: 1558-2531. DOI: 10.1109/TBME.1970.4502688.
- [80] Piet Bergveld. “Development, Operation, and Application of the Ion-Sensitive Field-Effect Transistor as a Tool for Electrophysiology”. In: *IEEE Transactions on Biomedical Engineering* BME-19.5 (Sept. 1972). Conference Name: IEEE Transactions on Biomedical Engineering, pp. 342–351. ISSN: 1558-2531. DOI: 10.1109/TBME.1972.324137.
- [81] Aurelio Barbaro, Claudio Colapicchioni, Enrico Davini, Giuseppina Mazzamurro, Andrea Piotta, and Filippo Porcelli. “CHEMFET Devices for biomedical and environmental applications”. In: *Advanced Materials* 4.6 (1992), pp. 402–408. ISSN: 1521-4095. DOI: 10.1002/adma.19920040605. URL: <https://onlinelibrary.wiley.com/doi/abs/10.1002/adma.19920040605> (visited on 04/14/2023).
- [82] J. A. Voorthuyzen and P. Bergveld. “The pressfet: an integrated electret-mosfet based pressure sensor”. In: *Sensors and Actuators* 14.4 (Aug. 1, 1988), pp. 349–360. ISSN: 0250-6874. DOI: 10.1016/0250-6874(88)80024-6. URL: <https://www.sciencedirect.com/science/article/pii/0250687488800246> (visited on 04/14/2023).
- [83] Michael J. Schöning and Arshak Poghosian. “Recent advances in biologically sensitive field-effect transistors (BioFETs)”. In: *Analyst* 127.9 (Sept. 10, 2002). Publisher: The Royal Society of Chemistry, pp. 1137–1151. ISSN: 1364-5528. DOI: 10.1039/B204444G. URL: <https://pubs.rsc.org/en/content/articlelanding/2002/an/b204444g> (visited on 04/14/2023).
- [84] Daeun Sung and Jahyun Koo. “A review of BioFET’s basic principles and materials for biomedical applications”. In: *Biomedical Engineering Letters* 11.2 (May 1, 2021), pp. 85–96. ISSN: 2093-985X. DOI: 10.1007/s13534-021-00187-8. URL: <https://doi.org/10.1007/s13534-021-00187-8> (visited on 04/14/2023).
- [85] P. Bergveld. “Thirty years of ISFETOLOGY: What happened in the past 30 years and what may happen in the next 30 years”. In: *Sensors and Actuators B: Chemical* 88.1 (Jan. 1, 2003), pp. 1–20. ISSN: 0925-4005. DOI: 10.1016/S0925-4005(02)00301-5. URL: <https://www.sciencedirect.com/science/article/pii/S0925400502003015> (visited on 04/08/2023).
- [86] P. Bergveld and Alastair Sibbald. *Analytical and Biomedical Applications of Ion-selective Field-effect Transistors*. Google-Books-ID: LHPprQEACAAJ. Elsevier, 1988. 172 pp. ISBN: 978-0-444-42976-6.

- [87] R. E. G. van Hal, J. C. T. Eijkel, and P. Bergveld. "A novel description of ISFET sensitivity with the buffer capacity and double-layer capacitance as key parameters". In: *Sensors and Actuators B: Chemical* 24.1 (Mar. 1, 1995), pp. 201–205. ISSN: 0925-4005. DOI: 10.1016/0925-4005(95)85043-0. URL: <https://www.sciencedirect.com/science/article/pii/0925400595850430> (visited on 04/08/2023).
- [88] David E. Yates, Samuel Levine, and Thomas W. Healy. "Site-binding model of the electrical double layer at the oxide/water interface". In: *Journal of the Chemical Society, Faraday Transactions 1: Physical Chemistry in Condensed Phases* 70.0 (Jan. 1, 1974). Publisher: The Royal Society of Chemistry, pp. 1807–1818. ISSN: 0300-9599. DOI: 10.1039/F19747001807. URL: <https://pubs.rsc.org/en/content/articlelanding/1974/f1/f19747001807> (visited on 04/08/2023).
- [89] L. Bousse, N.F. De Rooij, and P. Bergveld. "Operation of chemically sensitive field-effect sensors as a function of the insulator-electrolyte interface". In: *IEEE Transactions on Electron Devices* 30.10 (Oct. 1983). Conference Name: IEEE Transactions on Electron Devices, pp. 1263–1270. ISSN: 1557-9646. DOI: 10.1109/T-ED.1983.21284.
- [90] A. Van Den Berg, P. Bergveld, D.N. Reinhoudt, and E.J. Sudhölter. "Sensitivity control of ISFETs by chemical surface modification". In: *Sensors and Actuators* 8.2 (Oct. 1985), pp. 129–148. ISSN: 02506874. DOI: 10.1016/0250-6874(85)87010-4. URL: <https://linkinghub.elsevier.com/retrieve/pii/0250687485870104> (visited on 05/29/2023).
- [91] R. E. G. van Hal, J. C. T. Eijkel, and P. Bergveld. "A general model to describe the electrostatic potential at electrolyte oxide interfaces". In: *Advances in Colloid and Interface Science* 69.1 (Dec. 1, 1996), pp. 31–62. ISSN: 0001-8686. DOI: 10.1016/S0001-8686(96)00307-7. URL: <https://www.sciencedirect.com/science/article/pii/S0001868696003077> (visited on 04/15/2023).
- [92] Sara Rigante. "High-K Dielectric FinFETs on Si-Bulk for Ionic and Biological Sensing Integrated Circuits". In: ().
- [93] Vinod Kumar Khanna. "Remedial and adaptive solutions of ISFET non-ideal behaviour". In: *Sensor Review* 33.3 (Jan. 1, 2013). Publisher: Emerald Group Publishing Limited, pp. 228–237. ISSN: 0260-2288. DOI: 10.1108/02602281311324681. URL: <https://doi.org/10.1108/02602281311324681> (visited on 06/21/2023).
- [94] Enming Song, Yoon Kyeung Lee, Rui Li, Jinghua Li, Xin Jin, Ki Jun Yu, Zhaoqian Xie, Hui Fang, Yiding Zhong, Haina Du, Jize Zhang, Guanhua Fang, Yerim Kim, Younghee Yoon, Muhammad A. Alam, Yongfeng Mei, Yonggang Huang, and John A. Rogers. "Transferred, Ultrathin Oxide Bilayers as Biofluid Barriers for Flexible Electronic Implants". In: *Advanced Functional Materials* 28.12 (2018), p. 1702284. ISSN: 1616-3028. DOI: 10.1002/adfm.201702284. URL: <https://onlinelibrary.wiley.com/doi/abs/10.1002/adfm.201702284> (visited on 04/17/2023).

## BIBLIOGRAPHY

---

- [95] Sungho Kim, Taiuk Rim, Kihyun Kim, Unsang Lee, Eunhye Baek, Hojoon Lee, Chang-Ki Baek, M. Meyyappan, M. Jamal Deen, and Jeong-Soo Lee. "Silicon nanowire ion sensitive field effect transistor with integrated Ag/AgCl electrode: pH sensing and noise characteristics". In: *Analyst* 136.23 (Nov. 7, 2011). Publisher: The Royal Society of Chemistry, pp. 5012–5016. ISSN: 1364-5528. DOI: 10.1039/C1AN15568G. URL: <https://pubs.rsc.org/en/content/articlelanding/2011/an/c1an15568g> (visited on 04/17/2023).
- [96] Xuan Thang Vu, Jan Felix Eschermann, Regina Stockmann, Ranjita GhoshMoulick, Andreas Offenhäusser, and Sven Ingebrandt. "Top-down processed silicon nanowire transistor arrays for biosensing". In: *physica status solidi (a)* 206.3 (2009). \_eprint: <https://onlinelibrary.wiley.com/doi/pdf/10.1002/pssa.200880475>, pp. 426–434. ISSN: 1862-6319. DOI: 10.1002/pssa.200880475. URL: <https://onlinelibrary.wiley.com/doi/abs/10.1002/pssa.200880475> (visited on 05/15/2023).
- [97] H. Abe, M. Esashi, and T. Matsuo. "ISFET's using inorganic gate thin films". In: *IEEE Transactions on Electron Devices* 26.12 (Dec. 1979). Conference Name: IEEE Transactions on Electron Devices, pp. 1939–1944. ISSN: 1557-9646. DOI: 10.1109/T-ED.1979.19799.
- [98] Kuan-I Chen, Bor-Ran Li, and Yit-Tsong Chen. "Silicon nanowire field-effect transistor-based biosensors for biomedical diagnosis and cellular recording investigation". In: *Nano Today* 6.2 (Apr. 1, 2011), pp. 131–154. ISSN: 1748-0132. DOI: 10.1016/j.nantod.2011.02.001. URL: <https://www.sciencedirect.com/science/article/pii/S1748013211000168> (visited on 04/01/2023).
- [99] T. Akiyama, Y. Ujihira, Y. Okabe, T. Sugano, and E. Niki. "Ion-sensitive field-effect transistors with inorganic gate oxide for pH sensing". In: *IEEE Transactions on Electron Devices* 29.12 (Dec. 1982). Conference Name: IEEE Transactions on Electron Devices, pp. 1936–1941. ISSN: 1557-9646. DOI: 10.1109/T-ED.1982.21054.
- [100] V. Jankovic and J. P. Chang. "HfO<sub>2</sub> and ZrO<sub>2</sub>-Based Microchemical Ion Sensitive Field Effect Transistor (ISFET) Sensors: Simulation & Experiment". In: *Journal of The Electrochemical Society* 158.10 (Aug. 5, 2011). Publisher: IOP Publishing, P115. ISSN: 1945-7111. DOI: 10.1149/1.3623421. URL: <https://iopscience.iop.org/article/10.1149/1.3623421/meta> (visited on 04/18/2023).
- [101] Meng-Nian Niu, Xin-Fang Ding, and Qin-Yi Tong. "Effect of two types of surface sites on the characteristics of Si<sub>3</sub>N<sub>4</sub>-gate pH-ISFETs". In: *Sensors and Actuators B: Chemical* 37.1 (Nov. 1, 1996), pp. 13–17. ISSN: 0925-4005. DOI: 10.1016/S0925-4005(97)80067-6. URL: <https://www.sciencedirect.com/science/article/pii/S0925400597800676> (visited on 04/18/2023).
- [102] Alexey Tarasov, Mathias Wipf, Ralph L. Stoop, Kristine Bedner, Wangyang Fu, Vitaliy A. Guzenko, Oren Knopfmacher, Michel Calame, and Christian Schönenberger. "Understanding the Electrolyte Background for Biochemical Sensing with Ion-Sensitive Field-Effect Transistors". In: *ACS Nano* 6.10 (Oct. 23, 2012). Publisher: American Chem-



- ical Society, pp. 9291–9298. ISSN: 1936-0851. DOI: 10.1021/nn303795r. URL: <https://doi.org/10.1021/nn303795r> (visited on 04/17/2023).
- [103] Songyue Chen, Johan G. Bomer, Edwin T. Carlen, and Albert van den Berg. “Al<sub>2</sub>O<sub>3</sub>/Silicon NanoISFET with Near Ideal Nernstian Response”. In: *Nano Letters* 11.6 (June 8, 2011). Publisher: American Chemical Society, pp. 2334–2341. ISSN: 1530-6984. DOI: 10.1021/nl200623n. URL: <https://doi.org/10.1021/nl200623n> (visited on 04/18/2023).
- [104] Luc Bousse, H. H. van den Vlekkert, and N. F. de Rooij. “Hysteresis in Al<sub>2</sub>O<sub>3</sub>-gate ISFETs”. In: *Sensors and Actuators B: Chemical* 2.2 (May 1, 1990), pp. 103–110. ISSN: 0925-4005. DOI: 10.1016/0925-4005(90)80018-U. URL: <https://www.sciencedirect.com/science/article/pii/092540059080018U> (visited on 04/18/2023).
- [105] Hung-Kwei Liao, Jung-Chuan Chou, Wen-Yaw Chung, Tai-Ping Sun, and Shen-Kan Hsiung. “Study of amorphous tin oxide thin films for ISFET applications”. In: *Sensors and Actuators B: Chemical* 50.2 (July 31, 1998), pp. 104–109. ISSN: 0925-4005. DOI: 10.1016/S0925-4005(98)00162-2. URL: <https://www.sciencedirect.com/science/article/pii/S0925400598001622> (visited on 04/18/2023).
- [106] Cheng-En Lue, Ting-Chun Yu, Chia-Ming Yang, Dorota G. Pijanowska, and Chao-Sung Lai. “Optimization of Urea-EnFET Based on Ta<sub>2</sub>O<sub>5</sub> Layer with Post Annealing”. In: *Sensors* 11.5 (May 2011). Number: 5 Publisher: Molecular Diversity Preservation International, pp. 4562–4571. ISSN: 1424-8220. DOI: 10.3390/s110504562. URL: <https://www.mdpi.com/1424-8220/11/5/4562> (visited on 04/17/2023).
- [107] Dae-Hyuk Kwon, Byung-Woog Cho, Chang-Soo Kim, and Byung-Ki Sohn. “Effects of heat treatment on Ta<sub>2</sub>O<sub>5</sub> sensing membrane for low drift and high sensitivity pH-ISFET”. In: *Sensors and Actuators B: Chemical* 34.1 (Aug. 1, 1996), pp. 441–445. ISSN: 0925-4005. DOI: 10.1016/S0925-4005(96)01938-7. URL: <https://www.sciencedirect.com/science/article/pii/S0925400596019387> (visited on 04/18/2023).
- [108] Hiranya Ranjan Thakur, Gaurav Keshwani, and Jiten Chandra Dutta. “Sensitivity of carbon nanotube based junctionless ion sensitive field effect transistor (CNTJLISFET) for HfO<sub>2</sub> and ZrO<sub>2</sub> gate dielectrics: Experimental and theoretical investigation”. In: *2017 International Conference on Innovations in Electronics, Signal Processing and Communication (IESC)*. 2017 International Conference on Innovations in Electronics, Signal Processing and Communication (IESC). Apr. 2017, pp. 137–142. DOI: 10.1109/IESPC.2017.8071880.
- [109] Sufi Zafar, Christopher D’Emic, Ali Afzali, Benjamin Fletcher, Y. Zhu, and Tak Ning. “Optimization of pH sensing using silicon nanowire field effect transistors with HfO<sub>2</sub> as the sensing surface”. In: *Nanotechnology* 22.40 (Sept. 2011), p. 405501. ISSN: 0957-4484. DOI: 10.1088/0957-4484/22/40/405501. URL: <https://dx.doi.org/10.1088/0957-4484/22/40/405501> (visited on 06/21/2023).

## BIBLIOGRAPHY

---

- [110] Vladimir Kesler, Boris Murmann, and H. Tom Soh. "Going beyond the Debye Length: Overcoming Charge Screening Limitations in Next-Generation Bioelectronic Sensors". In: *ACS Nano* 14.12 (Dec. 22, 2020). Publisher: American Chemical Society, pp. 16194–16201. ISSN: 1936-0851. DOI: 10.1021/acsnano.0c08622. URL: <https://doi.org/10.1021/acsnano.0c08622> (visited on 03/31/2023).
- [111] Kaveh Shoorideh and Chi On Chui. "On the origin of enhanced sensitivity in nanoscale FET-based biosensors". In: *Proceedings of the National Academy of Sciences* 111.14 (Apr. 8, 2014). Publisher: Proceedings of the National Academy of Sciences, pp. 5111–5116. DOI: 10.1073/pnas.1315485111. URL: <https://www.pnas.org/doi/full/10.1073/pnas.1315485111> (visited on 05/14/2023).
- [112] Inkyu Park, Zhiyong Li, Albert P. Pisano, and R. Stanley Williams. "Top-down fabricated silicon nanowire sensors for real-time chemical detection". In: *Nanotechnology* 21.1 (Nov. 2009), p. 015501. ISSN: 0957-4484. DOI: 10.1088/0957-4484/21/1/015501. URL: <https://dx.doi.org/10.1088/0957-4484/21/1/015501> (visited on 05/23/2023).
- [113] Sung Keun Yoo, Sung Yang, and Jong-Hyun Lee. "Hydrogen Ion Sensing Using Schottky Contacted Silicon Nanowire FETs". In: *IEEE Transactions on Nanotechnology* 7.6 (Nov. 2008). Conference Name: IEEE Transactions on Nanotechnology, pp. 745–748. ISSN: 1941-0085. DOI: 10.1109/TNANO.2008.2005727.
- [114] Yu Chen, Xihua Wang, Shyamsunder Erramilli, Pritiraj Mohanty, and Agnieszka Kalinowski. "Silicon-based nanoelectronic field-effect pH sensor with local gate control". In: *Applied Physics Letters* 89.22 (Nov. 29, 2006), p. 223512. ISSN: 0003-6951. DOI: 10.1063/1.2392828. URL: <https://doi.org/10.1063/1.2392828> (visited on 05/15/2023).
- [115] O. Knopfmacher, A. Tarasov, Wangyang Fu, M. Wipf, B. Niesen, M. Calame, and C. Schönenberger. "Nernst Limit in Dual-Gated Si-Nanowire FET Sensors". In: *Nano Letters* 10.6 (June 9, 2010). Publisher: American Chemical Society, pp. 2268–2274. ISSN: 1530-6984. DOI: 10.1021/nl100892y. URL: <https://doi.org/10.1021/nl100892y> (visited on 05/15/2023).
- [116] Guo-Jun Zhang, Zhan Hong Henry Luo, Min Joon Huang, Guang Kai Ignatius Tay, and Eu-Jin Andy Lim. "Morpholino-functionalized silicon nanowire biosensor for sequence-specific label-free detection of DNA". In: *Biosensors and Bioelectronics* 25.11 (July 15, 2010), pp. 2447–2453. ISSN: 0956-5663. DOI: 10.1016/j.bios.2010.04.001. URL: <https://www.sciencedirect.com/science/article/pii/S0956566310001715> (visited on 05/15/2023).
- [117] Tao Kong, Ruigong Su, Beibei Zhang, Qi Zhang, and Guosheng Cheng. "CMOS-compatible, label-free silicon-nanowire biosensors to detect cardiac troponin I for acute myocardial infarction diagnosis". In: *Biosensors and Bioelectronics* 34.1 (Apr. 15, 2012), pp. 267–272. ISSN: 0956-5663. DOI: 10.1016/j.bios.2012.02.019. URL: <https://www.sciencedirect.com/science/article/pii/S0956566312000978> (visited on 05/15/2023).

- [118] Jay Huiyi Chua, Ru-Ern Chee, Ajay Agarwal, She Mein Wong, and Guo-Jun Zhang. "Label-Free Electrical Detection of Cardiac Biomarker with Complementary Metal-Oxide Semiconductor-Compatible Silicon Nanowire Sensor Arrays". In: *Analytical Chemistry* 81.15 (Aug. 1, 2009). Publisher: American Chemical Society, pp. 6266–6271. ISSN: 0003-2700. DOI: 10.1021/ac901157x. URL: <https://doi.org/10.1021/ac901157x> (visited on 05/15/2023).
- [119] Kihyun Kim, Chanoh Park, Donghoon Kwon, Donghoon Kim, M. Meyyappan, Sangmin Jeon, and Jeong-Soo Lee. "Silicon nanowire biosensors for detection of cardiac troponin I (cTnI) with high sensitivity". In: *Biosensors and Bioelectronics* 77 (Mar. 15, 2016), pp. 695–701. ISSN: 0956-5663. DOI: 10.1016/j.bios.2015.10.008. URL: <https://www.sciencedirect.com/science/article/pii/S0956566315304735> (visited on 05/15/2023).
- [120] Stephanie Klinghammer, Tetiana Voitsekhivska, Nadia Licciardello, Kihyun Kim, Chang-Ki Baek, Hyeonsu Cho, Klaus-Jürgen Wolter, Clemens Kirschbaum, Larysa Baraban, and Gianarelio Cuniberti. "Nanosensor-Based Real-Time Monitoring of Stress Biomarkers in Human Saliva Using a Portable Measurement System". In: *ACS Sensors* 5.12 (Dec. 24, 2020). Publisher: American Chemical Society, pp. 4081–4091. DOI: 10.1021/acssensors.0c02267. URL: <https://doi.org/10.1021/acssensors.0c02267> (visited on 05/15/2023).
- [121] F. Puppo, M.-A. Doucey, T. S. Y. Moh, G. Pandraud, P.M. Sarro, G. De Micheli, and S. Carrara. "Femto-molar sensitive field effect transistor biosensors based on silicon nanowires and antibodies". In: *2013 IEEE SENSORS*. 2013 IEEE SENSORS. ISSN: 1930-0395. Nov. 2013, pp. 1–4. DOI: 10.1109/ICSENS.2013.6688205.
- [122] M. A. Mohd Azmi, Z. Tehrani, R. P. Lewis, K. -A. D. Walker, D. R. Jones, D. R. Daniels, S. H. Doak, and O. J. Guy. "Highly sensitive covalently functionalised integrated silicon nanowire biosensor devices for detection of cancer risk biomarker". In: *Biosensors and Bioelectronics* 52 (Feb. 15, 2014), pp. 216–224. ISSN: 0956-5663. DOI: 10.1016/j.bios.2013.08.030. URL: <https://www.sciencedirect.com/science/article/pii/S0956566313005794> (visited on 05/15/2023).
- [123] Carlos Duarte-Guevara, Fei-Lung Lai, Chun-Wen Cheng, Bobby Jr. Reddy, Eric Salm, Vikhram Swaminathan, Ying-Kit Tsui, Hsiao Chin Tuan, Alex Kalnitsky, Yi-Shao Liu, and Rashid Bashir. "Enhanced Biosensing Resolution with Foundry Fabricated Individually Addressable Dual-Gated ISFETs". In: *Analytical Chemistry* 86.16 (Aug. 19, 2014). Publisher: American Chemical Society, pp. 8359–8367. ISSN: 0003-2700. DOI: 10.1021/ac501912x. URL: <https://doi.org/10.1021/ac501912x> (visited on 08/01/2023).
- [124] Narendra Kumar, Jitendra Kumar, and Siddhartha Panda. "Back-Channel Electrolyte-Gated a-IGZO Dual-Gate Thin-Film Transistor for Enhancement of pH Sensitivity Over Nernst Limit". In: *IEEE Electron Device Letters* 37.4 (Apr. 2016). Conference Name: IEEE Electron Device Letters, pp. 500–503. ISSN: 1558-0563. DOI: 10.1109/LED.2016.2536359.

## BIBLIOGRAPHY

---

- [125] Hyun-June Jang and Won-Ju Cho. “Performance Enhancement of Capacitive-Coupling Dual-gate Ion-Sensitive Field-Effect Transistor in Ultra-Thin-Body”. In: *Scientific Reports* 4.1 (June 13, 2014). Number: 1 Publisher: Nature Publishing Group, p. 5284. ISSN: 2045-2322. DOI: 10.1038/srep05284. URL: <https://www.nature.com/articles/srep05284> (visited on 08/01/2023).
- [126] Hyun-June Jang and Won-Ju Cho. “Fabrication of high-performance fully depleted silicon-on-insulator based dual-gate ion-sensitive field-effect transistor beyond the Nernstian limit”. In: *Applied Physics Letters* 100.7 (Feb. 14, 2012), p. 073701. ISSN: 0003-6951. DOI: 10.1063/1.3685497. URL: <https://doi.org/10.1063/1.3685497> (visited on 08/01/2023).
- [127] Jonghyun Go, Pradeep R. Nair, Bobby Jr. Reddy, Brian Dorvel, Rashid Bashir, and Muhammad A. Alam. “Coupled Heterogeneous Nanowire–Nanoplate Planar Transistor Sensors for Giant (>10 V/pH) Nernst Response”. In: *ACS Nano* 6.7 (July 24, 2012). Publisher: American Chemical Society, pp. 5972–5979. ISSN: 1936-0851. DOI: 10.1021/nn300874w. URL: <https://doi.org/10.1021/nn300874w> (visited on 08/01/2023).
- [128] M. Spijkman, E. C. P. Smits, J. F. M. Cillessen, F. Biscarini, P. W. M. Blom, and D. M. de Leeuw. “Beyond the Nernst-limit with dual-gate ZnO ion-sensitive field-effect transistors”. In: *Applied Physics Letters* 98.4 (Jan. 24, 2011), p. 043502. ISSN: 0003-6951. DOI: 10.1063/1.3546169. URL: <https://doi.org/10.1063/1.3546169> (visited on 08/01/2023).
- [129] Mark-Jan Spijkman, Jakob J. Brondijk, Tom C. T. Geuns, Edsger C. P. Smits, Tobias Cramer, Francesco Zerbetto, Pablo Stoliar, Fabio Biscarini, Paul W. M. Blom, and Dago M. de Leeuw. “Dual-Gate Organic Field-Effect Transistors as Potentiometric Sensors in Aqueous Solution”. In: *Advanced Functional Materials* 20.6 (2010). eprint: <https://onlinelibrary.wiley.com/doi/pdf/10.1002/adfm.200901830>, pp. 898–905. ISSN: 1616-3028. DOI: 10.1002/adfm.200901830. URL: <https://onlinelibrary.wiley.com/doi/abs/10.1002/adfm.200901830> (visited on 08/01/2023).
- [130] Jie Li, Gen He, Hiroshi Ueno, Chuancheng Jia, Hiroyuki Noji, Chuanmin Qi, and Xuefeng Guo. “Direct real-time detection of single proteins using silicon nanowire-based electrical circuits”. In: *Nanoscale* 8.36 (Sept. 15, 2016). Publisher: The Royal Society of Chemistry, pp. 16172–16176. ISSN: 2040-3372. DOI: 10.1039/C6NR04103E. URL: <https://pubs.rsc.org/en/content/articlelanding/2016/nr/c6nr04103e> (visited on 05/15/2023).
- [131] Yurii Kutovyi, Jie Li, Ihor Zadorozhnyi, Hanna Hlukhova, Nazarii Boichuk, Dmytro Yehorov, Marcus Menger, and Svetlana Vitusevich. “Highly Sensitive and Fast Detection of C-Reactive Protein and Troponin Biomarkers Using Liquidgated Single Silicon Nanowire Biosensors”. In: *MRS Advances* 5.16 (Mar. 1, 2020), pp. 835–846. ISSN: 2059-8521. DOI: 10.1557/adv.2020.60. URL: <https://doi.org/10.1557/adv.2020.60> (visited on 05/15/2023).

- [132] Gengfeng Zheng, Fernando Patolsky, Yi Cui, Wayne U. Wang, and Charles M. Lieber. “Multiplexed electrical detection of cancer markers with nanowire sensor arrays”. In: *Nature Biotechnology* 23.10 (Oct. 2005). Number: 10 Publisher: Nature Publishing Group, pp. 1294–1301. ISSN: 1546-1696. DOI: 10.1038/nbt1138. URL: <https://www.nature.com/articles/nbt1138> (visited on 05/15/2023).
- [133] Roey Elnathan, Moria Kwiat, Alexander Pevzner, Yoni Engel, Larisa Burstein, Artium Khatchourints, Amir Lichtenstein, Raisa Kantaev, and Fernando Patolsky. “Biorecognition Layer Engineering: Overcoming Screening Limitations of Nanowire-Based FET Devices”. In: *Nano Letters* 12.10 (Oct. 10, 2012). Publisher: American Chemical Society, pp. 5245–5254. ISSN: 1530-6984. DOI: 10.1021/nl302434w. URL: <https://doi.org/10.1021/nl302434w> (visited on 03/31/2023).
- [134] Yi Cui, Qingqiao Wei, Hongkun Park, and Charles M. Lieber. “Nanowire Nanosensors for Highly Sensitive and Selective Detection of Biological and Chemical Species”. In: *Science* 293.5533 (Aug. 17, 2001). Publisher: American Association for the Advancement of Science, pp. 1289–1292. DOI: 10.1126/science.1062711. URL: <https://www.science.org/doi/full/10.1126/science.1062711> (visited on 07/31/2023).
- [135] Cheol-Min Lim, In-Kyu Lee, Ki Joong Lee, Young Kyoung Oh, Yong-Beom Shin, and Won-Ju Cho. “Improved sensing characteristics of dual-gate transistor sensor using silicon nanowire arrays defined by nanoimprint lithography”. In: *Science and Technology of Advanced Materials* 18.1 (Dec. 31, 2017). Publisher: Taylor & Francis \_eprint: <https://doi.org/10.1080/14686996.2016.1253409>, pp. 17–25. ISSN: 1468-6996. DOI: 10.1080/14686996.2016.1253409. URL: <https://doi.org/10.1080/14686996.2016.1253409> (visited on 07/31/2023).
- [136] Kangho Lee, Pradeep R. Nair, Adina Scott, Muhammad A. Alam, and David B. Janes. “Device considerations for development of conductance-based biosensors”. In: *Journal of Applied Physics* 105.10 (May 15, 2009). Publisher: American Institute of Physics, p. 102046. ISSN: 0021-8979. DOI: 10.1063/1.3116630. URL: <https://aip.scitation.org/doi/full/10.1063/1.3116630> (visited on 03/31/2023).
- [137] R. Midahuen, B. Previtali, C. Fontelaye, G. Nonglaton, S. Barraud, and V. Stambouli. “Wafer-scale fabrication of biologically sensitive Si nanowire FET: from pH sensing to electrical detection of DNA hybridization”. In: *ESSCIRC 2021 - IEEE 47th European Solid State Circuits Conference (ESSCIRC)*. ESSCIRC 2021 - IEEE 47th European Solid State Circuits Conference (ESSCIRC). Sept. 2021, pp. 175–178. DOI: 10.1109/ESSCIRC53450.2021.9567751.
- [138] Dong-Il Moon, Maxime Peycelon, Jee-Yeon Kim, Jae-Hyuk Ahn, Tae Jung Park, and Yang-Kyu Choi. “A biristor based on a floating-body silicon nanowire for biosensor applications”. In: *Applied Physics Letters* 102.4 (Jan. 28, 2013). Publisher: American Institute of Physics, p. 043701. ISSN: 0003-6951. DOI: 10.1063/1.4789904. URL: <https://aip.scitation.org/doi/full/10.1063/1.4789904> (visited on 03/31/2023).

## BIBLIOGRAPHY

---

- [139] Jae-Hyuk Ahn, Bongsik Choi, and Sung-Jin Choi. "Understanding the signal amplification in dual-gate FET-based biosensors". In: *Journal of Applied Physics* 128.18 (Nov. 14, 2020), p. 184502. ISSN: 0021-8979, 1089-7550. DOI: 10.1063/5.0010136. URL: <http://aip.scitation.org/doi/10.1063/5.0010136> (visited on 03/09/2023).
- [140] Jae-Hyuk Ahn, Jeonghoon Yun, Yang-Kyu Choi, and Inkyu Park. "Palladium nanoparticle decorated silicon nanowire field-effect transistor with side-gates for hydrogen gas detection". In: *Applied Physics Letters* 104.1 (Jan. 6, 2014). Publisher: American Institute of Physics, p. 013508. ISSN: 0003-6951. DOI: 10.1063/1.4861228. URL: <https://aip.scitation.org/doi/full/10.1063/1.4861228> (visited on 03/31/2023).
- [141] Xuan P. A. Gao, Gengfeng Zheng, and Charles M. Lieber. "Subthreshold Regime has the Optimal Sensitivity for Nanowire FET Biosensors". In: *Nano Letters* 10.2 (Feb. 10, 2010). Publisher: American Chemical Society, pp. 547–552. ISSN: 1530-6984. DOI: 10.1021/nl9034219. URL: <https://doi.org/10.1021/nl9034219> (visited on 03/31/2023).
- [142] Mengwei Si, Chun-Jung Su, Chunsheng Jiang, Nathan J. Conrad, Hong Zhou, Kerry D. Maize, Gang Qiu, Chien-Ting Wu, Ali Shakouri, Muhammad A. Alam, and Peide D. Ye. "Steep-slope hysteresis-free negative capacitance MoS<sub>2</sub> transistors". In: *Nature Nanotechnology* 13.1 (Jan. 2018). Number: 1 Publisher: Nature Publishing Group, pp. 24–28. ISSN: 1748-3395. DOI: 10.1038/s41565-017-0010-1. URL: <https://www.nature.com/articles/s41565-017-0010-1> (visited on 03/31/2023).
- [143] Nicolò Oliva, Jonathan Backman, Luca Capua, Matteo Cavaliere, Mathieu Luisier, and Adrian M. Ionescu. "WSe<sub>2</sub>/SnSe<sub>2</sub> vdW heterojunction Tunnel FET with subthermionic characteristic and MOSFET co-integrated on same WSe<sub>2</sub> flake". In: *npj 2D Materials and Applications* 4.1 (Apr. 30, 2020). Number: 1 Publisher: Nature Publishing Group, pp. 1–8. ISSN: 2397-7132. DOI: 10.1038/s41699-020-0142-2. URL: <https://www.nature.com/articles/s41699-020-0142-2> (visited on 03/03/2023).
- [144] D.M. Binkley, M. Bucher, and D. Foty. "Design-oriented characterization of CMOS over the continuum of inversion level and channel length". In: *ICECS 2000. 7th IEEE International Conference on Electronics, Circuits and Systems (Cat. No.00EX445)*. ICECS 2000. 7th IEEE International Conference on Electronics, Circuits and Systems. Vol. 1. Jounieh, Lebanon: IEEE, 2000, pp. 161–164. ISBN: 978-0-7803-6542-1. DOI: 10.1109/ICECS.2000.911508. URL: <http://ieeexplore.ieee.org/document/911508/> (visited on 03/03/2023).
- [145] Reza Ghandi, Cheng-Po Chen, Liang Yin, Xingguang Zhu, Liangchun Yu, Stephen Arthur, Faisal Ahmad, and Peter Sandvik. "Silicon Carbide Integrated Circuits With Stable Operation Over a Wide Temperature Range". In: *IEEE Electron Device Letters* 35.12 (Dec. 2014), pp. 1206–1208. ISSN: 0741-3106, 1558-0563. DOI: 10.1109/LED.2014.2362815. URL: <http://ieeexplore.ieee.org/document/6936289/> (visited on 03/03/2023).
- [146] Alessandro Girardi and Sergio Bampi. "Power Constrained Design Optimization of Analog Circuits Based on Physical gm/ID Characteristics". In: ().

- [147] Fernando Silveira, Denis Flandre, and P.G.A. Jespers. “A gm/ID based methodology for the design of CMOS analog circuits and its application to the synthesis of a silicon-on-insulator micropower OTA”. In: *Solid-State Circuits, IEEE Journal of* 31 (Oct. 1, 1996), pp. 1314–1319. DOI: 10.1109/4.535416.
- [148] Linjie Liu, Qinghua Han, Sergej Makovejev, Stefan Trelenkamp, Jean-Pierre Raskin, Siegfried Mantl, and Qing-Tai Zhao. “Analog and RF analysis of gate all around silicon nanowire MOSFETs”. In: *2017 Joint International EUROSOI Workshop and International Conference on Ultimate Integration on Silicon (EUROSOI-ULIS)*. 2017 Joint International EUROSOI Workshop and International Conference on Ultimate Integration on Silicon (EUROSOI-ULIS). ISSN: 2472-9132. Apr. 2017, pp. 176–179. DOI: 10.1109/ULIS.2017.7962575.
- [149] Christian Enz, Maria-Anna Chalkiadaki, and Anurag Mangla. “Low-power analog/RF circuit design based on the inversion coefficient”. In: *ESSCIRC Conference 2015 - 41st European Solid-State Circuits Conference (ESSCIRC)* (Sept. 2015). Conference Name: ESSCIRC Conference 2015 - 41st European Solid-State Circuits Conference ISBN: 9781467374705 9781467374729 Place: Graz, Austria Publisher: IEEE, pp. 202–208. DOI: 10.1109/ESSCIRC.2015.7313863. URL: <http://ieeexplore.ieee.org/document/7313863/> (visited on 03/10/2023).
- [150] Shokoofeh Sheibani, Luca Capua, Sadegh Kamaei, Sayedeh Shirin Afyouni Akbari, Junrui Zhang, Hoel Guerin, and Adrian M. Ionescu. “Extended gate field-effect-transistor for sensing cortisol stress hormone”. In: *Communications Materials* 2.1 (Jan. 19, 2021). Number: 1 Publisher: Nature Publishing Group, pp. 1–10. ISSN: 2662-4443. DOI: 10.1038/s43246-020-00114-x. URL: <https://www.nature.com/articles/s43246-020-00114-x> (visited on 03/03/2023).
- [151] Michael Nastasi, James Mayer, and James K. Hirvonen. *Ion-Solid Interactions: Fundamentals and Applications*. Google-Books-ID: P0xfvcJGNfMC. Cambridge University Press, Mar. 29, 1996. 572 pp. ISBN: 978-0-521-37376-0.
- [152] Francesco Bellando. “SWEAT MONITORING WITH CMOS COMPATIBLE”. In: ().
- [153] M. A. Martínez-Puente, P. Horley, F. S. Aguirre-Tostado, J. López-Medina, H. A. Borbón-Núñez, H. Tiznado, A. Susarrey-Arce, and E. Martínez-Guerra. “ALD and PEALD deposition of HfO<sub>2</sub> and its effects on the nature of oxygen vacancies”. In: *Materials Science and Engineering: B* 285 (Nov. 1, 2022), p. 115964. ISSN: 0921-5107. DOI: 10.1016/j.mseb.2022.115964. URL: <https://www.sciencedirect.com/science/article/pii/S092151072200352X> (visited on 04/01/2023).
- [154] Dieter K. Schroder. *Semiconductor Material and Device Characterization*. Google-Books-ID: EmozDwAAQBAJ. John Wiley & Sons, June 29, 2015. 800 pp. ISBN: 978-0-471-73906-7.

## BIBLIOGRAPHY

---

- [155] N.D. Arora, J.R. Hauser, and D.J. Roulston. "Electron and hole mobilities in silicon as a function of concentration and temperature". In: *IEEE Transactions on Electron Devices* 29.2 (Feb. 1982). Conference Name: IEEE Transactions on Electron Devices, pp. 292–295. ISSN: 1557-9646. DOI: 10.1109/T-ED.1982.20698.
- [156] K.R. Williams, K. Gupta, and M. Wasilik. "Etch rates for micromachining processing-Part II". In: *Journal of Microelectromechanical Systems* 12.6 (Dec. 2003). Conference Name: Journal of Microelectromechanical Systems, pp. 761–778. ISSN: 1941-0158. DOI: 10.1109/JMEMS.2003.820936.
- [157] Bingtao Gao, Roberth Anthony Rojas Chávez, Walla I. Malkawi, Daniel W. Keefe, Rasheid Smith, Hillel Haim, Aliasger K. Salem, and Fatima Toor. "Sensitive detection of SARS-CoV-2 spike protein using vertically-oriented silicon nanowire array-based biosensor". In: *Sensing and Bio-Sensing Research* 36 (June 1, 2022), p. 100487. ISSN: 2214-1804. DOI: 10.1016/j.sbsr.2022.100487. URL: <https://www.sciencedirect.com/science/article/pii/S2214180422000162> (visited on 05/15/2023).
- [158] Guo-Jun Zhang, Li Zhang, Min Joon Huang, Zhan Hong Henry Luo, Guang Kai Ignatius Tay, Eu-Jin Andy Lim, Tae Goo Kang, and Yu Chen. "Silicon nanowire biosensor for highly sensitive and rapid detection of Dengue virus". In: *Sensors and Actuators B: Chemical* 146.1 (Apr. 8, 2010), pp. 138–144. ISSN: 0925-4005. DOI: 10.1016/j.snb.2010.02.021. URL: <https://www.sciencedirect.com/science/article/pii/S0925400510001255> (visited on 04/01/2023).
- [159] Guo-Jun Zhang and Yong Ning. "Silicon nanowire biosensor and its applications in disease diagnostics: A review". In: *Analytica Chimica Acta* 749 (Oct. 24, 2012), pp. 1–15. ISSN: 0003-2670. DOI: 10.1016/j.aca.2012.08.035. URL: <https://www.sciencedirect.com/science/article/pii/S0003267012012056> (visited on 07/30/2023).
- [160] Guo-Jun Zhang, Jay Huiyi Chua, Ru-Ern Chee, Ajay Agarwal, and She Mein Wong. "Label-free direct detection of MiRNAs with silicon nanowire biosensors". In: *Biosensors and Bioelectronics* 24.8 (Apr. 15, 2009), pp. 2504–2508. ISSN: 0956-5663. DOI: 10.1016/j.bios.2008.12.035. URL: <https://www.sciencedirect.com/science/article/pii/S0956566308006933> (visited on 04/01/2023).
- [161] Guo-Jun Zhang, Zhan Hong Henry Luo, Min Joon Huang, Jun'An Jason Ang, Tae Goo Kang, and Hongmiao Ji. "An integrated chip for rapid, sensitive, and multiplexed detection of cardiac biomarkers from fingerprick blood". In: *Biosensors and Bioelectronics* 28.1 (Oct. 15, 2011), pp. 459–463. ISSN: 0956-5663. DOI: 10.1016/j.bios.2011.07.007. URL: <https://www.sciencedirect.com/science/article/pii/S0956566311004350> (visited on 04/01/2023).
- [162] Guo-Jun Zhang, Min Joon Huang, Zhan Hong Henry Luo, Guang Kai Ignatius Tay, Eu-Jin Andy Lim, Edison T. Liu, and Jane S. Thomsen. "Highly sensitive and reversible silicon nanowire biosensor to study nuclear hormone receptor protein and response element DNA interactions". In: *Biosensors and Bioelectronics* 26.2 (Oct. 15, 2010),



- pp. 365–370. ISSN: 0956-5663. DOI: 10.1016/j.bios.2010.07.129. URL: <https://www.sciencedirect.com/science/article/pii/S095656631000504X> (visited on 04/01/2023).
- [163] Yousra Benserhir, Anne-Claire Salaün, Florence Geneste, Nolwenn Oliviero, Laurent Pichon, and Anne Jolivet-Gougeon. “Silicon nanowires-based biosensors for the electrical detection of *Escherichia coli*”. In: *Biosensors and Bioelectronics* 216 (Nov. 15, 2022), p. 114625. ISSN: 0956-5663. DOI: 10.1016/j.bios.2022.114625. URL: <https://www.sciencedirect.com/science/article/pii/S0956566322006650> (visited on 04/01/2023).
- [164] Guo-Jun Zhang, Min Joon Huang, Jun’An Jason Ang, Edison T. Liu, and Kartiki Vasant Desai. “Self-assembled monolayer-assisted silicon nanowire biosensor for detection of protein–DNA interactions in nuclear extracts from breast cancer cell”. In: *Biosensors and Bioelectronics* 26.7 (Mar. 15, 2011), pp. 3233–3239. ISSN: 0956-5663. DOI: 10.1016/j.bios.2010.12.032. URL: <https://www.sciencedirect.com/science/article/pii/S0956566310008675> (visited on 04/01/2023).
- [165] Marzhan Sypabekova, Aidan Hagemann, Donggee Rho, and Seunghyun Kim. “Review: 3-Aminopropyltriethoxysilane (APTES) Deposition Methods on Oxide Surfaces in Solution and Vapor Phases for Biosensing Applications”. In: *Biosensors* 13.1 (Jan. 2023). Number: 1 Publisher: Multidisciplinary Digital Publishing Institute, p. 36. ISSN: 2079-6374. DOI: 10.3390/bios13010036. URL: <https://www.mdpi.com/2079-6374/13/1/36> (visited on 03/31/2023).
- [166] Ahmed A. Issa and Adriaan S. Luyt. “Kinetics of Alkoxysilanes and Organoalkoxysilanes Polymerization: A Review”. In: *Polymers* 11.3 (Mar. 2019). Number: 3 Publisher: Multidisciplinary Digital Publishing Institute, p. 537. ISSN: 2073-4360. DOI: 10.3390/polym11030537. URL: <https://www.mdpi.com/2073-4360/11/3/537> (visited on 03/31/2023).
- [167] Nesrine Aissaoui, Latifa Bergaoui, Jessem Landoulsi, Jean-François Lambert, and Souhir Boujday. “Silane Layers on Silicon Surfaces: Mechanism of Interaction, Stability, and Influence on Protein Adsorption”. In: *Langmuir* 28.1 (Jan. 10, 2012). Publisher: American Chemical Society, pp. 656–665. ISSN: 0743-7463. DOI: 10.1021/la2036778. URL: <https://doi.org/10.1021/la2036778> (visited on 03/31/2023).
- [168] Naga Siva Kumar Gunda, Minashree Singh, Lana Norman, Kamaljit Kaur, and Sushanta K. Mitra. “Optimization and characterization of biomolecule immobilization on silicon substrates using (3-aminopropyl)triethoxysilane (APTES) and glutaraldehyde linker”. In: *Applied Surface Science* 305 (June 30, 2014), pp. 522–530. ISSN: 0169-4332. DOI: 10.1016/j.apsusc.2014.03.130. URL: <https://www.sciencedirect.com/science/article/pii/S0169433214006813> (visited on 03/31/2023).
- [169] “Bioconjugation and crosslinking technical handbook”. In: ().
- [170] Albert S. Lee, Seung-Sock Choi, Kyung-Youl Baek, and Seung Sang Hwang. “Hydrolysis kinetics of a sol-gel equilibrium yielding ladder-like polysilsesquioxanes”. In: *Inorganic Chemistry Communications* 73 (Nov. 1, 2016), pp. 7–11. ISSN: 1387-7003. DOI: 10.1016/

## BIBLIOGRAPHY

---

- j.inoche.2016.09.004. URL: <https://www.sciencedirect.com/science/article/pii/S1387700316302908> (visited on 03/31/2023).
- [171] Claus-Peter Klages, Vitaly Raev, Divagar Murugan, and Vemulakonda Venkata Raghavendra Sai. "Argon–water DBD pretreatment and vapor-phase silanization of silica: Comparison with wet-chemical processes". In: *Plasma Processes and Polymers* 17.7 (2020). \_eprint: <https://onlinelibrary.wiley.com/doi/pdf/10.1002/ppap.201900265>, p. 1900265. ISSN: 1612-8869. DOI: 10.1002/ppap.201900265. URL: <https://onlinelibrary.wiley.com/doi/abs/10.1002/ppap.201900265> (visited on 03/31/2023).
- [172] Thomas A. Morton and David G. Myszka. "[13] Kinetic analysis of macromolecular interactions using surface plasmon resonance biosensors". In: *Methods in Enzymology*. Vol. 295. Energetics of Biological Macromolecules Part B. Academic Press, Jan. 1, 1998, pp. 268–294. DOI: 10.1016/S0076-6879(98)95044-3. URL: <https://www.sciencedirect.com/science/article/pii/S0076687998950443> (visited on 03/28/2023).
- [173] Xiaowei Guo. "Surface plasmon resonance based biosensor technique: A review". In: *Journal of Biophotonics* 5.7 (2012), pp. 483–501. ISSN: 1864-0648. DOI: 10.1002/jbio.201200015. URL: <https://onlinelibrary.wiley.com/doi/abs/10.1002/jbio.201200015> (visited on 03/28/2023).
- [174] Jiri Homola, Sinclair S. Yee, and Günter Gauglitz. "Surface plasmon resonance sensors: review". In: *Sensors and Actuators B: Chemical* 54.1 (Jan. 25, 1999), pp. 3–15. ISSN: 0925-4005. DOI: 10.1016/S0925-4005(98)00321-9. URL: <https://www.sciencedirect.com/science/article/pii/S0925400598003219> (visited on 03/28/2023).
- [175] Adrian C. Melissinos and Jim Napolitano. *Experiments in Modern Physics*. Google-Books-ID: eTK1IX\_oCUcC. Gulf Professional Publishing, Mar. 17, 2003. 562 pp. ISBN: 978-0-12-489851-6.
- [176] Maria Antoniou, Dimitra Tsounidi, Panagiota S. Petrou, Konstantinos G. Beltsios, and Sotirios E. Kakabakos. "Functionalization of silicon dioxide and silicon nitride surfaces with aminosilanes for optical biosensing applications". In: *MEDICAL DEVICES & SENSORS* 3.5 (2020). \_eprint: <https://onlinelibrary.wiley.com/doi/pdf/10.1002/mds3.10072>, e10072. ISSN: 2573-802X. DOI: 10.1002/mds3.10072. URL: <https://onlinelibrary.wiley.com/doi/abs/10.1002/mds3.10072> (visited on 04/01/2023).
- [177] Emanuele Luigi Sciuto, Corrado Bongiorno, Antonino Scandurra, Salvatore Petralia, Tiziana Cosentino, Sabrina Conoci, Fulvia Sinatra, and Sebania Libertino. "Functionalization of Bulk SiO<sub>2</sub> Surface with Biomolecules for Sensing Applications: Structural and Functional Characterizations". In: *Chemosensors* 6.4 (Dec. 2018). Number: 4 Publisher: Multidisciplinary Digital Publishing Institute, p. 59. ISSN: 2227-9040. DOI: 10.3390/chemosensors6040059. URL: <https://www.mdpi.com/2227-9040/6/4/59> (visited on 04/01/2023).

- [178] Amrita R. Yadav, Rashmi Sriram, Jared A. Carter, and Benjamin L. Miller. “Comparative study of solution–phase and vapor–phase deposition of aminosilanes on silicon dioxide surfaces”. In: *Materials Science and Engineering: C* 35 (Feb. 1, 2014), pp. 283–290. ISSN: 0928-4931. DOI: 10.1016/j.msec.2013.11.017. URL: <https://www.sciencedirect.com/science/article/pii/S0928493113006309> (visited on 04/01/2023).
- [179] A. Shchukarev and D. Korolkov. “XPS Study of group IA carbonates”. In: *Open Chemistry* 2.2 (2004), pp. 347–362. ISSN: 2391-5420. DOI: 10.2478/BF02475578. URL: [http://psjd.icm.edu.pl/psjd/element/bwmeta1.element-psjd-doi-10\\_2478\\_BF02475578](http://psjd.icm.edu.pl/psjd/element/bwmeta1.element-psjd-doi-10_2478_BF02475578) (visited on 04/01/2023).
- [180] *Carbon | XPS Periodic Table - CH*. URL: <https://www.thermofisher.com/uk/en/home/materials-science/learning-center/periodic-table/non-metal/carbon.html> (visited on 04/01/2023).
- [181] R. J. J. Jansen and H. van Bekkum. “XPS of nitrogen-containing functional groups on activated carbon”. In: *Carbon* 33.8 (Jan. 1, 1995), pp. 1021–1027. ISSN: 0008-6223. DOI: 10.1016/0008-6223(95)00030-H. URL: <https://www.sciencedirect.com/science/article/pii/000862239500030H> (visited on 04/01/2023).
- [182] Joanna S. Stevens, Alba C. de Luca, Michalis Pelendritis, Giorgio Terenghi, Sandra Downes, and Sven L. M. Schroeder. “Quantitative analysis of complex amino acids and RGD peptides by X-ray photoelectron spectroscopy (XPS): Quantitative XPS analysis of amino acids and RGD peptides”. In: *Surface and Interface Analysis* 45.8 (Aug. 2013), pp. 1238–1246. ISSN: 01422421. DOI: 10.1002/sia.5261. URL: <https://onlinelibrary.wiley.com/doi/10.1002/sia.5261> (visited on 04/01/2023).
- [183] Kateryna Artyushkova and Plamen Atanassov. “X-Ray Photoelectron Spectroscopy for Characterization of Bionanocomposite Functional Materials for Energy-Harvesting Technologies”. In: *ChemPhysChem* 14.10 (2013), pp. 2071–2080. ISSN: 1439-7641. DOI: 10.1002/cphc.201300037. URL: <https://onlinelibrary.wiley.com/doi/abs/10.1002/cphc.201300037> (visited on 04/01/2023).
- [184] A. Artemenko, A. Shchukarev, P. Štenclová, T. Wågberg, J. Segervald, X. Jia, and A. Kromka. “Reference XPS spectra of amino acids”. In: *IOP Conference Series: Materials Science and Engineering* 1050.1 (Jan. 2021). Publisher: IOP Publishing, p. 012001. ISSN: 1757-899X. DOI: 10.1088/1757-899X/1050/1/012001. URL: <https://dx.doi.org/10.1088/1757-899X/1050/1/012001> (visited on 04/01/2023).
- [185] *Nitrogen | XPS Periodic Table - CH*. URL: <https://www.thermofisher.com/uk/en/home/materials-science/learning-center/periodic-table/non-metal/nitrogen.html> (visited on 04/01/2023).
- [186] Günter Sauerbrey. “Verwendung von Schwingquarzen zur Wägung dünner Schichten und zur Mikrowägung”. In: *Zeitschrift für Physik* 155.2 (Apr. 1, 1959), pp. 206–222. ISSN: 0044-3328. DOI: 10.1007/BF01337937. URL: <https://doi.org/10.1007/BF01337937> (visited on 03/05/2023).

## BIBLIOGRAPHY

---

- [187] Ronen Fogel, Janice Limson, and Ashwin A. Seshia. "Acoustic biosensors". In: *Essays in Biochemistry* 60.1 (June 30, 2016). Ed. by Pedro Estrela, pp. 101–110. ISSN: 0071-1365. DOI: 10.1042/EBC20150011. URL: <https://doi.org/10.1042/EBC20150011> (visited on 03/05/2023).
- [188] K Keiji Kanazawa and Joseph G Gordon. "The oscillation frequency of a quartz resonator in contact with liquid". In: *Analytica Chimica Acta* 175 (Jan. 1, 1985), pp. 99–105. ISSN: 0003-2670. DOI: 10.1016/S0003-2670(00)82721-X. URL: <https://www.sciencedirect.com/science/article/pii/S000326700082721X> (visited on 03/05/2023).
- [189] Matthew C. Dixon. "Quartz Crystal Microbalance with Dissipation Monitoring: Enabling Real-Time Characterization of Biological Materials and Their Interactions". In: *Journal of Biomolecular Techniques : JBT* 19.3 (July 2008), pp. 151–158. ISSN: 1524-0215. URL: <https://www.ncbi.nlm.nih.gov/pmc/articles/PMC2563918/> (visited on 03/05/2023).
- [190] A. Evren Özçam, Kirill Efimenko, and Jan Genzer. "Effect of ultraviolet/ozone treatment on the surface and bulk properties of poly(dimethyl siloxane) and poly(vinylmethyl siloxane) networks". In: *Polymer* 55.14 (June 19, 2014), pp. 3107–3119. ISSN: 0032-3861. DOI: 10.1016/j.polymer.2014.05.027. URL: <https://www.sciencedirect.com/science/article/pii/S0032386114004042> (visited on 04/01/2023).
- [191] Jongsoo Kim, Manoj K. Chaudhury, and Michael J. Owen. "Hydrophobic Recovery of Polydimethylsiloxane Elastomer Exposed to Partial Electrical Discharge". In: *Journal of Colloid and Interface Science* 226.2 (June 15, 2000), pp. 231–236. ISSN: 0021-9797. DOI: 10.1006/jcis.2000.6817. URL: <https://www.sciencedirect.com/science/article/pii/S0021979700968176> (visited on 04/01/2023).
- [192] Alexandra Borók, Kristóf Laboda, and Attila Bonyár. "PDMS Bonding Technologies for Microfluidic Applications: A Review". In: *Biosensors* 11.8 (Aug. 2021). Number: 8 Publisher: Multidisciplinary Digital Publishing Institute, p. 292. ISSN: 2079-6374. DOI: 10.3390/bios11080292. URL: <https://www.mdpi.com/2079-6374/11/8/292> (visited on 04/01/2023).
- [193] David G. Myszka. "Improving biosensor analysis". In: *Journal of Molecular Recognition* 12.5 (Sept. 1999), pp. 279–284. ISSN: 0952-3499, 1099-1352. DOI: 10.1002/(SICI)1099-1352(199909/10)12:5<279::AID-JMR473>3.0.CO;2-3. URL: [https://onlinelibrary.wiley.com/doi/10.1002/\(SICI\)1099-1352\(199909/10\)12:5%3C279::AID-JMR473%3E3.0.CO;2-3](https://onlinelibrary.wiley.com/doi/10.1002/(SICI)1099-1352(199909/10)12:5%3C279::AID-JMR473%3E3.0.CO;2-3) (visited on 03/07/2023).
- [194] Tomáš Špringer, Markéta Bocková, and Jiří Homola. "Label-Free Biosensing in Complex Media: A Referencing Approach". In: *Analytical Chemistry* 85.12 (June 18, 2013). Publisher: American Chemical Society, pp. 5637–5640. ISSN: 0003-2700. DOI: 10.1021/ac401062m. URL: <https://doi.org/10.1021/ac401062m> (visited on 03/07/2023).

- [195] Meng Zhang, Chun Ge, Meng Lu, Zhixiong Zhang, and Brian T. Cunningham. "A self-referencing biosensor based upon a dual-mode external cavity laser". In: *Applied Physics Letters* 102.21 (May 27, 2013), p. 213701. ISSN: 0003-6951. DOI: 10.1063/1.4801427. URL: <https://www.ncbi.nlm.nih.gov/pmc/articles/PMC3683028/> (visited on 03/07/2023).
- [196] Yiran Yang and Wei Gao. "Wearable pH sensing beyond the Nernst limit". In: *Nature Electronics* 1.11 (Nov. 2018). Number: 11 Publisher: Nature Publishing Group, pp. 580–581. ISSN: 2520-1131. DOI: 10.1038/s41928-018-0166-1. URL: <https://www.nature.com/articles/s41928-018-0166-1> (visited on 04/01/2023).
- [197] Abir Shadman, Ehsanur Rahman, and Quazi D. M. Khosru. "Monolayer MoS<sub>2</sub> and WSe<sub>2</sub> Double Gate Field Effect Transistor as Super Nernst pH sensor and Nanobiosensor". In: *Sensing and Bio-Sensing Research* 11 (Dec. 1, 2016), pp. 45–51. ISSN: 2214-1804. DOI: 10.1016/j.sbsr.2016.08.005. URL: <https://www.sciencedirect.com/science/article/pii/S2214180416300629> (visited on 04/01/2023).
- [198] Sanggil Han, Shunsuke Yamamoto, Anastasios G. Polyravas, and George G. Malliaras. "Microfabricated Ion-Selective Transistors with Fast and Super-Nernstian Response". In: *Advanced Materials* 32.48 (2020), p. 2004790. ISSN: 1521-4095. DOI: 10.1002/adma.202004790. URL: <https://onlinelibrary.wiley.com/doi/abs/10.1002/adma.202004790> (visited on 04/01/2023).
- [199] Ting Wu, Abdullah Alharbi, Kai-Dyi You, Kim Kisslinger, Eric A. Stach, and Davood Shahrjerdi. "Experimental Study of the Detection Limit in Dual-Gate Biosensors Using Ultrathin Silicon Transistors". In: *ACS Nano* 11.7 (July 25, 2017). Publisher: American Chemical Society, pp. 7142–7147. ISSN: 1936-0851. DOI: 10.1021/acsnano.7b02986. URL: <https://doi.org/10.1021/acsnano.7b02986> (visited on 04/01/2023).
- [200] Sooraj Sanjay, Mainul Hossain, Ankit Rao, and Navakanta Bhat. "Super-Nernstian ion sensitive field-effect transistor exploiting charge screening in WSe<sub>2</sub>/MoS<sub>2</sub> heterostructure". In: *npj 2D Materials and Applications* 5.1 (Dec. 16, 2021). Number: 1 Publisher: Nature Publishing Group, pp. 1–8. ISSN: 2397-7132. DOI: 10.1038/s41699-021-00273-6. URL: <https://www.nature.com/articles/s41699-021-00273-6> (visited on 04/01/2023).
- [201] Jonghyun Go, Pradeep R. Nair, and Muhammad A. Alam. "Theory of signal and noise in double-gated nanoscale electronic pH sensors". In: *Journal of Applied Physics* 112.3 (Aug. 2012). Publisher: American Institute of Physics, p. 034516. ISSN: 0021-8979. DOI: 10.1063/1.4737604. URL: <https://aip.scitation.org/doi/full/10.1063/1.4737604> (visited on 03/24/2023).
- [202] *Operation and Modeling of the MOS Transistor (The Oxford Series in Electrical and Computer Engineering): Tividis, Yannis, McAndrew, Colin: 9780195170153: Amazon.com: Books.* URL: <https://www.amazon.com/Operation-Modeling-Transistor-Electrical-Engineering/dp/0195170156> (visited on 04/11/2023).

## BIBLIOGRAPHY

---

- [203] Qiuyang Lin, Wim Sijbers, Christina Avdikou, Didac Gomez, Dwaipayan Biswas, Sneha Sneha, Anastasios Malissovass, Bernardo Tacca, and Nick Van Helleputte. “21.2 A  $\mu$ W Peak Power Multimodal Electrochemical Sensor Interface IC for Bioreactor Monitoring”. In: *2023 IEEE International Solid- State Circuits Conference (ISSCC)*. 2023 IEEE International Solid- State Circuits Conference (ISSCC). ISSN: 2376-8606. Feb. 2023, pp. 314–316. DOI: 10.1109/ISSCC42615.2023.10067298.
- [204] Seulki Cho, Alexander Zaslavsky, Curt A. Richter, Jacob M. Majikes, J. Alexander Liddle, François Andrieu, Sylvain Barraud, and Arvind Balijepalli. “High-Resolution DNA Binding Kinetics Measurements with Double Gate FD-SOI Transistors”. In: *2022 International Electron Devices Meeting (IEDM)*. 2022 International Electron Devices Meeting (IEDM). ISSN: 2156-017X. Dec. 2022, pp. 24.2.1–24.2.4. DOI: 10.1109/IEDM45625.2022.10019493.



# Publications

**L. Capua** and Y. Sprunger, H. Eletto, F. Risch, A. Grammoustianou, R. Midahuen, T. Ernst, S. Barraud, R. Gill, and A. M. Ionescu. "Label-Free C-Reactive Protein Si Nanowire FET Sensor Arrays With Super-Nernstian Back-Gate Operation". In: IEEE Transactions on Electron Devices 69.4 (2022). IEEE, pp. 2159–2165

**L. Capua**, Y. Sprunger, H. Eletto, A. Grammoustianou, R. Midahuen, T. Ernst, S. Barraud, R. Gill, and A. M. Ionescu. "Double-Gate Si Nanowire FET Sensor Arrays For Label-Free C-Reactive Protein detection enabled by antibodies fragments and pseudo- super-Nernstian back-gate operation". In: 2021 IEEE International Electron Devices Meeting (IEDM). IEEE, 2021, pp. 16–2.

**L. Capua**, S. Sheibani, S. Kamaei, J. Zhang, and A. M. Ionescu. "Extended-Gate FET cortisol sensor for stress disorders based on aptamers-decorated graphene electrode: Fabrication, Experiments and Unified Analog Predictive Modeling". In: 2020 IEEE International Electron Devices Meeting (IEDM). IEEE, 2020, pp. 35–2

Y. Sprunger and **L. Capua**, T. Ernst, S. Barraud, A.M. Ionescu, and A. Saeidi. "Ultra-High Sensitivity Silicon Nanowire Array Biosensor Based on a Constant-Current Method for Continuous Real-Time pH and Protein Monitoring in Interstitial Fluid" In 2023 49th European Solid-State Device Research Conference (ESSDERC), (unpublished).

S. Sheibani, **L. Capua**, S. Kamaei, S. S. A. Akbari, J. Zhang, H. Guerin, and A. M. Ionescu. "Extended gate field-effect-transistor for sensing cortisol stress hormone". In: Communications Materials 2.1 (Jan. 19, 2021). Nature Publishing Group.

N. Oliva, J. Backman, **L. Capua**, M. Cavalieri, M. Luisier, and A. M. Ionescu. "WSe<sub>2</sub>/SnSe<sub>2</sub> vdW heterojunction Tunnel FET with subthermionic characteristic and MOSFET co-integrated on same WSe<sub>2</sub> flake". In: npj 2D Materials and Applications 4.1 (Apr. 30, 2020). Nature Publishing Group.



---

N. Oliva, **L. Capua**, M. Cavaliere, and A. M. Ionescu. “Co-integrated Subthermionic 2D/2D WSe<sub>2</sub>/SnSe<sub>2</sub> Vertical Tunnel FET and WSe<sub>2</sub> MOSFET on same flake: towards a 2D/2D vdW Dual-Transport Steep Slope FET”. In: 2019 IEEE International Electron Devices Meeting (IEDM). IEEE, 2019, pp. 37–2. 153

S. Kamaei, A. Saeidi, C. Gastaldi, T. Rosca, **L. Capua**, M. Cavaliere, and A. M. Ionescu. “Gate energy efficiency and negative capacitance in ferroelectric 2D/2D TFET from cryogenic to high temperatures”. In: npj 2D Materials and Applications 5.1 (2021). Nature Publishing Group, pp. 1–10.

P. W. Ruch, R. Hu, **L. Capua**, Y. Temiz, S. Paredes, A. Lopez, J. Barroso, A. Cox, E. Nakamura, and K. Matsumoto. “A portable potentiometric electronic tongue leveraging smartphone and cloud platforms”. In: 2019 IEEE International Symposium on Olfaction and Electronic Nose (ISOEN). IEEE, 2019, pp. 1–3.

# LUCA CAPUA

Microelectronics and sensors, young professional

📍 Lausanne, Vaud, Switzerland

✉ capua.luca@protonmail.com

in [linkedin.com/in/lucacapua](https://www.linkedin.com/in/lucacapua)

☎ Skype: live:..cid.2aedd6b056bda0e0



## STRENGTHS

- Cleanroom microfabrication
- Surface functionalization techniques
- FET Electrical characterization
- Biosensors design
- Data Analysis for visual representation
- Multidisciplinary project collaboration

## EDUCATION

**PhD Microsystems and microelectronics**

Swiss Federal Institute of Technology Lausanne (EPFL)

Oct 2018 - Sep 2023

**MSc Micro and Nanotechnologies, Triple degree program**

Swiss Federal Institute of Technology Lausanne (EPFL) – Politecnico di Torino – INP Grenoble

Oct 2016 - Sep 2018

**BSc Engineering physics**

Politecnico di Torino

Sep 2013 - Oct 2016

## PROFESSIONAL EXPERIENCE

**Nanoelectronic Devices Laboratory (Nanolab), Swiss Federal Institute of Technology Lausanne (EPFL)**

Lausanne, Switzerland

Oct 2018 - Sep 2023

**pH and protein detection in Human Biofluids using FD-SOI Silicon Nanowire Arrays, Ph.D. Thesis**

Development of FET-based biomarker sensor for pH and proteins monitoring, in the contest of Digipredict European project. Fabrication of a CMOS-compatible wearable protein biosensor that could function in human interstitial fluid for real-time biomarkers monitoring. Core tasks included:

- Design and microfabrication of silicon nanowires biosensors on SOI technology.
- DC and AC electrical characterization.
- Oxide surface functionalization for protein detection.
- Two scientific presentations at international conferences.
- Contributor to eight publications in high impact-factors peer-reviewed journals.

**IBM HyperTaste Project, IBM Research - Zürich**

Zürich, Switzerland

Feb 2018 – Sep 2018

Fabrication and characterization of miniaturized cross-sensitive electrochemical sensors for the investigation of the fingerprint of different food products.

- Obtained experimental results lead to filing of the **US Patent 11085894**, 'Sensor apparatus with liquid container and wiper'.
- Comprehension of the fabrication process flow of electrochemical potentiometric for ion sensing.
- Fabrication of the sensitive layer through electrodeposition of polymers.
- Beverages fingerprint elaboration through ML algorithms.

**IBM Cognitive Sensor Project, IBM Research - Almaden**

San Jose, California, USA

May 2017 – Sep 2017

Electrical characterization of polymeric based sensors for VOCs detection.

- Test of different materials and geometrical configurations.
- Study of the sensitivity and selectivity of different polymers.

## TECHNICAL SKILLS

### Electrical Characterization

- Steady state DC characterization of Field-Effect transistors based on novel materials and geometries.
- Cascade and Karl Suss probers manipulation and setup design.
- PalmSens potentiostat for chronoamperometry, potentiometry and electrochemical impedance spectroscopy.
- Conducted training sessions for electrical instrumentation for new users.
- Collaborated with EPFL start-ups for electrical measurements, and statistical analysis of results.

### Surface Functionalization

- Self-Assembled Monolayer techniques: silanization chemistry, specific molecules cross-linking.
- Antibody immobilization on high-k oxide surfaces.
- Quartz Crystal Microbalance Analysis (QCM-D).

### Microfabrication

Cleanroom proficiency.

- Layout design: KLayout, L-edit.
- Lithography: direct-write (maskless) lithography, E-beam lithography.
- Dry and wet etching techniques.
- Thin film deposition: Atomic Layer Deposition (ALD), e-beam PVD, sputter deposition.
- PDMS microfluidics: soft lithography techniques.

### Material Analysis

- X-Ray Photoelectron Spectroscopy (XPS).
- Energy-Dispersive X-Ray (EDX).
- Scanning Electron Microscopy (SEM).
- Fourier Transform Infrared Spectroscopy (FTIR).

### Project Management

- Technical reporting: technical reports for European Projects.
- Writing amendments of deliverables for European Projects.
- Problem-solving.
- Scientific setup design and purchase.
- Laboratory organization: cleaning, instrumentation log files, consumables supplies.
- Team building: yearly organization of laboratory activities.
- Wide international experience: collaboration with engineers and researchers from industry and academy within the Digipredict Consortium<sup>1</sup>.

### Data Analysis & IT

- Statistical analysis and data visualization for data collected from electrical characterization of semiconductor devices: Matlab, OriginLab, Python.
- Technical reports and scientific divulgation: Latex, Office Suite.
- Creation of professional quality images for research papers and reports: Adobe Illustrator, Blender, Fusion360.

### Languages

- Italian, native language.
- English, professional proficiency.
- French, B1 level oral, A2 written.

### Publications

- Three first-author articles in IEEE Publishing Group.
- Two presentations at IEEE International Electron Devices Meeting (IEDM 2020 and 2021).
- Three co-author papers in Nature Publishing Group (Nature Comm. Materials, Npj 2D Materials)

### Extra Activities

- Video Editing
- Kitesurfing
- Hiking
- Football

---

<sup>1</sup> Link to Digipredict Project Webpage : <https://www.digipredict.eu/>